FINAL REPORT ~ FHWA-OK-21-03

EVALUATION OF ULTRA-HIGH PERFORMANCE CONCRETE, FIBER REINFORCED SELF-CONSOLIDATING CONCRETE, AND MALP CONCRETE FOR PRESTRESSED GIRDER REPAIR

Royce W. Floyd, Ph.D., P.E., S.E.(OK)
Jeffery S. Volz, S.E., P.E., Ph.D.
Trevor Looney, P.E. Ph.D. Candidate
Michael Mesigh, M.S. Candidate
Mujtaba Ahmadi, M.S. Candidate
Stephen Roswurm, Ph.D. Candidate
Phuoc Huynh, M.S. Candidate
Michelle Manwarren, M.S.

School of Civil Engineering and Environmental Science (CEES)
The University of Oklahoma
Norman, Oklahoma

February 2021

OKLAHOMA Transportation

The Oklahoma Department of Transportation (ODOT) ensures that no person or groups of persons shall, on the grounds of race, color, sex, religion, national origin, age, disability, retaliation or genetic information, be excluded from participation in, be denied the benefits of, or be otherwise subjected to discrimination under any and all programs, services, or activities administered by ODOT, its recipients, sub-recipients, and contractors. To request an accommodation please contact the ADA Coordinator at 405-521-4140 or the Oklahoma Relay Service at 1-800-722-0353. If you have any ADA or Title VI questions email ODOT-ada-titlevi@odot.org.

EVALUATION OF ULTRA-HIGH PERFORMANCE CONCRETE, FIBER REINFORCED SELF-CONSOLIDATING CONCRETE, AND MALP CONCRETE FOR PRESTRESSED GIRDER REPAIR

FINAL REPORT ~ FHWA-OK-21-03
ODOT SPR ITEM NUMBER 2284

Submitted to:
Office of Research and Implementation
Oklahoma Department of Transportation

Submitted by:
Royce W. Floyd, Ph.D., P.E., S.E.(OK)
Jeffery S. Volz, S.E., P.E., Ph.D.
Trevor Looney, P.E. Ph.D. Candidate
Michael Mesigh, M.S. Candidate
Mujtaba Ahmadi, M.S. Candidate
Stephen Roswurm, Ph.D. Candidate
Phuoc Huynh, M.S. Candidate
Michelle Manwarren, M.S.
School of Civil Engineering and Environmental Science (CEES)
The University of Oklahoma

OKLAHOMA
Transportation

February 2021

TECHNICAL REPORT DOCUMENTATION PAGE

1. REPORT NO.	2. GOVERNMENT ACCESSION NO.	3. RECIPIENT'S CATALOG NO.
FHWA-OK-21-03		

4. TITLE AND SUBTITLE	5. REPORT DATE
Evaluation of Ultra-High Performance Concrete, Fiber Reinforced Self-Consolidating Concrete, and MALP Concrete for Prestressed Girder Repair	Feb 2020
	6. PERFORMING ORGANIZATION CODE

7. AUTHOR(S)	8. PERFORMING ORGANIZATION REPORT
Royce W. Floyd, Jeffery S. Volz, Trevor Looney, Michael Mesigh, Mujtaba Ahmadi, Stephen Roswurm, Phuoc Huynh, Michelle Manwarren	Click here to enter text.

9. PERFORMING ORGANIZATION NAME AND ADDRESS	10. WORK UNIT NO.
Donald G. Fears Structural Engineering Laboratory School of Civil Engineering and Environmental Science The University of Oklahoma, 303 E. Chesapeake St., Norman, OK 73019	11. CONTRACT OR GRANT NO. ODOT SPR Item Number 2284

12. SPONSORING AGENCY NAME AND ADDRESS	13. TYPE OF REPORT AND PERIOD COVERED
Oklahoma Department of Transportation Office of Research and Implementation 200 N.E. 21st Street, Room G18 Oklahoma City, OK 73105	Final Report Oct 2018 - Dec 2020
	14. SPONSORING AGENCY CODE

15. SUPPLEMENTARY NOTES

Click here to enter text.

16. ABSTRACT

Ultra-high performance concrete (UHPC), fiber-reinforced self-consolidating concrete, and magnesium-alumino-liquid-phosphate (MALP) concrete all have significant potential for use in bridge repair in Oklahoma. The project described in this report examined the use of these materials in repairs of prestressed concrete girder continuity connections and beam end regions including both experimental testing and field implementation. Bond between the repair materials and conventional concrete and corrosion behavior were examined for each repair material. Twelve composite beam and continuity joint specimens were damaged and repaired using FR-SCC, MALP concrete, and UHPC. All repair materials restored capacity of the joints. Six girder specimens were loaded to failure in shear and repaired using FR-SCC, MALP concrete, and UHPC. Repaired specimens exhibited similar performance for all three repair materials and measured capacities exceeded those for the original beams in all cases. The soffit of the bridge deck cantilevers on the S.H. 3 bridge over Fulton Creek in Beaver County, Oklahoma was repaired using pneumatically placed MALP mortar and the repairs were monitored over time. Some difficulties were encountered in placing the material, but the repair exhibited good performance over time. The continuity joints on the U.S. 183/412 bridge over Wolf Creek in Fort Supply, Oklahoma were replaced using UHPC and load tests indicated the repair reestablished continuity.

17. KEY WORDS	18. DISTRIBUTION STATEMENT
ultra-high performance concrete, fiber reinforced self-consolidating concrete, MALP	No restrictions. This publication is available from the Office of Research and Implementation, Oklahoma DOT.

19. SECURITY CLASSIF. (OF THIS REPORT)	20. SECURITY CLASSIF. (OF THIS PAGE)	21. NO. OF PAGES	22. PRICE
Unclassified	Unclassified	313	N/A

SI* (MODERN METRIC) CONVERSION FACTORS

APPROXIMATE CONVERSIONS TO SI UNITS

SYMBOL	WHEN YOU KNOW	MULTIPLY BY	TO FIND	SYMBO
		LENGTH		
in	inches	25.4	millimeters	mm
ft	feet	0.305	meters	m
yd	yards	0.914	meters	m
mi	miles	1.61	kilometers	km
		AREA		
in^2	square inches	645.2	square millimeters	mm^2
ft^2	square feet	0.093	square meters	m^2
yd^2	square yard	0.836	square meters	m^2
ac	acres	0.405	hectares	ha
mi^2	square miles	2.59	square kilometers	km^2
		VOLUME		
fl oz	fluid ounces	29.57	milliliters	m
gal	gallons	3.785	liters	L
ft^3	cubic feet	0.028	cubic meters	L
yd^3	cubic yards	0.765	cubic meters	m^3
	NOTE: volumes greater than 1000 L shall be		shown in m^3	m^3
		MASS		
oz	ounces	28.35	grams	g
lb	pounds	0.454	kilograms	kg
T	short tons (2000 lb)	0.907	megagrams (or "metric ton")	Mg (or "t")
		TEMPERATURE (exact degrees)		
°F	Fahrenheit	5 (F-32)/9 or (F-32)/1.8	Celsius	°C
		ILLUMINATION		
fc	foot-candles	10.76	lux	lx
fl	foot-Lamberts	3.426	$candela/m^2$	cd/m^2
		FORCE and PRESSURE or STRESS		
lbf	poundforce	4.45	newtons	N
lbf/in^2	poundforce per square inch	6.89	kilopascals	kPa

APPROXIMATE CONVERSIONS FROM SI UNITS

SYMBOL	WHEN YOU KNOW	MULTIPLY BY	TO FIND	SYMBO
		LENGTH		
mm	millimeters	0.039	inches	in
m	meters	3.28	feet	ft
m	meters	1.09	yards	yd
km	kilometers	0.621	miles	mi
		AREA		
mm^2	square millimeters	0.0016	square inches	in^2
m^2	square meters	10.764	square feet	ft^2
m^2	square meters	1.195	square yards	yd^2
ha	hectares	2.47	acres	ac
km^2	square kilometers	0.386	square miles	mi^2
		VOLUME		
mL	milliliters	0.034	fluid ounces	fl oz
L	liters	0.264	gallons	gal
m^3	cubic meters	35.314	cubic feet	ft^3
m^3	cubic meters	1.307	cubic yards	yd^3
		MASS		
g	grams	0.035	ounces	oz
kg	kilograms	2.202	pounds	lb
Mg (or "t")	megagrams (or "metric ton")	1.103	short tons (2000 lb)	T
		TEMPERATURE (exact degrees)		
°C	Celsius	1.8C+32	Fahrenheit	°F
		ILLUMINATION		
lx	lux	0.0929	foot-candles	fc
cd/m^2	$candela/m^2$	0.2919	foot-Lamberts	fl
		FORCE and PRESSURE or STRESS		
N	newtons	0.225	poundforce	lbf
kPa	kilopascals	0.145	poundforce per square inch	lbf/in^2

*SI is the symbol for the International System of Units. Appropriate rounding should be made to comply with Section 4 of ASTM E380. (Revised March 2003)

ACKNOWLEDGEMENTS

The following students who participated in the project and made a contribution are acknowledged: Cole Walker, Levi Kell, Jacob Starks, Mathew Alvarado, Yana Dyachkova, Richard Campos, Kim Serey Vuth Chea, Connor Casey, Jake Choate and Stephen Roswurm. The work of Fears Lab Manager/Technician Mr. Michael Schmitz in providing support for this project is greatly appreciated.

The following companies provided materials and/or technical input at a reduced cost or at no cost for this project: LafargeHolcim Ductal®, Dolese Bros. Inc., Norchem Corporation, Bekaert, and Phoscrete Corporation.

The authors also sincerely appreciate the collaboration of Walt Peters (Bridge), Wayne Roesner (Division 6), and Brad Harmon (Division 6) with ODOT on the two implementation projects.

EXECUTIVE SUMMARY

Ultra-high performance concrete (UHPC), fiber-reinforced self-consolidating concrete (FR-SCC), and magnesium-alumino-liquid-phosphate (MALP) concrete all have significant potential for use in bridge repair in Oklahoma. However limited data are available for performance of these materials in repair applications. The project described in this report examined the use of these materials in repairs of prestressed concrete girder continuity connections and beam end regions including both experimental testing and field implementation.

Mixing and placement methods, bond between the repair materials and conventional concrete, and corrosion behavior were examined for each repair material. Material property tests were conducted to evaluate the properties of FR-SCC as a repair material to use when strengthening degraded existing structures. Twelve composite beam and continuity joint specimens were loaded to induce damage and repaired using FR-SCC, MALP concrete, and UHPC. The repaired specimens were then loaded for either positive or negative moment to represent behavior in the field. All repair materials restored capacity of the joints. Six approximately half-scale AASHTO Type II girder specimens were loaded to failure and repaired using FR-SCC, MALP concrete, and UHPC. Repaired specimens exhibited similar performance for all three repair materials and measured capacities exceeded those for the original beams in all cases.

The soffit of the bridge deck cantilevers on the S.H. 3 bridge over Fulton Creek in Beaver County, Oklahoma was repaired using pneumatically placed MALP mortar and the repairs were monitored over time. Some difficulties were encountered in placing the material, but no significant deterioration was noted over time. The U.S. 183/412 bridge over Wolf Creek in Fort Supply, Oklahoma exhibited signs of continuity joint failure and all continuity connections were replaced using UHPC. A load test was conducted before and after the joint repair to assess the change in behavior after replacing the joints with UHPC. The load test results indicated that the repairs resulted in restoration of continuity for the bridge spans.

Table of Contents

ACKNOWLEDGEMENTS vi

EXECUTIVE SUMMARY vii

List of Figures xv

List of Tables xxviii

1.0 Introduction 1

1.1 Overview 1

1.2 Problem Statement 2

1.3 Project Objectives 3

2.0 Literature Review 4

2.1 Prestressed Concrete Girder Deterioration 4

2.1.1 Continuity Joint Deterioration 4

2.1.2 End Region Deterioration 6

2.1.3 Prestressed Concrete Girder Repair 9

2.2 Ultra-High Performance Concrete (UHPC) as a Repair Material 10

2.2.1 Overview 10

2.2.2 Material Properties 12

2.2.3 Mix Designs 13

2.2.4 Mixing, Placement, and Curing 16

2.2.5 Overlays 20

2.2.6 Girder Repair 25

2.2.7 UHPC to Conventional Concrete Bond Strength 29

2.2.7.1 Overview 29

2.2.7.2 Direct Tension Pull-Off Test 31

2.2.7.3 Slant Shear Test 32

2.2.7.4 Splitting Tensile Strength Test 35

2.2.7.5 Flexural Beam Test....36
2.3 FR-SCC as a Repair Material....37
2.3.1 Overview....37
2.3.2 Previous Research on FR-SCC as a Repair Material....38
2.4 MALP Concrete as a Repair Material....43
2.5 Corrosion in Concrete Repair....44
2.6 Summary....47
3.0 Mixing and Placement Methods for Repair materials....48
3.1 Overview....48
3.2 FR-SCC Characterization....48
3.3 Bond Testing....55
3.3.1 Overview....55
3.3.2 FR-SCC Bond Tests....55
3.3.3 UHPC Bond Tests....68
3.3.4 Placement Method Evaluation....72
4.0 Live Load Continuity Connection Repairs....72
4.1 Overview....72
4.2 Girder Specimen Construction....73
4.2.1 Girder Design....73
4.2.2 Girder Formwork and Reinforcement....79
4.2.3 Girder Casting....83
4.3 Continuity Joint and Deck Construction....86
4.3.1 Continuity Joint Formwork....86
4.3.2 Composite Deck Slab Formwork....87
4.3.3 Deck and Continuity Joint Casting....91

4.4 Class AA Concrete Compressive Strength 93
4.5 Initial Specimen Testing 93
4.5.1 Specimen Testing Arrangement 93
4.5.2 Specimen Testing Procedure 95
4.6 Control Girder Testing and Results 96
4.6.1 Overview 96
4.6.2 Control Specimen C1 Results 96
4.6.3 Control Specimen C2 Results 100
4.6.4 Control Specimen C3 Results 104
4.6.5 Control Girder Testing Summary 107
4.7 Initial Cracking of Girders to be Repaired 108
4.7.1 Overview 108
4.7.2 Cracking of J3 UHPC Repair Specimens 109
4.7.3 Cracking FR-SCC Repair Specimens 112
4.7.4 Cracking of Phoscrete® Repair Specimens 114
4.7.5 Initial Cracking Load Summary 117
4.8 Joint Repair 117
4.8.1 Overview 117
4.8.2 Joint Repair Design 118
4.8.3 Joint Repair Reinforcement and Formwork 120
4.8.4 Mixing and Placing Repair Concrete 125
4.8.5 Repair Concrete Compressive Strengths 128
4.9 Repair Testing 128
4.9.1 Overview 128

4.9.2 Ultra-High-Performance Concrete Repair Results 129
4.9.2.1 Repair Specimen R1-J3 Results 129
4.9.2.2 Repair Specimen R2-J3 Results 132
4.9.2.3 Repair Specimen R3-J3 Results 135
4.9.3 Fiber Reinforced Self-Consolidating Concrete Repair Results 138
4.9.3.1 Repair Specimen R1-FRSCC Results 138
4.9.3.2 Repair Specimen R2-FRSCC Results 141
4.9.3.3 Repair Specimen R3-FRSCC Results 144
4.9.4 Phoscrete® Repair Results 147
4.9.4.1 Repair Specimen R1-PHOS Results 147
4.9.4.2 Repair Specimen R2-PHOS Results 151
4.9.4.3 Repair Specimen R3-PHOS Results 154
4.10 Summary of Results 157
4.10.1 Positive Moment Testing of R1-J3, R1-FRSCC, and R1-PHOS 157
4.10.2 Negative Moment Testing of Repaired Specimens 159
5.0 Beam End Region Repairs 163
5.1 Overview 163
5.2 Girder Specimen Construction 163
5.2.1 Specimen Design 163
5.2.2 Beam Construction 165
5.3 Initial Shear Testing 169
5.4 Girder Repair 171
5.4.1 Overview 171
5.4.2 FR-SCC Repairs 173
5.4.3 MALP Repairs 175
5.4.4 J3 UHPC repair mix 178
5.5 Girder Repair Testing Results 178

5.5.1 FR-SCC Repair Specimens 178
5.5.2 MALP Repair Specimens 181
5.5.3 J3 UHPC Repair Specimens 184
5.5.4 Summary of Results 188
6.0 Corrosion Testing 193
6.1 Overview 193
6.2 Small-Scale Corrosion Testing 194
6.2.1 Introduction 194
6.2.2 Testing 196
6.2.3 Results 200
6.3 Large-Scale Corrosion Testing 200
6.3.1 Procedure 200
6.3.2 Testing and Results 203
7.0 Field Implementation 223
7.1 Overview 223
7.2 S.H. 3 over Fulton Creek in Beaver County 223
7.2.1 Overview 223
7.2.2 Initial condition 224
7.2.3 Repairs 225
7.2.4 Monitoring 229
7.3 U.S. 183/412 over Wolf Creek in Woodward County 233
7.3.1 Overview 233
7.3.2 Bridge Description 234
7.3.3 Load Test Procedure 237

7.3.4 Continuity Joint Instrumentation and Repair 240
7.3.5 Post-Repair Load Test 246
7.3.6 Discussion of Results 247
7.3.6.1 UHPC Joint Construction Data 247
7.3.6.2 Load Test Results 248
7.3.6.3 Strain Gauge Results 251
7.3.7 MALP Deck Slab Cantilever Repairs 253
7.3.8 Monitoring 254
8.0 Specification Development 255
8.1 Overview 255
8.2 UHPC 255
8.2.1 Material Selection and Preparation 255
8.2.2 Mixing Procedure 257
8.2.3 Quality Control 258
8.2.4 Formwork and Surface Preparation 259
8.2.5 Placement 259
8.3 FR-SCC 261
8.3.1 Material Selection and Preparation 261
8.2.2 Mixing Procedure 262
8.2.3 Quality Control 262
8.2.4 Formwork and Surface Preparation 263
8.2.5 Placement 264
8.4 MALP Concrete 264
8.4.1 Material Selection and Preparation 264
8.4.2 Mixing Procedure 265

8.4.3 Quality Control 265
8.4.4 Formwork and Surface Preparation 266
8.4.5 Placement 266
9.0 Summary and Conclusions 268
9.1 Summary 268
9.2 Conclusions 269
9.2.1 Mixing and Placement Methods 269
9.2.2 Continuity Connection Repairs 269
9.2.3 Beam End Region Repairs 270
9.3.4 Corrosion Testing 270
9.2.5 Field Implementation 270
References 273

List of Figures

Figure 2.1. Bent bar continuity joint specimen (Miller et al. 2004) 5
Figure 2.2. Cracking in continuity linkage block (photo courtesy of Walt Peters) 6
Figure 2.3. Corrosion damage to a precast, prestressed concrete girder end region..... 7
Figure 2.4. UHPC field mixing operations using high shear mixers (Graybeal 2014).... 17
Figure 2.5. UHPC placement into a longitudinal connection of bridge elements (Graybeal 2014) 18
Figure 2.6. Final bridge deck substrate preparation (Graybeal 2017) 20
Figure 2.7. Direct pull-off test cores (Graybeal 2017)..... 21
Figure 2.8. Area of bond interruption at UHPC-conventional concrete interface (Graybeal 2017) 21
Figure 2.9. Finished overlay on the Mud Creek bridge (Wibowo and Sritharan 2018) .. 22
Figure 2.10. Typical direct pull-off test failure for the Mud Creek bridge overlay (Wibowo and Sritharan 2018)..... 23
Figure 2.11. Final experimental panel with UHPC overlay used by Khayat et al. (2018) 24
Figure 2.12. Four-point loading system for Habel et al. (2004) experiments. Notations f1-f7 are LVDT locations, and dimensions are given in cm. 25
Figure 2.13. Damaged girder end (Zmetra 2015)..... 26
Figure 2.14. Shear stud layout on the repaired girder (Zmetra 2015) 26
Figure 2.15. Final repaired girder (Zmetra 2015) 27
Figure 2.16. Undamaged girder failure (Zmetra 2015) 28
Figure 2.17. Damaged girder failure (Zmetra 2015) 28
Figure 2.18. Repaired girder failure (Zmetra 2015) 28
Figure 2.19. Cut beam segment marked for controlled damage (Shafei, 2020)..... 29
Figure 2.20. Loading setup for beam with UHPC patch (Shafei, 2020)..... 29
Figure 2.21. Direct tension pull-off test setup (Graybeal 2016) 31
Figure 2.22. (a) High, (b) medium, and (c) low aggregate exposure levels (Graybeal, 2016)..... 32
Figure 2.23. Slant shear compression test (Graybeal 2016) 33
Figure 2.24. Prismatic specimen and testing setup for Tayeh et al. (2013) experiments 34
Figure 2.25. Cylindrical specimen and testing setup for Sarkar (2010) experiments..... 34
Figure 2.26. Splitting cylinder test (Graybeal 2016) 35

Figure 2.27. Flexural beam bond test (Graybeal 2016) 36
Figure 2.28. Shear key conventional concrete substrate (Funderburg 2018) 37
Figure 2.29. Damaged (left) and SCC repaired bridge pier (right) (Ozyildirim 2013) 39
Figure 2.30. SCC repaired column and pier cap (Ozyildirim 2013) 39
Figure 2.31. (a) Undamaged control beam and (b) damaged beam (Abdulhameed 2018) (all dimensions are in in.) 41
Figure 2.32. FR-SCC repaired girder before (left) and after (right) testing 42
Figure 3.1. Hardened property specimens for FR-SCC characterization 49
Figure 3.2. Slump prior to HRWR addition 50
Figure 3.3. Slump flow after addition of HRWR 51
Figure 3.4. FR-SCC cylinder specimen preparation 51
Figure 3.5. Top surface of specimen that had to be removed before testing 52
Figure 3.6. Failure of an FR-SCC compressive strength specimen 52
Figure 3.7. Splitting tensile strength specimens 53
Figure 3.8: FR-SCC modulus of rupture specimens after testing 54
Figure 3.9. Typical FR-SCC modulus of rupture specimen failure surface 54
Figure 3.10. FR-SCC Modulus of elasticity specimen during testing 55
Figure 3.11 Chipped top surface of substrate (ODOT AA pull-off slabs) 57
Figure 3.12. Sandblasted top surface of substrate (ODOT AA pull-off slabs) 57
Figure 3.13. Slant shear cylinders prior to pouring FR-SCC Overlays 58
Figure 3.14. Slump flow of the low flowability FR-SCC overlay 59
Figure 3.15. Pull-off test slab preparation (coring) 60
Figure 3.16. Slant shear and pull-off bond testing specimens prior to testing 60
Figure 3.17. FR-SCC low flow slant shear failure 61
Figure 3.18. FR-SCC high flow slant shear failure from two sides 62
Figure 3.19. FR-SCC slant shear test sudden separation of materials 62
Figure 3.20. ODOT AA slant shear failure 63
Figure 3.21. Configuration of pull-off specimens for bond testing 64
Figure 3.22. Interface failure 66
Figure 3.23. Overlay failure 66
Figure 3.24. Substrate failure 67
Figure 3.25. Interface failure that enters substrate 67

Figure 3.26. Composite slant shear specimen prior to testing (left) and after testing (right) 68
Figure 3.27. Sandblasted (left) and chipped (right) surface preparations 70
Figure 3.28. Pull-off test specimens for Ductal® (left) and J3 (right) 70
Figure 3.29. Pull-off tests for J3 with overall layout (left) and test setup (right) 71
Figure 3.30. J3 UHPC continuity joint repair mock-up specimen 72
Figure 4.1 Girder dimensions and geometry 73
Figure 4.2. Continuity joint dimensions and geometry 74
Figure 4.3. Girder-joint-girder specimen dimensions 74
Figure 4.4. Hooked end bar dimensions used for continuity connection 75
Figure 4.5. Hooked end bar placement 75
Figure 4.6. (Left) Inside longitudinal bars and (right) outside longitudinal bars 75
Figure 4.7. Deck longitudinal reinforcement 76
Figure 4.8. Deck reinforcement placement 76
Figure 4.9. Half-length specimen stirrup spacing 77
Figure 4.10. (Left) Stirrup placement in the girder cross-section and (right) stirrup dimensions 77
Figure 4.11. Full specimen steel reinforcement 77
Figure 4.12. 3-Dimensional representation of full-length specimen steel reinforcement 78
Figure 4.13. Cross-section showing all steel reinforcement 78
Figure 4.14. Half-length specimen rebar cage 80
Figure 4.15. Rebar cages within formwork before specimen casting 80
Figure 4.16. Hooked ends arranged in the formwork 81
Figure 4.17. Hooked end bar mating alignment 82
Figure 4.18. Specimen forms ready for concrete placement 82
Figure 4.19. Filling round-gate bucket with concrete 83
Figure 4.20. Pouring and vibrating concrete in girder formwork 84
Figure 4.21. Completed girder specimens immediately after casting 85
Figure 4.22. Half-length girder specimens after moist cure 85
Figure 4.23. Orientation of half-length girders prior to deck/joint casting 86
Figure 4.24. Continuity joint formwork 87
Figure 4.25. Deck formwork 88
Figure 4.26. Strain gauge glued to longitudinal reinforcement 89

Figure 4.27. Room-temperature-vulcanizing (RTV) silicone covering strain gauge..... 89
Figure 4.28. Strain gauges attached to longitudinal reinforcement ready for installation 89
Figure 4.29. Top view of continuity joint prior to casting..... 90
Figure 4.30. Strain gauge wires before casting the continuity joint and deck..... 90
Figure 4.31. Two girder-joint-girder specimens prior to casting..... 91
Figure 4.32. Vibrating the continuity joint during casting 92
Figure 4.33. Girder-joint-girder specimen after final casting..... 92
Figure 4.34. Hydraulic ram, load cell, swivel spacer, and steel plate setup..... 94
Figure 4.35. End support setup 94
Figure 4.36. Wire potentiometer setup 95
Figure 4.37. Control beam test setup for negative moment bending..... 96
Figure 4.38. Specimen C1 shear cracking 97
Figure 4.39. Specimen C1 flexural cracking in the continuity joint 97
Figure 4.40 Specimen C1 cracking at girder-joint interface (left side) 98
Figure 4.41. Specimen C1 cracking at girder-joint interface (right side)..... 98
Figure 4.42. Specimen C1 girder-joint interface cracking across the deck..... 99
Figure 4.43. Deflected shape of unloaded C1 specimen..... 99
Figure 4.44. Specimen C1 load-deflection curve..... 99
Figure 4.45. Specimen C1 load-strain curve 100
Figure 4.46. Specimen C2 shear cracking 101
Figure 4.47. Specimen C2 flexural cracking in the continuity joint 101
Figure 4.48. Specimen C2 cracking at girder-joint interface (left side) 102
Figure 4.49. Specimen C2 cracking at girder-joint interface (right side)..... 102
Figure 4.50. Specimen C2 girder-joint interface cracking across the deck..... 103
Figure 4.51. Deflected shape of unloaded C2 specimen..... 103
Figure 4.52. Specimen C2 load-deflection curve..... 103
Figure 4.53. Specimen C2 load-strain curve 104
Figure 4.54. Specimen C3 shear cracking 105
Figure 4.55. Specimen C3 flexural cracking in the continuity joint 105
Figure 4.56. Specimen C3 girder-joint interface and centerline cracking across the deck 106
Figure 4.57. Deflected shape of unloaded specimen C3..... 106

Figure 4.58. Specimen C3 load-deflection curve 107
Figure 4.59. Specimen C3 load-strain curve 107
Figure 4.60. Load-deflection curves for control girder specimens 108
Figure 4.61. Setup for testing girders specimens to be repaired 109
Figure 4.62. Initial cracking of specimen R1-J3 on the front (left) and rear (right) of the joint face 110
Figure 4.63. Initial cracking of specimen R1-J3 on the bottom joint face 110
Figure 4.64. Initial cracking of specimen R2-J3 on the front (left) and rear (right) of the joint face 111
Figure 4.65. Initial cracking of specimen R2-J3 on the bottom joint face 111
Figure 4.66. Initial cracking of specimen R3-J3 on the front (left) and rear (right) of the joint face 111
Figure 4.67. Initial cracking of specimen R3-J3 on the bottom joint face 112
Figure 4.68. Initial cracking of specimen R1-FRSCC on the front (left) and rear (right) of the joint face 112
Figure 4.69. Initial cracking of specimen R1-FRSCC on the bottom joint face 113
Figure 4.70. Initial cracking of specimen R2-FRSCC on the front (left) and rear (right) of the joint face 113
Figure 4.71. Initial cracking of specimen R2-FRSCC on the bottom joint face 113
Figure 4.72. Initial cracking of specimen R3-FRSCC on the front (left) and rear (right) of the joint face 114
Figure 4.73. Initial cracking of specimen R3-FRSCC on the bottom joint face 114
Figure 4.74. Initial cracking of specimen R1-PHOS on the front (left) and rear (right) of the joint face 115
Figure 4.75. Initial cracking of specimen R1-PHOS on the bottom joint face 115
Figure 4.76. Initial cracking of specimen R2-PHOS on the front (left) and rear (right) of the joint face 116
Figure 4.77. Initial cracking of specimen R2-PHOS on the bottom joint face 116
Figure 4.78. Initial cracking of specimen R3-PHOS on the front (left) and rear (right) of the joint face 116
Figure 4.79. Initial cracking of specimen R3-PHOS on the bottom joint face 117
Figure 4.80. Top repair reinforcement shape and dimensions 119
Figure 4.81. Bottom repair reinforcement shape and dimensions 120
Figure 4.82. Vertical location of drilled holes for anchoring repair reinforcement 121
Figure 4.83. Horizontal location of drilled holes for anchoring repair reinforcement 122

Figure 4.84. Installation of repair reinforcement 122
Figure 4.85. Roughened surface of continuity joint to be repaired 123
Figure 4.86. Strain gauge installed on repair reinforcement 124
Figure 4.87. Repair formwork for side face of the continuity joint 124
Figure 4.88. Joint repair formwork 125
Figure 4.89. Specimen R1-J3 shear and flexural cracking 129
Figure 4.90. Specimen R1-J3 girder-joint interface crack on the left (left) side and right (right) side 130
Figure 4.91. Specimen R1-J3 deck crushing at failure 130
Figure 4.92. Deflected shape of specimen R1-J3 after testing 130
Figure 4.93. Specimen R1-J3 load-deflection curve 131
Figure 4.94. Specimen R1-J3 load-strain curves 132
Figure 4.95. Specimen R2-J3 shear and flexural cracking 132
Figure 4.96. Specimen R2-J3 continuity joint repair after testing 133
Figure 4.97. Specimen R2-J3 girder-joint interface cracking on the front left (left) and front right (right) 133
Figure 4.98. Specimen R2-J3 girder-joint interface cracking on the back right 133
Figure 4.99. Deflected shape of specimen R2-J3 after testing 134
Figure 4.100. Specimen R2-J3 load-deflection curve 134
Figure 4.101. Specimen R2-J3 load-strain curves 135
Figure 4.102. Specimen R3-J3 shear and flexural cracking 135
Figure 4.103. Specimen R3-J3 continuity joint repair after testing 136
Figure 4.104. Specimen R3-J3 girder-joint interface cracking 136
Figure 4.105. Deflected shape of specimen R3-J3 after testing 136
Figure 4.106. Specimen R3-J3 load-deflection curve 137
Figure 4.107. Specimen R3-J3 load-strain curves 137
Figure 4.108. Specimen R1-FRSCC shear and flexural cracking 138
Figure 4.109. Specimen R1-FRSCC back right joint transverse face cracking 139
Figure 4.110. Specimen R1-FRSCC girder-joint interface cracking on the front left (left) and front right (right) 139
Figure 4.111. Deflected shape of specimen R1-FRSCC after testing 139
Figure 4.112. Specimen R1-FRSCC load-deflection curve 140
Figure 4.113. Specimen R1-FRSCC load-strain curve 141

Figure 4.114. Specimen R2-FRSCC shear and flexural cracking 141
Figure 4.115. Specimen R2-FRSCC joint cracking on longitudinal and transverse faces from the front left (left) and front right (right)..... 142
Figure 4.116. Specimen R2-FRSCC joint cracking on longitudinal and transverse faces from the back left (left) and back right (right)..... 142
Figure 4.117. Deflected shape of specimen R2-FRSCC after testing 142
Figure 4.118. Specimen R2-FRSCC load-deflection curve 143
Figure 4.119. Specimen R2-FRSCC load-strain curve..... 144
Figure 4.120. Specimen R3-FRSCC shear and flexural cracking 144
Figure 4.121. Specimen R3-FRSCC joint cracking on the longitudinal and transverse faces from the front left (left) and front right (right) 145
Figure 4.122. Specimen R3-FRSCC joint cracking on the longitudinal and transverse faces from the back left 145
Figure 4.123. Specimen R3-FRSCC deck cracking 146
Figure 4.124. Specimen R3-FRSCC load-deflection curve 146
Figure 4.125. Specimen R3-FRSCC load-strain curves..... 147
Figure 4.126. Specimen R1-PHOS shear and flexural cracking..... 147
Figure 4.127. Specimen R1-PHOS girder-joint interface and joint transverse face cracking from the front left (left) and front right (right) 148
Figure 4.128. Specimen R1-PHOS girder-joint interface and joint transverse face cracking from the back left (left) and back right (right)..... 148
Figure 4.129. Specimen R1-PHOS girder-joint separation..... 149
Figure 4.130. Deflected shape of specimen R1-PHOS 149
Figure 4.131. Specimen R1-PHOS load-deflection curve 150
Figure 4.132. Specimen R1-PHOS load-strain curves 151
Figure 4.133. Specimen R2-PHOS shear and flexural cracking..... 151
Figure 4.134. Specimen R2-PHOS joint cracking on the longitudinal and transverse faces from the front left (left) and front right (right) 152
Figure 4.135. Specimen R2-PHOS joint cracking on the longitudinal and transverse faces from the back right..... 152
Figure 4.136. Specimen R2-PHOS deck cracking 152
Figure 4.137. Deflected shape of specimen R2-PHOS after testing 153
Figure 4.138. Specimen R2-PHOS load-deflection curve 153
Figure 4.139. Specimen R2-PHOS load-strain curves 154
Figure 4.140. Specimen R3-PHOS shear and flexural cracking..... 154

Figure 4.141. Specimen R3-PHOS girder-joint interface and joint transverse face cracking from the front left (left) and front right (right) 155
Figure 4.142. Specimen R3-PHOS joint transverse face cracking from the back left (left) and back right (right) 155
Figure 4.143. Specimen R3-PHOS deck cracking 155
Figure 4.144. Deflected shape of specimen R3-PHOS after testing 156
Figure 4.145. Specimen R3-PHOS load-deflection curve 156
Figure 4.146. Specimen R3-PHOS load-strain curves 157
Figure 4.147. Summary of positive moment repair specimen load-deflection curves.. 158
Figure 4.148. Summary of negative moment repair specimen load-deflection curves 160
Figure 4.149. Summary of negative moment control group load-deflection cures..... 161
Figure 5.1. Prestressed beam specimen cross-section..... 164
Figure 5.2. Prestressed beam specimen reinforcement details..... 165
Figure 5.3. Stirrup spacing along the half length of the prestressed beam specimens 165
Figure 5.4. Panoramic picture of the prestressing setup 166
Figure 5.5. Reinforcement cage for a typical girder..... 167
Figure 5.6. (a) Deck formwork and (b) deck concrete immediately after casting..... 169
Figure 5.7. Uncracked girder arranged in the test setup 170
Figure 5.8. Tracing paper on one side of the cracked girder to copy the crack locations after testing 170
Figure 5.9. (a) Cross-sectional view of concrete anchor locations, (b) front face showing distribution of anchors, (c) back face showing distribution of anchors..... 172
Figure 5.10. Concrete anchors used for shear studs in the web of a girder specimen ready for repair..... 172
Figure 5.11. Repair formwork..... 173
Figure 5.12. (a) Repair dimensions for UHPC and (b) repair dimensions for FR-SCC and MALP concrete..... 173
Figure 5.13. (a) FR-SCC repair for beam M-2 and (b) FR-SCC repair for beam M-3.. 175
Figure 5.14. (a) Expansion of the MALP above the formwork and (b) gap under the beam resulting from poor workability of the new MALP..... 177
Figure 5.15. (a) Old MALP repair for beam M-4 and (b) new MALP repair for beam M-1 177
Figure 5.16. Load-deflection curves for the initial and post-repair shear tests of specimen M2-FRSCC 179
Figure 5.17. Load-deflection curves for the initial and post-repair shear tests of specimen M3-FRSCC 179

Figure 5.18. Load-slip curves for the initial and post-repair shear tests of specimen M2-FRSCC 180
Figure 5.19. Load-slip curves for the initial and post-repair shear tests of specimen M3-FRSCC 180
Figure 5.20. Specimen M2-FRSCC at failure showing cracking in the specimen and concrete crushing at the load point 181
Figure 5.21. Load-deflection curves for the initial and post-repair shear tests of specimen M1-MALP 182
Figure 5.22. Load-deflection curves for the initial and post-repair shear tests of specimen M4-MALP 182
Figure 5.23. Load-slip curves for the initial and post-repair shear tests of specimen M1-MALP 183
Figure 5.24. Load-slip curves for the initial and post-repair shear tests of specimen M4-MALP 183
Figure 5.25. Specimen M1-MALP at failure showing cracking in the specimen and concrete crushing at the load point 184
Figure 5.26. Specimen M4-MALP at failure showing cracking in the specimen and concrete crushing at the load point 184
Figure 5.27. Load-deflection curves for the initial and post-repair shear tests of specimen M5-UHPC 185
Figure 5.28. Load-deflection curves for the initial and post-repair shear tests of specimen M6-UHPC 186
Figure 5.29. Load-slip curves for the initial and post-repair shear tests of specimen M5-UHPC 186
Figure 5.30. Load-slip curves for the initial and post-repair shear tests of specimen M6-UHPC 187
Figure 5.31. Specimen M6-UHPC at failure showing cracking in the specimen and concrete crushing at the load point 188
Figure 5.32. Comparison of load-deflection curves for the post-repair shear tests of specimens M2-FRSCC, M1-MALP, and M5-UHPC 189
Figure 5.33. Comparison of load-deflection curves for the post-repair shear tests of specimens M2-FRSCC, M1-MALP, and M5-UHPC 189
Figure 5.34. Comparison of load-deflection curves for the post-repair shear tests of all specimens except M4-MALP 190
Figure 5.35. Comparison of average cracking and ultimate loads for specimens with all repair materials 191
Figure 5.36. Comparison of average deflection at cracking and ultimate loads for specimens with all repair materials 191

Figure 5.37. Comparison of ultimate load before and after repair 192
Figure 6.1. Small-scale corrosion specimen molds 195
Figure 6.2. Typical small-scale corrosion testing specimen in the chloride solution 195
Figure 6.3. Initial joint corrosion in Ductal® small-scale corrosion testing specimen D0 - patching 196
Figure 6.4. Initial joint corrosion in Ductal® small-scale corrosion testing specimen - corrosion spotting 196
Figure 6.5. Corrosion state of rebar reinforcing at joint of ODOT Class AA small-scale corrosion specimens with 4% NaCl (left) and 8% NaCl (right) 198
Figure 6.6. Corrosion state of rebar reinforcing at joint of J3 small-scale corrosion specimens with 4% NaCl (left) and 8% NaCl (right) 198
Figure 6.7. Corrosion state of rebar reinforcing at joint of Ductal® small-scale corrosion specimens with 4% NaCl (left) and 8% NaCl (right) 199
Figure 6.8. Corrosion state of rebar reinforcing at joint of Phoscrete® small-scale corrosion specimens with 4% NaCl (left) and 8% NaCl (right) 199
Figure 6.9. Steel rebar before testing - typical 199
Figure 6.10. Large-scale corrosion joint specimens before chipping 201
Figure 6.11. Large-scale corrosion joint specimens after chipping 201
Figure 6.12. Large-scale corrosion joint specimen with longitudinal connection bar in place 201
Figure 6.13. Stainless steel rod and electrical wiring for large-scale corrosion testing 202
Figure 6.14. Large-scale corrosion testing setup showing power supplies (left) and all specimens in place (right) 203
Figure 6.15. White film in water of Phoscrete large-scale corrosion specimen 204
Figure 6.16. Corrosion in water of typical large-scale corrosion specimens 204
Figure 6.17. Joint corrosion in Ductal® large-scale corrosion testing specimen during week 2 of testing (Ductal® on left side of image) 205
Figure 6.18. Joint corrosion in Ductal® large-scale corrosion specimen during week 5 of testing 205
Figure 6.19. Green liquid in joint of Phoscrete large-scale corrosion specimen during week 7 of testing 206
Figure 6.20. Green liquid in joint of Ductal® large-scale corrosion specimen during week 8 of testing 207
Figure 6.21. Green liquid in joint of Phoscrete® large-scale corrosion specimen during week 10 of testing 207
Figure 6.22. Green liquid in joint of Ductal® large-scale corrosion specimen during week 10 of testing 207

Figure 6.23. Visible confirmation of reinforcing bar corrosion during week 1 208
Figure 6.24. Typical reinforcing bar corrosion at the conclusion of testing - week 10 . 208
Figure 6.25. Chipping sequence of large-scale corrosion specimens 209
Figure 6.26. Week 1 update for large-scale corrosion specimens using (a) ODOT AA, (b) J3, (c) Ductal®, and (d) Phoscrete® 210
Figure 6.27. Week 3 update for large-scale corrosion specimens using (a) ODOT AA, (b) J3 (c) Ductal®, and (d) Phoscrete® 211
Figure 6.28. Week 6 update for large-scale corrosion specimens using (a) ODOT AA, (b) J3, (c) Ductal®, and (d) Phoscrete® 212
Figure 6.29. Week 10 update for large-scale corrosion specimens using (a) ODOT AA, (b) J3, (c) Ductal®, and (d) Phoscrete® 213
Figure 6.30. First rebar excavation for large-scale corrosion specimens using (a) ODOT AA, (b) J3, (c) Ductal®, and (d) Phoscrete® 214
Figure 6.31. Second rebar excavation for large-scale corrosion specimens using (a) ODOT AA, (b) J3, (c) Ductal®, and (d) Phoscrete® 215
Figure 6.32. Fourth rebar excavation for large-scale corrosion specimens using (a) ODOT AA, (b) J3, (c) Ductal®, and (d) Phoscrete® 216
Figure 6.33. Fifth rebar excavation for large-scale corrosion specimens using (a) ODOT AA, (b) J3, (c) Ductal®, and (d) Phoscrete® 217
Figure 6.34. Fifth rebar excavation for large-scale corrosion specimens using (a) ODOT AA, (b) J3, (c) Ductal®, and (d) Phoscrete® after 24 hours 218
Figure 6.35. Evidence of surficial corrosion on large-scale corrosion specimens using (a) J3, (b) Ductal®, and (c) Phoscrete® 220
Figure 6.36. Change in voltage over time for all large-scale corrosion specimens..... 221
Figure 6.37. Final state of Phoscrete® large-scale corrosion specimen after week 10 222
Figure 6.38. J3 (left) and Ductal® (right) split cylinder test specimens..... 222
Figure 7.1. S.H. 3 bridge over Fulton Creek (NBI No.: 21700) 224
Figure 7.2. Typical spalling on slab cantilever of Fulton Creek bridge 225
Figure 7.3. Approximate location of vibrating wire strain gauges for monitoring temperature and shrinkage of MALP concrete repair on SH-3 over Fulton Creek bridge 225
Figure 7.4. Slab cantilever section after removal of loose material (left) and forms in place for the repair (right) 226
Figure 7.5. Strain gauge placement within the area to be repaired on the south side of span 3 of the S.H. 3 bridge over Fulton Creek in Beaver County 227
Figure 7.6. Placement of MALP mortar on the S.H. 3 bridge over Fulton Creek in Beaver County 228

Figure 7.7. Repaired section at the location of the westernmost strain gages (Figure 7.4) after the first layer of MALP was placed 228
Figure 7.8. Close-up of MALP repair after placement of the first layer 228
Figure 7.9. Close-up initial MALP placement on the southeast side (left) and later MALP placement on the northeast side (right) showing difference in surface finish of repair 229
Figure 7.10. Rust spot in thin section of MALP repair where drip edge was cut on the south side of the bridge 230
Figure 7.11. Repair spalling on the northeast side of the bridge 18 months after repair 230
Figure 7.12. Section of completed MALP mortar repair on south side of span 3 of the S.H. 3 bridge over Fulton Creek in Beaver County near the west end of the span 3 months (left), 8 months (middle), and 18 months (right) after placement 231
Figure 7.13. Rust spot within the MALP repaired area on the Packsaddle Bridge (NBI 21132) (left) and rust spots outside but near the repaired area (right). Photo courtesy of Walt Peters 232
Figure 7.14. Temperature history of MALP repair material on Fulton Creek bridge over the first month in service. 233
Figure 7.15. Measured strain over time for MALP repair material on Fulton Creek bridge over first month of service 233
Figure 7.16. Example of positive moment cracking in a continuity joint of the U.S. 183/412 bridge over Wolf Creek 234
Figure 7.17. Plan view of U.S. 183/412 over Wolf Creek bridge 235
Figure 7.18. Cross-section view of U.S. 183/412 over Wolf Creek bridge 235
Figure 7.19. Joints at pier 3 prior to repair (left) and typical damage (right) 236
Figure 7.20. U.S. 183/412 over Wolf Creek continuity joint details from original drawings 237
Figure 7.21. Laser measurer and plumb bob setup (left), clamp on the girder bottom (middle), and method used for measurement with the plumb bob (right) 238
Figure 7.22. Truck locations for each load stage 240
Figure 7.23. Trucks located for Load Stage 6 240
Figure 7.24. Strain gauge placement in the joint 241
Figure 7.25. High shear pan mixer in place on the bridge deck (left) and placement of UHPC materials in the mixer (right) 242
Figure 7.26. Pour holes for UHPC joints on the Wolf Creek bridge 243
Figure 7.27. Placement of UHPC into fill hole in the bridge deck 243
Figure 7.28. UHPC from failed formwork 244
Figure 7.29. Final joint forms after adding bracing 245

Figure 7.30. Completed UHPC continuity joint after form removal 246
Figure 7.31. UHPC heat evolution for center and exterior joint on pier 3 248
Figure 7.32. Span 4 midspan deflections during each of the six load stages 249
Figure 7.33. Foil strain gauge data for post-repair load test 252
Figure 7.34. Collected average strain gauge readings 252
Figure 7.35. Placement of a representative MALP concrete patch (left) and completed patch (right) 253
Figure 7.36. Vibrating wire strain gages placed for shrinkage and temperature monitoring 254

List of Tables

Table 2.1. Typical material properties of field-cast UHPC (taken from Graybeal 2014) 13
Table 2.2. Potential UHPC mix designs developed by FHWA for various regions of the U.S. (Graybeal 2013) 14
Table 2.3. Mix proportion for J3 UHPC..... 16
Table 2.4. Average UHPC material properties for different curing regimens (Graybeal 2006)..... 19
Table 2.5. Hansson (2006) mix designs..... 46
Table 3.1. Final FR-SCC mix design..... 49
Table 3.2. Summary of tests performed for FR-SCC characterization 49
Table 3.3. Fresh properties of FR-SCC characterization batch..... 50
Table 3.4. Compressive strength of FR-SCC..... 52
Table 3.5. Splitting tensile strength of FR-SCC..... 53
Table 3.6. Modulus of rupture of FR-SCC (beams with third-point loading)..... 53
Table 3.7. Measured modulus of elasticity for FR-SCC..... 55
Table 3.8. Fresh properties of ODOT AA bond test substrates used for FR-SCC..... 56
Table 3.9. ODOT AA concrete bond test substrate compressive strength 56
Table 3.10. HRWR Content and slump flow of FR-SCC overlays 59
Table 3.11. Compressive strengths of the FR-SCC mixes with varying flowability..... 59
Table 3.12. Slant shear results for the FR-SCC mixes with varying flowability 63
Table 3.13. FR-SCC pull-off bond test results..... 65
Table 3.14. Average FR-SCC pull-off bond test results..... 66
Table 3.15. Maximum load and bond strength for Ductal® slant shear specimens..... 69
Table 3.16. Maximum load and bond strength for J3 slant shear specimens..... 69
Table 3.17. Slant shear test results..... 70
Table 3.18. Direct pull-off test results..... 71
Table 4.1. Summary of steel reinforcement used for continuity connection specimens 78
Table 4.2. Steel reinforcement tensile test results..... 79
Table 4.3. Class AA concrete specifications 83
Table 4.4. Class AA concrete cylinder compression testing results 93
Table 4.5. Summary of Initial Cracking Loads..... 117
Table 4.6. J3 UHPC Mixture Proportions 126

Table 4.7. FR-SCC Mixture Proportions 127
Table 4.8. 28-Day Repair Concrete Compressive Strengths 128
Table 4.9. Initial cracking results for positive moment repair specimens 157
Table 4.10. Repair group positive moment bending results 158
Table 4.11. Repair Group Negative Bending Results 159
Table 4.12. Control group negative moment bending results 160
Table 4.13. Initial cracking results for negative moment repair specimens 161
Table 5.1. SCC Mix Design 168
Table 5.2. FR-SCC repair material expressed as percentage of components 174
Table 5.3. FR-SCC mix design 174
Table 7.1 Truck information 239
Table 7.2. Compressive strength test results for the UHPC used on Wolf Creek bridge 248
Table 7.3. Measured vs. calculated deflections (mm) for center girder of span 4 251
Table 8.1. UHPC material property requirements 256
Table 8.2. UHPC quality control testing requirements 258
Table 8.3. FR-SCC material property requirements 261
Table 8.4. FR-SCC quality control testing requirements 263
Table 8.5. UHPC quality control testing requirements 265

1.0 Introduction

1.1 Overview

A large percentage of the beam and stringer bridges in Oklahoma are precast, prestressed concrete girder bridges and many of these are reaching the end of their expected design lives. Precast, prestressed girders made continuous for live load using a cast in place continuity connection allow for a reduction in the required prestress force and elimination of interior deck joints. However, these continuity joints are often damaged due to creep and shrinkage over time in the connected girders, and numerous instances of continuity connection blocks with vertical cracks that leave this heavily reinforced region open to further degradation have been observed in Oklahoma. In addition, many simple span prestressed concrete bridges with damage to the beam end regions due to corrosion and spalling have been observed in Oklahoma. This end region damage is often caused or exacerbated by leaking deck joints that contribute to ingress of chlorides from deicing agents. Continued deterioration at these locations can lead to serviceability concerns and strength degradation due to bond loss between the steel and concrete.

Effective repair materials have the potential to extend the service life of these bridges, providing significant cost savings to the state of Oklahoma. Both ultra-high performance concrete (UHPC) and fiber reinforced self-consolidating concrete (FR-SCC) are two such specialty repair materials that can provide a durable repair to spalled or deteriorated areas of bridge continuity connections and girder end regions. UHPC is a relatively recent advancement in cementitious composite materials with mechanical and durability properties far exceeding those of conventional concrete. It is a fiber-reinforced cementitious composite with an optimized gradation of granular constituents, a compressive strength typically in excess of 22 ksi, and a high post-cracking tensile strength. FR-SCC is a highly flowable concrete with compressive strength similar to conventional concrete, but with fibers added for cracking resistance. A shrinkage compensating or low shrinkage cement can also be included to reduce or eliminate cracking from differential shrinkage. Both UHPC and FR-SCC have the potential to produce effective encapsulation-type repairs of deteriorated continuity connections or

beam end regions that will both protect the area from further degradation and potentially restore or increase the strength of the member. The high flowability of these materials allows placement around damaged areas and into complex geometries without the need for external consolidation. The high tensile strength and shrinkage resistance of the materials provide resistance against reflective cracking from the base concrete. Locally developed UHPC mix designs and FR-SCC mixes previously investigated by the authors (Wirkman 2016; McDaniel 2017, Choate 2018; Looney et al. 2019, Looney et al. 2021) provide alternatives to proprietary UHPC depending on the requirements for the specific repair application. An additional repair material that is less well established but shows promise in these applications is Magnesium-Alumino-Liquid Phosphate (MALP) concrete. A readily available proprietary form, Phoscrete, can rapidly gain strength, allowing for shorter closure times for roadways during repair, and has been shown to exhibit excellent durability over time.

The project described in this report consisted of both laboratory and field investigation of repair methods for prestressed concrete continuity connections and beam ends using UHPC, FR-SCC, and MALP concrete. Laboratory investigations included examination of mixing and placement methods, material properties of the repair materials, corrosion performance, structural testing of continuity joint repairs, and structural testing of beam end repairs. Field investigations included repairs made to two bridges located in ODOT Division 6 using UHPC and MALP concrete and monitoring of these repairs over the course of the project. The results of these investigations resulted in recommendations for specifications for bridge repair using UHPC, FR-SCC, and MALP concrete in Oklahoma.

1.2 Problem Statement

UHPC, FR-SCC, and MALP concrete have great potential for repair and retrofit of precast, prestressed concrete bridge girders and continuity connections. However, additional information is needed to provide standard guidance for using these materials in bridge superstructure repair applications. Specifically, bond behavior between the repair material and base concrete, corrosion performance of the repair materials, and structural behavior of repaired girders all need additional investigation.

1.3 Project Objectives

The objectives of the research were intended to achieve the goal of using UHPC, FR-SCC, and MALP concrete to construct durable repairs to continuity joints and end regions of Oklahoma prestressed concrete bridge girder systems. These objectives consist of the following:

1) Identify best practices for mixing and placement of thin encapsulation repairs using UHPC, FR-SCC, and MALP concrete,
2) Evaluate cracking resistance and contribution of thin UHPC, FR-SCC, and MALP concrete repairs to structural strength,
3) Implement UHPC, FR-SCC, and MALP concrete repairs to an in-service bridge and monitor over time,
4) Create specifications for mixing, placement, and quality control of UHPC, FR-SCC, and MALP concrete materials, and for use in Oklahoma bridge repair.
5) Evaluate economic implications of prestressed girder repairs constructed with UHPC, FR-SCC, and MALP concrete.

The research will directly result in information and guidance ODOT can use to implement UHPC, FR-SCC, and MALP concrete repairs in the future.

2.0 Literature Review

2.1 Prestressed Concrete Girder Deterioration

2.1.1 Continuity Joint Deterioration

To improve the structural efficiency in concrete bridges of multiple spans, precast prestressed bridge girders are often made continuous through cast-in-place decks and diaphragms. Construction of this type of bridge connection has been commonly used throughout the United States since the 1960's. Once the deck and diaphragm have cured, they allow the girders and composite deck to act continuous for any additional dead and live loads (Miller et al. 2004). Prior to the final cured structure, placed girders behave as simply supported members with self-weight and the uncured composite deck as dead loads (Saadeghvaziri et al. 2004).

After continuity is established, the precast prestressed bridge girders camber upward due to time-dependent deformations. These time-dependent effects are due to temperature, creep, and shrinkage. The effects cause a restraint moment to develop at the interior supports of the continuous structure. This is a condition that does not emerge from simply supported connections.

The continuity gained from the composite deck and diaphragm tends to keep the bridge girder ends from rotating, providing a positive moment restraint at the bottom of the diaphragm (Saadeghvaziri et al. 2004). This restraint, with the addition of time-dependent effects, can cause cracking of the diaphragm propagating upward from the positive moment region. These cracks can cause behavioral issues relative to continuity and create openings prone to diaphragm reinforcement corrosion.

To prevent positive moment cracking in the diaphragm, several studies by the Portland Cement Authority in the 1960's recommended a moment connection be made between the girder ends and the diaphragm. In these studies, various connection details were evaluated and reinforcing bars with hooked ends embedded in the ends of precast girders proved to be the most practical application for this type of moment restraint connection (Freyermuth 1969).

A more recent study from by Miller et al. (2004) tested bent bars and bent strands with and without beam ends embedded into the diaphragm and additional stirrups or web bars within the diaphragm. Figure 2.1 shows an example of one configuration tested by Miller et al. (2004).

In this study, the specimen configurations were analytically determined through a model of a continuous two-span structure. The program developed could compute internal moments within the diaphragm caused by creep from the girder and shrinkage from the girder and deck. To verify the program's accuracy, scaled I-girders from the Portland Cement Authority's previous study were modeled and the program displayed agreement with results of that research. The tests concluded that each positive moment restraint connection detail performed adequately, had separate advantages and disadvantages, and that selecting specific member details should be up to the engineer, the Department of Transportation, or both (Miller et al. 2004).

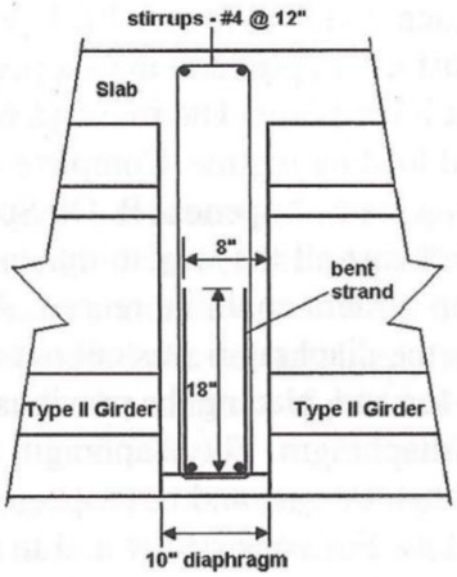

Figure 2.1. Bent bar continuity joint specimen (Miller et al. 2004)

A number of in-service bridges in Oklahoma were designed using simply supported precast, prestressed concrete girders made continuous for live load with approximately 12 in. thick continuity connections between the two girder ends. These joints were typically connected to the base of the girders using up-turned prestressing strands and mild steel bars and were cast simultaneously with the deck such that the

deck reinforcement served as the negative moment reinforcement. Creep and shrinkage in the precast concrete girders over time caused cracking at the base of the joints such as that shown in Figure 2.2. These cracks have the potential to allow water ingress leading to additional cracking and spalling as the internal joint reinforcement corrodes. This cracking resulted in the use of this detail being discontinued by ODOT.

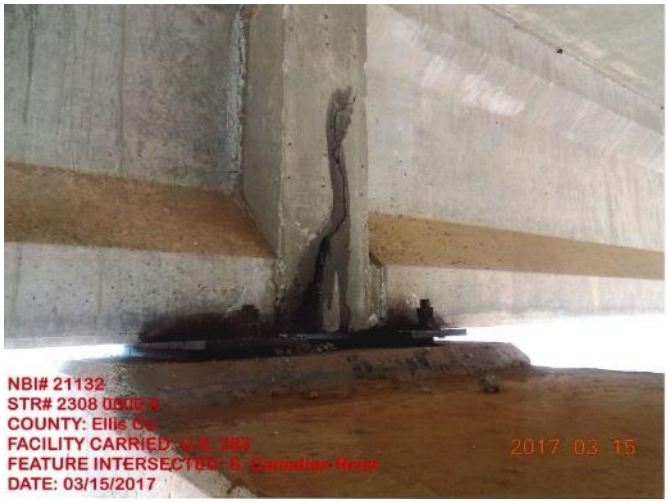

Figure 2.2. Cracking in continuity linkage block (photo courtesy of Walt Peters)

2.1.2 End Region Deterioration

The end regions of prestressed concrete girders play an important role in the overall function of the girder design. In the end regions of pretensioned girders, the prestressing force is transferred to the beam through bond between the prestressing strands and the concrete. This force distribution, known as prestress transfer, requires higher concentrations of mild steel reinforcement in the end region to resist transverse cracking. Additionally, greater shear demand at the ends and reduced prestress force within the transfer length creates a need for more transverse shear reinforcement. The girder end region's high percentage of steel combined with being located near the joints of the bridge deck, which often leak and provide a path for water and chlorides from deicing salts to reach the girder ends, makes the end region more susceptible to reinforcement corrosion and concrete spalling than the remainder of the girder. Exterior girders on the upstream traffic side also have a susceptibility to chloride exposure from vehicle spray, but this spray typically affects the girders to a lesser extent. A recent study by the PI (Mayhorn 2016, Pough et al. 2017) surveyed 19 bridges spread

throughout the state of Oklahoma, and while some form of deterioration was observed in nearly all cases, corrosion damage was only observed at the girder ends. An example of a corroded girder end is shown in Figure 2.3. Similarly, while researching chloride ion distribution in 20-year-old prestressed concrete girders in Minnesota, Coggins and French (1990) found that the only evidence of strand corrosion was observed at the ends of the beams. Damage due to corrosion in this region can have a lasting impact on the girder's overall strength, especially the shear capacity, and can accelerate the overall deterioration of the bridge.

Figure 2.3. Corrosion damage to a precast, prestressed concrete girder end region

Corrosion of concrete reinforcing steel can cause a variety of distress, such as cracking, concrete spalling, and loss of steel tensile strength. Reinforcing steel in most structures is now coated (typically with epoxy) to protect against the corrosion process. This was not always the case. Epoxy was not applied to reinforcing steel in bridges constructed in the mid-1900s, which are now reaching the end of their design lives, and epoxy is still not typically applied to prestressing strands in new construction. One major potential consequence of deterioration in concrete caused by steel corrosion is a reduction of the live load capacity. This capacity is impacted by both the reduction of the steel cross-section (reducing steel tensile strength) and loss of bond between the concrete and steel (reducing composite action). In their study on the bond of reinforcing bars subjected to accelerated corrosion, Abosrra et al. (2011) found that the first day of corrosion acceleration caused a slight increase in steel/concrete bond strength. However, after durations of corrosion acceleration exceeding one week, significantly

reduced steel/concrete bond strength was observed. In a study focused on deterioration of prestressed concrete bridge beams, Bruce et al. (2008) concluded that corrosion in prestressing strands reduces the structural performance of a beam faster than corrosion exhibited in conventional reinforced beams because a larger proportion of the steel cross-section is lost. Szilard (1969) emphasized that prestressing steel is also subjected to significantly higher stresses with smaller diameters in relation to conventional reinforcement.

Several recent studies have investigated the capacity of decommissioned bridge beams with corrosion damage. Rogers et al. (2012) performed destructive tests on 19, 40-year-old pretensioned concrete beams that had corroded pretensioned reinforcement. Their results indicated that “the most severely corroded beam sustained 69% of the load of an equivalent good-condition beam” (Rogers et al. 2012). El-Batanouny et al. (2014) found that pitting corrosion in prestressed strands caused a reduction in residual capacity in only 140 days. They found that the most corroded member had a tested capacity of 86.7% when compared to the original control specimen (El-Batanouny et al. 2014). Pape and Melchers (2013) found that as the degree of corrosion loss in the prestressing strands increased, the maximum capacity of the girder decreased linearly. In determining the performance of three 45-year-old corroded prestressed concrete beams, the researchers concluded that using current design theory, estimated material properties, and neglecting cracking and corrosion damage ultimately overestimates the actual capacity of the beams. In one beam, they found that a 64% loss in prestressing cross-sectional area due to corrosion at the failure location contributed to a 49% reduction in original, theoretical design capacity (Pape and Melchers 2013). Mayhorn et al. (2018) tested a series of half-scale prestressed beams designed to fail due to bond-shear and subjected to an accelerated corrosion environment. They found that minor corrosion at the strand ends may have improved prestressing strand bond strength for the members tested but anticipated lower capacities with higher levels of deterioration (Mayhorn et al. 2018).

2.1.3 Prestressed Concrete Girder Repair

Continuity joints for precast, prestressed girders and girder end regions are often subject to deterioration caused by cracking and chloride laden water ingress. Interior regions of these girders can also experience damage due to impacts from over-height vehicles or from salt spray from passing vehicles. Replacement is always a possible option for damaged or deteriorated girders, but in-situ repair techniques can be significantly less expensive and extend the life of the bridge, while still providing the required life safety. Repairs should restore live load capacity at the required limit states and ensure, at minimum, equal durability to the original system (Shanafelt and Horn 1980, Harries et al. 2009). The type of repair chosen for a given situation should be based on the damage to the girder or bridge system, ensuring life safety, the urgency of repair, time required to make the repair, durability of the repair, aesthetics of the repair, and cost (Shanafelt and Horn 1980). In order for the engineer to make a sound decision on whether girder repair is appropriate and which repair method to use, sufficient information must be available on the application, structural performance, durability, and cost of the repair method.

A number of repair methods are available for prestressed concrete girders that have been used effectively for both impact damage and deteriorated end regions. Several studies have been conducted to examine these repair methods for prestressed concrete bridges (e.g., Shanafelt and Horn 1980, Shanafelt and Horn 1985, Harries et al. 2009, Shield and Bergson 2018, and Gangi et al. 2018). Methods investigated include addition of fiber reinforced polymer (FRP) in a number of forms, preloading to restore effective prestress, strand splicing, adding mild steel reinforcement, external steel post-tensioning, encasement with shotcrete, patching with conventional and latex modified mortar, patching with specialty concrete mixtures, steel jacketing, fabric reinforced cementitious matrix composites, epoxy coating, and epoxy injection to seal cracks (Shanafelt and Horn 1980, Tabatabai et al. 2004, Harries et al. 2009, Gangi et al. 2018). In most cases these studies focused on impact damage and restoring flexural strength near midspan, and not on continuity connections (where flexure is a concern) and girder end regions (where shear is the primary concern). Experimental testing recorded in the literature was primarily related to performance of external post-

tensioning and strand splices, which are also highly influenced by durability of the repair. However, some studies focused specifically on mitigating corrosion induced deterioration in the girder end region and are discussed in more detail in later sections (e.g., Shield and Bergson 2018, Tabatabai et al. 2004).

FRP wrapping is one of the most common repair methods for girder end regions. It has been shown to be effective for increasing shear strength of girder end regions (e.g., Reed and Peterman 2004, Pei et al. 2008, Higgins et al. 2012) and can provide additional durability when used to repair a deteriorated end region (Tabatabai et al. 2004). However, a specialty contractor is usually necessary and bond of the FRP reinforcement to the substrate is critical to performance (e.g., Harries et al. 2009, Reed et al. 2007, Ramanathan and Harries 2008). FRP may also be susceptible to environmentally caused degradation in harsh environments, which should be taken into consideration (Harries et al. 2012). Shield and Bergson (2018) tested two girders whose corroded end regions were repaired with supplementary mild steel reinforcement encased in shotcrete over a 4 ft length from the end of the girders and two undamaged girders from the same bridge that did not require repair. Shear tests showed that the repair returned the girders to the strength of the companion girders, indicating an effective repair (Shield and Bergson 2018). Limited information is available on repairs of continuity joints and precast prestressed concrete girder end regions using FR-SCC, UHPC, or MALP concrete even though each of these materials has great potential for these applications.

2.2 Ultra-High Performance Concrete (UHPC) as a Repair Material

2.2.1 Overview

Ultra-High Performance Concrete (UHPC) is a cementitious composite material with increased durability and strength properties compared to conventional concrete. UHPC was first developed in the late 20th century and is a product of advancements in superplasticizers, fiber reinforcement, supplementary cementitious materials, and optimized gradation of dry materials (Graybeal 2014). Its properties differ from those of typical portland cement concrete, so many of the methods for casting UHPC and determining its fresh and hardened material properties have been modified from the

methods used for conventional concrete. UHPC has been successfully used in multiple applications related to connection of precast concrete bridge components due to its superior bond development characteristics with steel reinforcement, ease of placement, and long-term durability compared to conventional concrete. The long-term benefits of using UHPC in many applications are evident, but commercially available proprietary mixture formulations are very expensive and mix design using local materials is much more complicated than for conventional concrete.

The superior mechanical properties of UHPC allow for the optimization of structural elements, including bridge girders, where the enhanced tensile strength can lead to the elimination of mild steel shear reinforcement (Graybeal 2006a). It can also be used to construct relatively lightweight deck systems (Aaleti et al. 2014). The cost of commercially available UHPC is often approximately 10-20 times that of conventional concrete due to the high cementitious materials content and fiber reinforcement, but the superior mechanical properties and durability have led to much recent interest in applications where small amounts can be used for long-term gain (Graybeal 2011). Such applications include connections between precast bridge components such as deck panels, deck bulb-tee girders, and adjacent box girders. Other applications of UHPC include precast piles, seismic retrofits, thin-bonded overlays for deteriorated decks, and blast mitigation (Graybeal 2011). UHPC formulations can also be made with local materials (e.g., Wille 2011) in order to reduce costs.

Connections cast using UHPC can extend the life of a structure and allow for less maintenance over time. Joints replaced or connections made using this material will have better durability, better resistance to impacts and abrasion, and will allow for a smaller quantity of material to be used while still obtaining adequate load transfer between connected components. Using UHPC allows for small, simple connections without the need for post-tensioning (when connecting precast elements) or large amounts of field-cast concrete (Graybeal 2010). Joints cast using UHPC also tend to behave more like monolithic construction than typical field-cast connections. The use of UHPC for connecting precast elements has been the focus of many cases studies and research projects. It has also been studied as an overlay material to repair and/or extend the life of existing bridges.

The strength and durability properties of UHPC make it useful as a repair material that may provide a longer life to structures that are deteriorated or have been weakened. However, the use of UHPC as a repair material for existing bridges has not been extensively studied. Only a few studies have been conducted on application of UHPC to specific types of bridge repair.

2.2.2 Material Properties

The Federal Highway Administration (FHWA) has performed extensive investigation of the properties of UHPC for use in bridge and other infrastructure components (Graybeal 2011, Graybeal 2014). FHWA defines UHPC as “a cementitious composite material composed of an optimized gradation of granular constituents, a water-to-cementitious materials ratio less than 0.25, and a high percentage of discontinuous internal fiber reinforcement. The mechanical properties of UHPC include compressive strength greater than 21.7 ksi (150 MPa) and sustained postcracking tensile strength greater than 0.72 ksi (5 MPa). UHPC has a discontinuous pore structure that reduces liquid ingress, significantly enhancing durability as compared to conventional and high-performance concretes” (Graybeal 2011). The post-cracking tensile strength is such that it can be included in design of structural elements.

In order for UHPC to be a more valid material for everyday practice in the bridge community, several studies funded by FHWA have extensively examined UHPC material properties (Graybeal 2006, Graybeal and Stone 2012, Graybeal and Baby 2013, Swenty and Graybeal 2013). The authors followed the American Society for Testing and Materials (ASTM) and the American Association of State Highway and Transportation Officials (AASHTO) recommended procedures for the material characterization tests that would typically be done on conventional concrete. In some cases, the authors had to modify or develop new tests to adequately test specimens to get useful information due to the vast differences in material properties. These studies found the tested formulations to have the typical material properties shown in Table 2.1 if cured in field conditions and deployed with 2% steel fibers by volume.

Table 2.1. Typical material properties of field-cast UHPC (taken from Graybeal 2014)

Characteristic	Average Result
Density	155 lb/ft^3 (2,480 kg/m^3)
Compressive Strength (ASTM C39, 28-Days)	24 ksi (165 MPa)
Modulus of Elasticity (ASTM C469, 28-Days)	7,000 ksi (48 GPa)
Direct Tension Cracking Strength	1.2 ksi (8.5 MPa)
Split Cylinder Cracking Strength (ASTM C496)	1.3 ksi (9.0 MPa)
Prism Flexure Cracking Strength (ASTM C1018)	1.3 ksi (9.0 MPa)
Long-Term Creep Coefficient (ASTM C 512,11.2 ksi (77MPa) Stress)	0.78
Long-Term Shrinkage (ASTM C 157, initial reading after set)	555 με
Total Shrinkage (embedded vibrating wire strain gage)	790 με
Coefficient of Thermal Expansion (AASHTO TP60-00)	8.2 x 10^{-6} in./in./°F (14.7 x 10^{-6} in./in./°C)
Chloride Ion Permeability (ASTM C1202, 28-day test)	360 coulombs
Chloride Ion Permeability (AASHTO T259, 0.5 in. (12.7 mm) depth)	<0.10 lb/yd^3 (<0.06 kg/m^3)
Scaling Resistance (ASTM C672)	No scaling
Abrasion Resistance (ASTM C944 2x Weight, ground surface)	0.026 oz. (0.73 g) lost
Freeze-Thaw Resistance (ASTM C666A, 600 cycles)	RDM = 99%
Alkali-Silica Reaction (ASTM C1260, tested for 28 days)	Innocuous

Note: RDM = relative dynamic modulus

2.2.3 Mix Designs

The most commonly used UHPC material in the United States is a proprietary formulation produced by Lafarge under the trade name Ductal®, which has been subjected to significant testing (Graybeal 2011) and used in many previous research projects. FHWA has identified several other proprietary products available in the United States including: BCV®, BSI®, CRC®, and Densit®. The U.S. Army Corps of Engineers has developed their own product, Cor-Tuf® (Williams et al. 2009) and other products are available. Several state DOTs have investigated (or are currently investigating) the potential for developing non-proprietary mix designs with a reduced cost compared to the typically available formulations (Wille 2011, Wille 2013, Graybeal 2013, Berry et al. 2017, El-Tawil et al. 2016, El-Tawil et al. 2018, Mobasher et al. 2019, Looney et al. 2019) or are evaluating more cost effective UHPC materials developed by others (Phares 2014). Willie et al. (2011, 2012) and work by FHWA (Graybeal 2013) provided recommendations for the basic material constituents that should be utilized since the very high compressive strength requirements make the mixtures more sensitive to the quality of the component materials. Work by FHWA proposed mix designs for various

regions of the United States, summarized in Table 2.2, but these did not consider the region including Oklahoma (Graybeal 2013). Each proposed mix included high-strength steel fibers at 1.5% by volume.

Table 2.2. Potential UHPC mix designs developed by FHWA for various regions of the U.S. (Graybeal 2013)

Material/Topic	UHPC-1 (B, NE)	UHPC-2 (L, Upper MW)	UHPC-3 (VR; NW)	UHPC-4 (Q; U.S.)
White Cement, lb/yd^3	1311	1268	1256	1248
Silica Fume, lb/yd^3	328	317	314	312
Fly Ash, lb/yd^3	318	308	305	303
HRWR, lb/yd^3	48	46	45	45
Fine Agg. (75 µm-1.2 mm), lb/yd^3	1966	1903	1884	1871
Agg.-to-cement ratio	1.5	1.5	1.5	1.5
w/c	0.23	0.24	0.23	0.23
Spread, in.	11.4	10.4	11.3	12.4
Avg. f'_c, ksi	26.9	24.1	23.5	29.0
Cost, \$/yd^3	494	472	496	652

Note: B = basalt aggregate, L = limestone aggregate, VR = volcanic rock aggregate, Q = quartz aggregate, all mixes do not include fibers

Exact compositions of UHPC may vary among products with the same performance goals in mind. Some characteristics and components are typical of all UHPC mixtures such as: dry components (cement, silica fume, and fine aggregates), chemical admixtures (accelerators and high range water reducers (HRWR)), water, and steel fibers. Dry components are graded to facilitate adequate flowability and supplementary cementitious materials or coarse aggregates are sometimes included (Graybeal 2014, Wille 2011). Typical mix designs include a w/cm between 0.2 and 0.3, a cement to silica fume to supplemental material ratio of 1.0:0.25:0.25, a fine aggregate to cement ratio of 1.0 to 2.0, and fibers included at 1.0 to 2.0 percent by volume (Graybeal 2013). Wille (2011) recommended a fine aggregate to cement ratio of 1.4 and *w*/*c* between 0.16 and 0.27. Due to the low w/cm and high cementitious material content, a large portion of the cement does not hydrate and simply acts as filler material. Inert filler materials or fly ash have been considered as a partial replacement of cement with the intention of reducing the cement content and overall cost of the material (Wille 2012). The low water content of UHPC requires optimized gradation and large doses of HRWR to obtain proper rheology. Replacement of a portion of the cement with nanoparticles has been shown to speed up hydration of the cement and

improve material properties by improving the gradation and facilitating dispersion (Li 2016, Wille 2012). The fiber type, geometry, and volume fraction are very important to the performance of a UHPC mix design and should be carefully considered (Graybeal 2014).

Berry et al. (2017) developed a UHPC mix design using materials locally available in Montana including Type I/II portland cement, class F fly ash, fine masonry sand, silica fume and superplasticizer. El-Tawil et al. (2016, 2018) developed a mix design for use in bridge repair in Michigan that was used in an implementation project. The final mix design achieved 21.5 ksi at 28 days and consisted of Type I portland cement, slag cement, silica fume, two silica sands, superplasticizer and steel fibers. Mobasher et al. (2019) developed multiple mix designs using materials available in Arizona. Their study focused on particle packing, cement chemistry, and rheology to develop mix designs with compressive strength in excess of 22 ksi using 3 percent steel fibers by volume (Mobasher et al. 2019).

Previous work sponsored by ODOT (Looney et al. 2019, Floyd et al. 2021) led to development of a UHPC class mix design using constituent materials locally available in Oklahoma. This mix design, designated J3, was extensively evaluated for material properties (Dyachkova 2020, Campos 2020), joint structural behavior (Looney et al. 2021, Chea 2020), bond behavior to concrete and steel (Floyd et al. 2021) and durability (Leggs 2019). It was shown to have similar performance to proprietary UHPC formulations in each of these aspects. The mix uses 10% silica fume, 30-40% ground granulated blast furnace slag (GGBFS), Type I/II cement, a w/cm ratio of 0.2, an aggregate/cementitious material ratio of 1.0 when the aggregate is washed, fine sand, and sufficient HRWR reducer to produce a mortar flow of 7 in. to 8 in. (McDaniel 2017, Looney et al. 2019). The final J3 mix design is presented in Table 2.3.

Table 2.3. Mix proportion for J3 UHPC

Material	Quantity
Type I/II Cement (lb/yd^3)	1180
Silica Fume (lb/yd^3)	197
GGBFS (lb/yd^3)	590
Masonry Sand (lb/yd^3)	1966
Steel Fibers (lb/yd^3)	255
Steel Fibers (%)	2.0
HRWR (oz/cwt)	18
w/cm	0.2

2.2.4 Mixing, Placement, and Curing

Typical UHPC mixing procedures first involve dry mixing all constituents, followed by adding the water and then HRWR. Once the mix becomes fluid, or turns over, the fibers are added. The mixing energy required for UHPC is higher than for conventional concrete and the reduced coarse aggregate content and low water content may lead to overheating of the mix. A high shear mixer is typically recommended for mixing UHPC. However, most conventional concrete mixers can be used to mix UHPC if the mixing energy requirements are taken into account through modified mixing procedures. UHPC can be mixed in mortar/grout mixers as well as in traditional concrete mixers; however, traditional concrete mixers and ready-mix trucks may be less efficient than mixers with higher shear (Graybeal 2014). Higher shear mixers can decrease the duration of the mixing process since they impart greater energy into the mix. It should also be noted that, typically, the maximum amount of UHPC that should be mixed in any mixer is about half the volume of conventional concrete that could be mixed (Graybeal 2014). Cubed ice is often used to control temperature during mixing, which also helps provide additional mixing action. Tackett et al. (2009) found that a small high shear mixer, small rotating drum mixer, and a ready-mix truck produced UHPC with adequate performance. Curing procedures had more influence on final behavior than mixer type. Figure 2.4 shows UHPC being mixed in the field with typical mixers.

Figure 2.4. UHPC field mixing operations using high shear mixers (Graybeal 2014)

Placement and consolidation procedures must also be considered carefully to ensure proper fiber distribution and orientation (Graybeal 2011). UHPC is typically placed and moved using wheelbarrows or buckets. Figure 2.5 depicts the process for transporting UHPC from the mixer to the site of the pour and the pouring procedure for a longitudinal connection of bridge elements. When there are two successive pours, the new UHPC should be poured directly over the most recently poured layer; sometimes rodding is necessary to limit the amount of separation between layers. The flowability of UHPC places higher pressure on formwork and requires special attention be paid to joint seals. UHPC does not require the same type of finishing as traditional concrete. Because of its flowability and viscid nature, finishing with a trowel is not effective or necessary. UHPC can be poured into closed forms to provide a smooth top surface and minimize dehydration (Graybeal 2014). It is also common for UHPC to be cast higher than the required elevation and ground after curing to the desired surface texture or appearance.

Figure 2.5. UHPC placement into a longitudinal connection of bridge elements (Graybeal 2014)

Proper curing of UHPC is critical to ensure proper performance. UHPC must be sealed with an impermeable layer immediately after casting or else surface dehydration can lead to cracking and degradation of material properties (Graybeal 2011). It must remain sealed until it can self-support and not self-desiccate, often taken to be when the compressive strength reaches 14 ksi (97 MPa). Moist curing is also an option. Heat curing is helpful but must not contribute to dehydration and steam treatment is often used to enhance properties. A common steam treatment is 194 °F (90 °C) and 95% relative humidity for at least 48 hours (Graybeal 2011). Graybeal (2006) examined four different curing regimens on specimens for each of the material characterization tests. The first regimen was the control specimen that followed the manufacture's recommendation for steam curing the UHPC at 194 ºF (90 ºC) and 95 percent relative humidity for 48 hours. The second regimen was not steam cured but cured at the standard laboratory environment from demolding until testing. The third regimen was tempered steam curing, which was similar to the steam curing recommended by the manufacturer, but the temperature was limited to 140 ºF (60 ºC). The fourth regimen was a delayed steam curing that did not begin until the 15th day after initial casting and used the same recommended specifications for steam curing by the manufacturer. Table 2.4 shows the average UHPC material properties determined from testing.

Table 2.4. Average UHPC material properties for different curing regimens (Graybeal 2006)

Material Characteristic	Steam	Untreated	Tempered Steam	Delayed Steam	Supplemental Description
Compressive Strength (MPA)	193	126	171	171	ASTM C39; 28-day strength
Modulus of Elasticity (GPa)	52.4	42.7	51.0	50.3	ASTM C469; 28-day modulus
Split Cylinder Cracking Strength (MPa)	11.7	9.0	11.7	11.7	ASTM C496
Prism Flexure Cracking Strength (MPa)	9.0	9.0	10.3	9.7	ASTM C1018; 305-mm span; corrected AASHTO T132
Mortar Briquette Cracking Strength (MPa)	8.3	6.2	9.7	6.9	AASHTO T132
Direct Tension Cracking Strength (MPa)	9.7-11.0	5.5-6.9	7.6-9.0	9.0-11.0	Axial tensile load
Prism Flexural Tensile Toughness (I_{30})	53.0	48.3	43.1	48.3	ASTM C1018; 305-mm span
Long-Term Creep (C_{cu})	0.29	0.78	0.66	0.31	ASTM C512; 77-MPa sustained load
Long-Term Shrinkage (microstrain)	850	790	--	--	Embedded vibrating wire gage
Coeff. Of Thermal Exp. ($x10^{-6}$ mm/mm/°C)	15.6	14.7	15.4	15.2	AASHTO TP60-00
Chloride Ion Penetrability (coulombs)	18	360	39	18.00	ASTM C1202; 28-day test
Chloride Ion Permeability (kg/m^3)	< 0.06	< 0.06	< 0.06	< 0.06	AASHTO T259; 12.7-mm depth
Scaling Resistance (grams lost)	No Scaling	No Scaling	No Scaling	No Scaling	ASTM C672
Abrasion Resistance (grams lost)	0.17	0.73	0.20	0.13	ASTM C944 2x weight; ground surface
Freeze-Thaw Resistance (RDM)	96%	112%	100%	99%	ASTM C666A; 600 cycles
Alkali-Silica Reaction	Innocuous	Innocuous	Innocuous	Innocuous	ASTM C1260; tested for 28 days

Multiple factors contribute to the extended initial set time observed for UHPC: temperature at time of placement, ambient temperature, admixtures, cement type, and constituent material properties (Graybeal 2014). Heat curing is often used to accelerate strength gain, or an accelerator is added to the mix if high early strength is needed.

Heat curing is usually done in the field by using external sources such as heating mats or lamps, or internal sources like resistance heating wires (Graybeal 2014).

2.2.5 Overlays

Several studies have been conducted on the effectiveness of UHPC as an overlay material on bridge decks and pavements. The low permeability and high durability of UHPC lends itself to this use. The FHWA investigated the first bridge in the U.S. to use UHPC as an overlay, which was completed in 2016 in Brandon, IA, (the Laporte Road bridge). The overlay was intended to be 1.5 in. thick, and the deck was ground down to remove unsound concrete, grooved, then pre-wetted for several hours prior to placing the UHPC deck overly. The substrate preparation prior to UHPC placement is shown in Figure 2.6.

Figure 2.6. Final bridge deck substrate preparation (Graybeal 2017)

Several months after completion of the overlay, a field inspection indicated there were several areas where delamination could have occurred. This prompted the FHWA to conduct an investigation on the UHPC overlay. The UHPC overlay was visually inspected, examined for delamination using the chain drag test, and the direct pull-off test according to ASTM C1583 was conducted at various locations. The chain drag test revealed eight potential areas of delamination, and two were chosen for the direct pull-off test. Three more regions where delamination was not indicated were also tested, including sections of roadway with and without the scarified substrate preparation. An example of the cores after testing and failure of the conventional concrete substrate is shown in Figure 2.7.

Figure 2.7. Direct pull-off test cores (Graybeal 2017)

In every pull-off test conducted, the failure occurred either in the conventional concrete substrate, or in the adhesive used to bond the testing cap to the concrete, showing that the bond strength between the UHPC overlay and conventional concrete was sufficient. An electron microscope was used to examine several bonded areas and it was noted the bonded surface was interrupted by debris or entrapped air, as shown in Figure 2.8. However, these bond interruptions did not appear to adversely affect the overall integrity of the UHPC overlay (Graybeal 2017).

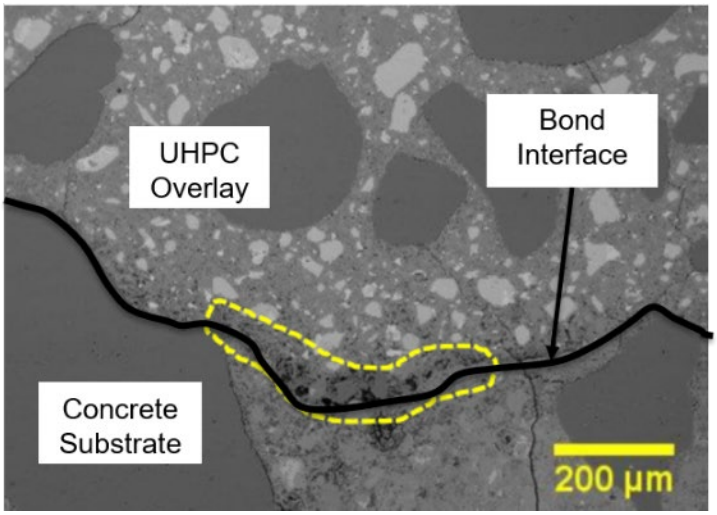

Figure 2.8. Area of bond interruption at UHPC-conventional concrete interface (Graybeal 2017)

Testing of a field-cast bridge overlay was also conducted by Iowa State University (Wibowo and Sritharan 2018). A 1.5 in. thick UHPC overlay was placed on the Mud Creek bridge in Iowa as a repair for the bridge deck. A special UHPC mix (Ductal® NaG3 TX) was developed by LafargeHolcim to ensure proper placement of the UHPC over the crown of the bridge. The asphalt wearing surface and damaged concrete were removed, then the deck was grooved to create an exposed aggregate surface with a 1/8 in. amplitude. Welded wire mesh was also placed at the pier locations in one lane to determine whether it can provide additional negative moment capacity. Once the UHPC overlay hardened, the surface was ground and grooved to provide adequate roughness for traffic. The final overlay is shown in Figure 2.9.

Figure 2.9. Finished overlay on the Mud Creek bridge (Wibowo and Sritharan 2018)

A chain drag test was conducted on the bridge and eight areas were noted that showed signs of delamination. Two of those areas were selected for testing with the direct pull-off test according to ASTM C1583. Three locations without suspected delamination were also tested as a control. The typical failure mode of the direct pull-off test occurred in the conventional concrete substrate and not at the bond interface, as shown in Figure 2.10. It was concluded that the delamination found during the chain drag test was most likely in the conventional concrete substrate prior to the application of the overlay.

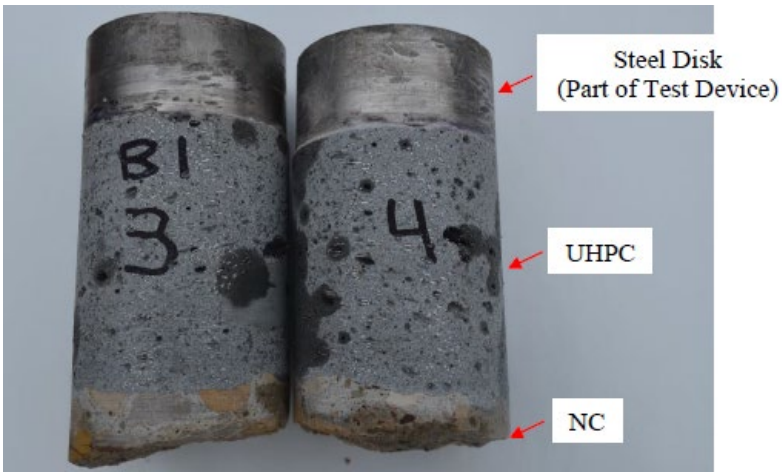

Figure 2.10. Typical direct pull-off test failure for the Mud Creek bridge overlay (Wibowo and Sritharan 2018)

The negative moment capacity was shown to increase in lab testing but mainly due to the additional thickness provided by the overlay. The welded wire mesh in the overlay did not appear to significantly improve the capacity due to its small area (Wibowo and Sritharan 2018).

Another study on the effectiveness of UHPC as an overlay material was conducted at Missouri University of Science and Technology (Khayat et al. 2018). The researchers first developed UHPC mix designs to be placed as overlays at thicknesses of 1 in., 1.5 in., and 2 in., using various methods to mitigate shrinkage such as lightweight sand aggregate and expansive agents. The conventional concrete substrate specimens were cured in ambient air conditions for twelve months prior to application of the overlay. A chemical retarder was applied to each surface during casting to create an exposed aggregate surface roughness. Five UHPC mix designs were used for the overlays with varying percentages of lightweight sand and expansive agents to control shrinkage. The final slabs with overlays were stored indoors for the testing and are shown in Figure 2.11.

Figure 2.11. Final experimental panel with UHPC overlay used by Khayat et al. (2018)

The slabs were monitored for a total of 200 days. Shrinkage of the UHPC overlay was monitored over time to determine the effectiveness of the methods used to reduce shrinkage. Each slab was also examined for evidence of delamination. The surface and interfacial layer of the UHPC showed no signs of cracking throughout the testing, and there appeared to be no evidence of delamination during testing. Since all overlay thicknesses performed well, the overlay thickness of 1 in. was chosen as the most cost-effective (Khayat et al. 2018).

Sarkar (2010) and Denarie and Bruhwiler (2006) explored the feasibility of UHPC as an overlay repair material to be poured as a thin top layer on an existing roadway or bridge. While conducting research on the process of field implementation of a 3 cm thick UHPC overlay on a bridge in Switzerland, Denarie and Bruhwiler (2006) found that implementing UHPC in this capacity could “simplify the construction process, increase the durability of structures and their mechanical performance (stiffness and resistance), and decrease the number of interventions during their service life”. They performed analysis of the rehabilitation by noting the construction process and performing compressive and uniaxial tensile tests, ultimately determining that the benefits of implementing UHPC far outweigh the costs and surpass those of lower quality traditional solutions (Denarie and Bruhwiler 2006). Sarkar (2010) performed extensive evaluation of UHPC and its feasibility as an overlay material by performing slant shear tests, splitting tensile tests, and third point loading flexural tests on specimens with a 1 in. thick UHPC overlay. This study found that, based on its mechanical properties and

the tensile properties exhibited during testing, UHPC achieves adequate bond strength to other concrete materials and is likely feasible as a repair material.

Habel et al. (2004) also performed testing on a UHPC composite overlay configuration to determine the bending behavior of the composite element. The study used a four-point loading system, seen in Figure 2.12. Three different types of overlays were studied (each having different depths and rebar configurations), and the following conclusions were made: (1) the enhanced mechanical properties of UHPC contribute to improved structural response of composite elements due to its strain-hardening behavior under uniaxial tension (2) the stiffness of the composite elements was increased under service loads, and no large cracks formed until the maximum force was reached, and (3) the addition of tensile reinforcement in the UHPC layer increased resistance and stiffness of the composite elements and delayed localized macrocracks (Habel et al., 2004).

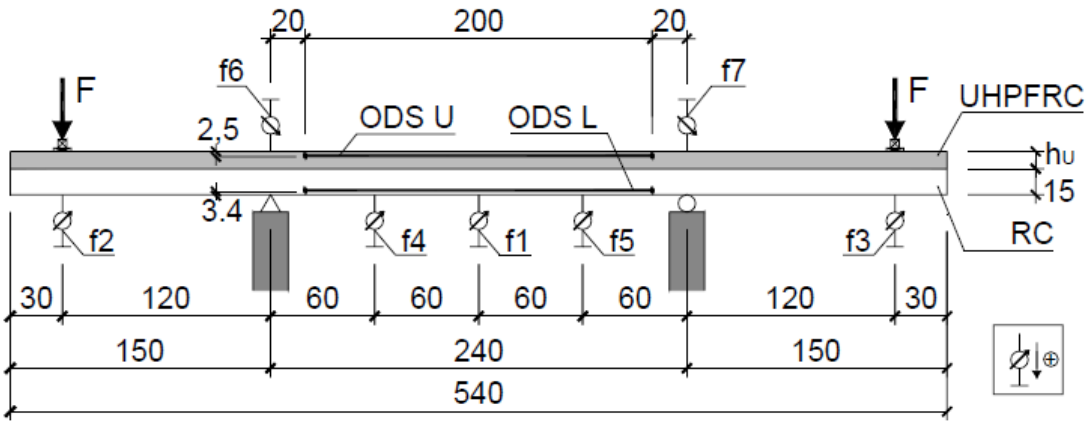

Figure 2.12. Four-point loading system for Habel et al. (2004) experiments. Notations f1-f7 are LVDT locations, and dimensions are given in cm.

2.2.6 Girder Repair

Some states are investigating the use of UHPC for repairs of girder end regions (Connecticut DOT 2016, Shafei et al. 2020). Researchers at the University of Connecticut conducted laboratory testing of three large-scale W21x55 girder specimens to determine the effectiveness of UHPC in restoring the bearing capacity of damaged steel girder ends. One girder was undamaged as a control test, one was artificially

damaged by removing a portion of the cross section to mimic corrosion damage observed on an in-service bridge, and the last was damaged the same way and then repaired using UHPC. The damaged girder is shown in Figure 2.13.

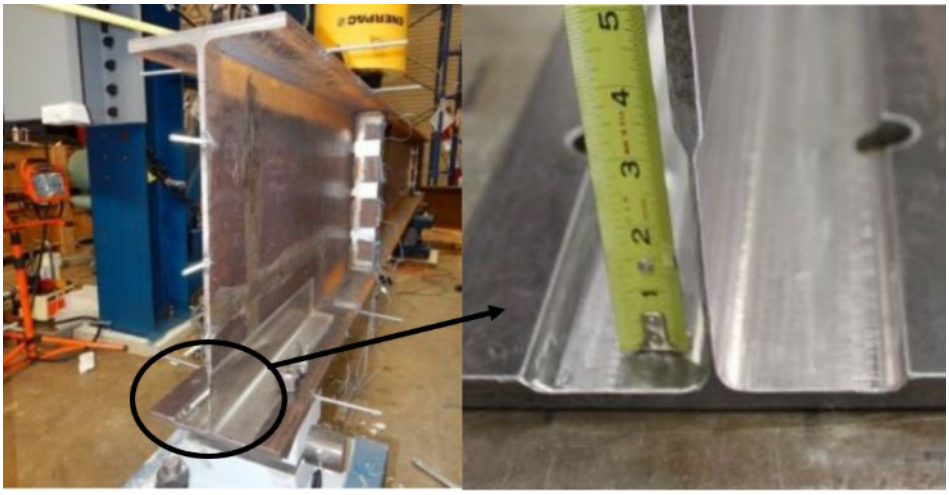

Figure 2.13. Damaged girder end (Zmetra 2015)

Composite action between the UHPC and the damaged girder was achieved by attaching 3/8 in. diameter, 1-1/4 in. long headed shear studs to the girder, as shown in Figure 2.14. The thickness of the UHPC repair was no less than 1-3/4 in. to ensure a minimum stud clear cover of ½ in. The repair was only added to the bottom two-thirds of the girder due to the strength limitations of the test setup. The final repaired girder is shown in Figure 2.15. Mineral oil was applied to the portion of the girder bonding to the UHPC to mimic the effect of paint on an in-service girder.

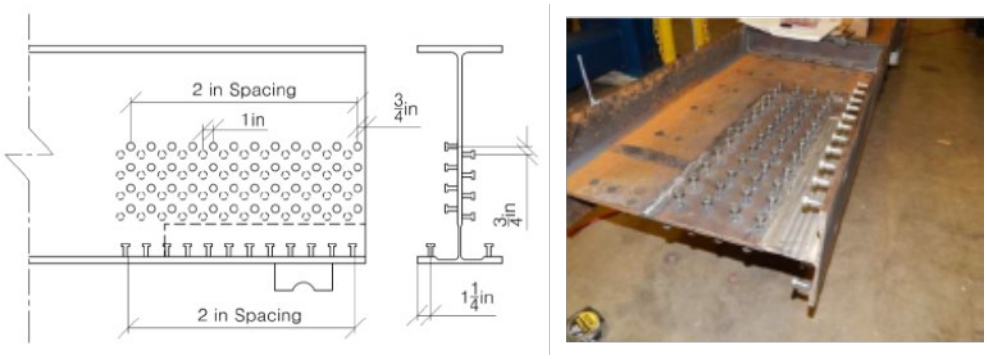

Figure 2.14. Shear stud layout on the repaired girder (Zmetra 2015)

Figure 2.15. Final repaired girder (Zmetra 2015)

A concentrated load was applied to each girder 32 in. from the rocker support and the span length of the simple supports was 12 ft. The UHPC used for the encasement achieved a flow of 11 in. and reached a compressive strength of 16,000 psi at time of testing, four days after casting. The failed girders are shown in Figures 2.16, 2.17, and 2.18.

The undamaged girder failed at a load of 180 kips by web buckling and the damaged girder failed at a load of 43 kips by web buckling at the location of removed material. However, the repaired girder end failed at a load of 230 kips by flexural yielding (Zmetra 2015). This change in failure mode appears to show that, at 16,000 psi, the UHPC was able to provide enough bracing to preclude a web buckling failure, thus ensuring a yield failure. Overall, the repair was able to enhance the end bearing capacity beyond that of the undamaged girder.

Figure 2.16. Undamaged girder failure (Zmetra 2015)

Figure 2.17. Damaged girder failure (Zmetra 2015)

Figure 2.18. Repaired girder failure (Zmetra 2015)

In another research project by Shafei (2020), an Iowa bulb-tee-C- shaped beam was used to evaluate the performance of a UHPC patch to rehabilitate induced end region damage. The web of the girder was thinned by approximately 30% to represent shear damage at the location marked in Figure 2.19. Forms were placed along the sides of the girder with weep holes at the top to avoid entrapped air and were wetted before casting to reduce water absorption. After the UHPC was poured and hardened, the beams were tested with the loading arrangement shown in Figure 2.20. It was reported that the patch demonstrated a good bond with the girder with substrate concrete failure before the UHPC patch.

Figure 2.19. Cut beam segment marked for controlled damage (Shafei, 2020)

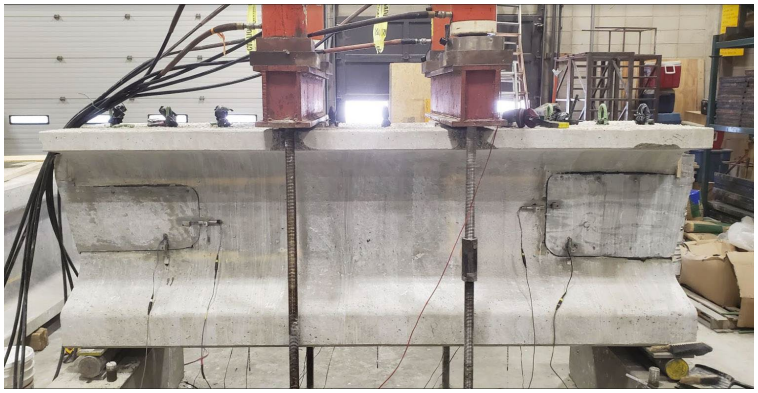

Figure 2.20. Loading setup for beam with UHPC patch (Shafei, 2020)

2.2.7 UHPC to Conventional Concrete Bond Strength

2.2.7.1 Overview

The most important property ensuring the effectiveness of any concrete repair is the bond strength between the existing concrete substrate and the repair material.

Without adequate interfacial bond strength, the bond of the two materials could fail prematurely without any failure of the repair material itself. Several factors can affect the bond performance between conventional concrete and the repair material. Rougher surface preparations allow for better bond strength than smooth finishes. Roughening can expose more capillaries in the conventional concrete substrate, allowing the repair material an easier path to fill them. Additionally, increased surface roughness allows for a better mechanical bond between the two materials. The flowability of the repair material directly affects how well it can fill the substrate's capillaries. Capillary action between the repair material and the substrate will be more effective the more fluid that the repair material. Also, exposed aggregate substrate finishes provide improved bond strength through aggregate interlock. Another important factor affecting the bond strength is the substrate moisture content. Dryer surfaces can potentially pull water from the repair material into the substrate's capillaries, thus reducing the level of hydration of the repair material at that interface. Too much moisture can locally increase the water content of the repair material, thereby lowering its strength. Graybeal (2016) tested a relatively simple method to ensure an adequate moisture content of the conventional concrete substrate involving placing wet burlap over the bond surface for several hours prior to placing the repair material.

Various studies have been conducted to determine the bond strength of UHPC when cast against conventional concrete in both laboratory and field conditions. The tests used to evaluate the bond strength between UHPC and conventional concrete in these studies included the direct tension pull-off test, slant shear compression test, splitting cylinder test, and the flexural beam test. Momayez et al. (2005) performed a study on the bond strength between concrete substrates and various repair materials. This study included several types of tensile and shear testing, including pull-off tests, splitting prism tests, slant shear, and bi-surface shear testing. Although the study did not use UHPC as a repair material, the six repair materials used (each with a different mix design) provided useful information on the factors that affect bond strength, especially when using slant shear tests. Momayez et al. (2005) drew the following conclusions:

- The measured bond strength is highly influenced by the type of test performed. Each test that was conducted had an acceptable coefficient of

variation, but it is crucial to select tests that represent the stress state of the structure or configuration in the field.

- Slant shear testing typically yields the highest measured bond strength.
- Bond strength between the repair material and the concrete substrate increases with the amount of silica fume in the repair material.
- Preparation of the concrete substrate surface that increases the roughness leads to a higher bond strength—about 25% higher for slant shear tests.

2.2.7.2 Direct Tension Pull-Off Test

The direct tension pull-off test follows ASTM C1583 and consists of casting UHPC over a cured conventional concrete slab. Then, after the UHPC is cured, a core bit is used to drill though the repair material and at least 0.5 in. into the conventional concrete substrate. A steel connector is then attached to the cored concrete and a direct tension load is applied until failure of either the conventional concrete substrate, the UHPC, or the interface between the two materials. The setup for this test is shown in Figure 2.21.

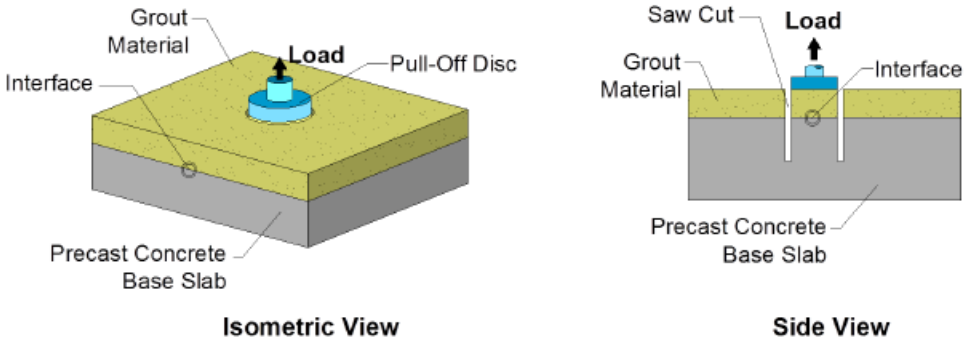

Figure 2.21. Direct tension pull-off test setup (Graybeal 2016)

A failure in the conventional concrete substrate indicates that the bond strength is larger than the tensile strength of the conventional concrete, thus adequate bond is provided. Failure in the UHPC is unlikely due to its relatively large strength compared to conventional concrete. The test method is an effective way to directly determine the tensile strength of the bond between the materials since the interface is only subjected

to tensile stresses. Munoz et al. (2014) conducted this test for the proprietary UHPC, Ductal®, using four different surface preparations on the conventional concrete: wire brushed, sandblasted, grooved, and exposed aggregate. All conventional concrete substrates were saturated, and their surfaces dried (SSD condition) prior to applying the UHPC. In all their pull-out tests but one, the failure occurred in the conventional concrete substrate (Munoz et al. 2014).

Graybeal (2016) conducted the direct pull-off test using different levels of aggregate exposure: high, medium, and low, as shown in Figure 2.22. Field-cast UHPC was used in this study. The results showed that the level of aggregate exposure did not drastically affect the bond strength between UHPC and the conventional concrete substrate, with all three levels gaining approximately 600 psi tensile strength. The effect of substrate moisture was then determined by testing the bond strength difference when the substrate was lightly sprayed, wet burlap was left on the substrate for 2-4 hours, and the SSD condition. When wet burlap and the SSD conditions were tested, the failure shifted from the bond interface to the substrate, indicating those two wetting methods improved the bond strength (Graybeal 2016).

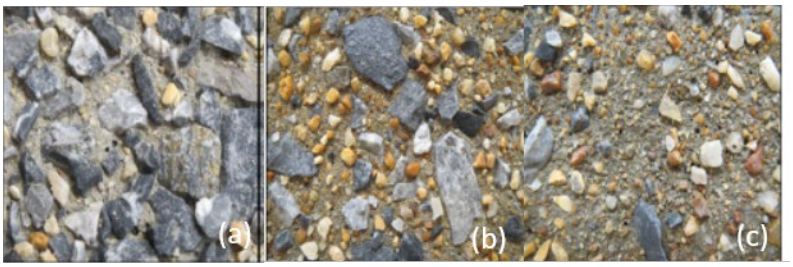

Figure 2.22. (a) High, (b) medium, and (c) low aggregate exposure levels (Graybeal, 2016)

2.2.7.3 Slant Shear Test

The slant shear compression test follows ASTM C882, utilizing UHPC in lieu of epoxy-resin. A standard compression cylinder is tilted to whichever bond angle is desired, then conventional concrete is added until the edge of the concrete reaches the opening, filling roughly half of the mold while creating a slanted bond surface. The conventional concrete is allowed to cure, and then the UHPC is placed in the remainder

of the mold. When tested, a compression load is applied at the two ends of the cylinder, as shown in Figure 2.23.

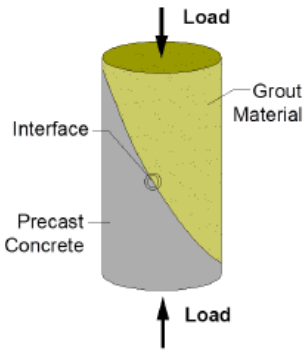

Figure 2.23. Slant shear compression test (Graybeal 2016)

This test creates shearing and compressive forces along the interface. The failure can either occur along the bond interface or the conventional concrete material can crush similar to a conventional compression test. Munoz et al. (2014) conducted this test with UHPC, and the same surface roughness and moisture conditions used on the direct pull-out tests, at three and eight days of age. The researchers tested bond angles of 60° and 70° from the horizontal. All specimens with a wire brushed interface failed in bond, while all other tests failed in the concrete substrate. This shows that the wire brushed surface provided lower bond strength than the other surface roughness levels tested (Munoz et al. 2014). Climaco et al. (2001) performed tests on prisms of different sizes and proportions, finding that the size of the specimens had little to no effect on the results obtained from testing. Tayeh et al. (2013) performed experiments on prismatic slant shear specimens with a cross-section length and width of 100 mm, height of 300 mm, and interface angle of 60 degrees from the horizontal. Figure 2.24 shows an example of a prismatic specimen.

Some researchers that have adapted tests for slant shear have used a larger cylindrical version of the original ASTM C882 slant shear test. ASTM C882 specifies the cylinder size to be 3 in. by 6 in. for assessing mortar bonds, but researchers like Diab et al. (2017) used larger composite cylinders with diameters that were half of the height, finding smaller coefficients of variation and results that were more consistent. Sarkar (2010) also performed slant shear tests on cylindrical specimens, seen in Figure 2.25.

This study utilized 3 in. by 6 in. composite cylinders composed of half normal-strength concrete and half UHPC at a 30-degree angle.

Figure 2.24. Prismatic specimen and testing setup for Tayeh et al. (2013) experiments

Figure 2.25. Cylindrical specimen and testing setup for Sarkar (2010) experiments

According to Climaco et al. (2001), the stress state in slant shear tests at failure depends on the quality of the bond. In many of the experiments in previous research, the composite specimen failure occurred within the normal concrete substrate rather than along the bond interface, indicating that the bond could have resisted higher stresses and demonstrating the superior bond behavior of UHPC (Tayeh et al. 2013; Munoz et al. 2014). In the Munoz et al. (2014) experiments, the specimens “obtained a bond capacity, at the age of 3 days, greater than the [strength] requirements given by

ACI 546-06 [Guide for Repair of Concrete Superstructures] (ACI 2006) at 7 days and also satisfies the requirements at 28 days."

2.2.7.4 Splitting Tensile Strength Test

The splitting cylinder test follows ASTM C496. A standard 6 in. x 12 in. cylinder mold is typically used, but the specimen size can be modified. Typically, the cylinder is filled with a single material for testing. However, slight modification to the ASTM allows for the testing of bonded UHPC materials. During casting, the mold is placed on its side and the conventional concrete is poured into the mold until it is filled halfway. After the conventional concrete has cured, the UHPC is used to fill the remainder of the mold. Once cured, the specimens are tested on their side with the load point lining up with the bond interface, as shown in Figure 2.26. This load application ensures a tensile force is applied along the bonded interface.

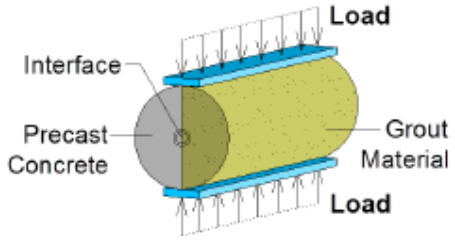

Figure 2.26. Splitting cylinder test (Graybeal 2016)

Munoz et al. (2014) conducted this test on rectangular specimens in lieu of circular. However, the loading was applied in the same manner to ensure tension stress at the bonded interface. For this test, the following surface preparations were tested: smooth, chipped, wire brushed, sandblasted, and grooved. All surfaces were tested in both the dry and SSD condition and testing was conducted after at least 278 days to evaluate long term bond strength. The researchers found that the specimens with a dry substrate failed during demolding except the grooved surfaces, since they provided a channel for interlocking between the UHPC and conventional concrete. The SSD condition performed excellently, with most of the specimens' splitting tensile stress at failure exceeding the expected tensile strength of the conventional concrete. Furthermore, splitting tensile specimens were tested following freeze-thaw cycles.

These specimens all failed at a higher load than the original specimens, showing that freeze-thaw cycles did not adversely affect the bond strength (Munoz et al. 2014)

2.2.7.5 Flexural Beam Test

The flexural beam bond test follows ASTM C78. A pour stop is placed in the center of the beam mold and half of the mold is filled with the conventional concrete substrate. After curing, the other half is filled with UHPC. Bond angles typically tested are 90°, 60°, and 45° from the horizontal with various surface preparations. The beams are then subjected to third-point loading according to ASTM C78, as shown in Figure 2.27. The test creates flexural stresses along the surface of the bond.

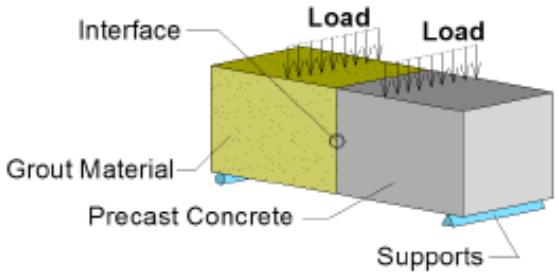

Figure 2.27. Flexural beam bond test (Graybeal 2016)

Funderburg (2018) conducted tests on flexural beam bond specimens with bond angles of 90°, 60°, and 45° between the conventional concrete and the proprietary UHPC, Ductal®. Each bond angle was tested with the following substrate preparations: sand blasted, wire brushed, and exposed aggregate. The sand blasted and wire brushed specimens were created by cutting a complete specimen in half to simulate a repair operation while the exposed aggregate specimens were cast using a form insert. Also, several specimens were cast with a shear key at the bond interface with the exposed aggregate surface. The shear key conventional concrete specimen before placement of the UHPC is shown in Figure 2.28.

Figure 2.28. Shear key conventional concrete substrate (Funderburg 2018)

The UHPC was cast against each surface without any pre-wetting, and each beam was tested 28 days after casting the UHPC. Three of the five wire brushed specimens with a 90° bond angle failed at the interface and the remaining eight specimens at that bond angle all failed in the conventional concrete. All tests with 45° and 60° bond angles failed in the conventional concrete. These results show that, even with a dry interface, Ductal® develops sufficient bond strength to ensure continuity of the beam specimens (Funderburg 2018). The tests completed by Funderburg (2018) were repeated by Coleman (2018) using the non-proprietary J3 UHPC developed at the University of Oklahoma. These results indicated a lower bond strength for the non-proprietary UHPC, but that bond strengths similar to the strength of the substrate concrete could be achieved with proper surface preparation and UHPC flowability (Coleman 2018).

2.3 FR-SCC as a Repair Material

2.3.1 Overview

Self-consolidating concrete (SCC) can be defined as a “highly flowable, non-segregating concrete that can spread into place, fill the formwork, and encapsulate the reinforcement without any mechanical consolidation.” (Kassimi, 2014). SCC was first developed in Japan in the 1980’s as structures were heavily reinforced to resist seismic loads, and there was a peak demand for a flowable concrete to fill the complex

formwork with congested reinforcement with little or no mechanical vibration. This new concrete decreased the construction time while producing a smooth finished surface. However, the remarkable mechanical properties of materials cannot guarantee that it will be a successful repair material unless experimentally proven (Abdulhameed, 2018). The recent increased use of SCC in structural concrete repair applications is derived from its many advantages offered before and after hardening. One highly favorable advantage of SCC is its ability to flow under its own weight. This means that it is capable of forming in and around uneven surfaces without the use of mechanical vibration making it an ideal candidate for repair applications.

Unfortunately, just like conventional concrete, SCC also shrinks and cracks throughout the process of curing. Fiber reinforced self-consolidating concrete (FR-SCC) is a relatively recent innovation of SCC made of cement, sand, coarse aggregate, water, admixtures, and fibers. The addition of polypropylene fibers can improve the properties of FR-SCC like post cracking response, energy absorption capacity, and reducing the possibility of cracking due to shrinkage (Kassemi et al. 2014). Concrete members containing fiber-reinforcement in general carry many benefits in comparison to traditional concrete members. These benefits include: a better cracking resistance, a higher ductility, a higher toughness, a greater tensile strength, a higher resistance to fatigue, an ability to absorb larger impacts/blast loadings, an ability to reduce the spalling of cover over reinforcing bars in columns, and an ability to increase beam shear strength (Khayat and Roussel 2000).

2.3.2 Previous Research on FR-SCC as a Repair Material

The first documented case study involving the use of SCC in repair operations involved the rehabilitation of a parking garage in downtown Sherbrooke, Quebec, in 1996 (Khayat and Aitcin 1998). SCC was used for the repair of the bottom and vertical sides of a 20-ft-long beam exhibiting advanced corrosion damage situated under an expansion joint at the entrance to the parking structure. The repair section contained longitudinal reinforcing bars and stirrups anchored into the existing concrete that presented serious obstacles for the spread of fresh concrete. The concrete was cast from two 4 in. diameter holes drilled from the upper deck of the beam along the outer

length of the beam between the existing concrete and formwork. The developed SCC mix was shown to flow under its own weight along the highly restricted section and around the vertical side to fill the opposite side of the formwork through narrow spacing. Due to its success, the Quebec Department of Transportation developed its first performance-based specifications for SCC in 1997 and has used SCC in several infrastructure rehabilitation projects since that time. Experience with SCC has shown that in addition to its ease of casting characteristics, the concrete can exhibit high durability and good bond to existing surfaces and reinforcement (Kassimi 2013).

Successful experience with the performance of SCC as a repair material has attracted the attention of state departments of transportation (DOTs) and construction firms in the U.S. and Canada. Complex repair geometries with congested reinforcement coupled with limited access has shown the benefits of SCC as a repair material. Two such projects involved the repair of an impact damaged bridge pier for the Colonial Parkway, shown in Figure 2.29, and repair of a corrosion damaged column and pier cap for a bridge on SR 712, shown in Figure 2.30, both completed by the Virginia DOT (Ozyildirim 2013).

Figure 2.29. Damaged (left) and SCC repaired bridge pier (right) (Ozyildirim 2013)

Figure 2.30. SCC repaired column and pier cap (Ozyildirim 2013)

When self-consolidating concrete is applied to an aged structural member, to the repair may be subject to debonding itself from the concrete substrate interface as the repair material begins to shrink and crack. Within the last decade or so, researchers have investigated methods to control and combat this unfavorable property. Research done at the University of Sherbrooke found the best combination to reduce potential cracking of SCC was to add steel fibers and expansive agent to the mix to create FR-SCC (Kassimi 2013). The initial research by Kassimi was the starting point to move forward with evaluating and developing optimum fiber types and mixtures in the repair of full-scale reinforced concrete beams. Kassimi et al. (2014) completed an extensive investigation to evaluate the performance of various fibers in SCC targeted for repair applications. The concrete mixtures were tested for workability, mechanical properties, drying and restrained shrinkage, flexural creep, and structural behavior in flexure. Polypropylene fibers, hybrid steel and polypropylene fibers, and steel fibers were used. The investigated structural performance included the testing of both conventional concrete and repaired beams made with FR-SCC. FR-SCC made with 0.25% or 0.5% steel fibers yielded the best overall performance, although some synthetic fibers incorporated at 0.5% also yielded excellent performance. The research showed that the fiber-reinforced self-consolidating mixtures were suitable for repair applications and can restore at least 95% of initial load-carrying capacity of structural elements made of conventional concrete. The beams repaired with steel and long multifilament polypropylene fiber-reinforced self-consolidating mixtures exhibited better structural performance in terms of load carrying capacity and stiffness than those repaired with either monofilament polypropylene or hybrid fiber reinforced SCC. Although limited in scope, the investigation revealed that the incorporation of fibers along with an expansive agent can enhance the resistance to restrained shrinkage. The improvement was greater than that observed in SCC with expansive agent or that for SCC and fibers; a synergetic effect was observed where the presence of both fibers and expansive agent can secure superior resistance to cracking in concrete, which is a key requirement to enhance the service life of the repair. (Kassimi et al. 2014).

Fantilli et al. (2011) conducted experiments testing the multi-axial compressive strengths of FR-SCC and SCC concrete mixes at 0, 1, 3, and 10 MPa lateral loadings.

Their results showed that steel fibers present in the mix act like a confining material creating a compressive pressure throughout the concrete similar to the compressive pressure when stirrups are present (Fantilli et al., 2011). The higher confinement present in concrete created higher ductility in compression. Khayat (2017) found that 4% Type G expansive agent FR-SCC had a 56-day flexural strength 32% higher, flexural toughness 23 times greater, and crack resistance 42% higher than FR-SCC with no expansive agent.

In a research project by Abdulhameed (2018), ten full-scale beams were cast to study the flexural behavior of FR-SCC as a repair material. Two of the beams were full-size to obtain the baseline values for comparison (Figure 2.31(a)), while the remaining eight were built with exposed tension-steel as hatched in Figure 2.31(b). The beams were tested with third point loading to observe the behavior of the repair under pure flexure. Despite a lower ultimate load for the repaired beams, the flexural cracking loads displayed significant improvement compared to the control beams.

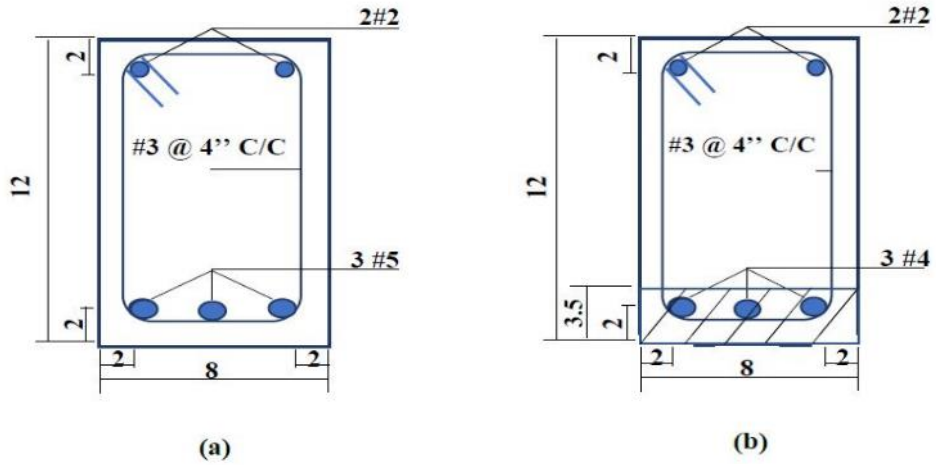

Figure 2.31. (a) Undamaged control beam and (b) damaged beam (Abdulhameed 2018) (all dimensions are in in.)

A recent study completed at the University of Oklahoma (Choate 2018) evaluated the ability of FR-SCC to repair a severely damaged, full scale, AASHTO Type II girder. The girder was removed from the I-244 bridge over the Arkansas River and transported to the Donald G. Fears Structural Engineering Laboratory in Norman, OK. Each end of the girder was then tested in shear to failure as part of the completed ODOT project

SPR 2256 (Floyd et al. 2016) to evaluate the behavior of prestressed girders after years of service. Subsequent repairs to the girder involved extensive concrete removal, repairs to internal reinforcement, and placement of an FR-SCC mixture developed in an earlier research project at the University of Oklahoma (Wirkman 2016). This FR-SCC mixture incorporated macro polypropylene fibers and a shrinkage compensating cement. Subsequent testing (Figure 2.32) revealed that the repairs restored 83% of the original tested capacity of the girder and 116% of the required factored load capacity for the bridge structure (Choate 2018). Wirkman (2016) conducted small-scale and large-scale flexural tests of composite beams cast using FR-SCC as a repair material. These tests showed similar performance of the repaired beams when compared to control monolithic beams cast with conventional concrete.

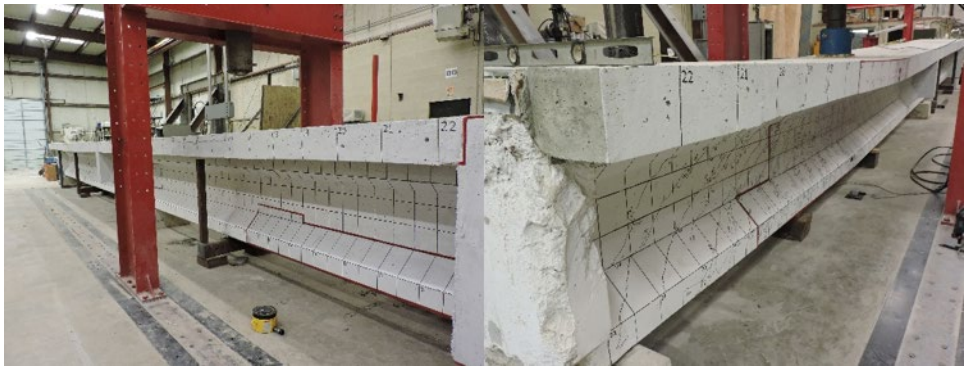

Figure 2.32. FR-SCC repaired girder before (left) and after (right) testing

An example of the application of FR-SCC in the field involved repairs to the 860-ft-long Jarry/Querbes Underpass in 2003 (Kassimi 2013). The structural elements of the underpass had undergone severe degradation due to aggressive exposure to freeze-thaw damage, as shown in Figure 2.33. For the retaining walls on both sides of the underpass, 29 panels were cast with FR-SCC containing either a naphthalene- or a polycarboxylate-based superplasticizer depending on the ambient temperature. Small and finely distributed surface cracking was obtained through the use of synthetic structural fibers (Khayat et al. 2005).

Figure 2.33. Application of FR-SCC in Jarry/Querbes underpass, Montreal (Khayat et al. 2005)

2.4 MALP Concrete as a Repair Material

Magnesium-Alumino-Liquid Phosphate (MALP) is a relatively new material for concrete structure repair. MALP concrete consists of a pre-packaged magnesium-alumino-aggregate dry powder with a mono-aluminum-liquid phosphate activator and is fast-setting with high-early strength (Phoscrete 2014). MALP materials should not be confused with traditional magnesium-ammonia-phosphate cements even though they produce similar properties. No water is used for mixing and placement of MALP concrete. In general, magnesium phosphate cements set and gain strength very rapidly, have high bond strength and have high durability (e.g., Ding and Li 2005, Yue and Bing 2013). Traditionally, magnesium-phosphate cements consisted of magnesia and ammonium phosphates, which react rapidly, but produce ammonia gas during mixing and after setting (Yue and Bing 2013, Ding et al 2014). MALP was initially developed for patching concrete industrial floors but has recently found use as a repair material for transportation structures (Fournier 2014). This material can be used for repair of horizontal, vertical, and overhead surfaces with a rapid strength gain that brings the structure to service faster. Once the MALP is cast, it expands and creates an excellent bond with the substrate and provides very low permeability for chloride ions. It also stops the corrosion of steel reinforcement by converting the iron oxide to metal phosphate which coats the reinforcement and prevents further corrosion (Concrete repair products 2020). Limited research has been conducted specifically on MALP concrete.

The commercially available proprietary product Phoscrete® is a fast-setting MALP concrete. It has a small aggregate and can be used for thin applications down to the point of a feather edge. It can reach compressive strengths in excess of 4000 psi in 30 minutes, which can allow for fast repair and return of the structure to traffic. Higher temperatures can result in a faster reaction, so care must be taken when using Phoscrete® to ensure that the material temperatures are controlled, and the desired result is achieved. Phoscrete® has a small expansion factor which can help mitigate differential shrinkage between the base concrete and repair. The chemical composition of Phoscrete® results in a strong bond to corroded reinforcing steel and an acidic environment, which reduces the possibility of the halo effect when used to encapsulate reinforcement that has already exhibited corrosion (K. Bartfay personal communication June 25, 2018). Phoscrete® bonds chemically to the base concrete creating a strong bond between the base concrete and repair. It has been used successfully for expansion joint headers in Washington, Oregon, North Carolina, and Florida, with data showing adequate performance after 5 years in service (Mintz 2018a). It has also been used as a patch material on bridge decks in Kentucky, California (Mintz 2018b), and New York (Fournier 2014). The fast set, rapid strength gain, and high durability provided by Phoscrete® make it a desirable repair material for portions of a bridge subject to extreme environmental impact. However, the current lack of performance information limits its use.

2.5 Corrosion in Concrete Repair

There is extensive research into many areas of UHPC durability. However, the reaction of bridge decks with previously corroded reinforcing steel to partial or full depth repairs using UHPC is less common. Even Graybeal (2006, 2007) only mentions corrosion of UHPC in terms of surface corrosion of steel fibers on and near the exterior of the concrete, calling it “more aptly described as surface staining”. The primary reasoning behind the concern over the likelihood of UHPC or other repair materials used in a bridge deck leading to further corrosion issues in the existing steel is the anodic ring phenomenon, or “Halo Effect”. The Halo Effect experienced by steel reinforcing in concrete is generally the result of the accelerated corrosion of steel in the base material that has come into contact with fresh concrete due to the very high pH in

fresh concrete as compared to concrete that has been in use for an extended period of time.

This specific kind of corrosion cell is more specifically called macrocell corrosion. Steel rebar corrosion occurs due to an oxidation process that breaks down the passive film covering steel rebar in the presence of chloride ions or carbon oxide (Jones 1996). That is to say, when an anode and a cathode are separated from each other, the concrete itself acts as an electrolyte solution and a macrocell is produced. According to Hansson (2006), a simplified definition can be used, which states that macrocell corrosion in steel rebar is when an actively corroded bar is coupled to a passive bar or one of lower corrosion rate. Coupling can consist of either direct contact or simply close proximity, since the concrete is acting as an electrolyte solution that connects the two closely located reinforcing bars. Differences in corrosion states can occur due to differences in composition (such as the use of different sizes or grades of rebar in the same section of concrete) or differences in environments (such as having rebar that goes through base concrete and the repair concrete). In these scenarios, the corroded bar becomes the anode, and the passive bar becomes the cathode.

This is all in comparison to microcell corrosion, which does not need a specific scenario to occur, only an anode and cathode present directly adjacent to one another, which is simply caused by having surface irregularities and is true of all steel reinforcing. This means that microcell corrosion occurs across every steel reinforcing bar on its own to varying degrees. Because of this, only macrocell corrosion indicates negative interaction between base concrete and repair material through the Halo Effect.

It should be noted that typically, fresh concrete has a pH of around 13, while concrete that has been allowed to age and experience carbonation from contact with the air has a pH of about 8. The high starting pH of typical concrete is mostly due to calcium hydroxide, which is a byproduct of cement hydration. However, no research has been done to find the exact pH of UHPC, in the fresh state or long-term state. It can be assumed that the low w/c ratio of UHPC that leads to often having large amounts of unhydrated cement within its densely packed matrix would lower the pH of fresh UHPC. On the other hand, the fact that UHPC also starts with such a higher level of

cementitious product compared to normal concrete, having no coarse aggregate (instead filling its voids with replacement cementitious materials such as silica fume), may increase the pH of UHPC.

Though no studies are currently available detailing how steel rebar reacts to UHPC as a repair material, a starting place for analysis is still necessary. A study by Hansson (2006) looked at the corrosion performance of different concrete mixes on their own. This study chose to look at three concrete mixes, one normal portland cement mix and two high performance concrete (HPC) mixes (one using 25% cement replacement of blast furnace slag and one with 25% replacement of class C fly ash) as detailed in Table 2.5. In this study, seven 11 in. x 6 in. x 4.5 in. (279 mm x 152 mm x 114 mm) prisms were tested for each mix, totaling to 21 specimens, each containing three 10M reinforcing bars, one with a 25 mm cover from the top and two with a 25 mm cover from the bottom. These small-scale specimens were cured with wet burlap for 7 days, stored outdoors for 5 months to prepare them for exposure to chlorides, and then tested for macrocell corrosion (Hansson 2006).

Table 2.5. Hansson (2006) mix designs

Material	Type 10 Portland Cement (kg)	Type 10SF Portland Cement (kg)	Slag (kg)	Fly Ash (kg)	Sand (kg)	Stone (20 mm) (kg)	Water (l)
Portland Cement	335	-	-	-	770	1,070	153
HPC - Slag	-	337	113	-	718	1,065	158
HPC - Fly Ash	-	337	-	113	718	1,065	158

For macrocell corrosion testing, the specimens were prepared for measurements as follows: coating the vertical surfaces with epoxy resin to prevent the access of oxygen into these surfaces, mounting a ponding well onto the top surface, connecting the bottom two bars to each other and finally, connecting the two bottom bars to the top bar through a 100-ohm resistor. From there, the ponding well was filled with a 3% NaCl solution off and on for two-week periods for a total of 180 weeks, with the voltage drop across the resistor of each specimen being measured daily. The macrocell corrosion current between the top (anode) bar and the bottom (cathode) bars was determined using the measured voltage drops and Ohm’s law for conversion. Overall, this study

showed the HPC's as performing significantly better at protecting the steel rebar from macrocell corrosion than normal portland cement concrete, having no active corrosion after 180 weeks in either HPC mix. In comparison, the portland cement concrete mix experienced corrosion initiation as soon as 35 days into testing. This is almost certainly due to the fact that HPC, like UHPC, has a high level of impermeability, and if no chloride ions can penetrate into the HPC specimens, there can be no electrical difference across the different levels of steel reinforcing (Hansson 2006).

This result does not, however, guarantee that UHPC will still produce such a satisfactory result when used as a repair material. The impenetrability of UHPC may in fact cause more chloride ion build up in the base concrete, creating a large macrocell current across any steel rebar that goes through both materials.

2.6 Summary

Precast prestressed concrete bridges are the most common type of slab and girder bridge in Oklahoma and many of these bridges are reaching the end of their design lives. Effective repair and rehabilitation methods are critical for extending the life of many of these bridges. Two specific areas of in-service bridges where cracking and corrosion are problems and durable repair materials are needed are girder continuity connections and girder end regions. UHPC, FR-SCC, and MALP concrete have great potential for use in repair of these regions. However, limited information is available on structural performance of these types of repairs and their effect on corrosion in the existing structure. In addition, limited information is available for design and construction practice of repairs constructed with these materials.

3.0 Mixing and Placement Methods for Repair materials

3.1 Overview

Mixing methods and equipment previously used in ODOT project SPR 2276 were used for small-scale UHPC batching and a rotating drum mixer was used for the FR-SCC to test fresh and hardened properties important for concrete repair. A large high shear mixer was used for mixing large quantities of all repair materials. Fresh properties were evaluated using the mortar flow test, and hardened properties were primarily evaluated using compressive strength. All tests on the UHPC materials were conducted according to ASTM C1856 and results were reported as part of SPR 2276 (Floyd et al. 2021). Similarly, the methods defined by Choate (2018) were used to determine the same fresh and hardened properties for FR-SCC, which included slump flow (ASTM C1611) and compressive strength (ASTM C39). Placement methods similar to those employed by Choate (2018) using closed forms with holes drilled through the bridge were used for both UHPC and FR-SCC. The Phoscrete® MALP material was mixed using the standard paddle mixer provided by the manufacturer. Procedures for mixing and placement methods suggested by the manufacturer were utilized throughout the project for the MALP concrete. Slant shear testing using a modified version of ASTM C882 with 6 in. x 12 in. cylinders and the direct tension pull-off test described by ASTM C1583 were used to compare bond strengths between different levels of flowability for the three materials.

3.2 FR-SCC Characterization

The FR-SCC mix design developed during previous research Wirkman (2016) and Choate (2018) was modified for workability and used for characterization testing. This mix design had a targeted slump flow of 28 ± 2 in., targeted air content of 6%, and 28-day compressive strength of 4000 psi. The mix design is given in Table 3.1. For hardened property testing, 6 in. x 12 in. cylinders and 6 in. x 6 in. x 24 in. long prisms were cast, shown in Figure 3.1 for compressive strength, splitting tensile strength, and modulus of rupture testing. For conventional concrete, the necessary cylinder size used for these tests would be a smaller 4 in. x 8 in. specimen; however, because of the 1.5 in. length of the polypropylene fibers, a larger mold for FR-SCC cylinder experiments

was required in order to allow the fibers orient themselves properly in the specimens. Table 3.2 highlights the property tests that were conducted to define the newly modified FR-SCC mix design.

Table 3.1. Final FR-SCC mix design

Material	Quantity (lb/yd^3)
Portland cement (Type I)	412.5
Fly Ash	225
Type K Cement (Komponent)	112.5
Water	230
Fine Aggregate	1441
Coarse Aggregate (River Rock; Pea-Gravel)	1276
Polypropylene Fibers	7.7
Air Entrainer (Master Builders AE-90)	0.54
High Range Water Reducer (Glenium 7920)	3.02
Citric Acid	0.41

Figure 3.1. Hardened property specimens for FR-SCC characterization

Table 3.2. Summary of tests performed for FR-SCC characterization

Test	Applicable Reference
Air Content	ASTM 1611
Unit Weight	ASTM C231
Slump Flow	ASTM C138
Compressive Strength	ASTM C39
Modulus of Rupture	ASTM C78
Modulus of Elasticity	ASTM C469
Splitting Tensile	ASTM C496

Fresh properties of the mix are reported in Table 3.3. The slump flow was 31 inches, which is slightly more than the desired 28 ± 2 in. diameter. This result is not

significantly out of the range expected, and the mix remained acceptable for hardened property tests. However, this slump flow diameter influenced the selection of the differing flowability of FR-SCC overlays used in bond testing.

Table 3.3. Fresh properties of FR-SCC characterization batch

Property	Value
Slump Prior to HRWR Addition (in.)	3.75
Slump Flow (in.)	31.0
Unit Weight (lb/ft^3)	134.2
Air Content (%)	7.5

Figure 3.2 and Figure 3.3 illustrate the necessary steps of the mixing process to check that the concrete mix is valid for further hardened property testing. Comparing Figure 3.2 to Figure 3.3 is a good representation of the effect that HRWR has on the mix to make it self-consolidating. Without the HRWR, the concrete mix is simply conventional concrete that depends on external assistance for consolidation. The reason for taking a conventional slump reading prior to the HRWR addition is to check that the water content is creating the result expected. If the slump reading is too low, either more water or more HRWR may be added to create the flowability necessary for self-consolidation. If the slump reading is too high, then the HRWR levels called for in the mix design may be reduced in order to achieve the target slump flow of self-consolidating concrete.

Figure 3.2. Slump prior to HRWR addition

Figure 3.3. Slump flow after addition of HRWR

The hardened specimens were prepared for testing 28 days after casting. Cylinder specimens were ground plane prior to testing (Figure 3.4). The cylinders required a series of grinding cycles in order to get the thick upper layer of weak material off of the specimen (Figure 3.5). This layer appeared for the self-consolidating concrete because as it is poured, a foam containing HRWR easily rises to the top of the specimen. Table 3.4 shows the 28-day compressive strength results and that the measured strength exceeded the targeted 4000 psi. Figure 3.6 shows a specimen after testing, which shows that the internal fibers helped keep the specimen intact after testing.

Figure 3.4. FR-SCC cylinder specimen preparation

Figure 3.5. Top surface of specimen that had to be removed before testing

According to the data in Table 3.4, the measured strength exceeded the target. Figure 3.6 shows a specimen after testing.

Table 3.4. Compressive strength of FR-SCC

Specimen	Compressive Strength (psi)
No. 1	6330
No. 2	6854
No. 3	6374
Average	6520

Figure 3.6. Failure of an FR-SCC compressive strength specimen

Table 3.5 shows the splitting tensile strength results. The expected splitting tensile strength of FR-SCC is equivalent to what is expected for conventional concrete, that is 300-700 psi. The test data indicate that the FR-SCC mix design met these anticipated values. Figure 3.7 shows the failure of the three splitting tensile specimens.

Table 3.5. Splitting tensile strength of FR-SCC

Specimen	Splitting Tensile Strength (psi)
No. 1	475
No. 2	440
No. 3	500
Average	470

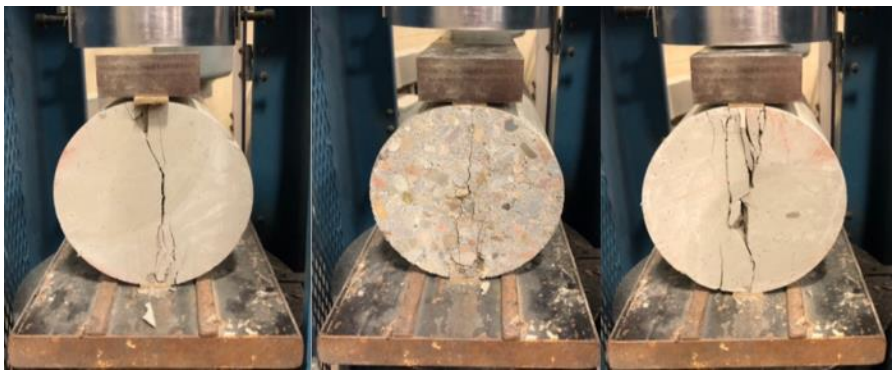

Figure 3.7. Splitting tensile strength specimens

Modulus of rupture results are shown in Table 3.6. The anticipated flexural strength of FR-SCC is equivalent to that of conventional concrete: 400-700 psi. Based on the modulus of rupture data shown in Table 3.6, this mix exceeded the anticipated flexural strength. Figures 3.8 and 3.9 show modulus of rupture (MOR) beams after testing. Figure 3.9 shows the even distribution of the mix's components at the failure surface and indicates a well-distributed amount of polypropylene fibers were present at the cracking region of the beam.

Table 3.6. Modulus of rupture of FR-SCC (beams with third-point loading)

Specimen	Result (psi)
No. 1	740
No. 2	820
No. 3	775
Average	780

Figure 3.8: FR-SCC modulus of rupture specimens after testing

Figure 3.9. Typical FR-SCC modulus of rupture specimen failure surface

Table 3.7 shows measured modulus of elasticity for the FR-SCC specimens. The target modulus of elasticity is equivalent to that of conventional concrete: 2 to 6 million psi. Results were recorded for the first specimen, but these results should be recognized as an erroneous value. The difference compared to the second and third specimens is vast and indicates a problem with the testing method rather than an actual difference in behavior. Only the latter two specimens were taken into account when reporting the average modulus of elasticity of the FR-SCC mix. The measured value was less than anticipated indicating a relatively low stiffness for the FR-SCC mixture. Figure 3.10 shows a modulus of elasticity specimen during testing.

Table 3.7. Measured modulus of elasticity for FR-SCC

Specimen	Value (psi)
No. 1	197,950
No. 2	2,183,650
No. 3	2,503,350
Average	2,343,500

Figure 3.10. FR-SCC Modulus of elasticity specimen during testing

3.3 Bond Testing

3.3.1 Overview

Direct pull-off (ASTM C1583) and slant shear tests (ASTM C882) were used to examine bond to conventional ODOT Class AA concrete substrate for the J3 UHPC and FR-SCC. Specimens were tested with three different surface preparations: wire brushed, sand blasted, and chipped. UHPC and FR-SCC specimens were tested for both bond tests. FR-SCC was also tested for three different slump flows – high, medium, and low – to determine if there is any impact on bond quality as a function of rheology.

3.3.2 FR-SCC Bond Tests

The ODOT AA mix was used as the existing conventional concrete substrate throughout testing, and the FR-SCC was used as the overlay material. Three different FR-SCC mixes that varied by flowability were compared and are presented throughout

the chapter. As well as testing how different flowabilities of FR-SCC affect its bond with existing concrete, the method of preparing the interface between substrate and overlay was also tested. A total of 15 slant shear cylinders (6 in. x 12 in.) and 6 pull-off test slabs (14 in. by 14 in.) were made for testing. Five cylinders and two slabs were cast for each flowability of FR-SCC. Fresh properties of the substrate material used for the FR-SCC specimens are shown in Table 3.8. The compressive strengths of the substrate at 28 days and 74 days after casting are shown in Table 3.9. The 74-day (bond testing day) compressive strengths of the ODOT AA mix were recorded on bond testing day for comparison and analysis.

Table 3.8. Fresh properties of ODOT AA bond test substrates used for FR-SCC

Property	Value
Slump (in.)	2.0
Unit Weight (lb/ft^3)	139.0
Air Content (%)	5.5

Table 3.9. ODOT AA concrete bond test substrate compressive strength

Specimen	Compressive Strength (psi)
1 – 28 days	5677
2 – 28 days	6465
3 – 28 days	6541
Average at 28 days	6230
1 – 74 days	6869
2 – 74 days	7070
3 – 74 days	6383
Average at 74 days	6770

In order to create a better bond between substrate and overlay materials for the slab specimens, the top surface of the substrate material was roughened using two different methods: sandblasting and chipping, as shown in Figures 3.11 and 3.12. Roughening the substrate material's top surface exposes aggregate beneath and removes the weak upper layer that is found when casting any concrete material, giving the bond between existing and new material a projected larger strength than if the substrate was only trowel finished for bond. Sandblasting the substrate's top surface exposes the fine aggregate present in the material while chipping the substrate's top surface exposes more coarse aggregate as well as fine aggregate. Chipping the top

surface of the substrate had a larger variation of amplitude into the substrate that the overlay could bond to, while sandblasting the top surface of the substrate created more of a uniform stripping of the weak upper layer.

Figure 3.11 Chipped top surface of substrate (ODOT AA pull-off slabs)

Figure 3.12. Sandblasted top surface of substrate (ODOT AA pull-off slabs)

For the slant shear specimens, the interface between the substrate and overlay materials was trowel finished, shown in Figure 3.13. No other preparations of the interface were tested for the cylinders. All slab and cylinder specimens were power washed as well in hopes of removing loose paste from the top surface of the existing substrates.

Figure 3.13. Slant shear cylinders prior to pouring FR-SCC Overlays

The three flowabilities of FR-SCC overlays were poured 42 days after pouring the ODOT AA substrate material for the testing specimens. Results from the characterization testing of FR-SCC were used to decide how much HRWR should be placed in the FR-SCC mixes in order to create a low, medium, and high flow. Due to the slump flow of the characterization FR-SCC mix being 31 in. (1 in. more than the preferred range of flowability 28 ± 2 in.), it was decided to use that HRWR content for the high flow FR-SCC overlay material. From there, the medium flow FR-SCC was decided to have a reduced HRWR content of 65% of the original mix from previous research, since the characterization mix used 75% of the original value. The slump flow of the high flow mix for this experiment was 27 in., and the slump flow of the medium flow mix was 29 in. A decision to change the mix with the medium HRWR content to the high flow mix was made because of its higher slump flow value. The reason why the mix with a smaller HRWR content created a larger flowability is unknown. The anomalous slump flow results between high and medium flows yielded the next decision to reduce the HRWR for the low flow mix to less than what was planned (44% HRWR content from the original FR-SCC mix instead of the planned 55%) in order to ensure a difference in flowability between low and the two higher flows. A photo of the low slump flow is shown in Figure 3.14. Table 3.10 presents a summary of the HRWR used to achieve the three different overlay flowabilities.

Figure 3.14. Slump flow of the low flowability FR-SCC overlay

Table 3.10. HRWR Content and slump flow of FR-SCC overlays

Flowability	HRWR Content (fl oz/cwt)	Slump Flow (in.)
Low	4.24	22.0
Medium	6.20	27.0
High	5.36	29.0

The compressive strengths of the FR-SCC mixes with varying flowability were tested 32 days after the overlay cast date and results are presented in Table 3.11. The FR-SCC mix with the lowest HRWR content as well as the lowest slump flow resulted in an average compressive strength of 3920 psi, lower than the desired 4000 psi minimum.

Table 3.11. Compressive strengths of the FR-SCC mixes with varying flowability

Specimen	Compressive Strength (psi)
Low-1	3742
Low-2	3908
Low-3	4114
Low-Average	3920
Medium-1	5591
Medium-2	6035
Medium-3	5650
Medium-Average	5760
High-1	5536
High-2	5851
High-3	5130
High-Average	5510

Preparing the slabs for the direct tensile (pull-off) tests required close attention. First, cored holes 2-5/8 in. deep were created using a 2 in. diameter diamond tip core bit attached to a drill press. The depth was decided based on the overlay thickness being 2 inches and ASTM requirements of coring at least ½ in. into the substrate layer. The diameter of the drill bit was set to match the steel puck glued to the concrete core for the testing apparatus, which has a 2 in. diameter. After drilling these circular cylinders of concrete through the overlay and substrate slabs, 2 in. diameter steel pucks were epoxied to the top surface of the FR-SCC material. Figures 3.15 and 3.16 show the process described to prepare the slabs for bond testing.

Figure 3.15. Pull-off test slab preparation (coring)

Figure 3.16. Slant shear and pull-off bond testing specimens prior to testing

The average slant shear strength for the cylinders containing the low flow FR-SCC mix was 3340 psi, which can be compared to an expected strength of 3920 psi based on the compressive strength of material. The slant shear strengths of the cylinders containing the medium and high flows of FR-SCC both exceeded the standard 4000 psi minimum strength in compression. However, neither of the shear strengths were greater than or equal to the compressive strengths of the two corresponding FR-SCC mixes. This result may be since the trowel finished interface preparation affected the bond from existing to overlay concrete materials.

All of the failure modes that occurred were at the interface between the two different materials. Figures 3.17 to 3.19 show representative failures as well as the locations of severe cracking. It seems that the existing ODOT AA material is crushed at the end of the interface and all of the cracks that branch away from the interface are contained in the FR-SCC. Many failures of the cylinders containing medium and high flows of FR-SCC had loud and sudden separations of materials.

Figure 3.17. FR-SCC low flow slant shear failure

Figure 3.18. FR-SCC high flow slant shear failure from two sides

Figure 3.19. FR-SCC slant shear test sudden separation of materials

Control specimens were made after these bond tests for comparison of FR-SCC performance to conventional concrete (ODOT AA mix) as the overlay material. The results from the control group testing confirms that the FR-SCC mixes with medium and high flows bond better as an overlay material than conventional concrete. It should be noted that while the ODOT AA mix as an overlay does succeed in having a slant shear strength greater than the minimum 4000 psi necessary, the slant shear cylinders containing the control ODOT AA as the overlay material had sudden abrupt failures at the interface (Figure 3.20). Also, it is noted that the areas of smallest cross-sectional area of the overlay material failed within itself as well as at the interface with the existing concrete material.

Figure 3.20. ODOT AA slant shear failure

All of the bond strengths of the specimens are reported alongside the slant shear strengths of the cylinders in Table 3.12.

Table 3.12. Slant shear results for the FR-SCC mixes with varying flowability

Specimen	Failure Type	Slant Shear Strength (psi)	Bond Strength at Interface (psi)
Low-1	Interface	2911	1456
Low-2	Interface	3403	1702
Low-3	Interface	3480	1740
Low-4	Interface	3374	3247
Low-5	Interface	3549	1775
Low-Average	NA	3340	1670
Medium-1	Interface	5004	2502
Medium-2	Interface	5716	2858
Medium-3	Interface	5272	2636
Medium-4	Interface	6173	3087
Medium-5	Interface	5616	2808
Medium-Average	NA	5560	2780
High-1	Interface	4592	2296
High-2	Interface	6504	3252
High-3	Interface	5775	2888
High-4	Interface	6447	3224
High-5	Interface	5764	2882
High-Average	NA	5820	2910
Control-1	Interface	5829	2915
Control-2	Interface	4015	2008
Control-3	Interface	3663	1832
Control-Average	NA	4500	2250

Note that control group had a different substrate than the experimental overlays: control substrate compressive strength was 6560 psi.

Direct tensile strengths between ODOT AA substrates and FR-SCC overlay slabs were found using a testing apparatus that attaches to the steel pucks and applies a gradually increasing tensile force to the concrete shafts that the pucks are connected to. Each core was tested, its failure load was recorded, and its failure type was noted. The failure stress was obtained by dividing the failure load by the cross-sectional area of the core. The desired resulting failure type from this test is to have the specimen fail in the substrate; this represents that the bond at the interface is stronger than that of the existing concrete and that the existing concrete would fail before the bond between old and new materials would fail. Figure 3.21 shows direct tension specimens ready for testing.

Figure 3.21. Configuration of pull-off specimens for bond testing

When conducting the pull-off tests, issues occurred that are noted. There were two testing days for these tests because during the 32-day tests, epoxy failure was a common result for three slabs: low flow overlay with a sandblasted interface, low flow overlay with a chipped interface, and a high flow overlay with a chipped interface. For those three slab specimens, additional cores were drilled, and steel pucks were epoxied in preparation for further experimentation at 42 days. The top surface of the overlay FR-SCC slabs was sandblasted in order to ensure less of a possibility for epoxy failure between the steel pucks and the overlay material. This added step to the methodology was thought to remove any loose particles from the overlay material that could weaken the bond between the epoxy and the concrete. Obtaining at least three data points per slab was imperative for the most accurate depiction of the bond interactions occurring between the two materials. Data from both days were averaged in the same category to achieve the overall bond strength of the slabs.

Table 3.13 and Table 3.14 display the results from the slabs by differing FR-SCC overlay flowability and then by differing method of interface preparation. It is noted that sandblasted interfaces have higher failure stresses than those with chipped interfaces. It is hypothesized that the reason that the slabs with chipped interfaces contain weaker tensile strengths is because during the surface preparation process, the automated chisel weakens the substrate material below the surface, and thus weakens the bond between the substrate and the overlay material.

Table 3.13. FR-SCC pull-off bond test results

Flowability	Interface Prep	Specimen No.	Time (days)	Failure Type	Failure Load (lb)	Failure Stress (psi)
Low	Sandblasted	1	32	Substrate	1029	328
Low	Sandblasted	2	42	Overlay	1374	438
Low	Sandblasted	3	42	Overlay	1046	333
Low	Sandblasted	4	42	Overlay	1169	372
Low	Chipped	1	32	Interface	801	255
Low	Chipped	2	32	Interface	590	188
Low	Chipped	3	42	Interface	772	246
Low	Chipped	4	42	Interface	888	283
Low	Chipped	5	42	Interface	456	145
Medium	Sandblasted	1	32	Overlay	1128	359
Medium	Sandblasted	2	32	Substrate	1111	354
Medium	Sandblasted	3	32	Overlay	947	301
Medium	Sandblasted	4	32	Overlay	1292	411
Medium	Sandblasted	5	32	Substrate	1561	497
Medium	Chipped	1	32	Interface	731	233
Medium	Chipped	2	32	Interface	842	268
Medium	Chipped	3	32	Interface	1186	378
Medium	Chipped	4	32	Interface	842	268
High	Sandblasted	1	32	Substrate	1262	402
High	Sandblasted	2	32	Substrate	1461	466
High	Sandblasted	3	32	Substrate	1146	365
High	Chipped	1	32	Substrate	696	222
High	Chipped	2	42	Interface	275	88
High	Chipped	3	42	Interface	894	285
High	Chipped	4	42	Interface	666	212

Table 3.14. Average FR-SCC pull-off bond test results

Flowability	Interface Prep	Average Failure stress (psi)
Low	Sandblasted	368
Low	Chipped	223
Medium	Sandblasted	384
Medium	Chipped	287
High	Sandblasted	411
High	Chipped	201

Figures 3.22 to 3.25 illustrate the failure types that occurred during testing. All three failure types (in the substrate, at the interface, and in the overlay) are presented.

Figure 3.22. Interface failure

Figure 3.23. Overlay failure

Figure 3.24. Substrate failure

Figure 3.25. Interface failure that enters substrate

Two control group slabs using Class AA concrete for the substrate and overlay were constructed for pull-off bond testing. One slab contained a sandblasted interface, and one slab contained a chipped interface. The same methodologies used to prepare the FR-SCC overlay slabs were used to prepare the control slabs for experimentation. One crucial difference between control slabs and FR-SCC slabs was that the control slab overlays were 3 in. thick. Most of the attempts to create separated concrete shafts for testing broke off from the slabs before the drill bit reached the necessary 3-5/8 in. depth in order to achieve a ½ in. minimum penetration of the substrate. The depth that the drill bit failed the concrete was at a maximum 3 in. into the slab at the interface between existing and new concrete. It is hypothesized that the friction forces created

from the drill bit onto the concrete core resembles a loading onto a cantilever with increasing length, and once the length reaches a certain value, the loading exceeds the cantilever (or concrete core) capacity, and the concrete shaft gives way from the rest of the slab. Also, it was noticed that the cement from the concrete, as it was being cored, stayed on the inside of the drill-bit, and over time, dried into a paste that contributed to the forces pulling the core away from the slab specimen. Pull-off tests were completed on the control specimens, and results indicated bond strengths of 439 psi for the sandblasted surface preparation and 382 psi for the chipped surface preparation. These results are consistent with the FR-SCC bond tests, which indicated noticeably better performance with a sandblasted surface.

3.3.3 UHPC Bond Tests

Slant shear specimens were cast in the form of 6 in. x 12 in. cylinders based on an adaptation of ASTM C882. A completed UHPC slant shear specimen before and after testing is shown in Figure 3.26.

Figure 3.26. Composite slant shear specimen prior to testing (left) and after testing (right)

Slant shear tests were first conducted with a trowel finished conventional concrete surface. The normal strength concrete and UHPC casting occurred during the same timeframe as casting for the composite MOR specimens. Slant shear tests were carried out after both portions of the specimen were cured for 28 days. The results from these tests with Ductal® are shown in Table 3.15 and for the J3 specimens in Table 3.16. The 28-day compressive strength of the base concrete was 5850 psi for the

Ductal® Specimens and was 5750 psi for the J3 specimens. So, the Ductal® bond strength nearly developed the full strength of the concrete in all cases, while the J3 bond strength resulted in a load about 20 percent less than the concrete compressive strength. However, the bond strengths of both materials were within 10 percent of one another.

Table 3.15. Maximum load and bond strength for Ductal® slant shear specimens

Specimen	Maximum Load (lb)	Bond Strength (psi)	Corresponding Compressive Strength (psi)
Cylinder 1	122,670	2170	4340
Cylinder 2	146,840	2600	5190
Cylinder 3	177,245	3130	6270
Cylinder 4	154,800	2740	5480
Cylinder 5	153,430	2710	5430
Average	150,997	2670	5340
Std. Deviation	17,487	308	619

Table 3.16. Maximum load and bond strength for J3 slant shear specimens

Specimen	Maximum Load (lb)	Bond Strength (psi)	Corresponding Compressive Strength (psi)
Cylinder 1	123,670	2280	4370
Cylinder 2	110,130	2230	3900
Cylinder 3	152,010	2870	5380
Cylinder 4	123,290	2380	4360
Average	127,275	2440	4500
Std. Deviation	15,286	254	541

Additional slant shear tests were conducted for both Ductal® and J3 specimens using three different surface preparations: wire brushed, sand blasted, and chipped. The base concrete cured for 28 days before testing. Slant shear test results are shown in Table 3.17. With the revised surface preparation and improved flowability of the mix design, the J3 results were within approximately 5 percent of the Ductal® results.

Table 3.17. Slant shear test results

Surface Preparation	Ductal®	J3
Wire brushed	2873 psi	2989 psi
Chipped	2982 psi	3204 psi
Sand blasted	3380 psi	3276 psi

The research team constructed Class AA substrate specimens for direct pull-off testing and the surfaces of these specimens were prepared for overlay casting with different surface preparations: wire brushed, sand blasted, and chipped, shown in Figure 3.27. These specimens cured for 28 days before Ductal® and J3 overlay placement, which was then also cured for 28 days before testing. Completed specimens are shown in Figure 3.28.

Figure 3.27. Sandblasted (left) and chipped (right) surface preparations

Figure 3.28. Pull-off test specimens for Ductal® (left) and J3 (right)

Pull-off tests were conducted for both Ductal® and J3 specimens using the methods of ASTM C1583 as shown in Figure 3.29. The results of the pull-off tests are shown in Table 3.18. The Ductal® UHPC performed better than the J3 in the direct pull-off tests.

Figure 3.29. Pull-off tests for J3 with overall layout (left) and test setup (right)

Table 3.18. Direct pull-off test results

Surface Preparation	Ductal®	J3
Wire brushed	267 psi	160 psi
Chipped	291 psi	183 psi
Sand blasted	311 psi	226 psi

A control set of pull-off specimens were cast consisting of a Class AA substrate and Class AA overlay. Pull-off tests were completed on the control specimens, and results indicated bond strengths of 439 psi for the sandblasted surface preparation and 382 psi for the chipped surface preparation. These results are consistent with the UHPC bond tests, which indicated noticeably better performance with a sandblasted surface.

Additional J3 UHPC pull-off specimens were cast to evaluate alternative substrate saturation levels. Previous testing of the J3 mix indicated improved performance with higher substrate saturation prior to placement of the overlay. Pull-off tests were conducted on the revised J3 overlay specimens, and results indicated bond strengths of 318 psi for the sandblasted surface preparation and 255 psi for the chipped surface preparation. These results represent an improvement over the previous test results and are likely due to maintaining a saturated surface dry condition of the substrate prior to installation of the overlay. For comparison, the results for the Ductal® overlay bond tests indicated 408 psi for the sandblasted surface preparation and 291 psi for the chipped surface preparation.

3.3.4 Placement Method Evaluation

The research team developed mock-ups of the proposed continuity connection repairs in order to evaluate and refine mixing and placement techniques for these types of applications. The research team constructed mock-ups of the continuity connection repairs for the UHPC and FR-SCC materials. The UHPC mock-ups allowed for a minimum 1-inch-thick encapsulation, while the FR-SCC mock-ups allowed for a 1-1/2-inch-thick encapsulation. A completed J3 continuity repair mock-up specimen is shown in Figure 3.30. The UHPC was placed with the same methods that will be used on the full-scale laboratory specimens, and the material filled the mold completely without any external vibration. Additional evaluation of placement methods is included in the sections describing the laboratory test specimens or field implementation.

Figure 3.30. J3 UHPC continuity joint repair mock-up specimen

4.0 Live Load Continuity Connection Repairs

4.1 Overview

Twelve test specimens were constructed to examine the three repair materials, UHPC, FR-SCC, and MALP concrete. Three specimens were constructed and tested with no damage as control and three specimens were precracked to simulate damage observed in the field and repaired with each repair material. Each specimen consisted

of two 9 ft long approximately half-scale AASHTO Type II girder specimens connected at one end with a conventional concrete continuity joint. Non-prestressed beam specimens were used instead of prestressed specimens to limit the difficulty of construction and since it was determined that the prestressing would have little effect on the joint performance.

4.2 Girder Specimen Construction

4.2.1 Girder Design

The approximately half-scale AASHTO Type II girders used in this research were constructed using the same design as in previous research at the University of Oklahoma (Mayhorn 2016, Murray 2017, Casey 2019). This geometry and reinforcement is based on a girder taken out of service from a bridge spanning over the Arkansas River in Tulsa County, Oklahoma and is typical of many aging girders across Oklahoma. The girder-joint-girder design consisted of two half-length specimens each stretching 9 ft in length with a 10 in. continuity joint and deck connecting them together. This fabrication process creates a final dimension of 18 ft – 10 in. in length for each specimen. The height of the final specimen, including the deck, was 2 ft – 3.125 in. The geometry and dimensions of the girder cross-section are shown in Figure 4.1.

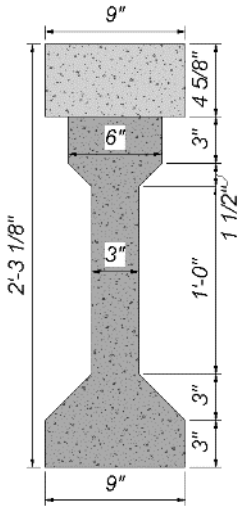

Figure 4.1 Girder dimensions and geometry

The continuity joint connecting each half-length specimen had an overall dimension of 10 in. (length) x 9 in. (width) x 2 ft – 3.125 in. (height). This section is a

rectangular prism outlining the width of the deck and bottom bell as well as the height of the overall specimen. Figure 4.2 shows the dimensions and geometry of the continuity joint section. Joining the two half-length specimens via the continuity joint and deck created the final geometry of the girder-joint-girder specimen as shown in Figure 4.3.

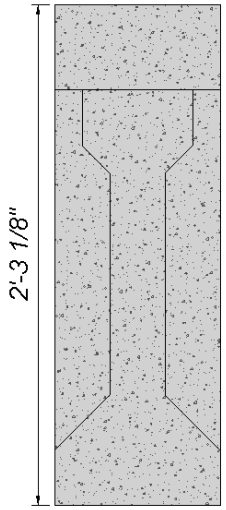

Figure 4.2. Continuity joint dimensions and geometry

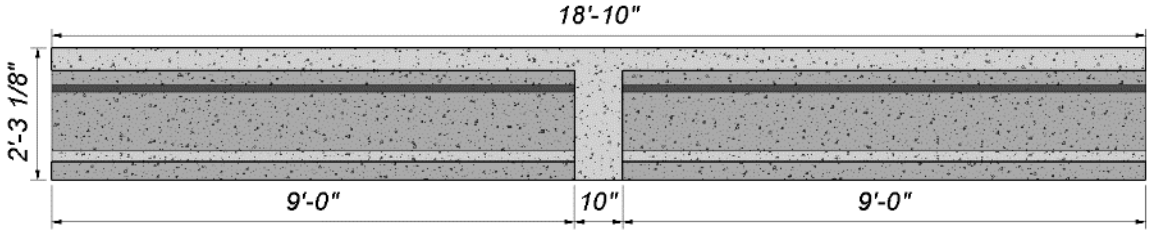

Figure 4.3. Girder-joint-girder specimen dimensions

Steel reinforcement was designed and used for two separate load cases. The first load case was a static point load at midspan, directly above the continuity joint, with the girder-joint-girder supported at each end. This load case simulates a flexural failure in the positive moment region of the continuity joint based on a design positive moment capacity of 1.2 times the cracking moment in accordance with the AASHTO LRFD Bridge Design Specifications (2014). Longitudinal steel reinforcement with ninety-degree hooks placed at the bottom of the continuity joint was designed with the intention of yielding under the first load case. Each half-length specimen received identical longitudinal reinforcement but offset from one another to allow for clearance within the

joint when connecting the two girders. Two No. 3 and No. 5 bars were placed within the girders as shown in Figures 4.4 to 4.6.

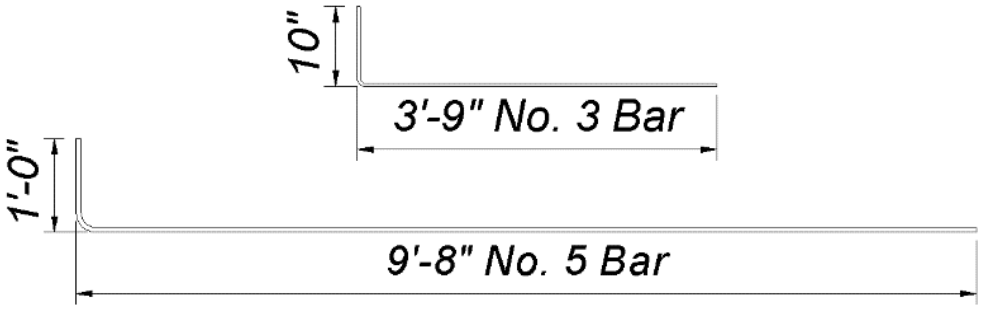

Figure 4.4. Hooked end bar dimensions used for continuity connection

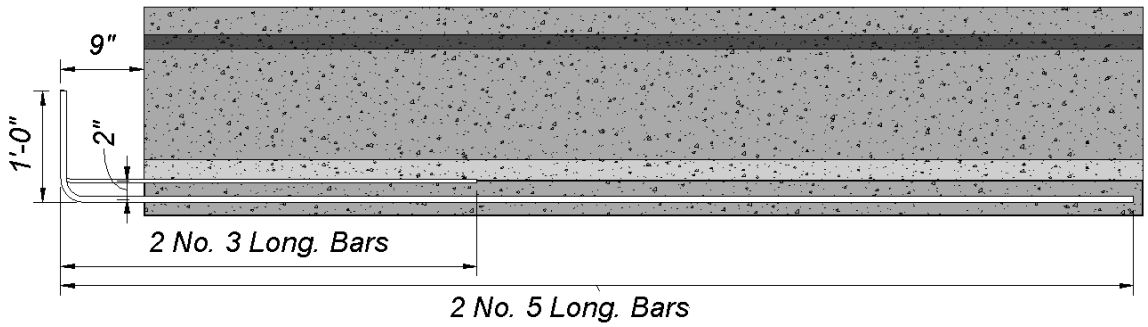

Figure 4.5. Hooked end bar placement

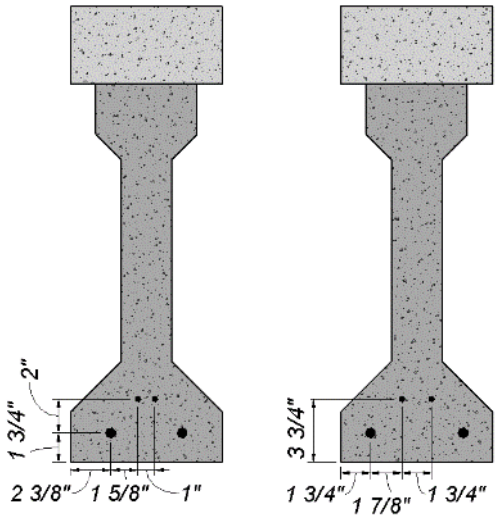

Figure 4.6. (Left) Inside longitudinal bars and (right) outside longitudinal bars

The second load case used for design was two static point-loads, one at each end of the specimen, while being supported at midspan. This load case simulates live

load on the deck, resulting in girder-joint-girder negative moment bending. Steel reinforcement placed within the deck was designed to yield under the second load case. Four No. 5 bars were used in the design of the negative bending moment and were centered over the joint as done in previous research (Casey 2019). Figure 4.7 and Figure 4.8 show the deck longitudinal reinforcement dimensions and placement.

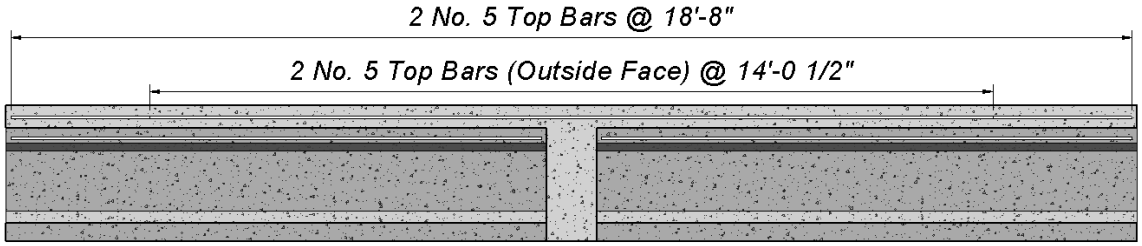

Figure 4.7. Deck longitudinal reinforcement

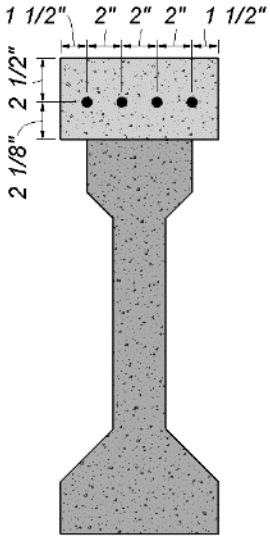

Figure 4.8. Deck reinforcement placement

Lastly, to ensure each load case led to the intended failure mechanism, shear reinforcement was accounted for during the design phase and adequate stirrups were placed within the specimens. Bent pairs of No. 3 c-shaped stirrups were used in the girder design based on previous work (Mayhorn 2016). The stirrups did not allow for any specimen to fail in shear during testing. The dimensions and spacing of the stirrups for each half-length specimen are shown in Figure 4.9 and Figure 4.10.

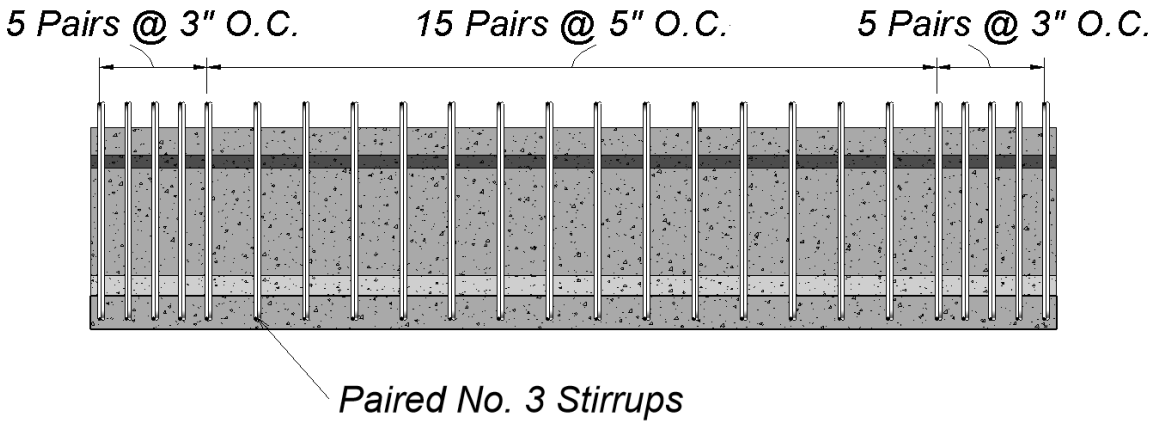

Figure 4.9. Half-length specimen stirrup spacing

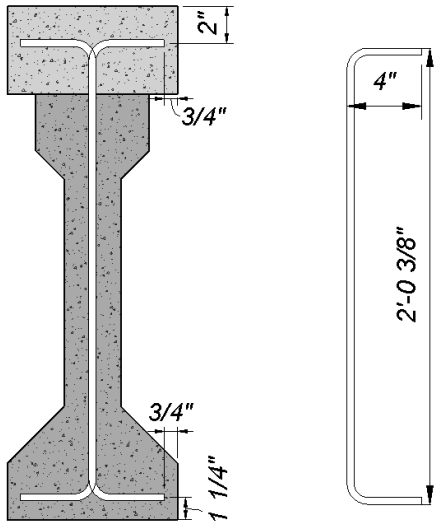

Figure 4.10. (Left) Stirrup placement in the girder cross-section and (right) stirrup dimensions

Figures 4.11 to 4.13 and Table 4.1 show the reinforcement types, spacing, and placement throughout the full-length specimens after casting the continuity joints.

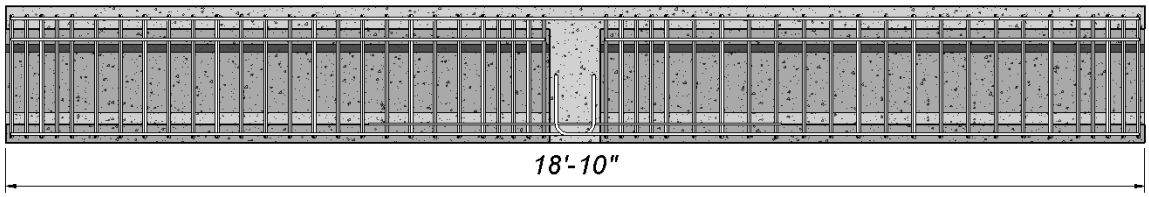

Figure 4.11. Full specimen steel reinforcement

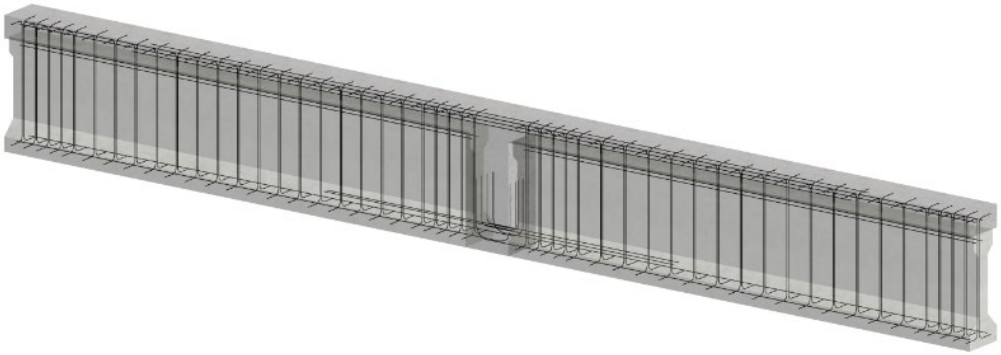

Figure 4.12. 3-Dimensional representation of full-length specimen steel reinforcement

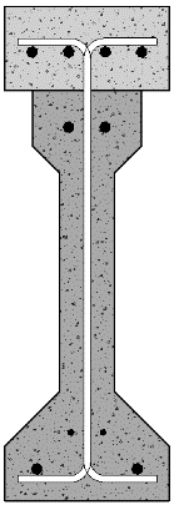

Figure 4.13. Cross-section showing all steel reinforcement

Table 4.1. Summary of steel reinforcement used for continuity connection specimens

Reinforcement Type	(QTY) Size @ Spacing	Length
Longitudinal Deck Reinforcement	(4) No. 5 @ 2 in. O.C.	(2): L = 18 ft – 8 in. (2): L = 14 ft – 0.5 in. (Centered over Joint)
Longitudinal Girder Compression Reinforcement	(2) No. 5 @ 2 in. O.C.	L = 8 ft – 9.75 in.
Longitudinal Girder Tension Steel Hooked into Continuity Joint	(2) Bent No. 5 @ 5.5 in. O.C. *OR* (2) Bent No. 5 @ 4.25 in. O.C.	Refer to Figure 4.4 and Figure 4.5 for dimensions
Mild Girder Tension Steel Hooked into Continuity Joint	(2) Bent No. 3 @ 1.25 in. O.C. *OR* (2) Bent No. 3 @ 3.25 in. O.C.	Refer to Figure 4.4 and Figure 4.5 for dimensions
Shear Reinforcement	(25) C-Shaped No. 3 tied pairs: (5) Pairs @ 3 in. O.C. (both ends) (15) Pairs @ 5 in. O.C. (middle)	Refer to Figure 4.9 and Figure 4.10 for dimensions

All steel reinforcement used in the specimen design was Grade 60, which has a minimum yield strength of 60 ksi. Prior to placement of reinforcement, tensile tests were performed on the steel batches as per ASTM A370 and the results are shown in Table 4.2.

Table 4.2. Steel reinforcement tensile test results

Test	Elastic Modulus (ksi)	Yield (psi)	Ultimate (psi)
1	26,618	62,546	102,668
2	26,712	63,639	103,652
3	30,105	63,368	103,698
Average	**27,812**	**63,184**	**103,339**

Based on the longitudinal reinforcement designs and tensile testing, nominal moment capacities were calculated for both positive and negative moment bending per ACI 318-14. The positive nominal moment capacity was calculated as 107.6 ft-k. The negative nominal moment capacity was calculated as 152.4 ft-k.

4.2.2 Girder Formwork and Reinforcement

To begin the process of constructing the girders, steel reinforcement was cut, bent, and tied into cages. Each cage was built to be placed inside a half-length girder specimen. A total of 50 stirrups were used in this construction and tied in pairs. For ease of fabrication, the cages were constructed upside down using the bottom longitudinal reinforcement to act as supports to hang stirrups. Once the alignment and placement of the stirrups was achieved, they were then tied into place. Figure 4.14 shows one cage ready to be installed within the formwork before casting concrete.

Steel formwork for casting the concrete was used to house the cages for the specimens. Used in previous research and built by an undergraduate student at the University of Oklahoma, these forms were 18 ft in length with the approximately half-scale AASHTO Type II profile. This formwork allowed for two half-length specimens to be cast at the same time. A total of four forms were used, yielding four half-length specimens per concrete pour. Figure 4.15 shows the arrangement of cages placed within the form.

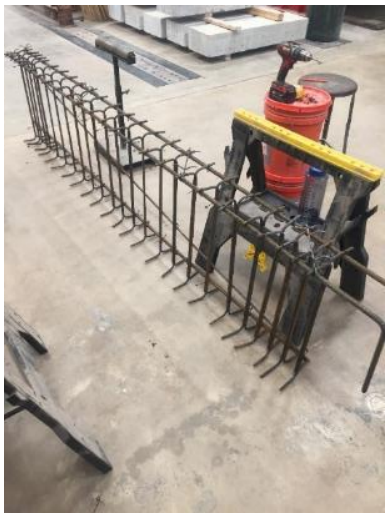

Figure 4.14. Half-length specimen rebar cage

Figure 4.15. Rebar cages within formwork before specimen casting

Figure 4.15 shows how two specimens were built using this formwork. A plywood divider between the two specimens, seen in the center of the metal form, separated the two specimens throughout the casting and curing processes. A No. 3 bar extended diagonally across each cage to alleviate any racking that might occur during the handling and placement of the cages. This reinforcement is not intended to be of any structural benefit after placement of the cages within the formwork.

The plywood shown at the end of the forms not only kept concrete from escaping during the casting process but was also used to align the bottom longitudinal reinforcement. This alignment of the hooked ends of the reinforcement was crucial in

that it allowed two half-length specimens to mate well prior to casting the deck and continuity joint. Baling wire was also wrapped around the hooked ends in order to keep them from shifting and rotating during casting. A closer look at the formwork and hooked reinforcement ends is shown in Figure 4.16.

Figure 4.16. Hooked ends arranged in the formwork

As stated previously, each casting yielded four half-length specimens. To ensure the hooked ends would mate correctly, two different end forms were constructed like that shown in Figure 4.16 – one for the inner reinforcement and one for the outer reinforcement. Each casting consisted of two of each type of formwork, yielding two final full-length specimens upon joining. The difference of each end form and the alignment dimensions is shown from the cross section of the final specimen in Figure 4.17.

Plywood and construction grade lumber platforms were built for the casting process. These platforms allowed the specimens to sit level by way of shims beneath. Additionally, the platform allowed for the metal forms to be clamped down to ensure dimensional accuracy and stability throughout the casting process. To restrain the formwork from bulging away from the girder's centerline due to head pressure during the pouring process, square steel tube stock was fabricated to clamp across the tops of the formwork. Figure 4.18 shows these clamps and the final stage of the formwork construction prior to casting.

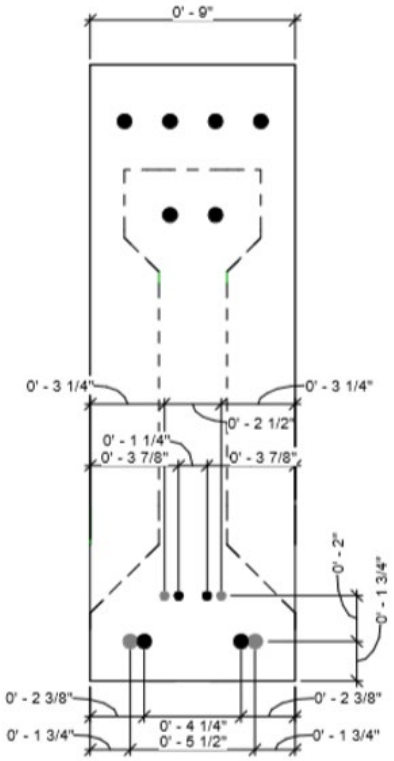

Figure 4.17. Hooked end bar mating alignment

Figure 4.18. Specimen forms ready for concrete placement

4.2.3 Girder Casting

Class AA concrete meeting the Oklahoma Department of Transportation 2019 Standard Specifications for Highway Construction, Section 701.01: Mix Design and Proportioning was used in this design for the girders, including the deck and continuity joint. Table 4.3 shows the specifications for this class of concrete. Class P concrete would typically be used for prestressed girder construction, but it was determined that use of Class AA concrete would simplify specimen construction without substantially affecting the results.

Table 4.3. Class AA concrete specifications

Class of Concrete	Minimum Cement Content (lb/yd^3)	Air Content (%)	Water/Cement Ratio (lb/lb)	Slump (in.)	Minimum 28-day Compressive Strength (psi)
AA	564	6.5 ± 1.5	0.25-0.44	2 ± 1	4,000

The concrete was ordered and brought to the laboratory by truck from Dolese Bros. Company. Each half-length specimen needed 6.61 ft^3 of concrete. An additional 0.88 ft^3 was used to fill three cylinders for compression testing for each pour. To expedite the casting process, the concrete was transported across the lab using a large, round-gate bucket attached to a top running single girder overhead crane. Figure 4.19 shows the concrete flowing from the truck's discharge chute to the round-gate bucket.

Figure 4.19. Filling round-gate bucket with concrete

Using the overhead crane to transport the concrete to the girder forms, the concrete was then discharged. This process was a four-person operation. One person manned the crane and moved the bucket down the girder while another released the concrete into the formwork. Once a sufficient amount of concrete was placed, the bucket was moved down the girder to begin adding more concrete into the formwork. Following behind this process was a two-person crew using a concrete vibrator. While one operated the vibrating end of the machine, another held the motor and supplied electrical power when needed. This process reduces the internal friction of the mix and removes any air pockets formed within the fresh concrete.

Figure 4.20 shows the previously mentioned process in motion. In order to allow the fresh concrete to flow unobstructed down through the girder's web and to the bottom bell, one of the top longitudinal No. 5 bars was removed before casting. This increased the clearance of which the concrete could flow. Once the formwork was nearly full of concrete, these bars were then re-tied to their original location.

Figure 4.20. Pouring and vibrating concrete in girder formwork

Also shown in Figure 4.20 are hooks to aid in transporting the specimens using the overhead crane. These hooks were made from No. 3 bars and extended 9 in. down into the girder and 3 in. above the eventual deck. Finally, the top surface of the girder, which is the interface where the deck meets the girder, was roughened using a trowel. Transport hooks and two sets of poured girders are shown in Figure 4.21.

Figure 4.21. Completed girder specimens immediately after casting

The half-length girder specimens were moist cured for seven days. Wet burlap was placed over all exposed concrete and was monitored to ensure it remained wet throughout the seven days. In addition to the wet burlap, plastic sheeting covered the specimens to mitigate the evaporation of water. After the seven-day moist cure, the half-length girders were stripped of all formwork and were ready to be joined together, as shown in Figure 4.22.

Figure 4.22. Half-length girder specimens after moist cure

4.3 Continuity Joint and Deck Construction

4.3.1 Continuity Joint Formwork

Immediately after the seven-day moist cure was completed, the half-length girder specimens were arranged to prepare for the casting of the deck and continuity joint. Figure 4.23 shows how the hooked ends of two specimens were arranged for casting.

Figure 4.23. Orientation of half-length girders prior to deck/joint casting

Plywood and construction grade lumber was again used to construct the formwork for the continuity joint. Because the joint was a rectangular prism extending out from either side of the bells and webs of the two half-length specimens, sheets of plywood were cut in the shape of the outer girder profile, including the deck. This allowed containment of the pour on the faces perpendicular to the length of the specimen. Plywood and lumber were used to house the two joint faces running parallel to the length of the specimens. Figure 4.24 shows the completed continuity joint formwork. The sheet of plywood on the floor was used for two reasons. The plywood maintained that the joint stay level with the two half-length girder specimens and allowed a stop block of wood at the base of the larger face of the joint. Much like the C-shaped clamps built for the top of the half-length girder specimens, this stop-block would not allow movement of the formwork due to head pressure during the pour.

Figure 4.24. Continuity joint formwork

Figure 4.24 shows a piece of lumber stretched across the top of the joint. This lumber was set in place to keep the forms from bowing out during the pour. One problem with this method was that during the pour the round-gate bucket would drop concrete onto the wood and not into the joint. An easy remedy to this problem used in the subsequent pours was to use F-style clamps placed across the joint, which worked very well.

4.3.2 Composite Deck Slab Formwork

After the half-length girder specimens were set in place with the mating hooked ends, the formwork for the deck was built. The formwork design was simple and built from plywood and construction lumber. Spanning the length of the half-length girders, 2x4 lumber was used as the formwork of the underside lip of the deck. The deck is 9 in. wide, which protrudes 1.5 in. away from the top bell of the girder. Plywood cut to length was attached to these 2x4's which encapsulated the side faces of the deck. These plywood pieces were 4.625 in. tall, the same height as the finished deck, and gave a perfect reference to screed the fresh concrete. This system of formwork was set in place by way of supports acting as stilts. These stilts not only held the formwork in place but allowed the formwork to be installed without directly anchoring into the specimen. This aided in the process of demolding the specimens and the reuse of the formwork. Figure 4.25 shows the specimens ready for deck concrete placement.

Figure 4.25. Deck formwork

Two strain gages, shown in Figure 4.26, were applied to two of the deck reinforcement bars over the joint. One strain gauge was installed on one of the outer bars, and another on one of the inner bars. The gages were placed at the midpoint of each bar after the appropriate amount of grinding, sanding, and cleaning (lacquer thinner, acid, and base) was applied to the area of interest. The midpoint of each bar corresponded to the center of the joint; the data that would come from this location is desired specifically for the negative moment load case where the deck bars are designed to fail after the joint has been repaired.

First, the longitudinal bars were ground down to the bare metal where the strain gauges would be installed. This process rids the bars of the mill scale and exposes the shiny steel beneath. After grinding was complete, sandpaper was used to further prepare the metal surface. The sandpaper grits used, in order, were 80, 120, 180, 220, and 320. After this step, the surface was cleaned using an acid and base treatment.

Cyanoacrylate (CA) glue was used to adhere the strain gauge to the bar surface, shown in Figure 4.26. Once the adhesive had time to dry completely, the strain gauge was covered in room-temperature-vulcanizing (RTV) silicone as shown in Figure 4.27. This provided the strain gauges a seal to mitigate water intrusion and also provided protection from falling concrete during pouring. The silicone was left to cure overnight and was then wrapped with aluminum tape. Plastic cable ties were used to connect the strain gauge wires to the rebar to provide strain relief (Figure 4.28).

Figure 4.26. Strain gauge glued to longitudinal reinforcement

Figure 4.27. Room-temperature-vulcanizing (RTV) silicone covering strain gauge

Figure 4.28. Strain gauges attached to longitudinal reinforcement ready for installation

The longitudinal deck reinforcement was installed, as shown in Figure 4.29, and tied to the stirrups. The strain gauge wires were incrementally zip tied down the longitudinal reinforcement to the first transport hook. Tape was used to cover the exposed strain gauge wires, labeling either inner or outer bar, and additional plastic cable ties were used to attach the wires to the top of the transport hooks. This process kept the strain gauge wires protected throughout the pour and would allow access to the wires after the concrete cured. Figure 4.30 shows a strain gauge wire emerging from the top of the deck and tied to a transport hook.

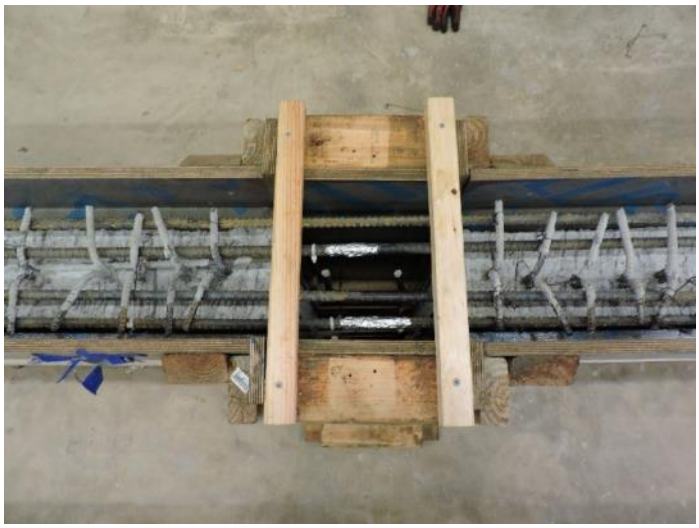

Figure 4.29. Top view of continuity joint prior to casting

Figure 4.30. Strain gauge wires before casting the continuity joint and deck

Additional C-shaped clamps were built from 2x4 and 2x6 lumber. These were used to keep the sides of the formwork from bulging throughout the casting process.

One clamp per half-length specimen proved to be sufficient and was placed at each of the specimen midspans. The clamps and the final formwork setup, ready for casting, is shown in Figure 4.31.

Figure 4.31. Two girder-joint-girder specimens prior to casting

4.3.3 Deck and Continuity Joint Casting

An amount of 5.44 ft^3 of concrete was needed for casting each deck and an amount of 1.17 ft^3 of concrete was needed for casting each joint, totaling 6.61 ft^3 for each full specimen. The process for casting the deck and joint was very much like casting the half-length girder specimens. The four-person crew had the same tasks as they did for the girder pour. One thing noted while casting the first deck and joint was that the clearance needed for vibrating the joint was hindered by concrete poured along the deck above the girder beforehand. This is shown in Figure 4.32.

It was decided that pouring the continuity joint prior to the deck along the girders allowed for better clearance for vibrating. This proved to be successful, and the method was used for the rest of the full-specimen castings. Figure 4.33 shows a complete girder-joint-girder specimen after final casting.

Figure 4.32. Vibrating the continuity joint during casting

Figure 4.33. Girder-joint-girder specimen after final casting

The full-length girder specimens were moist cured for seven days. Wet burlap was placed over all exposed concrete and was monitored to ensure it remained wet throughout the seven days. In addition to the wet burlap, plastic sheeting covered the specimens to mitigate the evaporation of water. After the seven-day moist cure the full-length girders were stripped of all formwork to await testing.

4.4 Class AA Concrete Compressive Strength

Concrete cylinder compression testing was performed in accordance with ASTM C39. Table 4.4 shows the 28-day compressive strengths for the Class AA concrete used for the girder-joint-girder specimens. Unfortunately, data for only two cylinders was obtained for the tests on 7/19/2019. All specimens except for those cast on 7/25/2020 had compressive strengths in excess of the target 4000 psi.

Table 4.4. Class AA concrete cylinder compression testing results

Date Poured	Cylinder 1 (psi)	Cylinder 2 (psi)	Cylinder 3 (psi)	Average (psi)
3/1/2019	5848	5392	5760	5670
3/18/2019	5466	5410	5437	5440
4/3/2019	4285	4814	5087	4730
4/10/2019	5840	6028	6042	5970
6/20/2020	5004	4894	4545	4810
7/19/2020	4067	3924	N/A	4000
7/25/2020	3456	3667	3858	3660
8/22/2020	5486	5408	5248	5380
9/16/2020	5685	6276	5642	5870

4.5 Initial Specimen Testing

4.5.1 Specimen Testing Arrangement

All tests were arranged as a simply supported beam with a concentrated load at midspan at the location of the continuity joint. Specimens were tested arranged either in the same orientation as cast or upside down depending on whether the test was intended to simulate positive moment in the joint (upright as cast) or negative moment (upside down). The concentrated load was applied by a hydraulic ram attached to a loading frame anchored to the Fears Lab strong floor.

A 50-kip capacity calibrated load cell was placed directly below the hydraulic ram to monitor and record the applied load. A ½ in. layer of sand was placed between a 1 in. thick steel plate and the specimen deck. This layer of sand allowed the plate to be leveled by hand prior to placement of a cylindrical swivel spacer and load cell. The swivel spacer allowed the load applied to make minor rotational adjustments for stability through the load path to the girder specimen. This setup is shown in Figure 4.34.

Figure 4.34. Hydraulic ram, load cell, swivel spacer, and steel plate setup

Each end support consisted of a large concrete block with a 6 in. wide neoprene pad resting on top. Figure 4.35 shows this setup with an upright girder-joint-girder specimen installed beneath the load frame.

Figure 4.35. End support setup

Two wire potentiometers were placed with one on each side of the girder-joint-girder specimen at midspan to measure deflection while testing. Steel angles were epoxied to the face of the continuity joint to allow the wire potentiometers to connect to the specimen. This setup is shown in Figure 4.36.

Figure 4.36. Wire potentiometer setup

4.5.2 Specimen Testing Procedure

Each test specimen was installed beneath the load frame using the overhead crane. A plumb bob suspended from a string attached to the center of the hydraulic ram allowed the research team to place the test specimens centered both laterally and longitudinally. After the test specimen was aligned with the hydraulic ram, the wire potentiometers, load cell, and strain gauges were attached to the data acquisition system. To ensure the data acquisition was working properly each sensor was tested for a signal change. After this sensor check, each signal was tared to zero within the data acquisition system in preparation for testing.

Load was applied to each specimen by two 5-kip intervals until 10-kips were applied. Loading increments were then adjusted to 2-kip intervals for the remainder of testing. This allowed for better precision when locating cracks. Shear and flexural cracks were assessed between each interval. Cracks were traced with black permanent marker with the corresponding load written at the end of the crack.

Two separate scenarios would govern when each specimen had completed its testing depending on what strength was being assessed. The first scenario was when the specimen would not take any more load, yielding the longitudinal reinforcement. This was considered a flexural failure. The second scenario was the initial cracking of

the specimens to be repaired. Testing for this second scenario was completed when the continuity joint had sufficient cracking that would simulate that of a damaged girder in the field. Each specimen was unloaded when finished with testing.

4.6 Control Girder Testing and Results

4.6.1 Overview

Three girder-joint-girder specimens were tested to failure in negative moment bending without any repair. These specimens acted as the control group and are denoted as C1, C2, and C3 throughout this research. To simulate negative moment bending the specimens were flipped upside down before installing them beneath the load frame. Loading the control group upside down resulted in a flexural failure in negative moment bending at the continuity joint. Figure 4.37 shows the test setup for a representative control beam prior to loading. Specimens were tested using the procedure described in Section 4.5.2.

Figure 4.37. Control beam test setup for negative moment bending

4.6.2 Control Specimen C1 Results

Initial shear cracking was observed within the web of the specimen at the 10-kip loading and continued to propagate diagonally upward as the loading progressed. The vast majority of the shear cracking developed within the web occurred between 14 kips and 36 kips of loading. Shear cracking marked with the corresponding loading increment, is shown in Figure 4.38.

Figure 4.38. Specimen C1 shear cracking

Initial flexural cracking began to form in the continuity joint at the same 10-kip loading interval as the initial shear cracking (Figure 4.39).

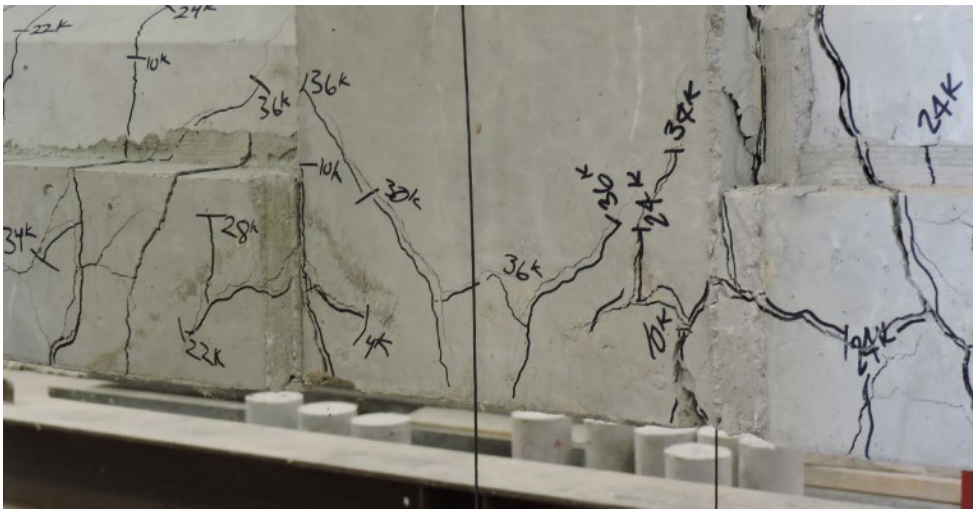

Figure 4.39. Specimen C1 flexural cracking in the continuity joint

These initial cracks continued to grow with increased loading. Flexural cracks at the girder-joint interface were observed on both sides of the specimen. As loading increased, these cracks not only continued propagating upward on the interface but also increased in width, showing visible joint separation (Figure 4.40 and Figure 4.41).

Figure 4.40 Specimen C1 cracking at girder-joint interface (left side)

Figure 4.41. Specimen C1 cracking at girder-joint interface (right side)

Figure 4.42 shows the girder-joint interface flexural cracking across the deck. This photo was taken after the specimen had been unloaded, removed from beneath the loading frame, and flipped right side up. The large cracks across the top of the deck indicate that the continuity joint had begun to detach from the two half-length girders. Figure 4.43 shows the overall girder-joint-girder specimen after testing.

Figure 4.42. Specimen C1 girder-joint interface cracking across the deck

Figure 4.43. Deflected shape of unloaded C1 specimen

Control specimen C1 showed a ductile behavior after an applied load of 33.1 kips and had an ultimate load capacity of 44.6 kips. At the ultimate load, C1 had deflected an average of 2.28 in. Figure 4.44 shows the load-deflection curve for specimen C1, which is typical of a beam flexural failure.

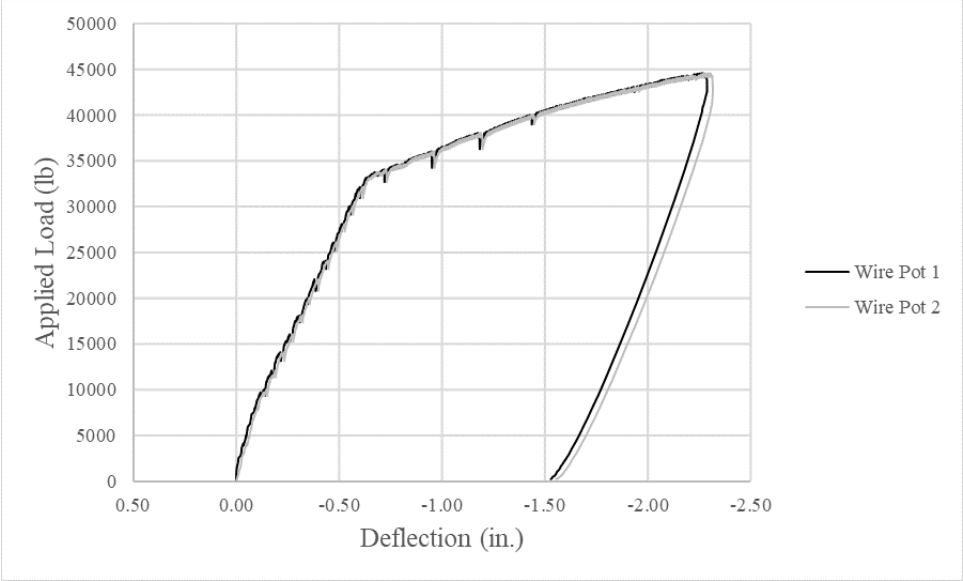

Figure 4.44. Specimen C1 load-deflection curve

The outer longitudinal reinforcement for negative moment bending began to yield at a loading of 27.7 kips. This was the point at which the strain in the steel reached 0.00218 in/in. Figure 4.45 shows a plot of the load-strain curve for control specimen C1. The inner reinforcement's strain gauge appears to have lost signal during the loading process. There are a number of reasons this may have happened, which include detaching from the rebar, or an open circuit caused by a shifting of the strain gauge wires within the specimen.

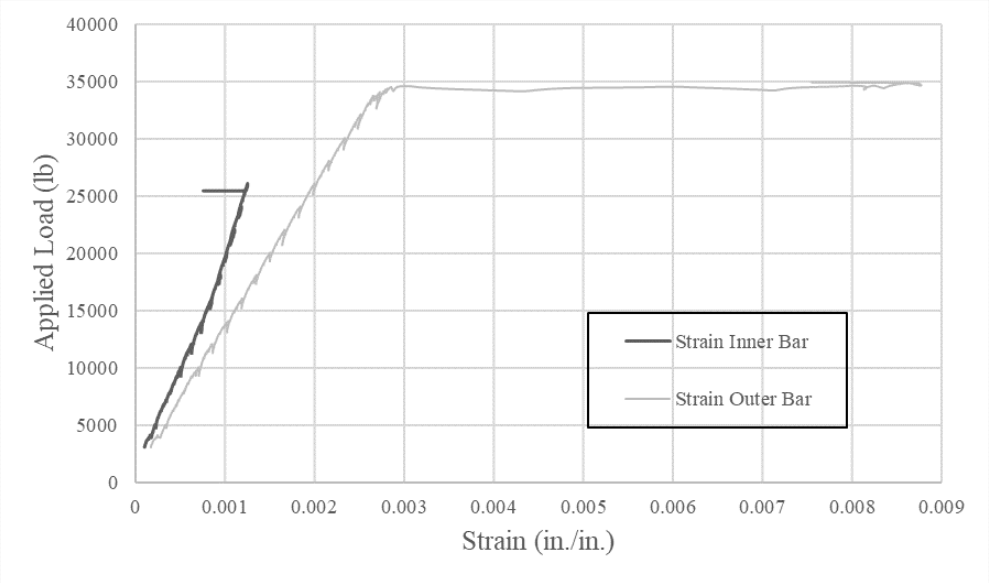

Figure 4.45. Specimen C1 load-strain curve

4.6.3 Control Specimen C2 Results

Initial shear cracking was observed within the web of the specimen at the 10-kip loading and continued to propagate diagonally upward as the loading progressed. The vast majority of the shear cracking developed within the web occurred between 12 kips and 36 kips of loading. Shear cracking marked with the corresponding loading increment is shown in Figure 4.46.

Figure 4.46. Specimen C2 shear cracking

At the same 10-kip loading interval, initial flexural cracking began to form in the continuity joint (Figure 4.47).

Figure 4.47. Specimen C2 flexural cracking in the continuity joint

These cracks continued to grow with increased loading. Flexural cracks at the girder-joint interfaced were observed on both sides of the specimen. As loading increased, these cracks not only continued propagating upward on the interface but also increased in width (Figure 4.48 and Figure 4.49).

Figure 4.48. Specimen C2 cracking at girder-joint interface (left side)

Figure 4.49. Specimen C2 cracking at girder-joint interface (right side)

Figure 4.50 shows the girder-joint interface flexural cracking across the deck. This photo was taken after the specimen had been unloaded, removed from beneath the loading frame, and flipped right side up. The large cracks across the top of the deck indicate that the continuity joint had begun to detach from the two half-length girders. Figure 4.51 shows the overall girder-joint-girder specimen after testing.

Figure 4.50. Specimen C2 girder-joint interface cracking across the deck

Figure 4.51. Deflected shape of unloaded C2 specimen

Control specimen C2 showed a ductile behavior after a load of 33.2 kips and had an ultimate load capacity of 44.6 kips. At the ultimate load, specimen C2 had deflected 2.40 in. Figure 4.52 shows the load-deflection curve for specimen C2, which is typical for a beam flexural failure.

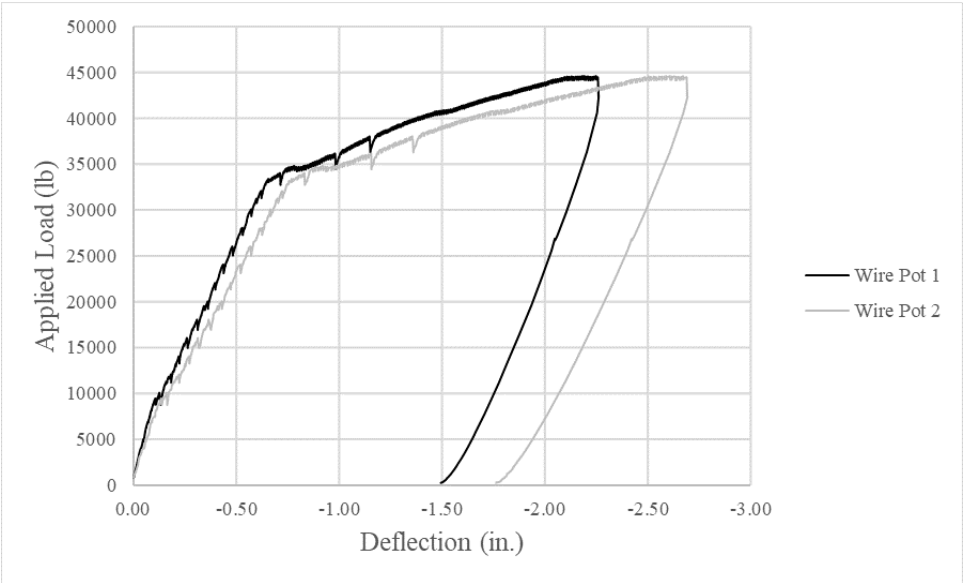

Figure 4.52. Specimen C2 load-deflection curve

The inner longitudinal reinforcement for negative moment bending began to yield at a loading of 29.2 kips. The outer longitudinal reinforcement began to yield at a loading of 28.0 kips. These were the points of which the strain in the steel reached 0.00218 in/in. Figure 4.53 shows a plot of the load-strain curve for control specimen C2.

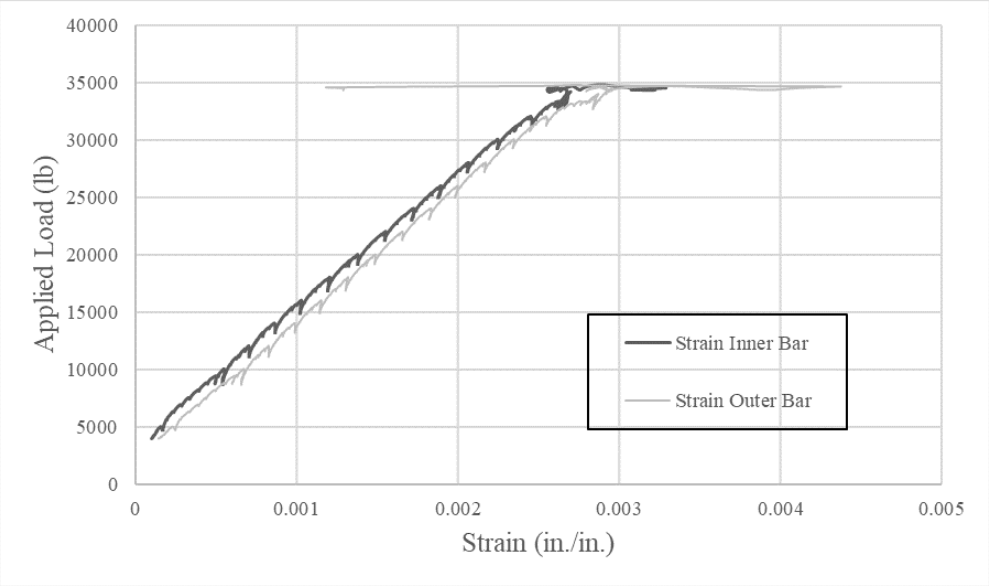

Figure 4.53. Specimen C2 load-strain curve

4.6.4 Control Specimen C3 Results

Initial shear cracking was observed within the web of the specimen at the 10-kip loading and continued to propagate diagonally upward as the loading progressed. The vast majority of the shear cracking developed within the web occurred between 12 kips and 36 kips of loading. Shear cracking marked with the corresponding loading increment is shown in Figure 4.54.

Figure 4.54. Specimen C3 shear cracking

At the same 10-kip loading interval, initial flexural cracking began to form in the continuity joint. At the 16-kip loading increment a flexural crack propagated straight upward from the center of the continuity joint. This significant crack continued until 30 kips of load was applied before branching off into two flexure-shear cracks. These cracks terminated at 38 kips and 34 kips of loading (Figure 4.55).

Figure 4.55. Specimen C3 flexural cracking in the continuity joint

Flexural cracks at the girder-joint interface were observed on both sides of the specimen. As loading increased, these cracks not only continued propagating upward on the interface but also increased in width, showing visible joint separation. Figure 4.56 shows the girder-joint interface flexural cracking across the deck. The centerline flexural

crack can also be seen. This photo was taken after the specimen had been unloaded, removed from beneath the loading frame, and flipped right side up. The large cracks across the top of the deck indicate that the continuity joint had begun to detach from the two half-length girders. Figure 4.57 shows the overall girder-joint-girder specimen after testing.

Figure 4.56. Specimen C3 girder-joint interface and centerline cracking across the deck

Figure 4.57. Deflected shape of unloaded specimen C3

Control specimen C3 showed a ductile behavior after 32.2 kips of load and had an ultimate load capacity of 41.5 kips. At the ultimate load, specimen C3 had deflected 2.16 in. Figure 4.58 shows the load-deflection curve for specimen C3, which is typical for a beam flexural failure.

The inner longitudinal reinforcement for negative moment bending began to yield at a loading of 40.5 kips which is inconsistent with the other strain gauge and all strain gauges from the other two control specimens. This may indicate a faulty reading. The outer longitudinal reinforcement began to yield at a loading of 31.3 kips. These were the points at which the strain in the steel reached 0.00218 in/in. Figure 4.59 shows a plot of the load-strain curve for control specimen C3.

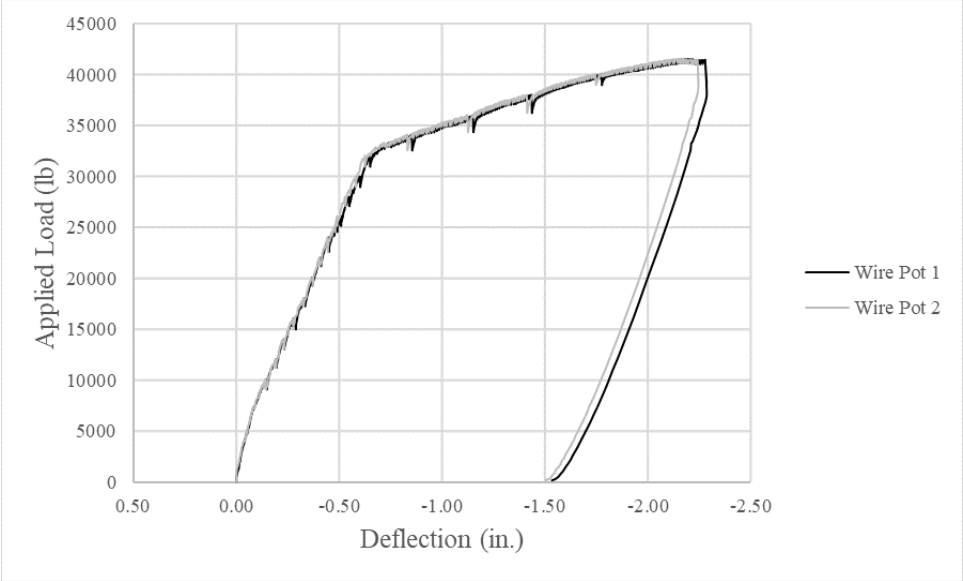

Figure 4.58. Specimen C3 load-deflection curve

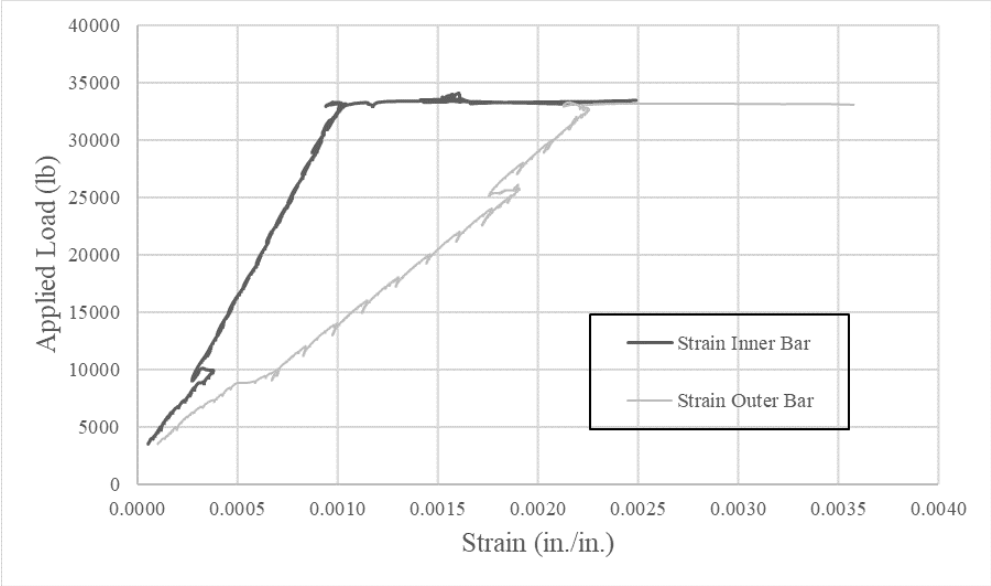

Figure 4.59. Specimen C3 load-strain curve

4.6.5 Control Girder Testing Summary

Figure 4.60 shows all load-deflection curves for the control girder specimens. This figure shows that all three specimens had very similar behavior. Specimen C3 had a slightly lower stiffness after first yielding and exhibited a slightly lower ultimate load.

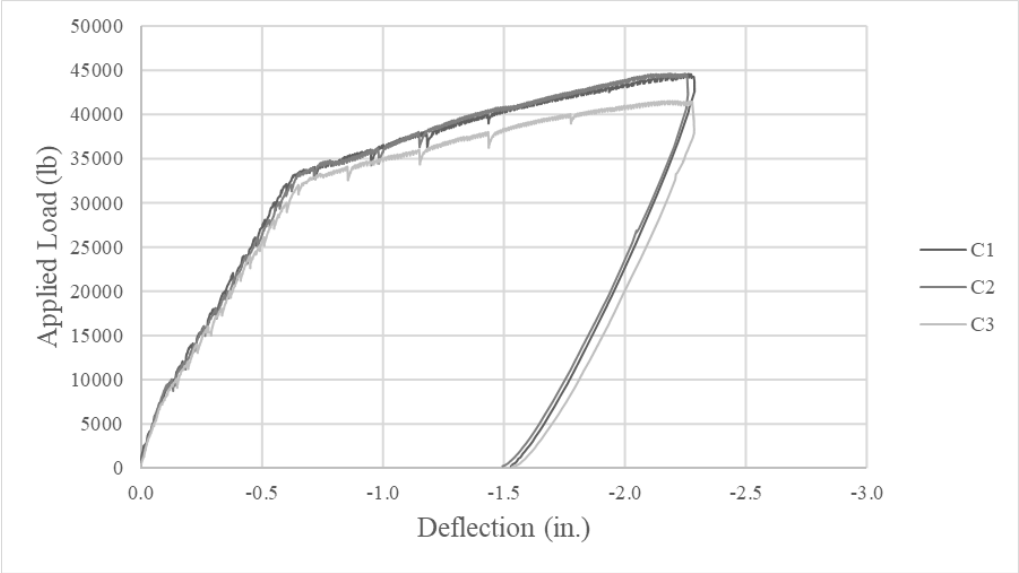

Figure 4.60. Load-deflection curves for control girder specimens

4.7 Initial Cracking of Girders to be Repaired

4.7.1 Overview

After the control specimens were tested, the remaining nine girder-joint-girder specimens were loaded to induce cracking within their continuity joints. This process simulated the time-dependent effects experienced in the field which cause the bottom of the continuity joint to crack due to induced positive moment. Unlike the control group, the remaining nine specimens were loaded upright as cast to induce positive moment bending. The data acquisition system was used in conjunction with only the load cell for these tests, outputting the load at which a sufficient amount cracking within the continuity joint replicated in-situ damage.

Besides loading in positive moment bending, the testing arrangement and procedure for the initial cracking of the repair girders was identical to that of the control specimens. Figure 4.61 shows this setup, which was used for all nine girder-joint-girder specimens.

Figure 4.61. Setup for testing girders specimens to be repaired

Specimens were divided into three groups. These groups corresponded to the material that would subsequently be used for repair. The nomenclature for each group within this research is as follows: R1-J3, R2-J3, and R3-J3 are used for the group of specimens repaired with ultra-high-performance concrete; R1-FRSCC, R2-FRSCC, and R3-FRSCC are used for the group of specimens repaired with fiber-reinforced self-consolidating concrete; and R1-PHOS, R2-PHOS, and R3-PHOS are used for the group of specimens repaired with magnesium-alumino-liquid phosphate (MALP) concrete (Phoscrete®).

4.7.2 Cracking of J3 UHPC Repair Specimens

The first set of three specimens cracked were to be repaired with ultra-high-performance concrete (J3). At an applied load of 23.0 kips sufficient cracking within the continuity joint of specimen R1-J3 had been achieved. Figure 4.62 and Figure 4.63 show joint cracking for specimen R1-J3.

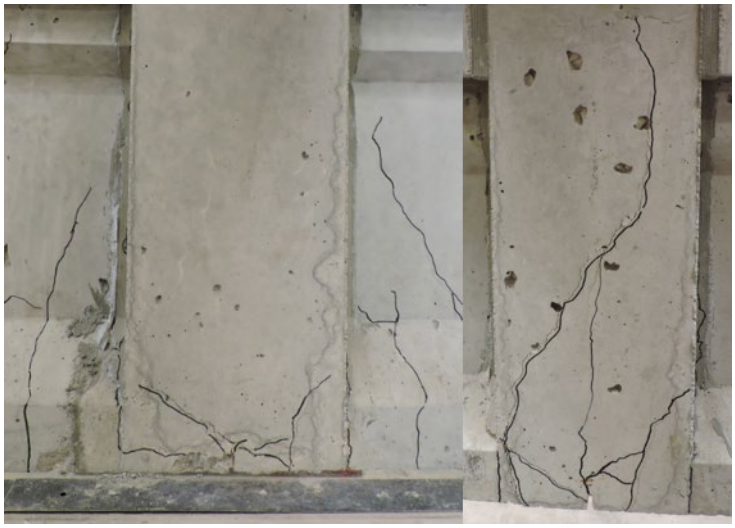

Figure 4.62. Initial cracking of specimen R1-J3 on the front (left) and rear (right) of the joint face

Figure 4.63. Initial cracking of specimen R1-J3 on the bottom joint face

At an applied load of 23.0 kips, sufficient cracking within the continuity joint of specimen R2-J3 had been achieved. Figure 4.64 and Figure 4.65 show joint cracking for R2-J3.

At an applied load of 20.1 kips sufficient cracking within the continuity joint of specimen R3-J3 had been achieved. Figure 4.66 and Figure 4.67 show joint cracking for R3-J3.

Figure 4.64. Initial cracking of specimen R2-J3 on the front (left) and rear (right) of the joint face

Figure 4.65. Initial cracking of specimen R2-J3 on the bottom joint face

Figure 4.66. Initial cracking of specimen R3-J3 on the front (left) and rear (right) of the joint face

Figure 4.67. Initial cracking of specimen R3-J3 on the bottom joint face

4.7.3 Cracking FR-SCC Repair Specimens

The second set of three specimens cracked were to be repaired with fiber-reinforced self-consolidating concrete (FR-SCC). At an applied load of 27.5 kips, sufficient cracking within the continuity joint of specimen R1-FRSCC had been achieved. Figure 4.68 and Figure 4.69 show joint cracking for specimen R1-FRSCC.

Figure 4.68. Initial cracking of specimen R1-FRSCC on the front (left) and rear (right) of the joint face

Figure 4.69. Initial cracking of specimen R1-FRSCC on the bottom joint face

At an applied load of 21.4 kips sufficient cracking within the continuity joint of specimen R2-FRSCC had been achieved. Figure 4.70 and Figure 4.71 show joint cracking for R2-FRSCC.

Figure 4.70. Initial cracking of specimen R2-FRSCC on the front (left) and rear (right) of the joint face

Figure 4.71. Initial cracking of specimen R2-FRSCC on the bottom joint face

At an applied load of 21.4 kips sufficient cracking within the continuity joint of specimen R3-FRSCC had been achieved. Figure 4.72 and Figure 4.73 show joint cracking for specimen R3-FRSCC.

Figure 4.72. Initial cracking of specimen R3-FRSCC on the front (left) and rear (right) of the joint face

Figure 4.73. Initial cracking of specimen R3-FRSCC on the bottom joint face

4.7.4 Cracking of Phoscrete® Repair Specimens

The third set of three specimens cracked were to be repaired with magnesium-alumino-liquid phosphate (MALP) concrete (Phoscrete®). At an applied load of 25.2 kips a sufficient amount of cracking within the continuity joint of specimen R1-PHOS had been achieved. Figure 4.74 and Figure 4.75 show joint cracking for R1-PHOS.

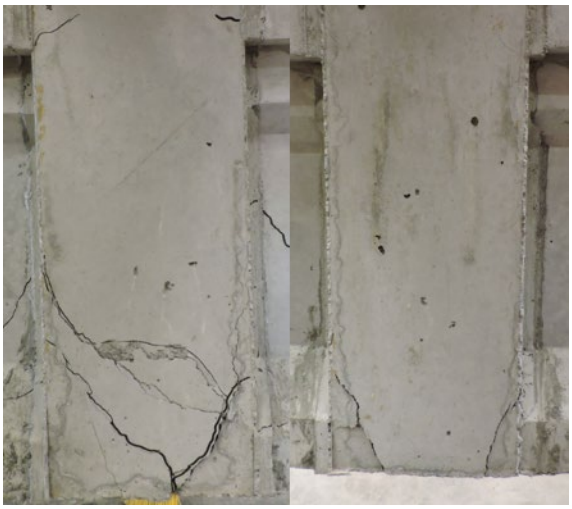

Figure 4.74. Initial cracking of specimen R1-PHOS on the front (left) and rear (right) of the joint face

Figure 4.75. Initial cracking of specimen R1-PHOS on the bottom joint face

At an applied load of 24.7 kips sufficient cracking within the continuity joint of specimen R2-PHOS had been achieved. Figure 4.76 and Figure 4.77 show joint cracking for specimen R2-PHOS.

At an applied load of 25.2 kips sufficient cracking within the continuity joint of specimen R3-PHOS had been achieved. Figure 4.78 and Figure 4.79 show joint cracking for R3-PHOS.

Figure 4.76. Initial cracking of specimen R2-PHOS on the front (left) and rear (right) of the joint face

Figure 4.77. Initial cracking of specimen R2-PHOS on the bottom joint face

Figure 4.78. Initial cracking of specimen R3-PHOS on the front (left) and rear (right) of the joint face

Figure 4.79. Initial cracking of specimen R3-PHOS on the bottom joint face

4.7.5 Initial Cracking Load Summary

Table 4.5 shows a summary of the initial cracking loads for each specimen to be repaired.

Table 4.5. Summary of Initial Cracking Loads

Specimen	Load at Sufficient Joint Cracking (kips)
R1-J3	22.99
R2-J3	23.02
R3-J3	20.06
R1-FRSCC	27.52
R2-FRSCC	21.43
R3-FRSCC	21.42
R1-PHOS	25.20
R2-PHOS	24.72
R3-PHOS	25.18
Average:	23.50

4.8 Joint Repair

4.8.1 Overview

The continuity joint repairs for the nine specimens consisted of three different specialized concretes. The first set of specimens were repaired with an ultra-high-performance concrete mix (J3). The second set of specimens were repaired with a fiber-reinforced self-consolidating concrete mix (FR-SCC). The final set of specimens were repaired with a magnesium-alumino-liquid (MALP) concrete mix (Phoscrete®).

4.8.2 Joint Repair Design

The continuity joint repair design was based on the time-dependent effects of temperature loading on reinforced concrete continuous girder bridges. Changes in the surrounding climate can cause expansion and contraction within the girders which may result in unfavorable internal stresses. Sections 3 and 4 of AASHTO LRFD (2017) were used to establish a steel reinforcement design that would counteract these time-dependent effects.

By considering a temperature gradient within a concrete girder bridge using AASHTO LRFD 3.12.3, internal stresses and structural deformations were determined in accordance with the provisions of AASHTO LRFD Article 4.6.6. Because plane sections remain plane, a curvature is imposed on the superstructure to accommodate the linearly variable component of the temperature gradient (AASHTO LRFD 2017). Section C4.6.6 gives the equation for this rotation due to a vertical temperature gradient, shown in Equation 4.1:

$$\phi = \frac{\alpha}{I_c} \iint T_G z dw dz = \frac{1}{R} \tag{4.1}$$

where

$\alpha = coefficient\ of\ thermal\ expansion;\ 6 * 10^{-6}/_{°\mathrm{F}}$

$I_c = moment\ of\ inertia\ of\ cross-section;\ 15{,}507\ in^4$

$T_G = temperature\ gradient;\ 46\ °\mathrm{F}$

$z = vertical\ distance\ from\ center\ of\ gravity\ of\ cross-section;\ 13.56\ in.$

$w = width\ of\ element\ in\ cross-section;\ 9\ in.$

Setting Oklahoma as the location, the temperature gradient of 46 °F was found from AASHTO LRFD Table 3.12.3-1, using Solar Radiation Zone 2 from AASHTO LRFD Figure 3.12.3-1. Evaluating Equation 4.1 gives a rotation per unit length corresponding to the girder-joint-girder specimens used in this research of $\phi = 0.00001459$.

The moment developed at the pier for a two-span structure needed to eliminate deflection where the temperature gradient flexes the structure into a segment of a circle in the vertical plane is given by Equation 4.2.

$$M_c = \frac{3}{2} E I_c \phi \tag{4.2}$$

Evaluating Equation 4.2 gave a moment value of 102 k-ft. Therefore, the amount of positive reinforcement needed was calculated as 0.752 in^2 of 60 ksi mild steel, or four No. 4 bars.

In this design, reinforcement was placed in two locations at the bottom of the continuity joint. The lower reinforcement was designed to be placed within the bottom bell, 2.5 in. from the bottom of the specimen. The upper reinforcement was designed to be placed in the bottom of the web, 6.25 in. above the bottom of the specimen.

The web reinforcement was designed to be two U-shaped No. 4 bars with legs extended horizontally across the face of the continuity joint. Each leg of each U-shaped bar was designed to lap with one another by a minimum development length of 9.49 in. and standard hook geometry as per ACI 25.4.3.1 (2014) and ACI 25.3.1 (2014), respectively. Figure 4.80 shows the top repair reinforcement.

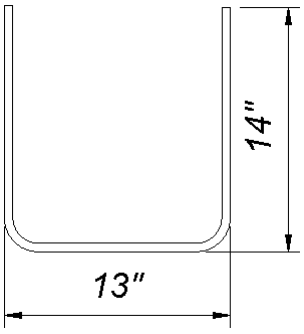

Figure 4.80. Top repair reinforcement shape and dimensions

The bottom repair reinforcement was designed to be two U-shaped No. 4 bars with legs extending halfway into the bottom bell. The reason for this was for ease of installation of the rebar. Each leg was anchored 4.5 in. into the bottom bell to provide the necessary bond strength using a Hilti HIT-HY 200-R epoxy. The bottom repair

reinforcement was also designed with a standard hook geometry per ACI 25.3.1 (2014). Figure 4.81 shows the bottom repair reinforcement.

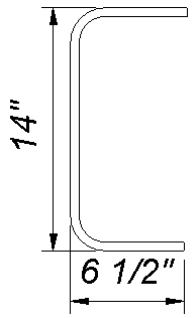

Figure 4.81. Bottom repair reinforcement shape and dimensions

The bars were placed 1.5 in. away from the initial joint, with a 1 in. outer cover, with a total repair thickness of 3 in. over the joint. This did not allow for the cover on the hooks required by ACI 318 (2014) but was chosen as a practical thickness to be used in the field.

Horizontal shearing forces between the front face of the continuity joint and repair concrete's interface were considered during the design. A 34-kip design load, obtained from the control specimen data, was used for these calculations. Negative moment bending causes a stress block within the bottom bell of the girder-joint-girder specimen with an area of 21.9 in^2. This stress block was transformed to the cross-sectional area of the repair concrete, requiring a horizontal shearing force of 14.9 kips to maintain equilibrium.

A total of twelve, ¼ in. x 2.75 in. Tapcon® screw anchors were used to transfer this shearing force across the interface between the original girder concrete and the repair concrete. With an embedment length of 1.5 in. and concrete compressive strength of 4,000 psi, the total design capacity of the Tapcon® screws was rated at 16.6 kips per the manufacturer's performance tables. Six screw anchors were designed to be installed on the front and back faces of the continuity joint.

4.8.3 Joint Repair Reinforcement and Formwork

Repair reinforcement was cut, bent, and placed within the repair specimens in accordance with the design. One strain gauge was placed on one bottom reinforcing bar

for each specimen. Formwork was fabricated to house the repair joint for casting each of the repair concretes.

An injectable adhesive, Hilti HIT-HY 200-R, was used to install the repair reinforcement. As per the Hilti Product Technical Guide, 5/8 in. holes were drilled through the vertical face of the bottom bell and the web of each specimen. To aid in the process of drilling out the 9 in. long hole in the bottom bell, a 5 in. long bit was used to bore from both sides. The allowed for better alignment of the overall void and quicker turnaround. The 5/8 in. diameter hole in the 3 in. thick web was drilled with ease using the same bit. The centerline of each hole was drilled 1.75 in. longitudinally from the side faces of the joint. This dimension allowed clearance from any vertical stirrup placed within the original specimen. A visual representation of the location of these holes is shown in Figure 4.82 and Figure 4.83.

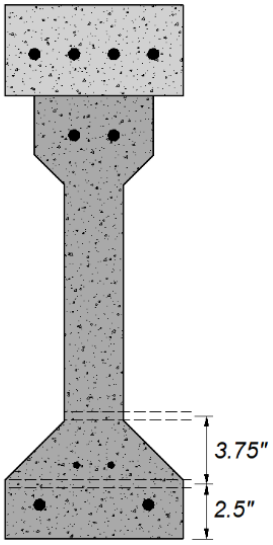

Figure 4.82. Vertical location of drilled holes for anchoring repair reinforcement

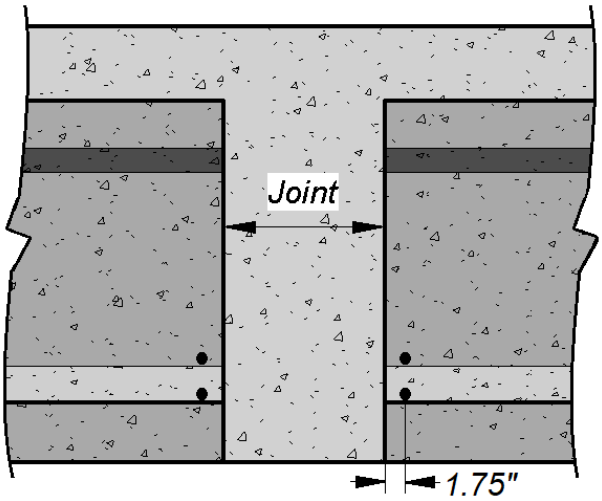

Figure 4.83. Horizontal location of drilled holes for anchoring repair reinforcement

After drilling each required hole in the specimens, an air compressor with a blow gun attachment was used to clear out any remaining dust particles left behind. This process helped the injectable adhesive adhere to the inside surfaces of the concrete holes. No. 4 bars were installed into the holes as designed. Approximately 1 oz of adhesive was used in each hole to anchor the reinforcement. The top reinforcing bars were tied together and orientated as horizontally as possible. Each reinforcing bar was left overnight to cure before any additional work on the specimens continued. Figure 4.84 shows the installation of the repair reinforcement.

Figure 4.84. Installation of repair reinforcement

An angle grinder with a diamond grinding wheel was used to roughen the repair surface. This process was done to increase the interface bond between the repair concretes and the cracked specimens. After roughening each surface, a water only pressure washer was used to eliminate concrete dust trapped within the concrete pores left by the grinding wheel. Figure 4.85 shows the roughened surface of a girder-joint-girder specimen.

Figure 4.85. Roughened surface of continuity joint to be repaired

One strain gauge was installed on one bottom repair bar of each specimen using the same procedure as described in Section 4.3.2. To ensure a smooth surface to adhere to, sanding the location of the strain gauge was done after installation. This order of operations allowed any scratches or markings created while installing, tying, grinding, or pressure washing to be removed prior to placing the strain gauges. Figure 4.86 shows the final set up of the repair reinforcement strain gauges.

Plywood and construction grade lumber was again used to create the formwork for the continuity joint repair. Much like the formwork to create the initial continuity joint, sheets of plywood were cut in the shape of the outer girder profile. The only difference in these shapes was that they extended farther away from the girder and did not include the profile of the deck above. Because these pieces were reused for multiple beams and since each girder profile was not exactly the same, silicone was used to fill any gaps between the side formwork and the girder specimens. In addition to the silicone, high-strength adhesive tape was used to hold the side formwork to the web of the specimens. Figure 4.87 shows the repair formwork mated with the girder profile.

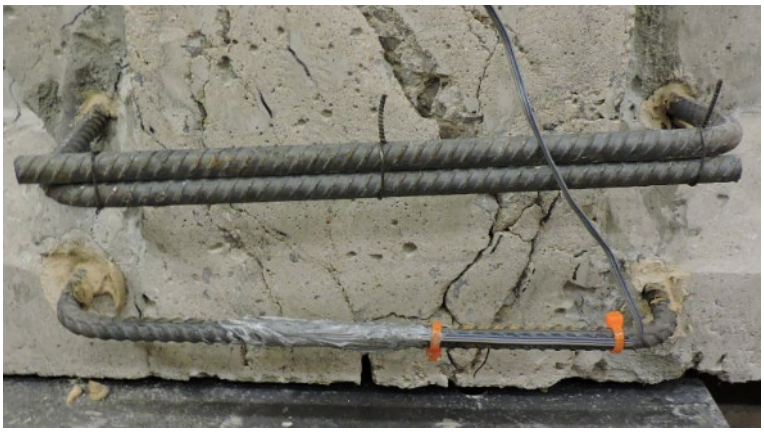

Figure 4.86. Strain gauge installed on repair reinforcement

Figure 4.87. Repair formwork for side face of the continuity joint

The front face formwork of the repair was built much like the initial continuity joint formwork. The outer dimensions of this formwork were 18 in. wide by 22.5 in. tall. A small cut was made 3 in. above the bottom of the 2x4 formwork to allow the strain gauge wires to pass through. This passage was also filled with silicone to mitigate any leak of repair concrete. A sheet of plywood on the floor was once again used for the bottom of the repair formwork. A stop block was placed on the outside of the face formwork to not allow movement of the formwork due to head pressure during the pour, and silicone was used between the base and the side pieces. Small wooden wedges were used between the top of the formwork and the bottom of the deck. These helped

keep pressure between the formwork and the floor plywood. Figure 4.88 shows the final joint repair formwork.

Figure 4.88. Joint repair formwork

4.8.4 Mixing and Placing Repair Concrete

Each repair concrete was mixed and placed at Fears Lab. Each side of the girder-joint-girder repairs needed 0.77 ft^3 of repair concrete. The repair specimens were poured in groups of three corresponding to the type of concrete used. Plastic five-gallon buckets were used to pour each material into the top of the formwork. Pouring continued until the joint repair concrete had filled to the bottom of the deck. Each concrete flowed very well around the sides of the repair with no vibration needed.

The J3 mixture, shown in Table 4.6, was mixed using a horizontal axis spiral blade mixer with a capacity of 21 ft^3. One batch of 5 ft^3 of the J3 mix was enough to fill the repair forms and cylinders for compression testing. The mix began with combining all the dry materials into the mixer. The dry materials were mixed for ten minutes. After the dry mixing, half of the Glenium 7920 high range water reducer was added to the water which was then added to the dry mix slowly over the course of two minutes. The rest of the Glenium 7920 was added directly to the mixer after a period of one minute. As soon as this mixture began to flow, Dramix OL 13/0.2 steel fibers (2% by volume) were added and given three minutes to distribute throughout the mixture.

The J3 was transported from the mixer to the three repair specimens using plastic 5-gallon buckets. The repair concrete was poured into the forms and cylinders required for compression testing without external consolidation. The J3 repair was cured for 7 days before removing the formwork around the continuity joint and the joint was allowed to cure in the ambient laboratory environment until testing day.

Table 4.6. J3 UHPC Mixture Proportions

Material	Quantity
Type I Cement (lb/yd^3)	1179.6
GGBFS (lb/yd^3)	589.8
Silica Fume (lb/yd^3)	196.6
Steel Fibers (lb/yd^3)	264.5
Fine Masonry Sand (lb/yd^3)	1966
Water (lb/yd^3)	393.2
Glenium 7920 (oz/cwt)	19.5

The FR-SCC mixture, shown in Table 4.7 was mixed using the same spiral blade mixer as the UHPC. One batch of 5 ft^3 of the FR-SCC mix was enough to fill the repair forms and cylinders for compression testing. The mix began with combining all the aggregates and half the amount of water and mixing for one minute. The air entrainer was poured into the sand prior to combining the aggregates and water. Fly ash, cement, and Komponent were then added immediately following in that order. The Glenium 7920 high range water reducer and the rest of the water were added slowly until desired flow had been met. Once the mixture was flowable, MasterFiber MAC Matrix macrosynthetic fibers and one dose of citric acid was added to the mix. Additional doses of citric acid were added to the mixer every 15 minutes until casting of the repairs had been completed. These doses were reduced proportionally to the amount of concrete still left in the mixer.

The FR-SCC was transported from the mixer to the three repair specimens using plastic 5-gallon buckets. The repair concrete was poured into the forms and cylinders for testing with no consolidation. The FR-SCC repair was cured for 7 days before removing the formwork around the continuity joint and then allowed to cure in the ambient laboratory conditions until testing day.

Table 4.7. FR-SCC Mixture Proportions

Material	Quantity
Type I Cement (lb/yd^3)	412.5
Fly Ash (lb/yd^3)	225.0
Komponent (lb/yd^3)	112.5
Water (lb/yd^3)	249.8
Coarse Aggregate (lb/yd^3)	1267.6
Fine Aggregate (lb/yd^3)	1429.0
Air Entrainer (oz/yd^3)	8.2
Glenium 7920 (oz/yd^3)	61.9
Citric Acid (oz/yd^3)	6.3
Macrosynthetic Fibers (lb/yd^3)	7.7

The mixing procedure provided by the manufacturer for the proprietary MALP mixture, Phoscrete®, was used to prepare the material. The mix ratio, 18.75% wet to dry, had already been established from the prepackaged manufacturer's kit. The large mixer at Fears Lab was not used for this set of repairs. Because of the fast-setting properties of Phoscrete®, with a roughly 8-minute set time, batches consisting of one 55 lb bag of dry mix and one 10 lb jug of liquid activator were mixed individually in 5-gallon buckets. A urethane auger, supplied from the manufacturer, attached to a 10-amp variable speed drill was used during the mixing process.

To begin, the Phoscrete® liquid activator was poured into a clean bucket. While mixing with the drill and auger, the dry mix was quickly added to the bucket and was mixed for one minute. Immediately following mixing, the bucket was lifted to pour the Phoscrete® into the repair specimen formwork. While some of the research team focused on pouring the already mixed concrete into the repairs, the rest of the team began a new batch in a new bucket immediately. This process was repeated until all repairs and compression cylinders had been cast.

The Phoscrete® materials expanded slightly while setting up. This was of no concern as the technical data provided by the manufacturer addresses this and it did not affect the outcome of the repairs.

4.8.5 Repair Concrete Compressive Strengths

Concrete cylinder compression testing was performed in accordance with ASTM C39 with modifications as required for UHPC. Table 4.8 shows the 28-day compressive strengths for each of the repair concretes. Data for only two cylinders of FR-SCC was obtained since the fiber length for this material required the use of 6 in. x 12 in. cylinders.

Table 4.8. 28-Day Repair Concrete Compressive Strengths

Repair Material	Compressive Strength (psi)
J3 UHPC 1	19,318
J3 UHPC 2	20,491
J3 UHPC 3	20,907
J3 UHPC Average	20,240
FR-SCC 1	6010
FR-SCC 2	8126
FR-SCC Average	7070
Phoscrete 1	4483
Phoscrete 2	4510
Phoscrete 3	4337
Phoscrete Average	4440

4.9 Repair Testing

4.9.1 Overview

Nine repair specimens were tested at Donald G. Fears Structural Engineering Lab at the University of Oklahoma. The first specimen from each repair group, denoted as R1-J3, R1-FRSCC, and R1-PHOS were tested to failure in positive moment bending. The remaining two specimens from each group were tested to failure in negative moment bending.

The arrangement used for testing in positive moment bending was the same as used for cracking the specimens with the addition of wire potentiometers (pots) and strain gauges connected to the data acquisition. The arrangement for testing the repair specimens in negative moment bending was identical to the setup and procedure used for the control specimens. As with the control group, each repair specimen tested in negative moment bending was flipped upside down using the overhead crane prior to

placement beneath the loading frame. Two wire pots were used for all repair specimen testing. Inputs to the data acquisition system included two strain gauges from the deck reinforcement, one strain gauge from the repair reinforcement, two wire pots used for deflection, and the load cell.

4.9.2 Ultra-High-Performance Concrete Repair Results

4.9.2.1 Repair Specimen R1-J3 Results

Specimen R1-J3 was tested to failure in positive moment bending. Shear cracking and flexural cracking were observed on the girder webs and either sides of the of the repaired continuity joint, respectively, during testing and are shown in Figure 4.89.

Figure 4.89. Specimen R1-J3 shear and flexural cracking

There were no noticeable cracks on the longitudinal face of either side of the repaired joint. Small surface cracks were observed on the transverse faces of the joint. Large cracks at the girder-joint interfaces continued to widen for the duration of the testing process. These cracks are shown in Figure 4.90.

Crushing of the deck was observed in the compression zone on either side of the steel loading plate and is shown in Figure 4.91. This is expected for a flexural failure after significant yielding of the flexural reinforcement and resulting strains. Figure 4.92 shows the overall girder-joint-girder repair specimen after testing. Note the failed specimen appears to consist of three separate members – each half girder and the continuity joint.

Figure 4.90. Specimen R1-J3 girder-joint interface crack on the left (left) side and right (right) side

Figure 4.91. Specimen R1-J3 deck crushing at failure

Figure 4.92. Deflected shape of specimen R1-J3 after testing

Specimen R1-J3 exhibited ductile behavior after 23.5 kips of load were applied and had an ultimate load capacity of 34.8 kips. At the ultimate load specimen R1-J3 exhibited an average deflection of 3.73 in. Figure 4.93 shows the load-deflection curve for specimen R1-J3, which is very typical for a beam flexural failure.

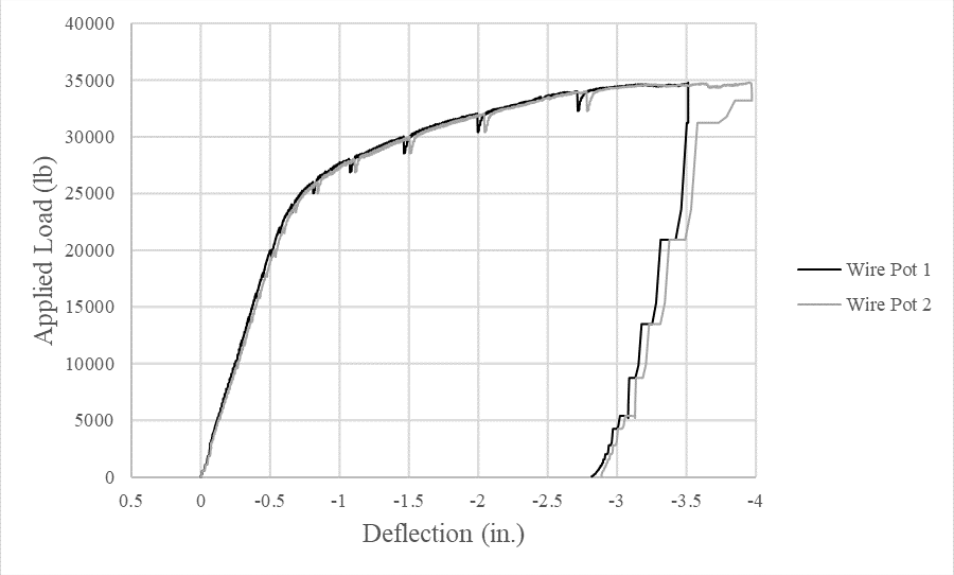

Figure 4.93. Specimen R1-J3 load-deflection curve

The repair reinforcing bars had negligible strain under loading with a maximum value of 2.2E-05 in./in. This may be due to the original hooked longitudinal reinforcement still taking significant load. The inner and outer deck reinforcement had maximum compression strains of -0.00032 in./in. and -0.00025 in./in., respectively. After this point, both bars began to decompress and eventually go into tension as the load increased. A possible reason for this may be due to the compression zone of the girder-joint-girder specimen rising above the deck reinforcement as loading increased beyond the linear-elastic range. The load-strain curves for specimen R1-J3's steel reinforcement is shown in Figure 4.94. The load-strain curves have been truncated for ease of the reader's interpretation.

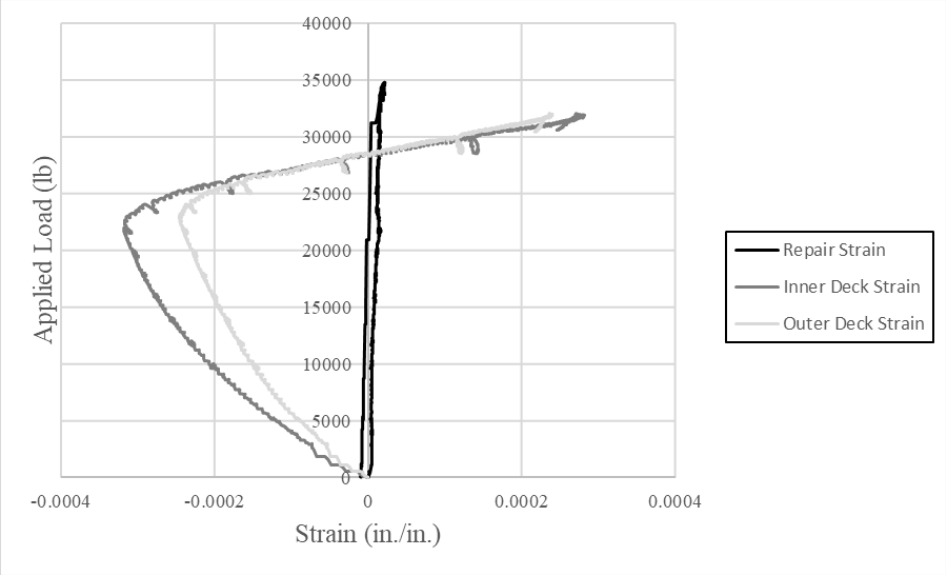

Figure 4.94. Specimen R1-J3 load-strain curves

4.9.2.2 Repair Specimen R2-J3 Results

Specimen R2-J3 was tested to failure in negative bending. Shear cracking and flexural cracking were observed during testing on the girder webs and on both sides of the of the repaired continuity joint, respectively, and are shown in Figure 4.95.

Figure 4.95. Specimen R2-J3 shear and flexural cracking

Small surface cracks were observed on the transverse faces of the joint, but not on the longitudinal faces as shown in Figure 4.96. Large cracks at the girder-joint interfaces continued to widen for the duration of the testing process. These cracks are shown in Figure 4.97 and Figure 4.98 along with significant flexural cracks within the deck. Figure 4.99 shows the overall girder-joint-girder repair specimen after testing.

Figure 4.96. Specimen R2-J3 continuity joint repair after testing

Figure 4.97. Specimen R2-J3 girder-joint interface cracking on the front left (left) and front right (right)

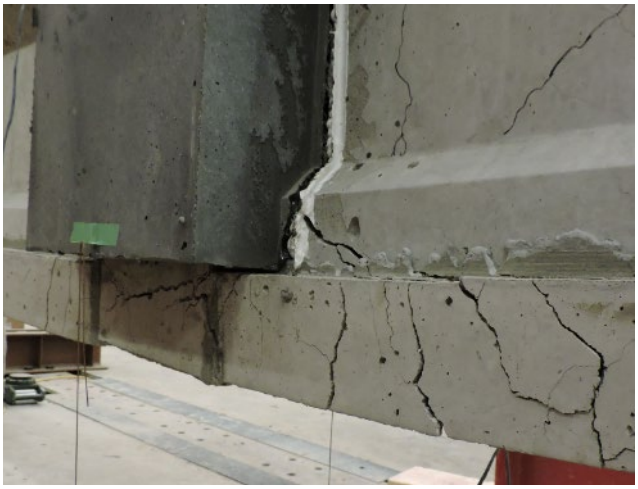

Figure 4.98. Specimen R2-J3 girder-joint interface cracking on the back right

Figure 4.99. Deflected shape of specimen R2-J3 after testing

Specimen R2-J3 exhibited ductile behavior after 33.4 kips of load were applied and had an ultimate load capacity of 46.0 kips. At the ultimate load, R2-J3 exhibited an average deflection of 3.65 in. Figure 4.100 shows the load-deflection curve for specimen R2-J3, which is very typical of a beam flexural failure.

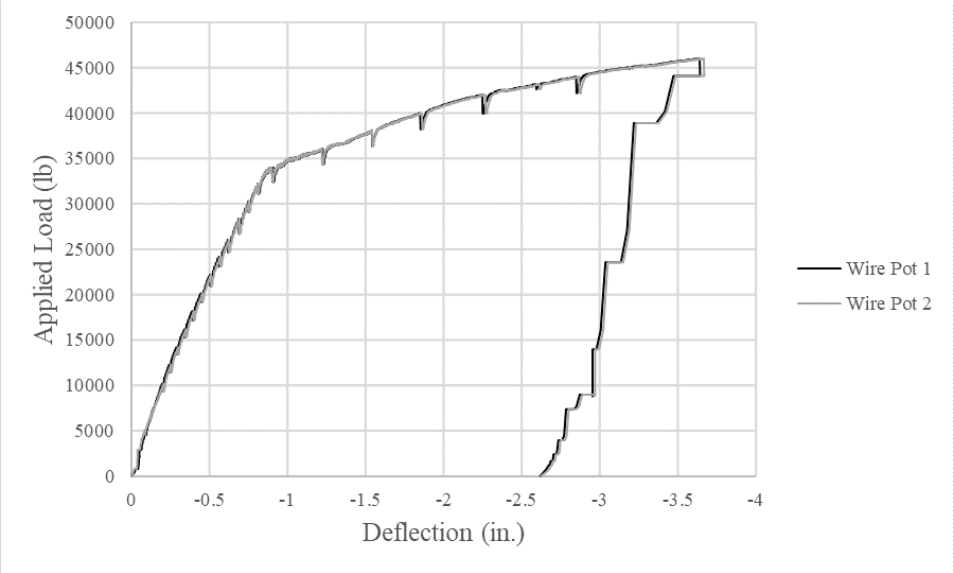

Figure 4.100. Specimen R2-J3 load-deflection curve

The outer longitudinal reinforcement in the deck began to yield at a loading of 29.5 kips. Figure 4.101 shows a plot of the load-strain curves for repair specimen R2-J3. The inner reinforcement's strain gauge appears to have lost signal during the loading process. The repair reinforcement strained in compression until a loading of 36.7 kips, then appears to have gone into tension until ultimate loading.

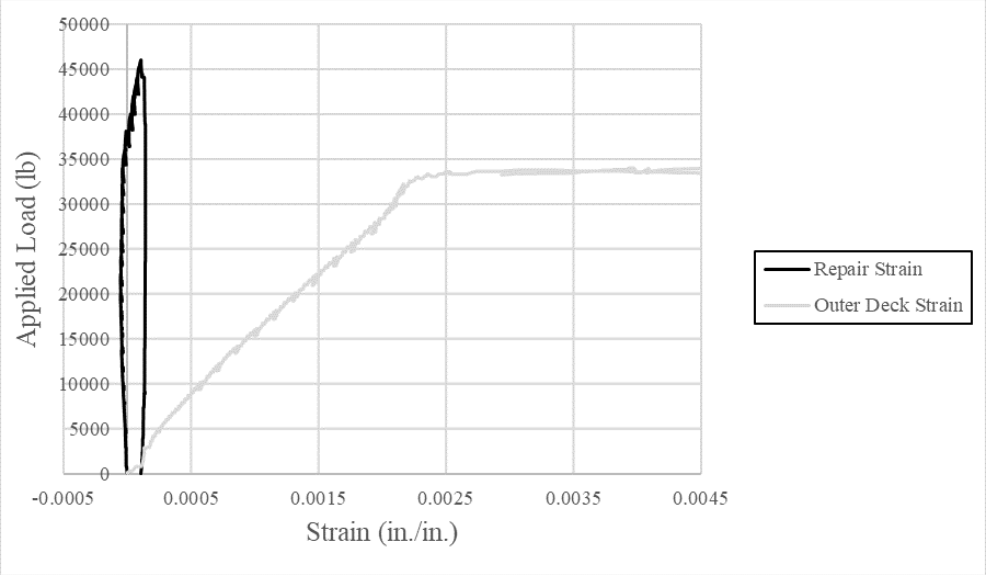

Figure 4.101. Specimen R2-J3 load-strain curves

4.9.2.3 Repair Specimen R3-J3 Results

Specimen R3-J3 was tested to failure in negative bending. Shear cracking and flexural cracking were observed during testing on the girder webs and on both sides of the of the repaired continuity joint, respectively, and are shown in Figure 4.102.

Figure 4.102. Specimen R3-J3 shear and flexural cracking

Small surface cracks were observed on the transverse faces of the joint, but no noticeable cracks were observed on the longitudinal face of either side of the repair joint, as shown in Figure 4.103. Large cracks at the girder-joint interfaces continued to widen for the duration of the testing process. These cracks are shown in Figure 4.104. Additionally, significant flexural cracks within the deck are shown in Figure 4.103. Figure 105 shows the overall girder-joint-girder repair specimen after testing.

Figure 4.103. Specimen R3-J3 continuity joint repair after testing

Figure 4.104. Specimen R3-J3 girder-joint interface cracking

Figure 4.105. Deflected shape of specimen R3-J3 after testing

Specimen R3-J3 exhibited ductile behavior after 33.4 kips of load were applied and had an ultimate load capacity of 46.0 kips. At the ultimate load, R3-J3 exhibited an average deflection of 3.48 in. Figure 4.106 shows the load-deflection curve for specimen R3-J3, which is very typical of a beam flexural failure.

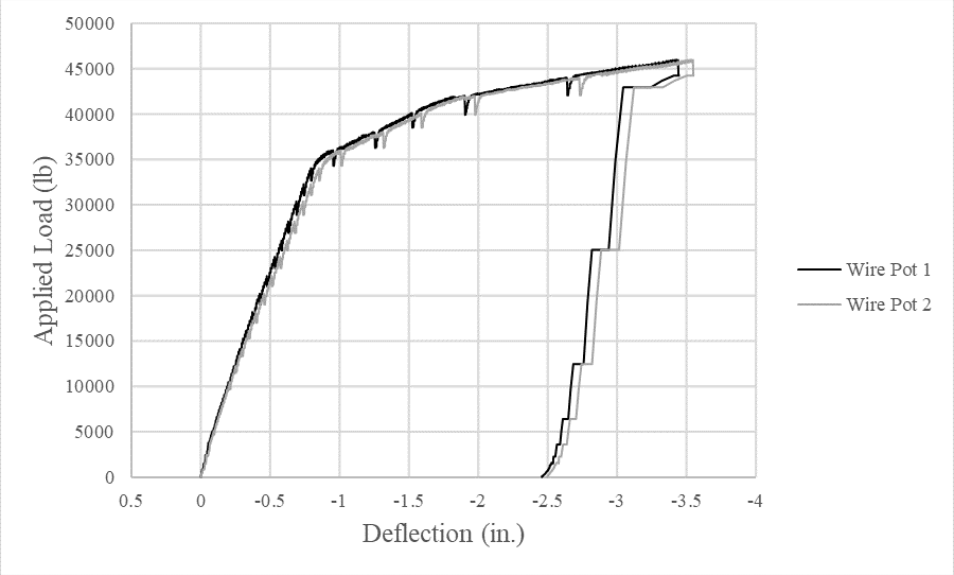

Figure 4.106. Specimen R3-J3 load-deflection curve

The outer longitudinal reinforcement in the deck began to yield at a loading of 31.1 kips. Figure 4.107 shows the load-strain curves for repair specimen R3-J3. The inner reinforcement's strain gauge appears to have lost signal during the loading process. The repair reinforcement strained in compression until a loading of 43.9 kips, then appears to have gone into tension until ultimate loading.

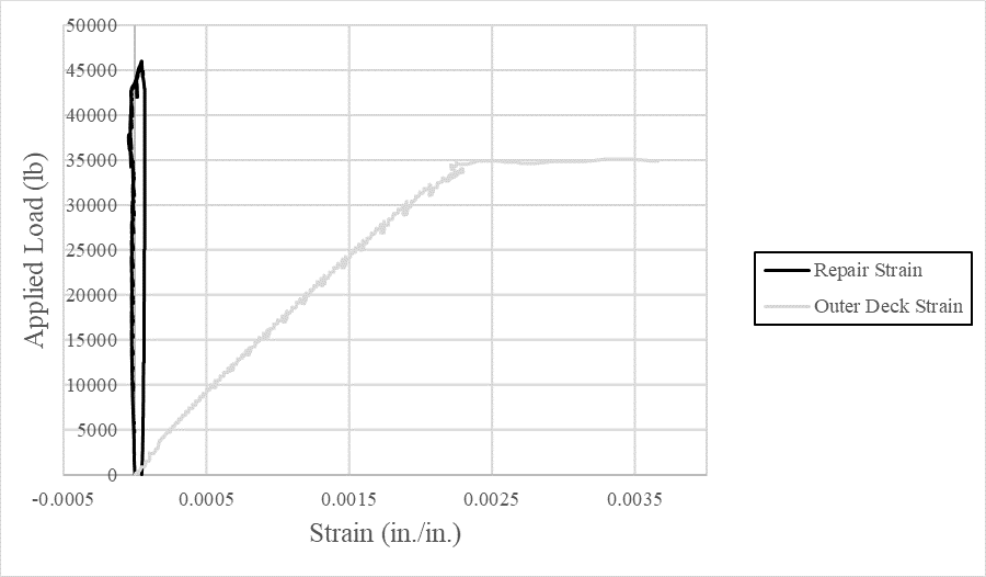

Figure 4.107. Specimen R3-J3 load-strain curves

4.9.3 Fiber Reinforced Self-Consolidating Concrete Repair Results

4.9.3.1 Repair Specimen R1-FRSCC Results

Specimen R1-FRSCC was tested to failure in positive moment bending. Shear cracking and flexural cracking were observed during testing on the girder webs and either sides of the of the repaired continuity joint, respectively, and are shown in Figure 4.108.

Figure 4.108. Specimen R1-FRSCC shear and flexural cracking

There were no noticeable cracks on the longitudinal face of either side of the repair joint. Flexural cracks were observed on the transverse faces of the joint and at the girder-joint interface. These cracks are shown in Figure 4.109 and Figure 4.110. These flexural cracks extended all the way through the specimen transverse to the span. Figure 4.111 shows the overall girder-joint-girder repair specimen after testing. The failed specimen appears to consist of three separate members – each half girder and the continuity joint.

Specimen R1-FRSCC exhibited ductile behavior after 25.6 kips of load were applied and had an ultimate load capacity of 32.9 kips. At the ultimate load, specimen R1-FRSCC exhibited an average deflection of 2.48 in. Figure 4.112 shows the load-deflection curve for specimen R1-FRSCC, which is very typical of a beam flexural failure.

Figure 4.109. Specimen R1-FRSCC back right joint transverse face cracking

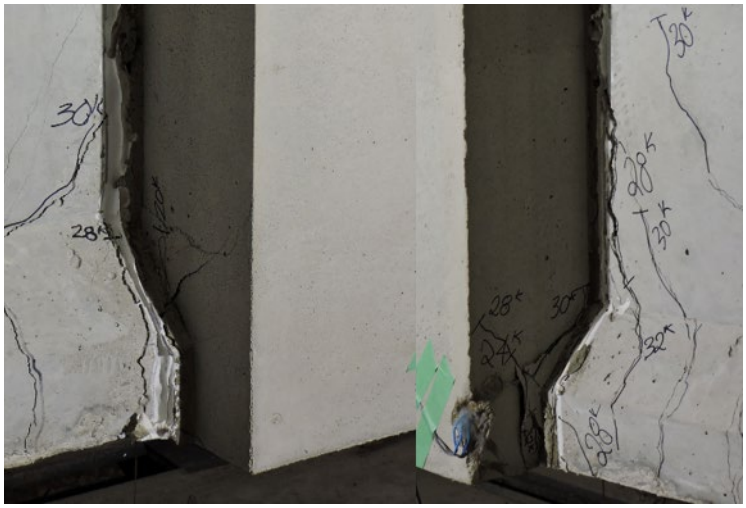

Figure 4.110. Specimen R1-FRSCC girder-joint interface cracking on the front left (left) and front right (right)

Figure 4.111. Deflected shape of specimen R1-FRSCC after testing

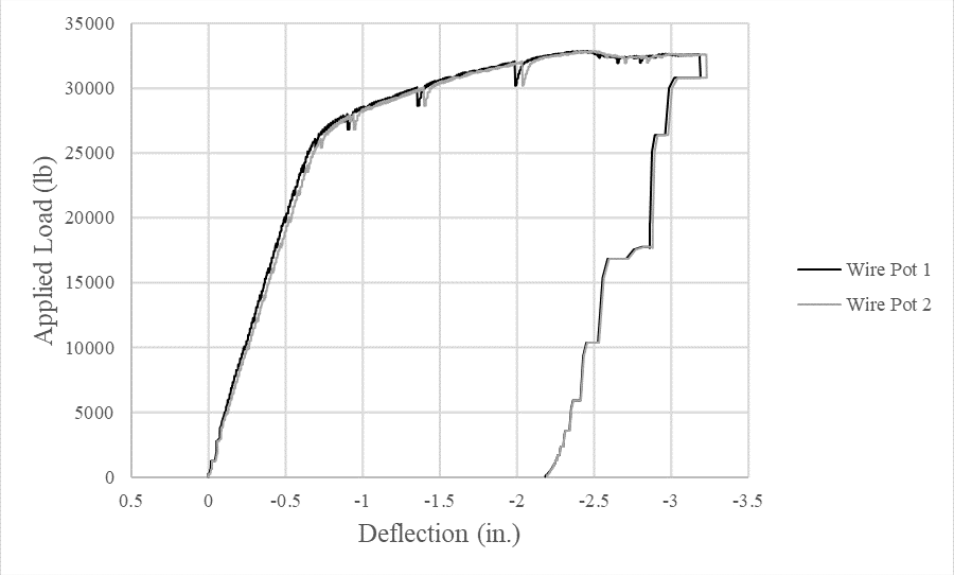

Figure 4.112. Specimen R1-FRSCC load-deflection curve

The repair reinforcement bars did not yield but did undergo tension strain with a maximum value of 0.00041 in./in. This may be due to the original hooked longitudinal reinforcement still taking significant load. The inner and outer deck reinforcement had maximum compression strains of -0.00021 in./in. and -0.00131 in./in., respectively. After this point, both bars began to decompress and eventually go into tension as the load increased. A possible reason for this may be due to the compression zone of the girder-joint-girder specimen rising above the deck reinforcement as loading increased beyond the linear-elastic range. Load-strain curves for specimen R1-FRSCC's steel reinforcement are shown in Figure 4.113. The load-strain curves have been truncated for ease of interpretation.

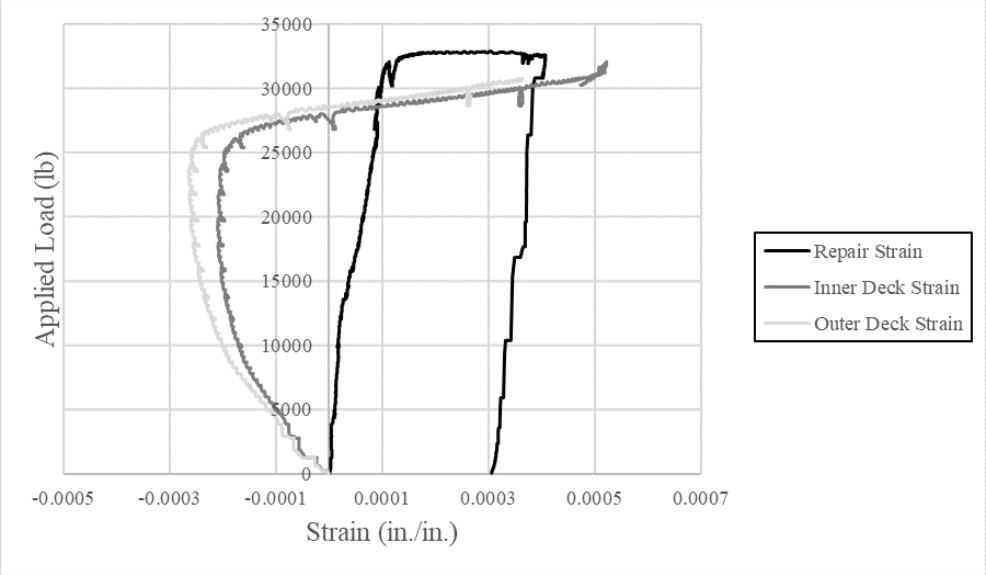

Figure 4.113. Specimen R1-FRSCC load-strain curve

4.9.3.2 Repair Specimen R2-FRSCC Results

Specimen R2-FRSCC was tested to failure in negative moment bending. Shear cracking and flexural cracking were observed during testing on the girder webs and either side of the of the repaired continuity joint, respectively, and are shown in Figure 4.114.

Figure 4.114. Specimen R2-FRSCC shear and flexural cracking

Significant flexural cracking was observed on all four transverse faces of the continuity joint. These cracks also extended onto the longitudinal faces of the continuity joint and can be seen in Figure 4.115 and 4.116. Additional longitudinal face cracks and

a substantial amount of flexural cracking within the deck can also be seen. Figure 4.117 shows the overall girder-joint-girder repair specimen after testing.

Figure 4.115. Specimen R2-FRSCC joint cracking on longitudinal and transverse faces from the front left (left) and front right (right)

Figure 4.116. Specimen R2-FRSCC joint cracking on longitudinal and transverse faces from the back left (left) and back right (right)

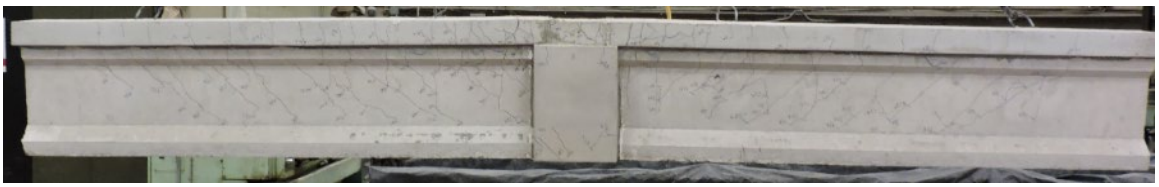

Figure 4.117. Deflected shape of specimen R2-FRSCC after testing

Specimen R2-FRSCC exhibited ductile behavior after 33.4 kips of load were applied and had an ultimate load capacity of 46.0 kips. At the ultimate load, specimen R2-FRSCC exhibited an average deflection of 2.75 in. Figure 4.118 shows the load-deflection curve for specimen R2-FRSCC, which is very typical of a beam flexural failure.

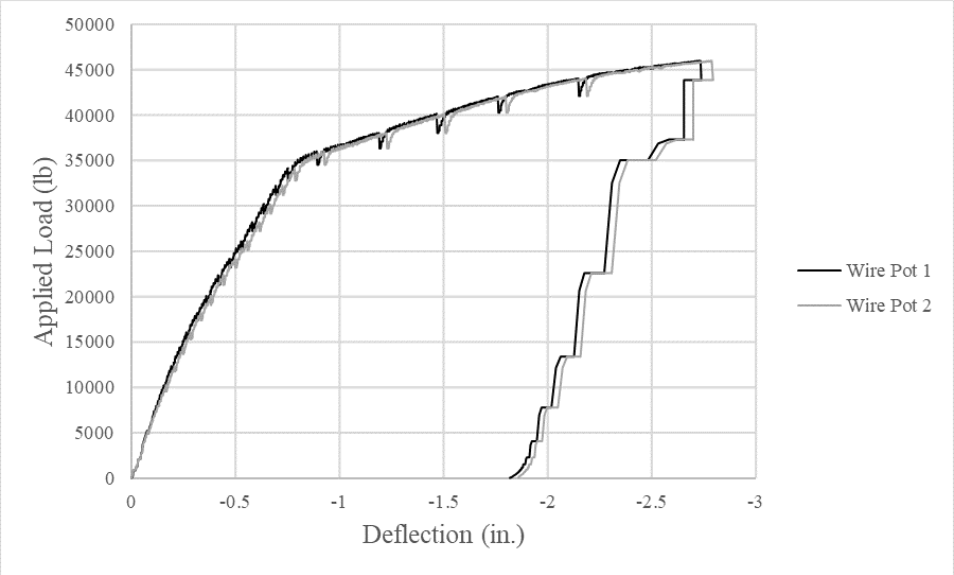

Figure 4.118. Specimen R2-FRSCC load-deflection curve

The repair reinforcement underwent compression strain and had a maximum strain of -0.000107 in/in. The outer longitudinal reinforcement in the deck began to yield at a loading of 29.3 kips. The inner longitudinal reinforcement in the deck began to yield at a loading of 29.6 kips. Figure 4.119 shows a plot of the load-strain curves for repair specimen R2-FRSCC. The load-strain curves have been truncated for ease of interpretation.

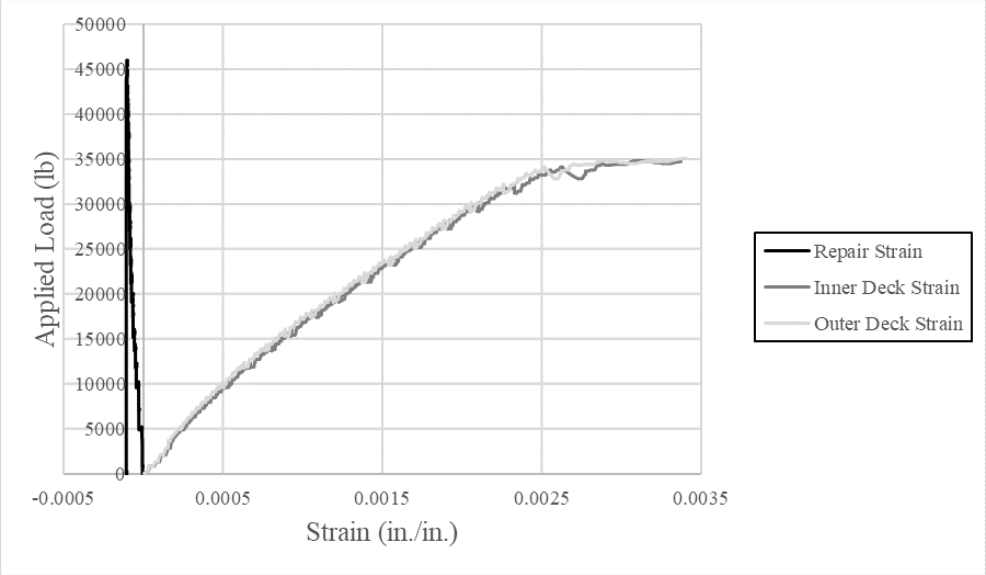

Figure 4.119. Specimen R2-FRSCC load-strain curve

4.9.3.3 Repair Specimen R3-FRSCC Results

Specimen R3-FRSCC was tested to failure in negative moment bending. Shear cracking and flexural cracking were observed during testing on the girder webs and either side of the of the repaired continuity joint, respectively, and are shown in Figure 4.120.

Figure 4.120. Specimen R3-FRSCC shear and flexural cracking

Significant flexural cracking was observed on all four transverse faces of the continuity joint. These cracks also extended onto the longitudinal faces of the continuity joint and can be seen in Figure 4.121 and Figure 4.122. Additional longitudinal face cracks and a substantial amount of flexural cracking within the deck can also be seen. A

considerable crack formed within the deck, just outside of the continuity joint, and continuously widened throughout the loading process. This crack propagated upward and into the joint which can be seen in Figure 4.123. Unfortunately, a photograph of the girder-joint-girder repair specimen's deflected shape was not taken after testing.

Figure 4.121. Specimen R3-FRSCC joint cracking on the longitudinal and transverse faces from the front left (left) and front right (right)

Figure 4.122. Specimen R3-FRSCC joint cracking on the longitudinal and transverse faces from the back left

Figure 4.123. Specimen R3-FRSCC deck cracking

Specimen R3-FRSCC exhibited ductile behavior after 34.7 kips of load were applied and had an ultimate load capacity of 46.0 kips. At the ultimate load, specimen R3-FRSCC exhibited an average deflection of 2.81 in. Figure 4.124 shows the load-deflection curve for specimen R3-FRSCC, which is typical of a beam flexural failure.

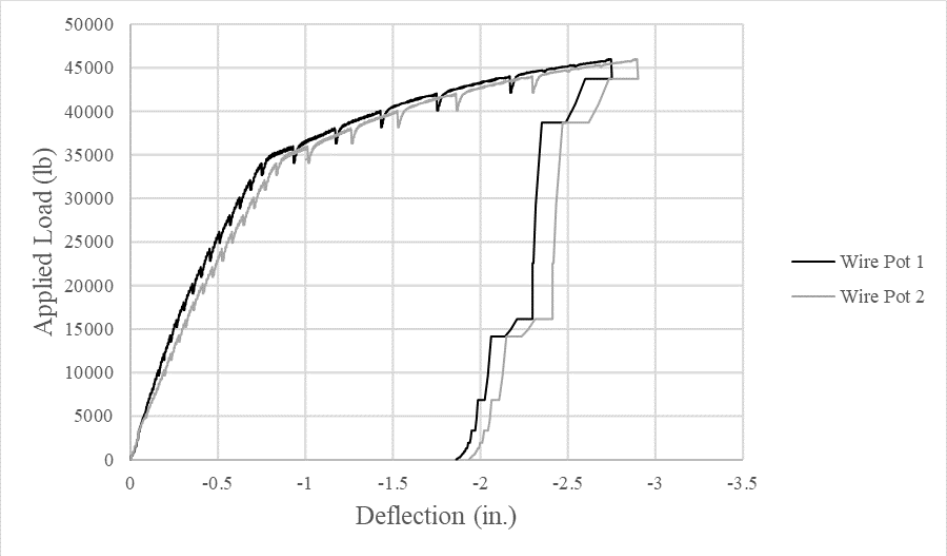

Figure 4.124. Specimen R3-FRSCC load-deflection curve

The outer longitudinal reinforcement in the deck began to yield at a loading of 28.3 kips. The inner longitudinal reinforcement in the deck began to yield at a loading of 28.7 kips. The repair reinforcement did not yield and had a maximum compression strain of -0.000101 in./in. At 31.7 kips, the repair reinforcement went into tension. A

possible reason for this may be due to the compression zone of the girder-joint-girder specimen rising above the repair reinforcement as loading increased beyond the linear-elastic range. Figure 4.125 shows a plot of the load-strain curves for repair specimen R3-FRSCC. The load-strain curves have been truncated for ease of interpretation.

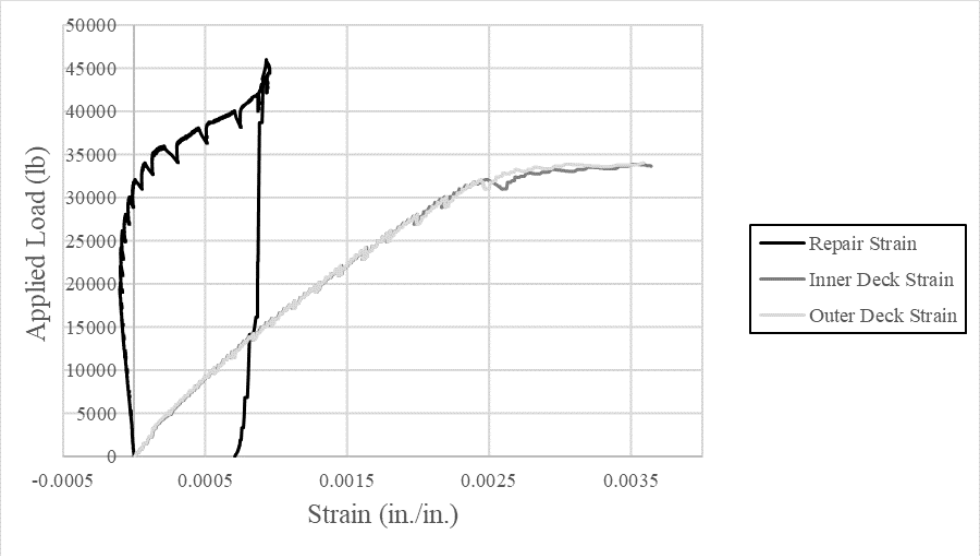

Figure 4.125. Specimen R3-FRSCC load-strain curves

4.9.4 Phoscrete® Repair Results

4.9.4.1 Repair Specimen R1-PHOS Results

Specimen R1-PHOS was tested to failure in positive moment bending. Shear cracking and flexural cracking were observed during testing on the girder webs and either side of the of the repaired continuity joint, respectively, and are shown in Figure 4.126.

Figure 4.126. Specimen R1-PHOS shear and flexural cracking

There were no noticeable cracks on the longitudinal face of either side of the repair joint. Flexural cracking was observed on all four transverse faces of the continuity joint. None of these cracks appeared to have extended onto the longitudinal faces of the continuity joint as shown in Figure 4.127 and Figure 4.128. Significant cracking was observed within the bottom bell of the specimen at the location of the continuity joint. The two original half-girder specimens separated away from the joint under loading. The bottom of the original and repaired continuity joint is shown in Figure 4.129.

Figure 4.127. Specimen R1-PHOS girder-joint interface and joint transverse face cracking from the front left (left) and front right (right)

Figure 4.128. Specimen R1-PHOS girder-joint interface and joint transverse face cracking from the back left (left) and back right (right)

Figure 4.129. Specimen R1-PHOS girder-joint separation

Figure 4.130 shows the overall girder-joint-girder repair specimen after testing. The failed specimen appears to consist of three separate members – each half girder and the continuity joint.

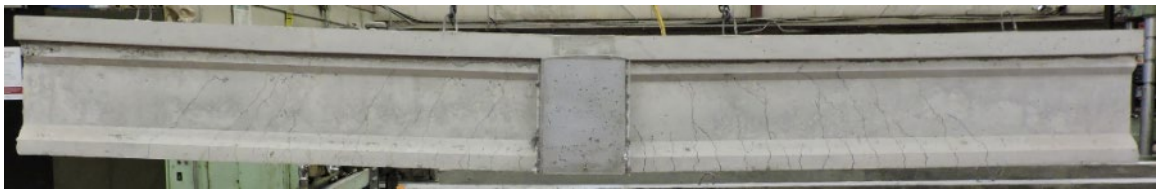

Figure 4.130. Deflected shape of specimen R1-PHOS

Specimen R1-PHOS exhibited ductile behavior after 17.2 kips of load were applied and had an ultimate load capacity of 23.4 kips. At the ultimate load specimen R1-PHOS exhibited an average deflection of 1.70 in. Figure 4.131 shows the load-deflection curve for specimen R1-PHOS, which is fairly typical of a beam flexural failure although the plateau is not as flat as normally observed.

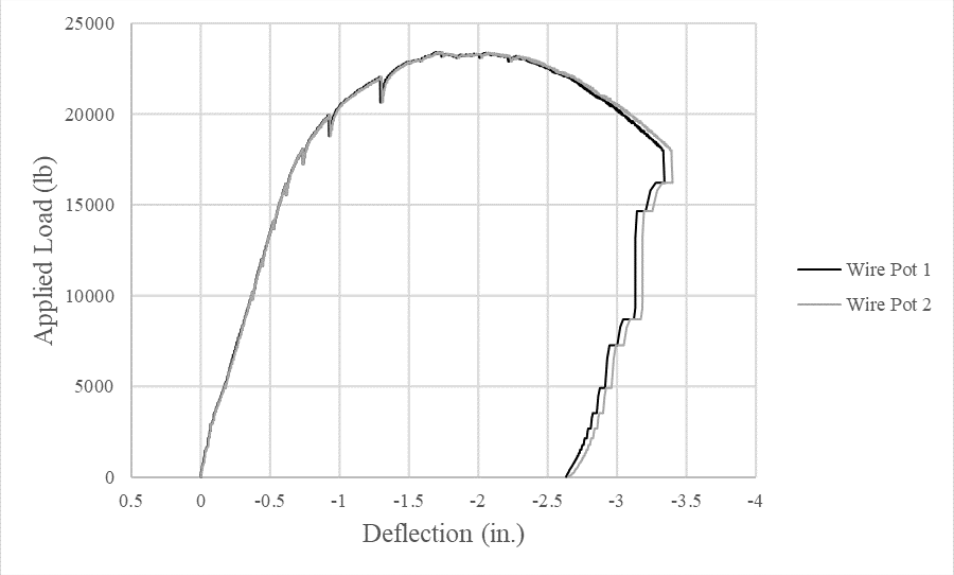

Figure 4.131. Specimen R1-PHOS load-deflection curve

The repair reinforcing bars had minimal strain under loading with a maximum value of 0.000999 in./in. This may be due to the original hooked longitudinal reinforcement still taking significant load. The inner and outer deck reinforcement initially underwent compression strain. After roughly 13.9 kips of load were applied, both bars went into tension and continued to strain as the load increased. The outer deck reinforcement yielded in tension at a loading of 20.0 kips. The inner deck reinforcement yielded in tension at a loading of 19.9 kips. Both the inner and outer deck reinforcement yielded after the ultimate load was achieved and while the girder-joint-girder specimen was allowed to deflect with additional load applied. A possible reason for the bars yielding in tension may be due to the compression zone of the girder-joint-girder specimen rising above the deck reinforcement as loading increased beyond the linear-elastic range. Load-strain curves for the steel reinforcement in specimen R1-PHOS are shown in Figure 4.132.

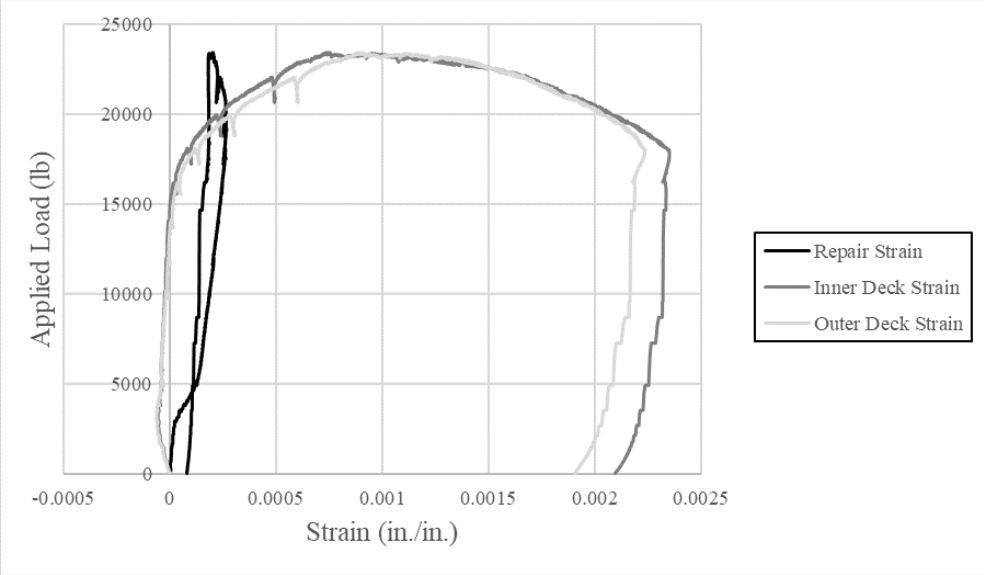

Figure 4.132. Specimen R1-PHOS load-strain curves

4.9.4.2 Repair Specimen R2-PHOS Results

Specimen R2-PHOS was tested to failure in negative moment bending. Shear cracking and flexural cracking were observed during testing on the girder webs and either side of the repaired continuity joint, respectively, and are shown in Figure 4.133.

Figure 4.133. Specimen R2-PHOS shear and flexural cracking

Flexural cracking was observed on all four transverse faces of the continuity joint. Many of these cracks also extended onto the longitudinal faces of the continuity joint and can be seen in Figure 4.134 and Figure 4.135. Additional longitudinal face cracks can also be seen. Flexural cracking extending across the deck is shown in Figure 4.136. Figure 4.137 shows the overall girder-joint-girder repair specimen after testing.

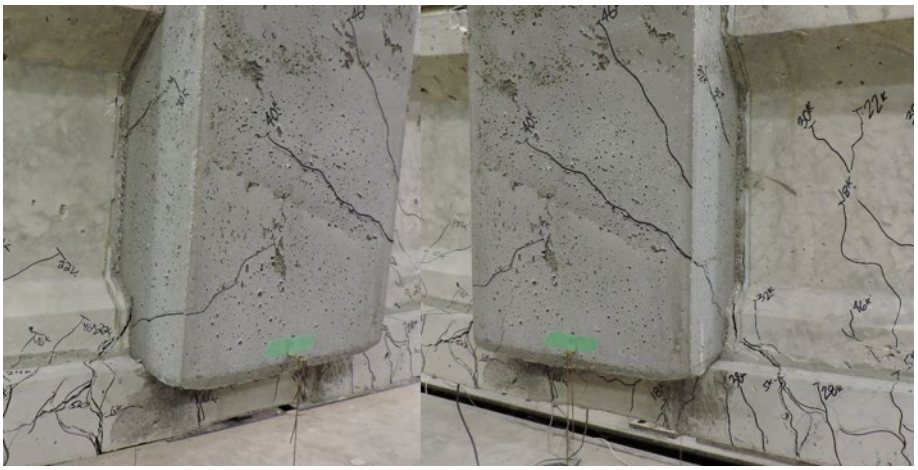

Figure 4.134. Specimen R2-PHOS joint cracking on the longitudinal and transverse faces from the front left (left) and front right (right)

Figure 4.135. Specimen R2-PHOS joint cracking on the longitudinal and transverse faces from the back right

Figure 4.136. Specimen R2-PHOS deck cracking

Figure 4.137. Deflected shape of specimen R2-PHOS after testing

Specimen R2-PHOS exhibited ductile behavior after 32.5 kips of load were applied and had an ultimate load capacity of 46.0 kips. At the ultimate load, specimen R2-PHOS exhibited an average deflection of 2.80 in. Figure 4.138 shows the load-deflection curve for specimen R2-PHOS, which is very typical of a beam flexural failure.

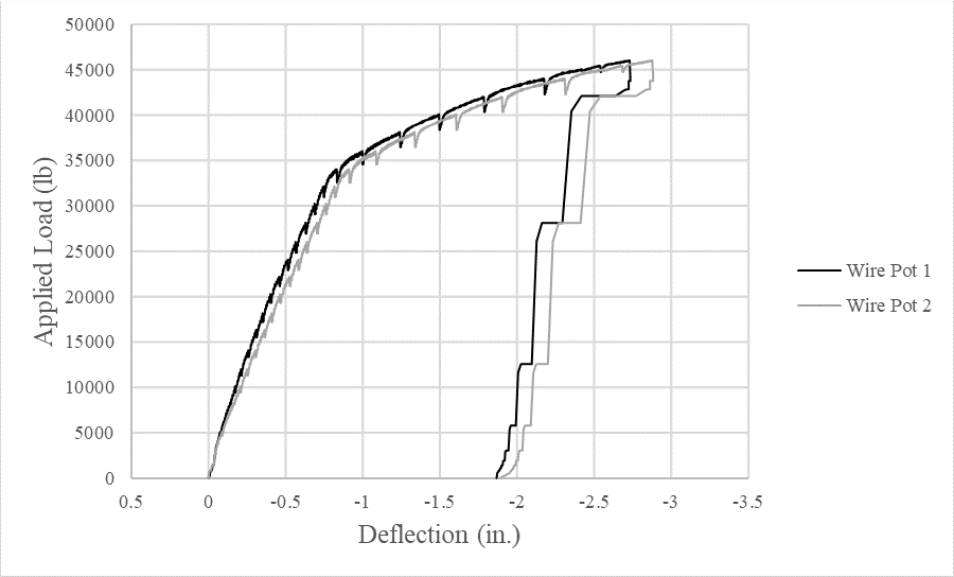

Figure 4.138. Specimen R2-PHOS load-deflection curve

The inner longitudinal reinforcement in the deck of specimen R2-PHOS began to yield at a loading of 27.8 kips. The strain gauge on the outer deck reinforcement lost signal during the loading process. The repair reinforcement strained in compression until a loading of 33.8 kips. At this loading, the repair bars began exhibiting tension strain until the ultimate load was achieved. A possible reason for this may be due to the compression zone of the girder-joint-girder specimen rising above the repair reinforcement as loading increased beyond the linear-elastic range. Figure 4.139 shows a plot of the load-strain curves for repair specimen R2-PHOS. The load-strain curves have been truncated for ease of interpretation.

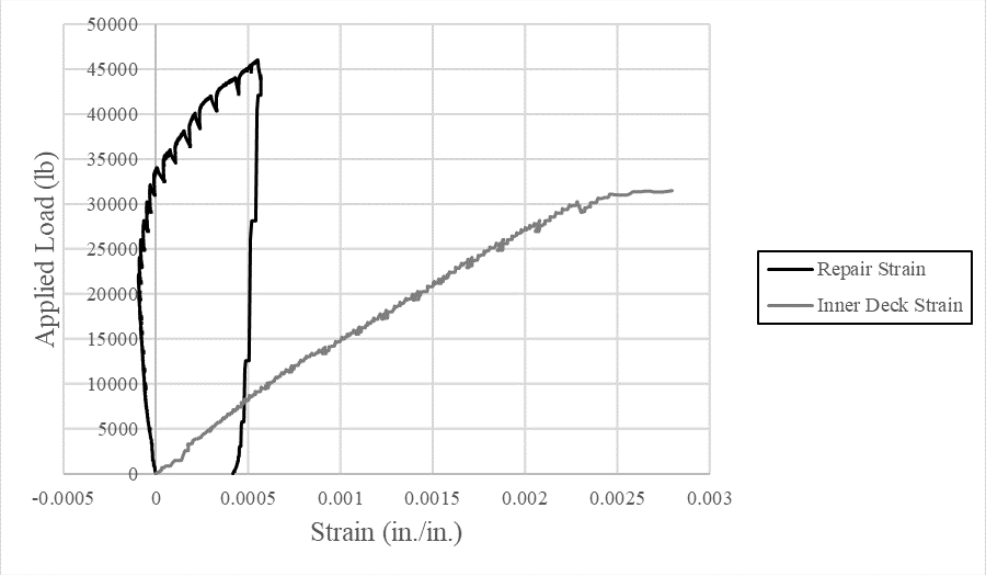

Figure 4.139. Specimen R2-PHOS load-strain curves

4.9.4.3 Repair Specimen R3-PHOS Results

Specimen R3-PHOS was tested to failure in negative moment bending. Shear cracking and flexural cracking were observed during testing on the girder webs and either side of the repaired continuity joint, respectively, and are shown in Figure 4.140.

Figure 4.140. Specimen R3-PHOS shear and flexural cracking

Limited flexural cracking was observed on the longitudinal and transverse faces of the repaired continuity joint. The only considerable crack at the girder-joint interface was on the front left and is shown in Figure 4.141. This crack initiated at the deck, propagated upward and across the joint's transverse face, and terminated on the longitudinal face of the joint around a loading of 46 kips. Flexural cracking of the other transverse faces of the joint are shown in Figure 4.139 and Figure 4.142. Flexural cracking extending across the deck is shown in Figure 4.143 and Figure 4.144 shows the overall girder-joint-girder repair specimen after testing.

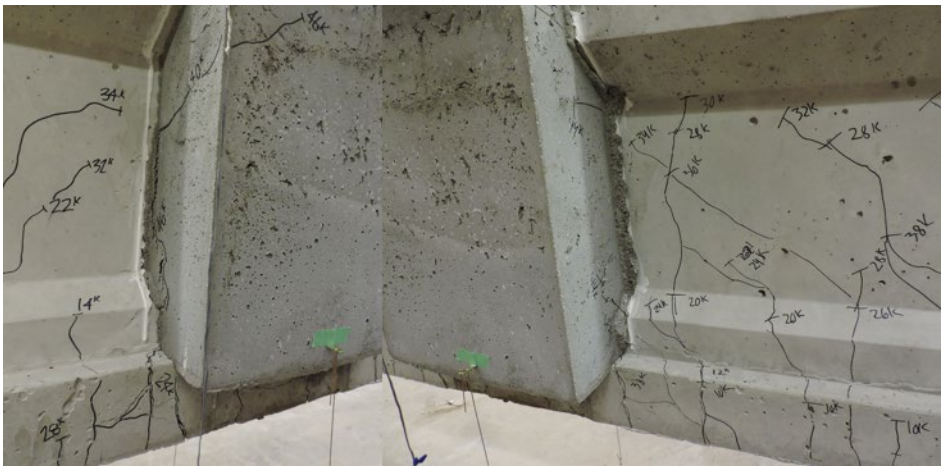

Figure 4.141. Specimen R3-PHOS girder-joint interface and joint transverse face cracking from the front left (left) and front right (right)

Figure 4.142. Specimen R3-PHOS joint transverse face cracking from the back left (left) and back right (right)

Figure 4.143. Specimen R3-PHOS deck cracking

Figure 4.144. Deflected shape of specimen R3-PHOS after testing

Specimen R3-PHOS exhibited ductile behavior after 34.7 kips of load were applied and had an ultimate load capacity of 46.1 kips. At the ultimate load, specimen R3-PHOS exhibited an average deflection of 2.07 in. Figure 4.145 shows the load-deflection curve for specimen R3-PHOS, which is very typical for a beam flexural failure.

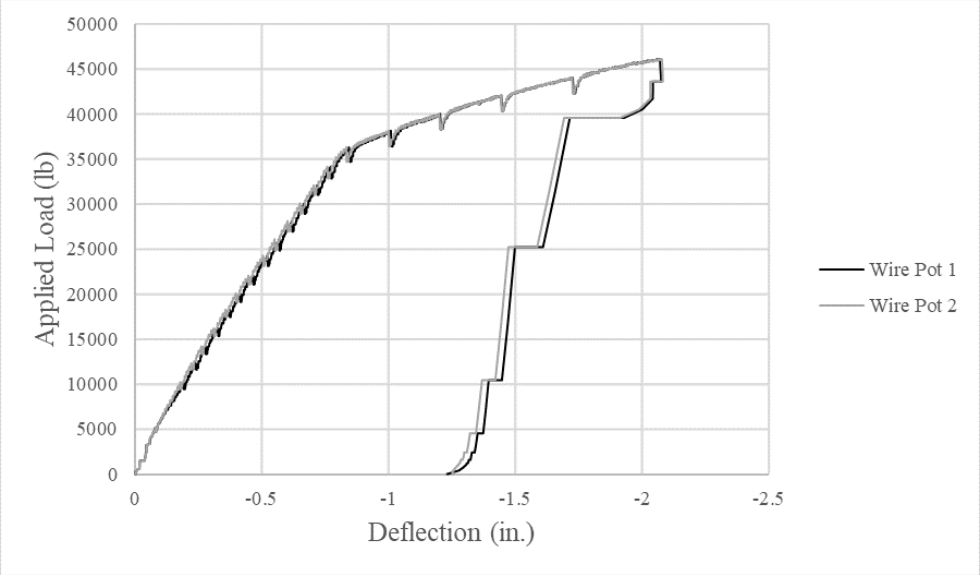

Figure 4.145. Specimen R3-PHOS load-deflection curve

The inner longitudinal reinforcement in the deck of specimen R3-PHOS began to yield at a loading of 26.4 kips. The outer deck reinforcement began to yield at a loading of 27.4 kips. The repair reinforcement strained in compression until a loading of 43.2 kips. At this loading, the repair bars began straining in tension until the ultimate load was achieved. A possible reason for this may be due to the compression zone of the girder-joint-girder specimen rising above the repair reinforcement as loading increased beyond the linear-elastic range. Figure 4.146 shows a plot of the load-strain curves for repair specimen R3-PHOS. The load-strain curves have been truncated for ease of interpretation.

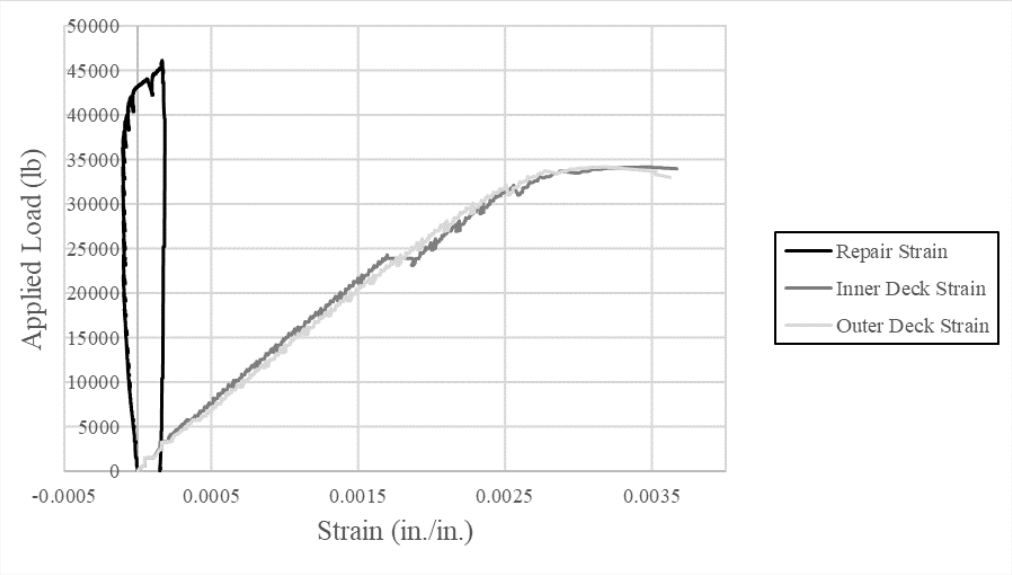

Figure 4.146. Specimen R3-PHOS load-strain curves

4.10 Summary of Results

4.10.1 Positive Moment Testing of R1-J3, R1-FRSCC, and R1-PHOS

The initial cracking loads and positive moment test results for the repair group are summarized in Table 4.9 and Table 4.10, respectively. All three specimens had an induced moment greater than the theoretical nominal moment capacity during the initial cracking phase. Ultimate flexural capacity for repaired specimens R1-J3 and R1-FRSCC far exceeded both the initial cracking moment and the theoretical moment capacity. Ultimate flexural capacity for repaired specimen R1-PHOS was 93% of its initial cracking moment but still exceeded the theoretical moment capacity.

Table 4.9. Initial cracking results for positive moment repair specimens

Specimen	Load Applied (lb)	Moment (k-ft)
R1-J3	22,987	108.2
R1-FRSCC	27,520	129.6
R1-PHOS	25,200	118.6

Table 4.10. Repair group positive moment bending results

Specimen	Ductile Behavior Load (lb)	Ultimate Load (lb)	Deflection at Ultimate (in.)	Ductile Moment (k-ft)	Ultimate Moment (k-ft)
R1-J3	23,466	34,785	3.73	110.5	163.8
R1-FRSCC	25,606	32,889	2.48	120.6	154.9
R1-PHOS	17,226	23,421	1.70	81.1	110.3

A summary of load-deflection curves for each positive moment repair specimen is shown in Figure 4.147. It is apparent that the ultimate load after repairing specimen R1-PHOS was significantly less, roughly 30%, than that of R1-J3 and R1-FRSCC. This is particularly interesting as the initial cracking load of R1-PHOS was near the average of the three specimens' initial cracking loads.

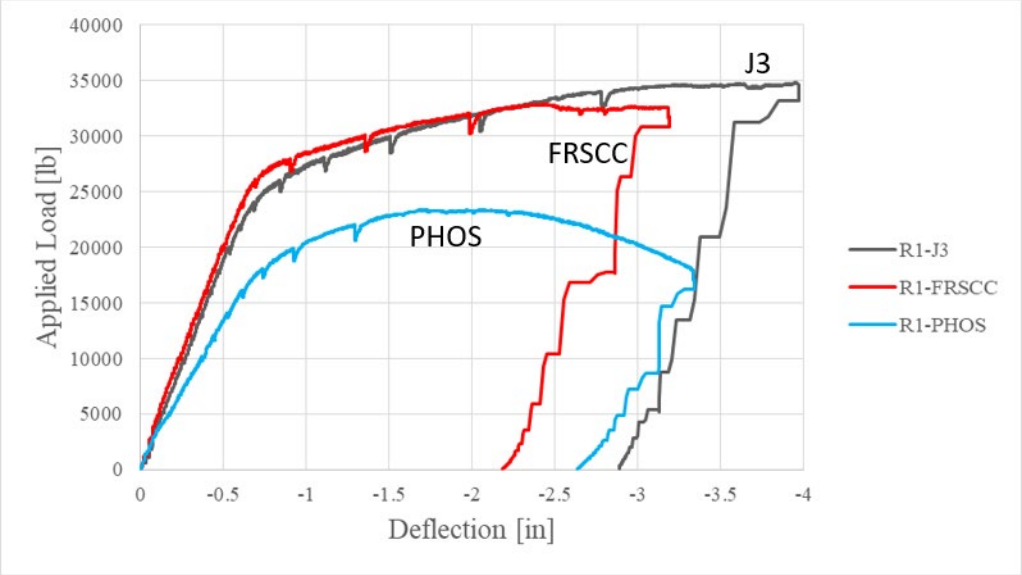

Figure 4.147. Summary of positive moment repair specimen load-deflection curves

The following specific observations can be made for the positive moment tests of the repaired specimens:

- All positive moment repairs restored full flexural capacity when compared to the theoretical nominal moment strength of 107.6 ft-k.
- The repair reinforcement in specimens R1-J3, R1-FRSCC, and R1-PHOS did not yield under loading of a positive moment flexural failure.

- Deck reinforcement in all positive moment repair specimens initially strained in compression, followed by tension strain.
- The deck reinforcement for specimen R1-PHOS was the only reinforcement to yield, which was in tension.
- No signs of any cracking on the longitudinal faces of the positive moment repair specimens were observed.
- Specimen R1-J3 had the least amount of girder-joint interface cracking, while specimen R1-PHOS had the most.
- Specimens R1-FRSCC and R1-PHOS both had significant transverse face joint cracking.
- All positive moment repair specimens' deflected shapes after testing appear to consist of three separate segments – each half girder and the continuity joint.

4.10.2 Negative Moment Testing of Repaired Specimens

The negative moment test results for the repair group and the control group are summarized in Table 4.11 and Table 4.12, respectively. The ultimate moment for all repairs exceeded the ultimate moment of the control group, demonstrating that the flexural capacity had been fully restored following the repair procedures.

Table 4.11. Repair Group Negative Bending Results

Specimen	Ductile Behavior Load (lb)	Ultimate Load (lb)	Deflection at Ultimate (in.)	Ductile Moment (k-ft)	Ultimate Moment (k-ft)
R2-J3	33,426	46,024	3.65	157.4	216.7
R3-J3	33,446	46,001	3.48	157.5	216.6
R2-FRSCC	33,393	46,006	2.75	157.2	216.6
R3-FRSCC	34,698	46,008	2.81	163.4	216.6
R2-PHOS	32,507	46,037	2.80	153.1	216.8
R3-PHOS	34,742	46,130	2.07	163.6	217.2

Table 4.12. Control group negative moment bending results

Specimen	Ductile Behavior Load (lb)	Ultimate Load (lb)	Deflection (in.)	Ductile Moment (k-ft)	Ultimate Moment (k-ft)
C1	33,086	44,601	2.28	155.8	210.0
C2	33,171	44,620	2.40	156.2	210.1
C3	32,223	41,525	2.16	151.7	195.5

Summaries of the load-deflection curves for each negative moment repair specimen and the control specimens are shown in Figure 4.148 and Figure 4.149, respectively. The repair specimens showed almost identical behavior to the control specimens throughout the range of loading. All repair specimens exceeded the ultimate deflections of the control specimens, with the exception of specimen R3-PHOS, which had a deflection of 2.07 in.

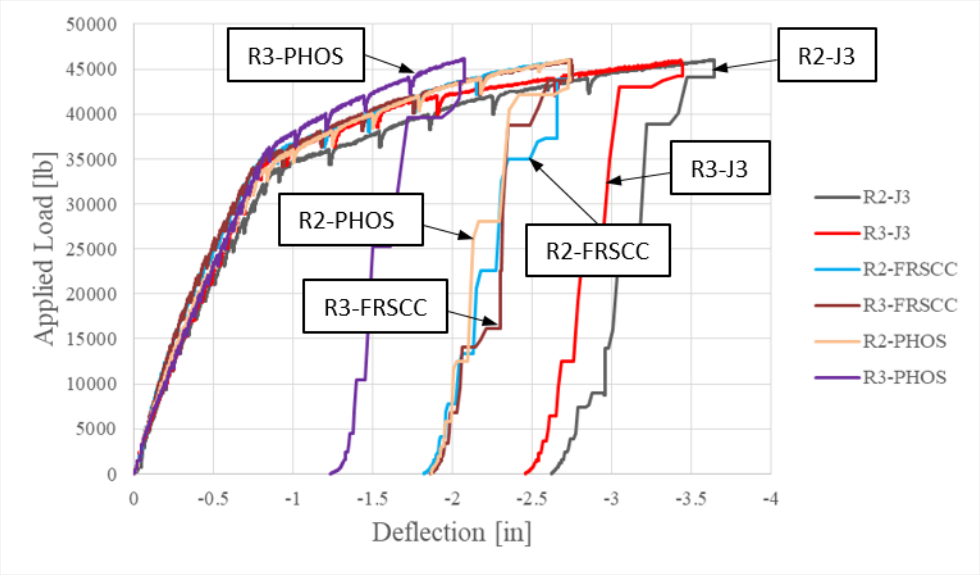

Figure 4.148. Summary of negative moment repair specimen load-deflection curves

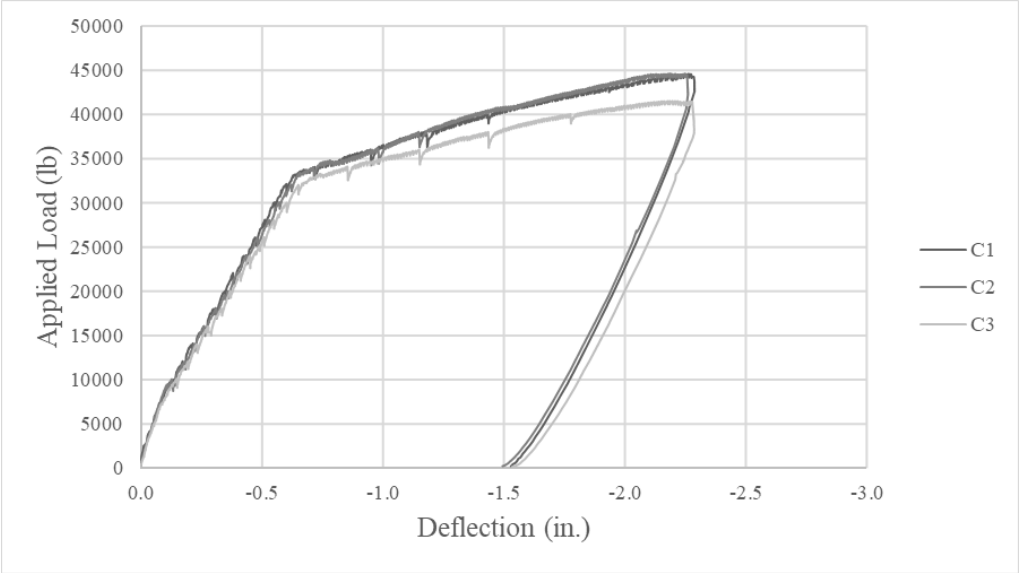

Figure 4.149. Summary of negative moment control group load-deflection cures

All six repair specimens had a positive moment induced within 12.3% of the theoretical calculated nominal moment, 107.6 ft-k, during the initial cracking. Table 4.13 gives a summary of results of the initial cracking of the negative moment repair specimens.

Table 4.13. Initial cracking results for negative moment repair specimens

Specimen	Load Applied (lb)	Moment (k-ft)
R2-J3	23,020	108.4
R3-J3	20,060	94.4
R2-FRSCC	21,430	100.9
R3-FRSCC	21,415	100.8
R2-PHOS	24,720	116.4
R3-PHOS	25,180	118.6

The following specific observations can be made for the negative moment tests of the repaired specimens:

- All negative moment repairs restored full moment capacity when compared to the theoretical calculated nominal moment, 152.4 ft-k.
- All repair reinforcement strain gauge data shows initial compression straining, followed by tension straining. No repair reinforcement yielded.

- Deck reinforcement in all negative moment repair specimens yielded.
- All specimens showed substantial flexural cracking spanning across the deck in the region of the continuity joint.
- The FRSCC specimens showed the greatest amount of flexural cracking on both the longitudinal and transverse faces of the joint of any group. The FRSCC specimens also showed significant girder-joint-girder interface separation.
- The J3 specimens showed no sign of flexural cracking on their longitudinal joint faces and a limited amount on the transverse faces. The J3 specimens also showed significant girder-joint-girder interface separation.
- The PHOS specimens showed limited cracking on the longitudinal and transverse joint faces and at the girder-joint-girder interface.

5.0 Beam End Region Repairs

5.1 Overview

Six prestressed beam specimens with the same design as those used for the continuity connections described in Section 4 were cast for testing end region repair behavior. The beams were loaded at one end using a single load point to produce shear cracking and bond failure to simulate the effects of end region deterioration in the field. After initial testing, the ends of the beam with induced damage were roughened and then repaired using an encapsulation repair with UHPC, FR-SCC, or MALP concrete. The thickness of the repair differed for the UHPC, but the same thickness was used for FR-SCC and MALP. Otherwise, the same dimensions were used for all repairs. Each repaired beam end was then subjected to a single point load shear test identical to the control test. Results of the repaired end tests were then compared to the original test to determine the contribution of the repair to beam strength for these two situations.

5.2 Girder Specimen Construction

5.2.1 Specimen Design

At this stage, the cross-sectional geometry, dimensions, strength, and material type were determined to provide the best representation of actual bridge girders. The SCC mix design used was take from previous work at OU (Mayhorn 2016) with the expectation to provide a minimum compressive strength of 4000 psi within the first 24 hours after casting for the prestress release and 8000 psi after 28 days.

Dimensions of the beam specimen including the composite deck section are shown in Figure 5.1. These dimensions are based on an approximately half-scale AASHTO Type II girder and a deck section that provides the same moment capacity as the full half-scale deck. Two grade 270 low relaxation strands having 0.52 in. diameter (1/2 in. special) were placed centered 2 in. from the bottom of the bottom flange for applying prestressing force, as shown in Figure 5.2. During design, it was found that stress at the girder top at midspan exceeded the tension limits given by ACI 318-19 section 24.5.3 at prestress release. To counter that and satisfy the code requirements, two No. 5, grade 60 reinforcing bars were provided in the top flange of the beam, which

were designed to resist the tension force. For shear reinforcement, double No. 3 C-shaped stirrups were used along with four stirrups spacing intervals in the 18 ft length of the girder with extra projection at the top of the beam for deck placement as shown in Figure 5.2 and Figure 5.3.

The composite deck section had dimensions of 9 in. x 4.625 in. was made of ordinary ODOT Class AA bridge deck concrete supplied by a local ready-mix company and was cast after the beam concrete reached a minimum of 28 days of age. Therefore, the elastic prestress losses were calculated based on non-composite section properties, while long term losses were calculated for both before casting the deck and after deck to the testing day. Four No. 5, grade 60 reinforcing bars were placed in the deck to provide sufficient flexural strength and avoid shrinkage cracks.

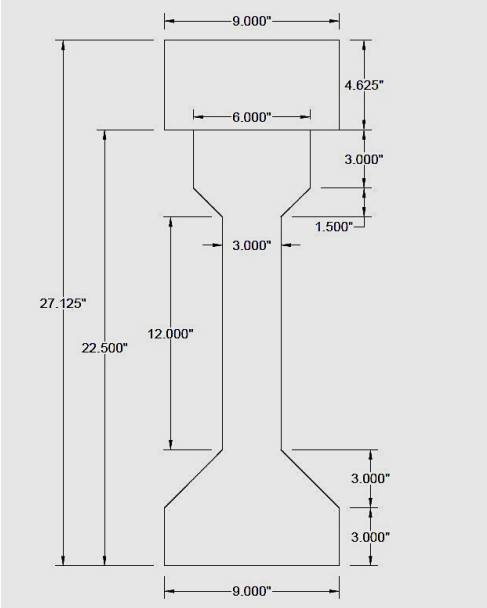

Figure 5.1. Prestressed beam specimen cross-section

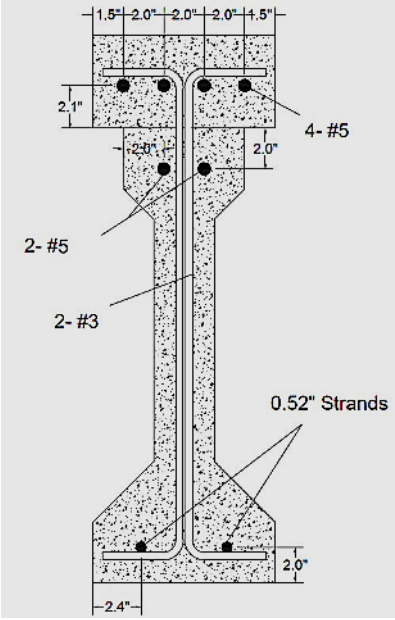

Figure 5.2. Prestressed beam specimen reinforcement details

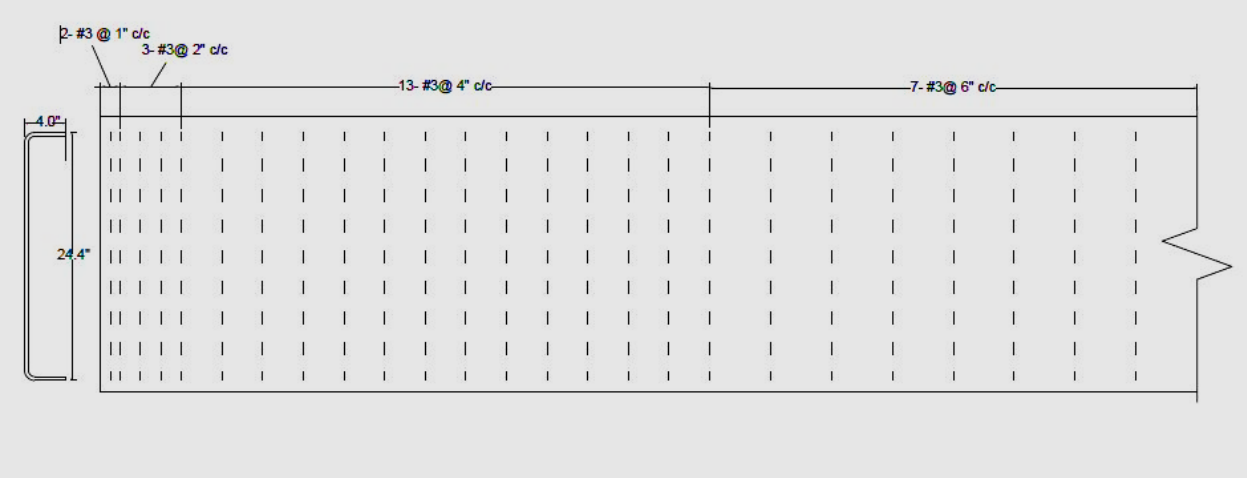

Figure 5.3. Stirrup spacing along the half length of the prestressed beam specimens

5.2.2 Beam Construction

All girders were cast at Fears Structural Engineering Lab on the OU campus using the available prestressing bed consisting of two steel abutments anchored to the strong floor. Due to space constraints from other testing, only one beam could be constructed at a time. Construction of the girders started with cutting and bending the shear stirrups. The stirrups were then tied to the top steel to create a reinforcement cage. After making the reinforcement cage, the prestressing bed was leveled and oiled

to avoid concrete sticking to the bed while hardening. Then the cage was placed on the prestressing bed, and the steel beam form was fixed on one side. At this stage, the prestressing strands were put in the cage and were carefully placed to avoid contact with the oiled bed. Figure 5.4 shows the prestressing bed after placement of the reinforcement cage and prestressing strands. The live end is defined as where the strands were pulled for tensioning and the dead end as where the strands are only anchored.

Figure 5.4. Panoramic picture of the prestressing setup

The strands were cut approximately 34 ft long to provide an extension beyond the prestressing bed at each end for the chucks to grip for proper application of pre-tensioning. Chucks were then placed on the strands at the abutments to hold the strands in place for tensioning, and strands were marked to measure their slip in the chucks when they were tensioned. Measurements were taken between the mark and the back of the chuck before and after tensioning. A 50-kip capacity through-hole load cell was attached to one of the strands between the chuck and abutment at the live end of the prestressing bed to show the instantaneous amount of applied load to the strands. The elongation of the strands was also noted using a ruler attached at the abutment with provision for chuck slip and strand sag to ensure the load cell was working properly and to avoid overstressing the strands. Strands were stressed to 75% of the ultimate strength of the strands (270 ksi) plus approximately 1.5% extra to count for minor anchor slip. The strain for applying the target stress ($0.75 \times f_{pu}$) in the strand is

0.7%, producing 3.5 in. to 4 in. elongation over the prestressing bed length. The strands were tensioned by applying a steady load to the large plate on the live end until the desired load was reached. The plate was then held in place using large nuts. After prestressing, the reinforcement cage was checked to make sure it had not moved during the application of the prestress and adjustments were made if required. Figure 5.5 shows the completed reinforcement cage after prestressing.

Figure 5.5. Reinforcement cage for a typical girder

Next, the other side of the steel form was put in place and concrete was cast. Concrete was mixed using a large horizontal shaft mixer at Fears Lab and was transported to the beam using a concrete transfer bucket. The SCC mix used for the beams was prepared in the proportion specified in Table 5.1. The coarse aggregate used for the mix was a 3/8 in. limestone aggregate and the fine aggregate was a washed concrete sand. The order used for mixing the components is as follows.

- Before adding the materials in the mixer, add half of the High Range Water Reducer (HRWR) to the water prepared for the batch.
- Wet the mixer.
- Add all the aggregate and sand in the mixer.
- Add half of the water prepared for the batch and mix it for at least 1 minute.
- Add the cement and gradually pour the remaining water evenly over the mixture.

- Add the remaining half of the HRWR.
- Mix all the materials for 2-5 minutes.
- Add additional HRWR if necessary to achieve desired flowability

Table 5.1. SCC Mix Design

Material	Quantity
Portland cement (Type I/II) (lb/yd^3)	851
Water (lb/yd^3)	315
Fine Aggregate (lb/yd^3)	1459
Coarse Aggregate (lb/yd^3)	1372
High Range Water Reducer (Glenium 7920)- (oz/cwt)	6

For each beam, nine 4 in. x 8 in. concrete cylinder specimens were prepared for compressive strength testing. Three of them were tested after twenty-four hours to determine the concrete release strength, f'_{ci}, and to ensure that the strength was high enough for prestress release. Three more were tested for the 28-day compressive strength, f'_c, and the final three were tested on the initial load test day. The slump flow values were also noted for each beam batch to make sure the mix had adequate workability for compaction requirements of the girders.

After 24 hours, almost all compression tests indicated an f'_{ci} higher than 4000 psi, which was deemed satisfactory, and the prestress force was transferred to the beam by loosening the nuts and allowing the hydraulic pressure to release gradually. Just before releasing the prestressing strands, the value of applied stress was noted based on the load cell readout, which later was used as the jacking force (f_j) in analysis calculations. The same work cycle described in the previous section was used for all six beams.

After 28 days, the formwork for deck placement was constructed, as shown in Figure 5.6. Based on the design, reinforcement was added to the deck and the deck sections were cast using ordinary ODOT Class AA concrete obtained from Dolese Bros. with a different compressive strength than the girders. After casting, the deck concrete was covered with plastic and regularly watered to ensure proper curing. Eighteen 4 in. by 8 in cylinders were cast from the deck concrete mix to determine compressive strength at 28 days and test day for each of the beams.

Figure 5.6. (a) Deck formwork and (b) deck concrete immediately after casting

5.3 Initial Shear Testing

Since the objective of this research was to repair shear damage, each girder was initially loaded to failure to provide induced shear damage for repair. Each 18 ft long girder was tested on a 17.5 ft simply supported span with a single point load applied using a load frame and hydraulic cylinder. The beam was supported on 6 in. neoprene bearing pads at each end. Before testing, the girders were analyzed to determine the location of the point load application that would cause shear failure prior to flexural failure. A point load 3.5 ft from the beam end was chosen for this loading. During each test, four linear voltage differential transformers (LVDTs) were attached to the exposed portion of each strand (two at each end) and used to measure the strand slip, which was used to determine if a bond failure contributed to the shear failure of each beam. Two wire potentiometers (pots) were used to measure the vertical deflection below the point load, and a load cell was used to record the applied loads. The load testing setup showing the sensors is presented in Figure 5.7. All sensors were connected to a single data acquisition system to collect the data. The beams were then loaded incrementally until the formation of shear cracks propagated from the bottom flange through the whole web and in some cases, even to the top flange. Cracks were marked on the beam at each load increment. With the formation of cracks, the strands' bond in the transfer zone was also reduced, causing the strands to slip and further increase the crack sizes.

The loading was stopped after achieving a noticeable deflection, significant strand slip, or a halt/drop in sustained load.

After removing the point load, tracing paper was used to document the cracks on both sides of the damaged end of each beam (Figure 5.8), which were superimposed to the repaired beams once tested to failure. This comparison was intended to develop a relation between the cracks of both the original member and repair material.

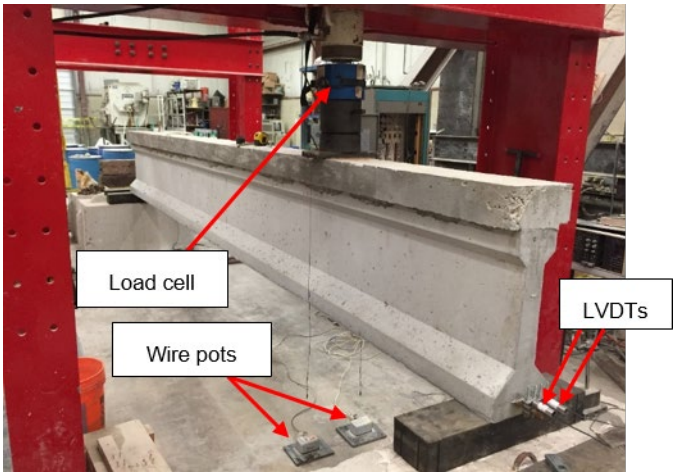

Figure 5.7. Uncracked girder arranged in the test setup

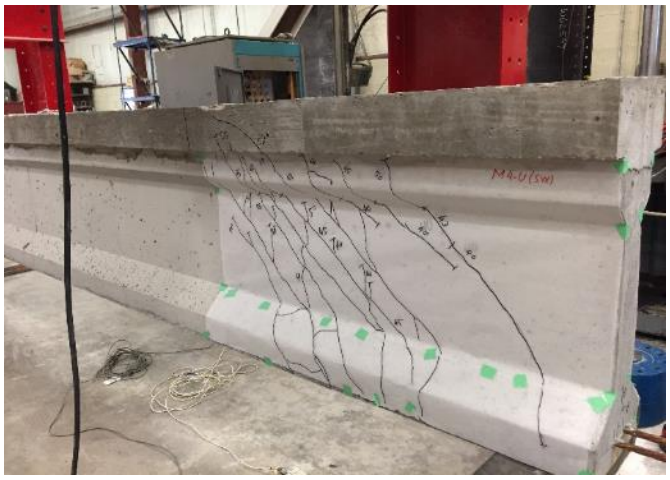

Figure 5.8. Tracing paper on one side of the cracked girder to copy the crack locations after testing

5.4 Girder Repair

5.4.1 Overview

After the girders were tested to induce damage, the damaged ends were repaired to restore the lost capacity using an encapsulation with UHPC, FR-SCC, or MALP concrete on the section between the beam end and the original load location (3.5 ft from the end). One of the main challenges for concrete repair materials is their bond with the parent structure. Two techniques were used to increase the bond between the girder and the repair material. First, the girder's surface throughout the 3.5 ft repair length was roughened using a grinding disk on an angle grinder. The roughened surface was then cleaned using compressed air to remove any dust from the surface.

Second, eighteen ¼ in. diameter and 3-1/4 in. length concrete anchors with 1.5 in. embedment in the web, as shown in the Figure 5.9(a), were used throughout the repair region to further increase the interlocking between the original member and the repair. The holes were first drilled using a masonry drill bit and hammer drill. The screws were then tightened in those holes using a drill with a screwdriver bit. The number of screws and their spacing was determined using the provisions for interface shear transfer of AASHTO LRFD (2017) Section 5.7.4.3 and considering concrete shear friction. The force demand was based on the shear force concentration in the 3.5 ft section of the girder end calculated using a strut and tie model and the load causing flexural failure. The total number of concrete anchors was distributed in an alternating pattern on both sides of the girder as shown in Figure 5.9(b) and (c) and Figure 5.10. The forms for the repair (Figure 5.11) were put in place creating a 3 in. projection from the vertical portion of the bottom flange on each side along the 3.5 ft repair length for the FR-SCC and MALP repairs and a 1.5 in. projection for the UHPC repair as shown in Figure 5.12. A 2 in. cover was also provided below the bottom of the bottom flange to depict protection of strands in the field against moisture ingress assuming cracks propagate to the bottom of the girder. After sealing the forms with silicone, the specimens for UHPC and FR-SCC were wetted using a spray bottle filled with water. No prewetting was used for the MALP material due to the nature of its chemical reaction. The repair material was then poured into the forms and was left to cure until it gained

sufficient strength. After 28 days, the repaired beams were tested with the same loading arrangement as the original girders, and the results compared with those from the undamaged beams.

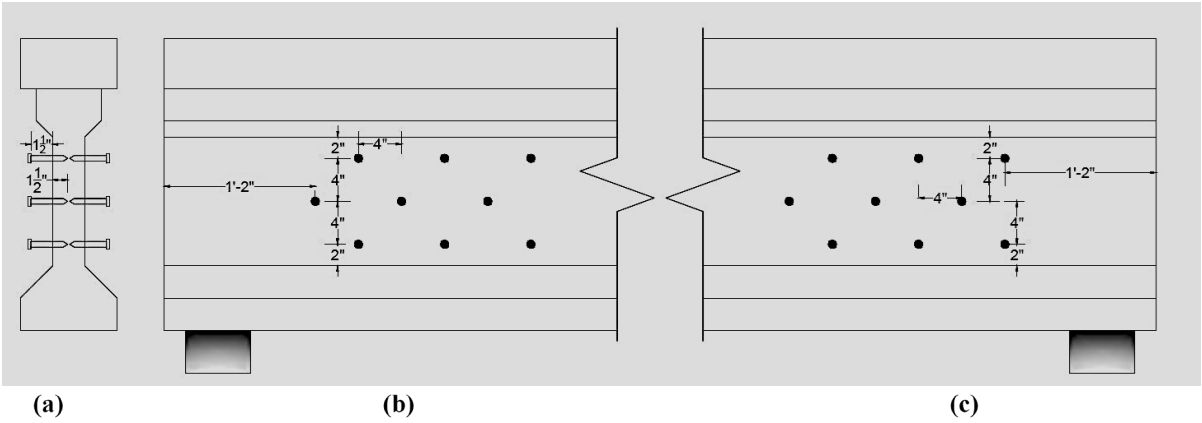

Figure 5.9. (a) Cross-sectional view of concrete anchor locations, (b) front face showing distribution of anchors, (c) back face showing distribution of anchors

Figure 5.10. Concrete anchors used for shear studs in the web of a girder specimen ready for repair

Figure 5.11. Repair formwork

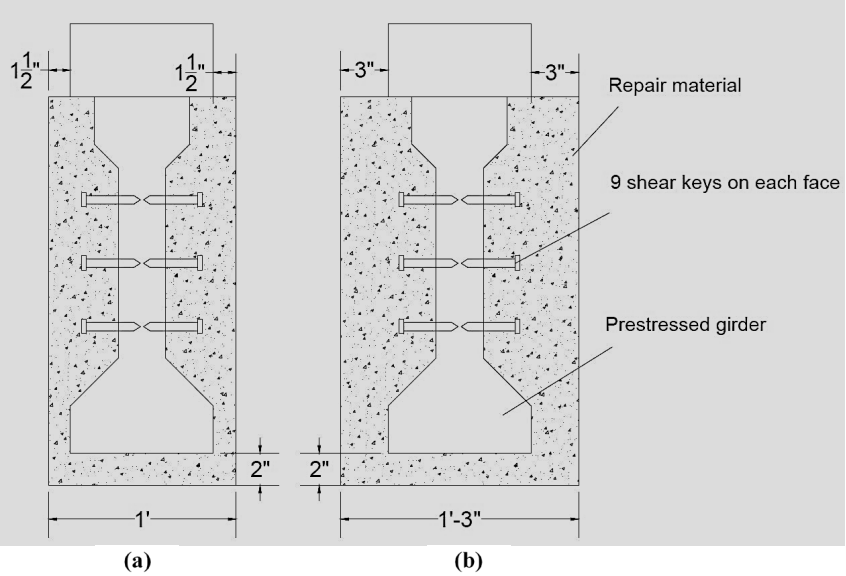

Figure 5.12. (a) Repair dimensions for UHPC and (b) repair dimensions for FR-SCC and MALP concrete

5.4.2 FR-SCC Repairs

FR-SCC is very sensitive to water content, therefore before the actual repair batch was mixed, several trial batches were performed to determine the mix design yielding the desired slump. Table 5.2 and Table 5.3 show the percentage of each material used for the FR-SCC mix and the quantities in the mix design, respectively.

Table 5.2. FR-SCC repair material expressed as percentage of components

Material	Amount
Cementitious Material (lb/yd^3)	750
Water/Cement Ratio	0.35
Fly Ash Percentage	30%
Komponent Percentage	15%
Fine Aggregate Percentage	50%
Design Air Content	6%
Design Slump Flow (in.)	28 ± 2
Master Builders Air Entrainer (AE-90) (fl oz/cwt)	1.1
Glenium 7920 (High Range Water Reducer) fl oz/cwt)	8.25
Required Strength (psi)	4000

Table 5.3. FR-SCC mix design

Material	Quantity (lb/yd^3)
Portland cement (Type I)	412.5
Fly Ash	225
Type K Cement (Komponent)	112.5
Coarse Aggregate (3/8 in. River Rock)	1276
Fine Aggregate	1441
Water	230
Polypropylene Fibers	7.70
Air Entrainer (Master Builders AE-90)	0.54
High Range Water Reducer (Glenium 7920)	4.02
Citric Acid	0.41

The FR-SCC material was mixed using the same mixer as for the continuity connection repairs. Key points for the mixing process of the FR-SCC repair are as follows:

- Add all the aggregates with half the water and mix for one minute.
- Add fly ash, cement, and Komponent in that order.
- Add HRWR and then the remaining water to get the desired flow.
- Add one full dose of citric acid along with the polypropylene fibers.
- Mix all the materials for 3 minutes, then allow materials to rest for 3 minutes, followed by 2 minutes of mixing.

- Keep the mixer turning until the repair casting is finished and add an additional full citric acid dose after every 15 minutes to retard the setting of cement. The dose can be reduced proportionally to the remaining concrete.

Once mixing was complete, the FR-SCC was transported to the forms using a concrete transfer bucket and overhead crane. The material was poured into one side of the forms and allowed to fill under the beam and up the opposite side without any external consolidation. Once one side of the formwork was filled the bucked was moved to the opposite side to top off the formwork. The repair was covered with plastic immediately after casting, then with wet burlap and plastic for 7 days. After 7 days, the formwork was removed, and the repairs allowed to cure in the laboratory environment until time of testing. Figure 5.13 shows the completed FR-SCC repairs.

Figure 5.13. (a) FR-SCC repair for beam M-2 and (b) FR-SCC repair for beam M-3

5.4.3 MALP Repairs

For preparing the MALP concrete, one bottle of the mono-aluminum-liquid phosphate activator was first poured into a plastic bucket. Then one bag of the pre-

packaged magnesium-alumino-aggregate dry powder was added and the two were mixed for 45-60 seconds with a drill mounted paddle provided by the MALP concrete manufacturer. The activators were kept in a cool place to slow down the chemical reaction after mixing and the setting time of the mixture. As soon as a batch was mixed it was placed in the forms and another batch was started immediately. The material was poured from one side until it had passed under the beam and started to fill the opposite side. Material placement was then alternated between the two sides of the form. This process was continued until the forms were filled.

MALP concrete hardens in few minutes after mixing, which generates a significant amount of heat and the material expands as shown in Figure 5.14(a). This expansion further increases the interlocking between the repair material and the girder and reduces the effect of shrinkage in the repair. Two different shipments of MALP concrete were used for the repairs. For the beam M-1 newly acquired activator and dry powder were used whereas for beam M-4 older (approximately 2 years old) MALP materials were used. The bags of dry material for the old MALP had lumps which could have been due to long term compaction under other bags or due to chemical reactions. Lumps were broken up using a rubber hammer before pouring the bag to the bucket. The workability of the old MALP material was better compared to the new material and the older material expanded slightly more than the new MALP after casting. The set time of the old MALP was also longer compared to the newly acquired material. It was also noted that the color of the activator for the old and new MALP repair materials were different, which could be a reason for the difference in physical and mechanical behavior of the mixture. The new MALP was more viscous and harder to mix. The completed MALP concrete repairs are shown in Figure 5.15. As can be seen from Figure 5.15 the texture of the repair is indicative of separate layers, which is due to hardening of lower layer while pouring the top one.

After the forms were removed it was noted that the repair cast with the old MALP had a better surface finish compared to the new material. Some construction defects were also noted, as shown in Figure 5.14 and Figure 5.15. These included lesser flow of the new MALP material to some portions of the bottom flange and slight honeycombing which was due to difficult mixing process and higher viscosity of the new MALP.

However, the web of the girder, which is responsible for resisting the shear force, was fully covered with repair materials having a smooth surface finish. The compressive strength of the new MALP was more than two times than that of the old material which can be due to age of the dry powder/activator or change in activator's composition.

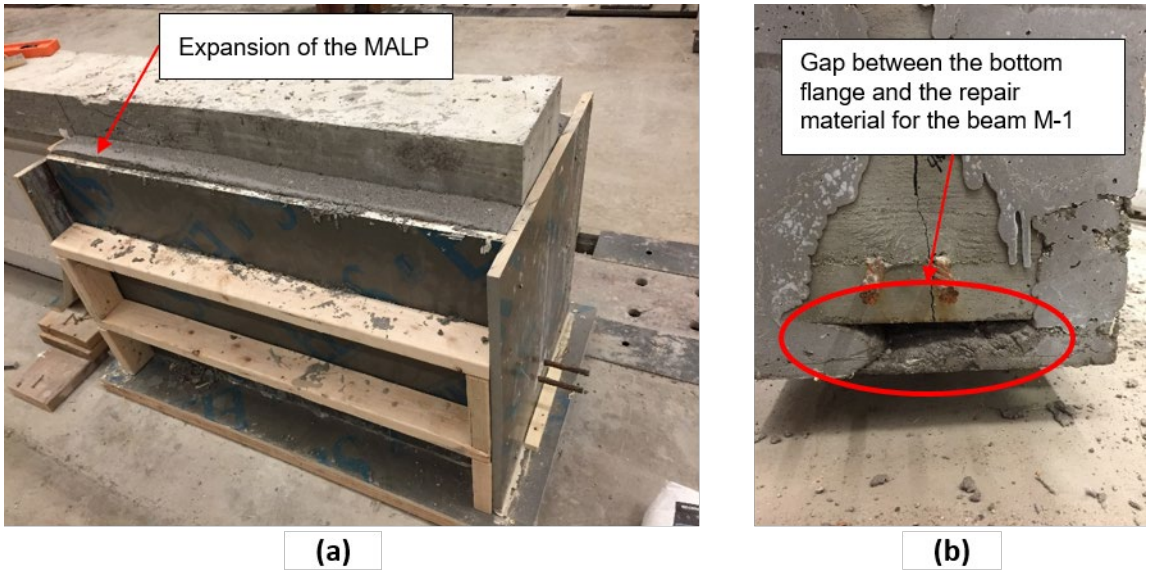

Figure 5.14. (a) Expansion of the MALP above the formwork and (b) gap under the beam resulting from poor workability of the new MALP

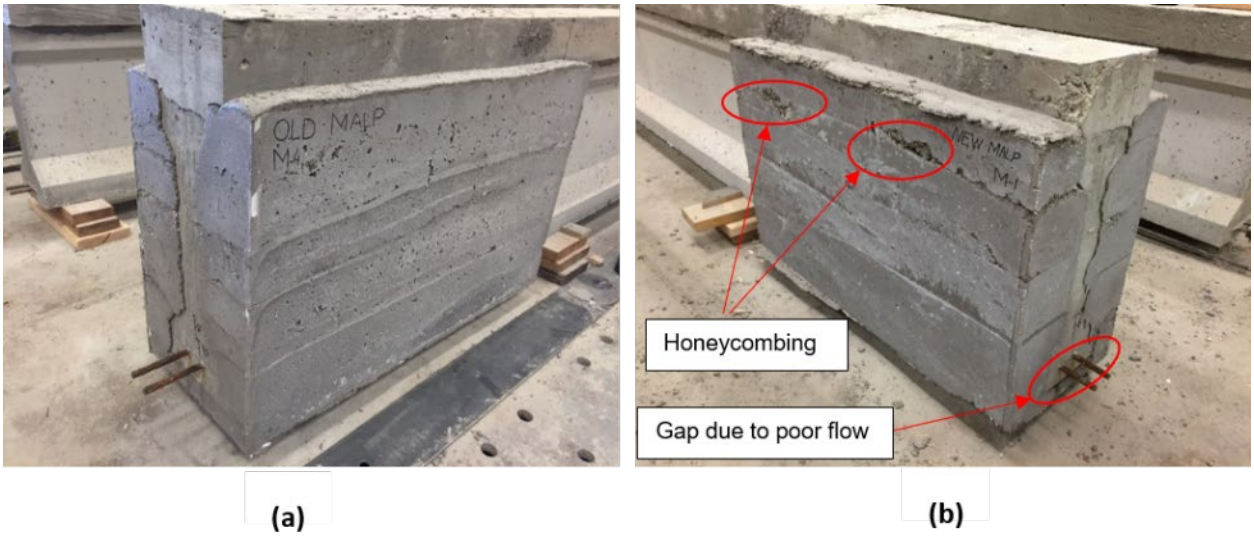

Figure 5.15. (a) Old MALP repair for beam M-4 and (b) new MALP repair for beam M-1

5.4.4 J3 UHPC repair mix

The J3 UHPC repair mix was the same as used for the repairs of the continuity connection repairs and was mixed and placed and in the same manner described in Section 4.8.4.

5.5 Girder Repair Testing Results

5.5.1 FR-SCC Repair Specimens

Figure 5.16 and Figure 5.17 show the load-deflection curves for specimens M2-FRSCC and M3-FRSCC repaired with FR-SCC. Two curves are shown in each figure: one representing the initial shear test and one representing the post-repair load test. For both specimens the load deflection curve for the initial test indicates a bond failure while the post-repair test is more indicative of a flexural failure. This was confirmed by the measured strand slip and visual observations. Strand slip was observed for both tests indicating some level of bond failure (Figure 5.18 and Figure 5.19). The initial test did not reach the maximum load expected for shear capacity for fully developed strands and reached a point where it could not sustain additional load, which is indicative of a bond failure. However, the maximum load of the repaired specimens exceeded the expected capacity for both flexure and shear and both specimens were able to sustain additional load even as they experienced additional slip. Concrete crushing was observed near the load point for each post-repair test (Figure 5.20). The flexural stiffness of both specimens was improved by the repair in addition to the maximum load capacity.

While multiple shear cracks occurred between the load and the support during the initial test of each specimen (see Figure 5.8 as typical), only 1 or two cracks appeared in the repair material during each test. It can be seen in Figure 5.20 that only one of these cracks occurred at a load less than the original failure load of the specimen. Shear cracks did appear in the beam extending from under the repair and past the load point, but failure was controlled by flexure and bond behavior.

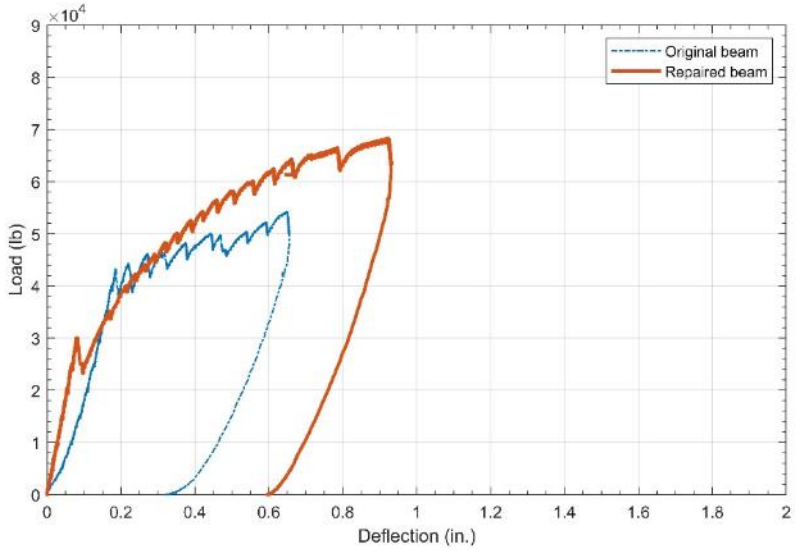

Figure 5.16. Load-deflection curves for the initial and post-repair shear tests of specimen M2-FRSCC

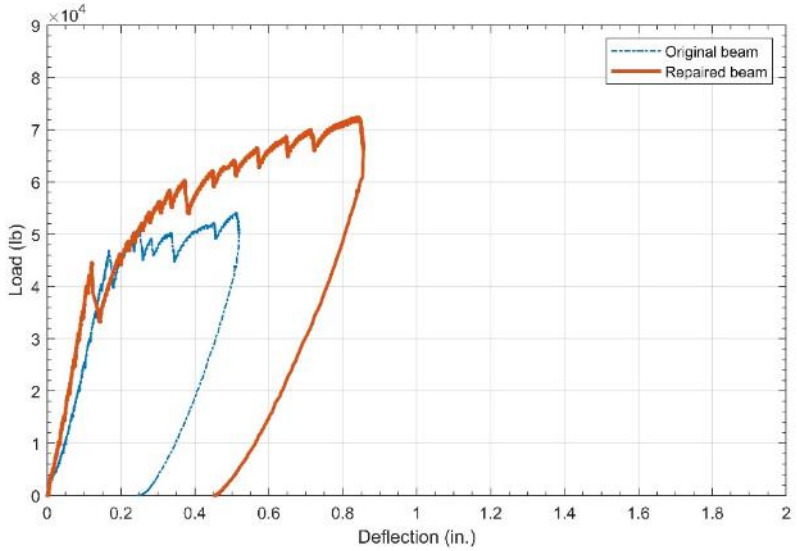

Figure 5.17. Load-deflection curves for the initial and post-repair shear tests of specimen M3-FRSCC

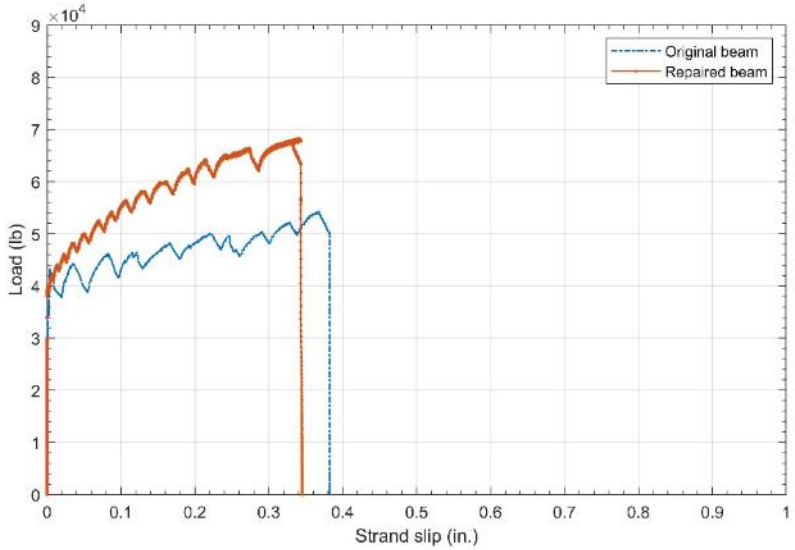

Figure 5.18. Load-slip curves for the initial and post-repair shear tests of specimen M2-FRSCC

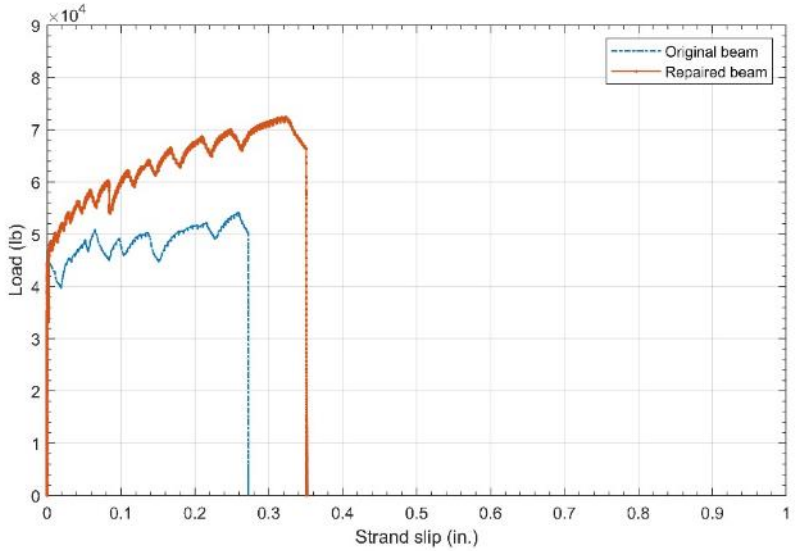

Figure 5.19. Load-slip curves for the initial and post-repair shear tests of specimen M3-FRSCC

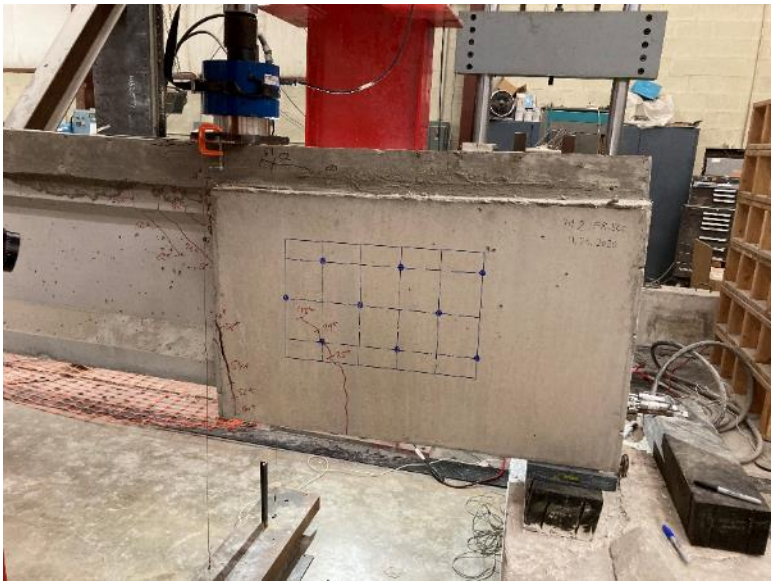

Figure 5.20. Specimen M2-FRSCC at failure showing cracking in the specimen and concrete crushing at the load point

5.5.2 MALP Repair Specimens

Figure 5.21 and Figure 5.22 show the load-deflection curves for specimens M1-MALP and M4-MALP repaired with MALP concrete. Two curves are shown in each figure: one representing the initial shear test and one representing the post-repair load test. For both specimens the load deflection curve for the initial test indicates a bond failure while the post-repair test is more indicative of a flexural failure. This was confirmed by the measured strand slip and visual observations. Strand slip was observed for both tests indicating some level of bond failure (Figure 5.23 and Figure 5.24). The initial test did not reach the maximum load expected for shear capacity for fully developed strands and reached a point where it could not sustain additional load, which is indicative of a bond failure. However, the maximum load of the repaired specimens exceeded the expected capacity for both flexure and shear and both specimens were able to sustain additional load even as they experienced additional slip. Concrete crushing was observed near the load point for each post-repair test (Figure 5.25 and Figure 5.26). The flexural stiffness of both specimens was improved by the repair in addition to the maximum load capacity. However, specimen M4-MALP exhibited less of an improvement in flexural stiffness and a lower stiffness after

cracking. This specimen was repaired with the older MALP material, which provides further indication of the difference in material affecting overall behavior.

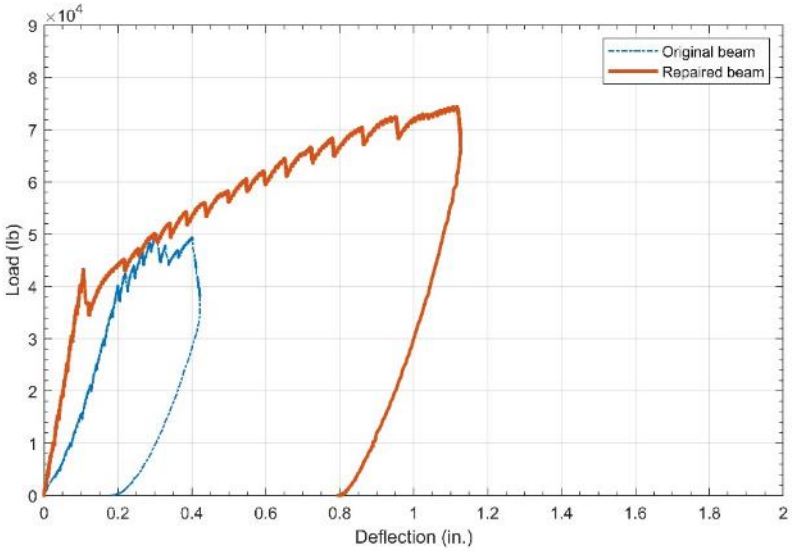

Figure 5.21. Load-deflection curves for the initial and post-repair shear tests of specimen M1-MALP

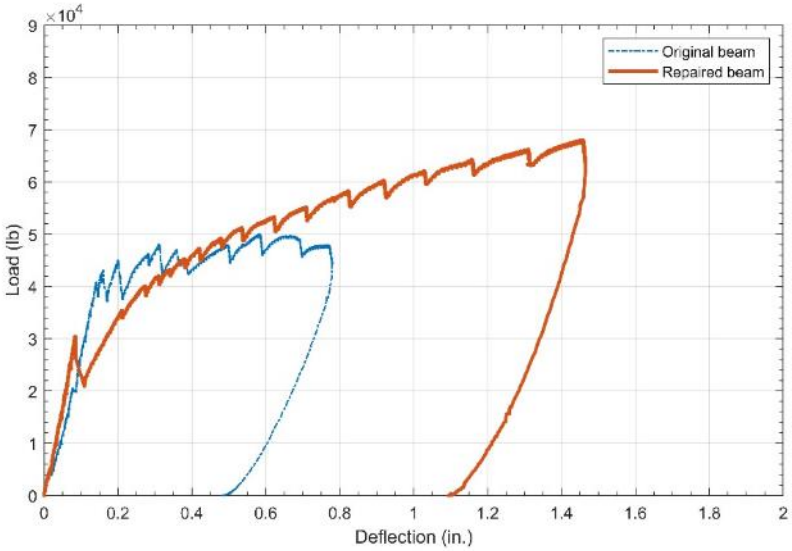

Figure 5.22. Load-deflection curves for the initial and post-repair shear tests of specimen M4-MALP

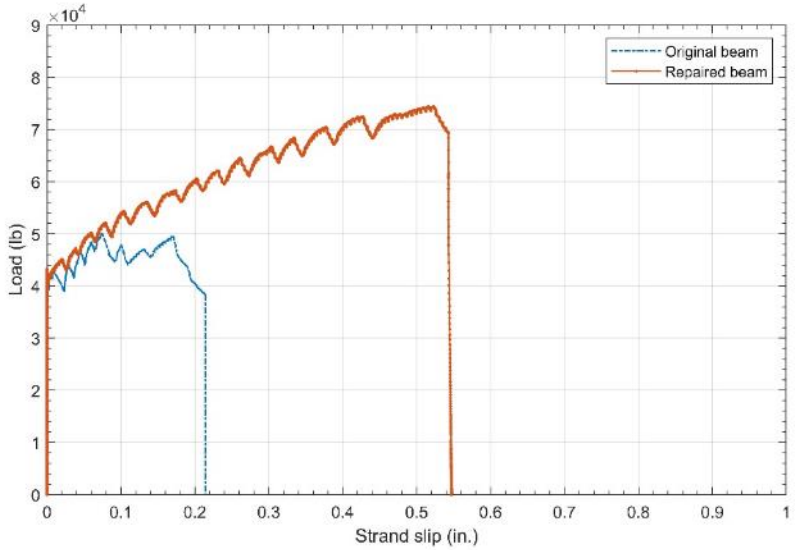

Figure 5.23. Load-slip curves for the initial and post-repair shear tests of specimen M1-MALP

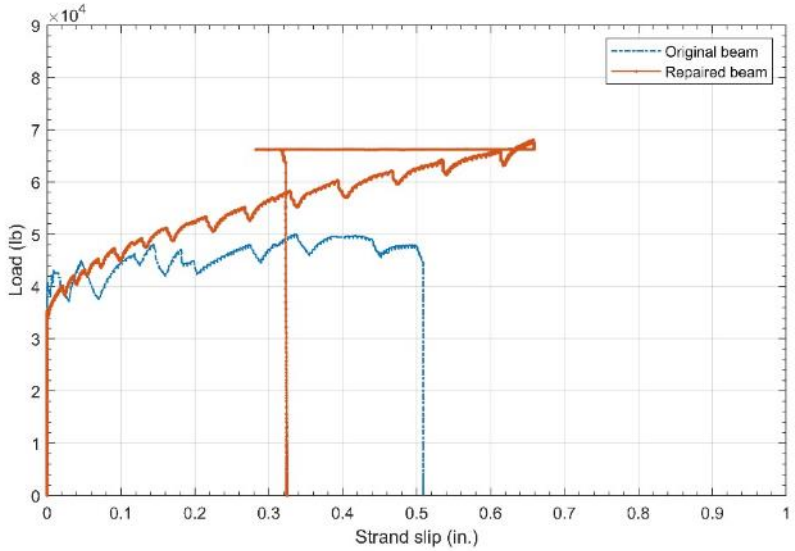

Figure 5.24. Load-slip curves for the initial and post-repair shear tests of specimen M4-MALP

While multiple shear cracks occurred between the load and the support during the initial test of each specimen (see Figure 5.8 as typical), no noticeable cracks appeared in the repair material during either test. Figure 5.25 and Figure 5.26 show the two specimens after testing. For both specimens shear cracks appeared in the web and appeared to propagate from under the repair and past the load point, but failure was

controlled by flexure and bond behavior. A large flexural crack appeared under the load point right at the interface between the beam and the repair material for both specimens and was the primary crack which influenced the failure.

Figure 5.25. Specimen M1-MALP at failure showing cracking in the specimen and concrete crushing at the load point

Figure 5.26. Specimen M4-MALP at failure showing cracking in the specimen and concrete crushing at the load point

5.5.3 J3 UHPC Repair Specimens

Figure 5.27 and Figure 5.28 show the load-deflection curves for specimens M5-UHPC and M6-UHPC repaired with J3 UHPC. Two curves are shown in each figure: one representing the initial shear test and one representing the post-repair load test. For

both specimens the load deflection curve for the initial test indicates a bond failure while the post-repair test is more indicative of a flexural failure. This was confirmed by the measured strand slip and visual observations. Strand slip was observed for both tests indicating some level of bond failure (Figure 5.29 and Figure 5.30). The initial test did not reach the maximum load expected for shear capacity for fully developed strands and reached a point where it could not sustain additional load, which is indicative of a bond failure. However, the maximum load of the repaired specimens exceeded the expected capacity for both flexure and shear and both specimens were able to sustain additional load even as they experienced additional slip. Concrete crushing was observed near the load point for each post-repair test (Figure 5.31). The flexural stiffness of both specimens was improved by the repair in addition to the maximum load capacity.

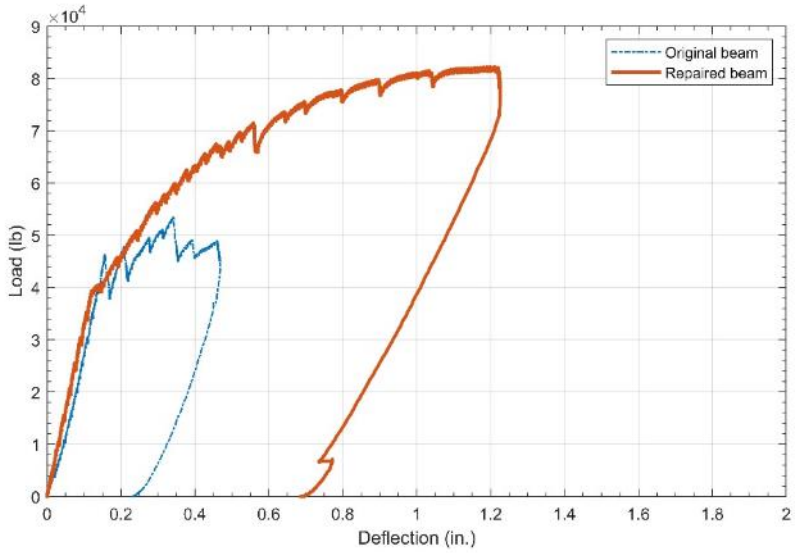

Figure 5.27. Load-deflection curves for the initial and post-repair shear tests of specimen M5-UHPC

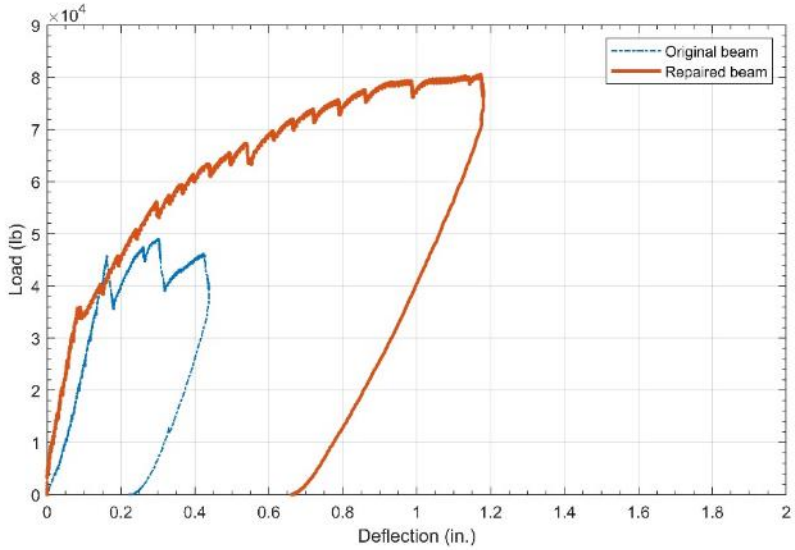

Figure 5.28. Load-deflection curves for the initial and post-repair shear tests of specimen M6-UHPC

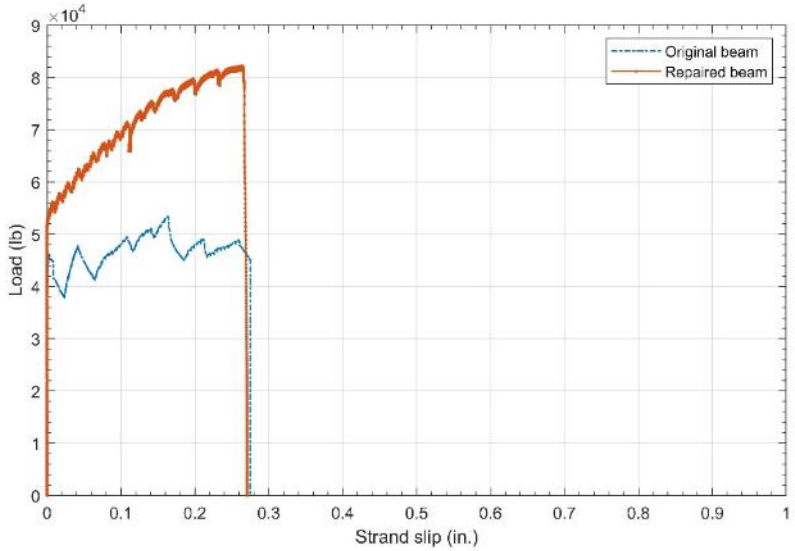

Figure 5.29. Load-slip curves for the initial and post-repair shear tests of specimen M5-UHPC

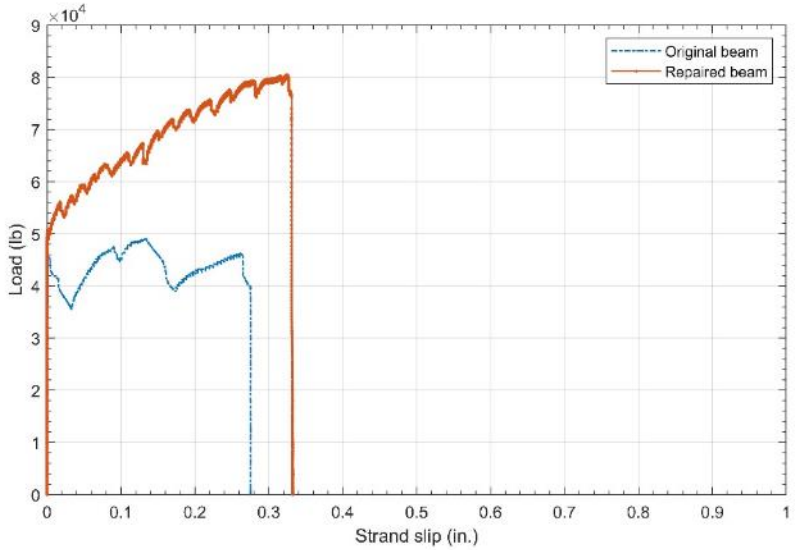

Figure 5.30. Load-slip curves for the initial and post-repair shear tests of specimen M6-UHPC

While multiple shear cracks occurred between the load and the support during the initial test of each specimen (see Figure 5.8 as typical), only a limited number of cracks appeared in the repair material during either test. Figure 5.31 shows the specimen M6-UHPC after testing, which is representative of both specimens. Cracks appeared in the repair material near the bottom at a low load level (10 – 15 kips) for both specimens, but these cracks did not widen after forming and were believed to be related to the thin repair thickness. For both specimens shear cracks appeared in the web and appeared to propagate from under the repair and past the load point, but failure was controlled by flexure and bond behavior. A large flexural crack appeared under or near the load point for both specimens and was the primary crack affecting failure.

Figure 5.31. Specimen M6-UHPC at failure showing cracking in the specimen and concrete crushing at the load point

5.5.4 Summary of Results

Figure 5.32 and Figure 5.33 show comparisons for the post-repair shear test load deflection curves for specimens using the different materials. While the two individual specimens were intended to be identical, the comparison was broken into two figures for ease of presentation. These figures indicate very similar behavior for the different repair materials before cracking and overall similar behavior up to the point of failure. The failure mechanism for all specimens was very similar. The notable exception is the behavior of specimen M4-MALP, which may have been affected by the age of the repair material and specimen. All the load deflection curves minus specimen M4-MALP are plotted together in Figure 5.34. This figure reinforces that all specimens exhibited similar behavior, but also indicates that the UHPC specimens had the best performance after cracking with a higher stiffness and greater ultimate load than the other repaired specimens in spite of the smaller repair thickness.

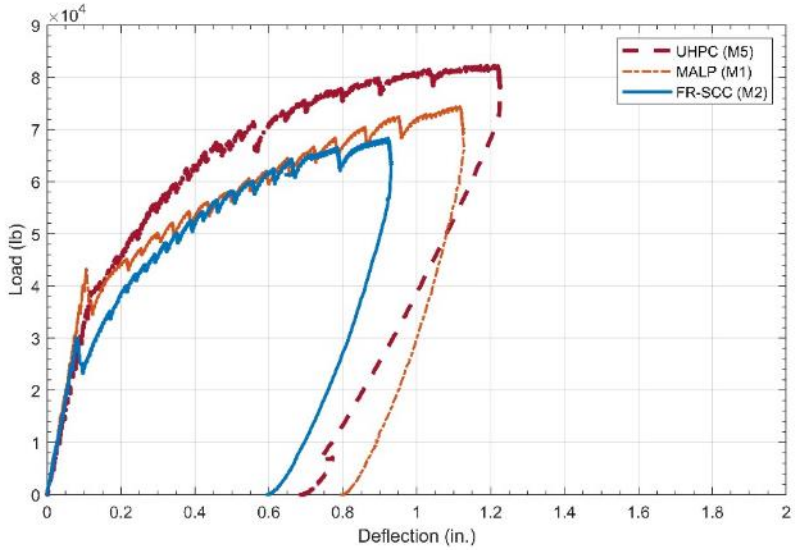

Figure 5.32. Comparison of load-deflection curves for the post-repair shear tests of specimens M2-FRSCC, M1-MALP, and M5-UHPC

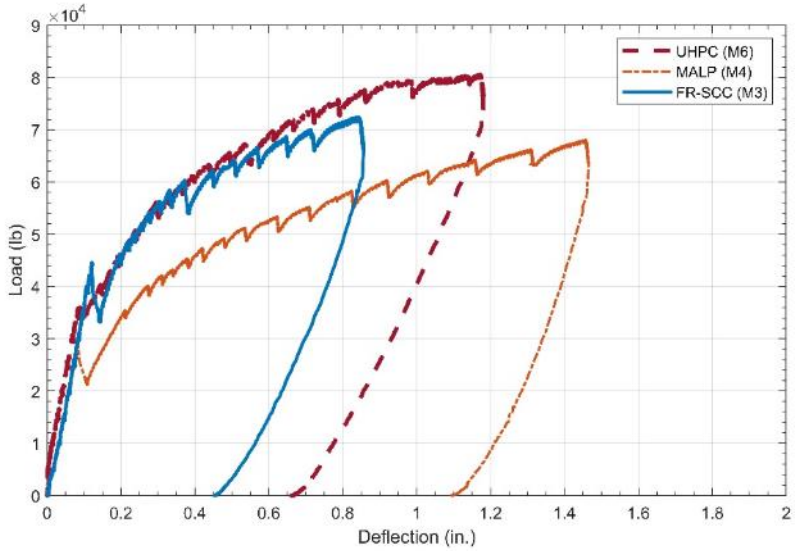

Figure 5.33. Comparison of load-deflection curves for the post-repair shear tests of specimens M2-FRSCC, M1-MALP, and M5-UHPC

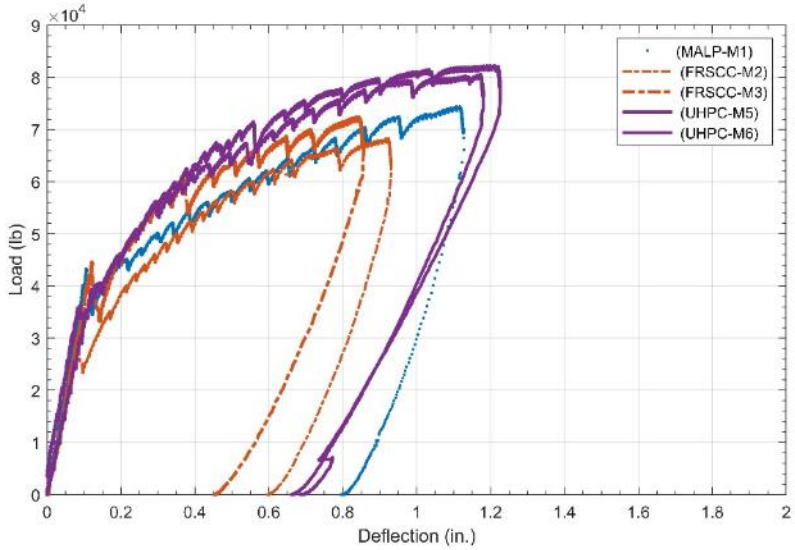

Figure 5.34. Comparison of load-deflection curves for the post-repair shear tests of all specimens except M4-MALP

Figure 5.35 shows a comparison of the average cracking and ultimate loads for specimens with each repair material. In this figure “cracking” is taken as first cracking observed in the beam specimen. All materials had very similar cracking loads and both the FR-SCC and MALP specimens had similar ultimate loads. Only the UHPC specimens exhibited a difference in ultimate load. This is likely due to the higher compressive strength of the UHPC and use of steel fibers in that material. Similar results are observed for deflection at cracking and ultimate loads as shown in Figure 5.36. All specimens had a similar deflection at the point of cracking with the UHPC specimen having a slightly higher deflection which could be indicative of a reduced initial stiffness compared to the others or of its slightly higher cracking load. The deflection at ultimate load increased in order of FR-SCC, MALP, and UHPC. This trend matches the comparative compressive strength values of each material. However, due to the failure criteria used to end each test (concrete crushing, magnitude of slip, deflection) this observation does not lead to a definite conclusion.

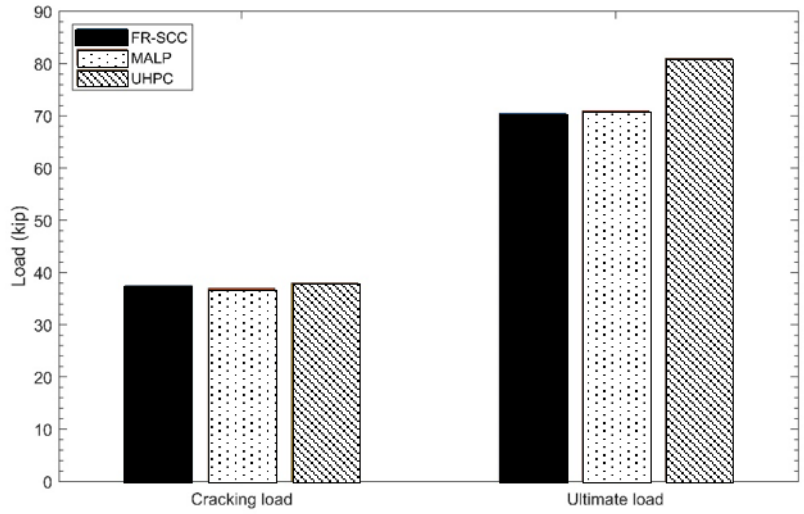

Figure 5.35. Comparison of average cracking and ultimate loads for specimens with all repair materials

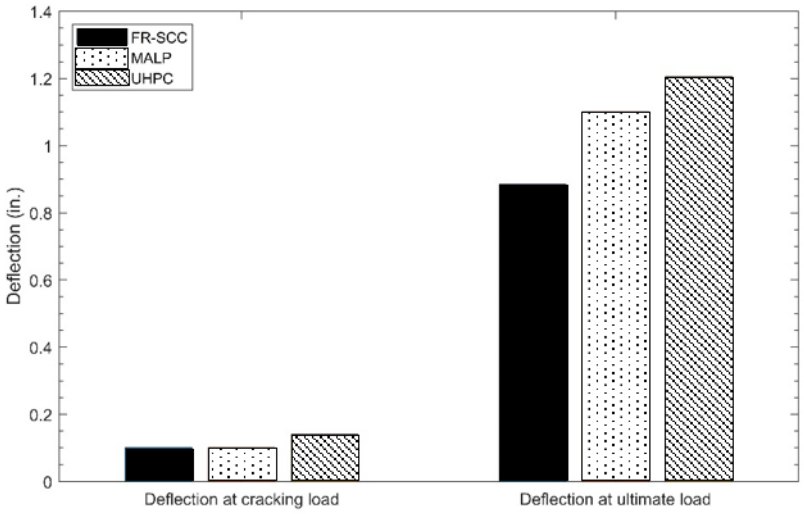

Figure 5.36. Comparison of average deflection at cracking and ultimate loads for specimens with all repair materials

The most telling result from these tests can be seen in the comparison of ultimate loads from the initial shear tests and those after the girders were repaired, shown in Figure 5.37. The full original capacity of the girders was restored using each of the repair materials and in each case the failure load of the repaired specimen significantly exceeded the failure load of the original beam.

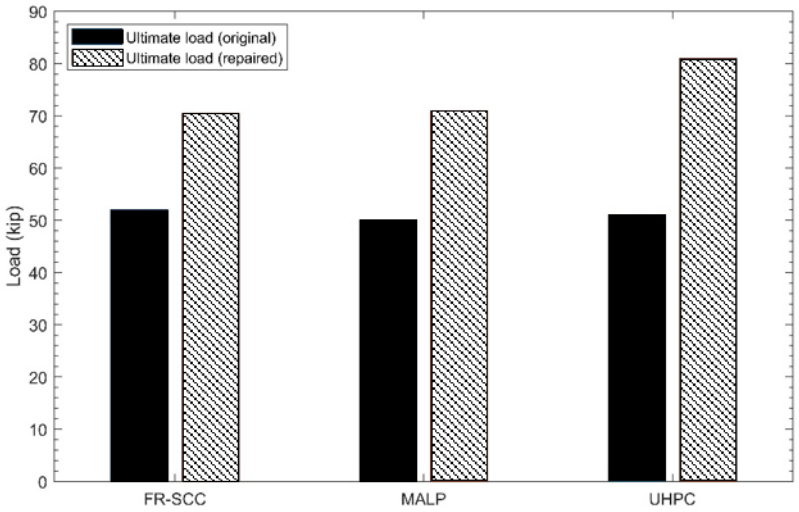

Figure 5.37. Comparison of ultimate load before and after repair

6.0 Corrosion Testing

6.1 Overview

This section outlines the testing procedure and results of both small- and large-scale corrosion testing of the ODOT Class AA, Ductal®, J3, and Phoscrete® concrete mixes. To obtain the most accurate understanding of the effects of a UHPC repair joint on reinforcing steel with previous corrosion, the ideal situation would be to test slabs that have been in active use. Therefore, the University of Oklahoma research team worked in conjunction with ODOT to identify and procure slab sections with existing corrosion that had been previously removed from service. These specimens were then retrofitted with a joint made of one of the four test mixes (ODOT Class AA, Ductal®, J3, and Phoscrete®) and subsequently corroded in an accelerated test setup to produce insight on the comparative corrosion protection capabilities of each mix through visual examination. This was what was referred to as “large-scale” corrosion testing. In addition, “small-scale” corrosion testing was performed to specifically measure the macrocell outputs, or “Halo Effect”, of each of the four mixes when used as a repair material.

It is important to note here the two distinct types of reinforcing steel corrosion that could occur as a result of this corrosion testing: pitting and surficial (Jones 1996). Pitting corrosion occurs when corrosion becomes concentrated, burrowing itself into the steel, and shows visually as dark spots of corrosion intermittently placed across the reinforcing steel’s surface. Surficial corrosion, on the other hand, occurs in a lighter color, with a uniform coating of corrosion across the surface of the steel reinforcing. This kind of surface corrosion is much more likely to stick to the concrete surrounding it because it is in direct and constant contact with the concrete. Neither type of corrosion is necessarily more severe than the other, both being quite harmful for the steel reinforcing; however, the “Halo Effect” is typically evident in a concrete repair by the presence of surficial corrosion of the reinforcing steel in the substrate (original) concrete and not of the reinforcing steel within the repair material. However, this is not always the case, and this kind of corrosion is often much harder to identify, since most of the surface corrosion is pulled away when the concrete is removed for visual examination.

Therefore, care was taken to identify all levels and kinds of corrosion (as applicable and feasible), since any indication of corrosion could be a sign of the “Halo Effect” at work.

6.2 Small-Scale Corrosion Testing

6.2.1 Introduction

Specific testing for the Halo Effect was accomplished on small scale composite specimens using an ODOT Class AA base concrete in conjunction with a Ductal®, J3, ODOT AA, or Phoscrete® “repair”. This testing focused on macrocell corrosion, because that is the type of corrosion that is indicative of the “Halo Effect” (i.e., corrosion only due to the contact of the two different materials). Microcell corrosion, despite being known to be the main contributor to corrosion of steel reinforcing, can be assumed to occur throughout all reinforcing, regardless the type of concrete, or whether that concrete is old or new. Therefore, microcell corrosion would not provide any information on the interaction of old concrete and repair material and was not measured in this testing.

The composite specimens used for the small-scale corrosion testing were 24 in. x 12 in. x 3 in., with each specimen consisting of half base concrete and half repair material. The base concrete halves included the addition of NaCl at dosage rates of 0, 4, and 8% by weight of cement, to represent base concrete with differing levels of previous chloride ion penetration. This method of having NaCl directly in the base concrete is more effective and direct than the ponding method employed by other studies for macrocell corrosion testing. This meant a total of 12 specimens were cast, three for each repair mix and three for the normal 0% NaCl ODOT class AA mix, which acted as a control. Each set of halves were cast one at a time (base concrete followed by repair material), cured for 28 days, and contained three No. 3 bars with electrical wiring soldered to each end, ultimately extending out of the top of the two different concrete halves. After the second 28 day curing time, each bar had its two halves electrically coupled via a 100-ohm resister to allow the measurement of the voltage drop across each bar over time, similar to the set-up used by Hansson (2006). Specimens were cured using a standard 7 days of wet curing and 21 days of air curing for both sets of curing times.

Although the base concrete already contained varying levels of NaCl, specimens were also placed in a 5% NaCl solution, with the water level 0.5 in. below the top of the specimens, to prevent any damage to the electrical wiring coming out of the specimens. This was done to allow for easier passage of ions through the different concrete halves while also accelerating the corrosion within the specimens. The small-scale corrosion molds and testing set-up are shown in Figure 6.1 and Figure 6.2, respectively.

Figure 6.1. Small-scale corrosion specimen molds

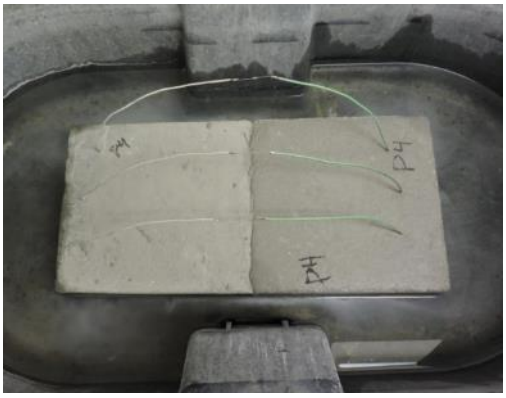

Figure 6.2. Typical small-scale corrosion testing specimen in the chloride solution

Though not a direct measurement of overall corrosion, the specific effect of different repair materials on the corrosion of steel rebar in base concrete are comparable to one another by comparing their macrocell currents. Macrocell current corrosion testing was done for a total of 10 weeks, after which the steel rebar was exposed in the 4% and 8% NaCl specimens for visual examination. The 0% specimens were left in their testing chambers and allowed to continue to corrode for an extended period of time. Using the visual examinations and the macrocell measurements it was

possible to determine if the repair materials were likely to accelerate the corrosion process more or less than a typical bridge joint repair

6.2.2 Testing

After a week of testing, the Ductal® small-scale corrosion specimen containing 0% NaCl, D0, began to show signs of corrosion at the joint, unlike any of the other 11 specimens, as shown in Figure 6.3. By week two, all of the Ductal® specimens began to show signs of corrosion. The second and third specimens, however, showed signs of corrosion not through the obvious patching seen on D0, but through corrosion spotting, as shown in Figure 6.4. None of the other small-scale specimens exhibited signs of surface corrosion directly at the joint between the two materials, only experiencing light coloration around their edges where they were in contact with the 5% NaCl solution.

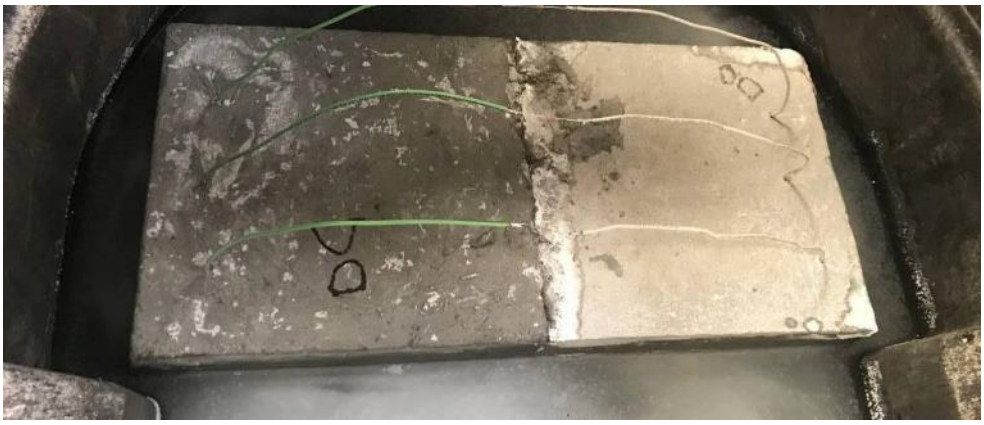

Figure 6.3. Initial joint corrosion in Ductal® small-scale corrosion testing specimen D0 - patching

Figure 6.4. Initial joint corrosion in Ductal® small-scale corrosion testing specimen - corrosion spotting

No measurable macrocell currents formed across any of the reinforcing bars in any of the specimens during the duration of this testing. This was due to insufficient amounts of corrosion across the reinforcing bars to induce a current that could travel across the two types of concrete that made up each specimen, despite the high levels of NaCl present in most specimens. This was a good sign for all of the concrete mixtures, since the presence of a measurable macrocell current would have indicated significant corrosion forming across the steel reinforcing on both sides of the bars.

Though no macrocell current values can be reported, the joints of the 4% and 8% NaCl specimens were chipped away to give some comparison of corrosion response of the four different repair materials, as discussed in the rest of this section and shown in Figures 6.5 – 6.8. Additionally, a photograph of the type of steel rebar put into these specimens before testing is presented as Figure 6.9 so that the difference between the typical amount and type of corrosion present on a piece of steel rebar before and after testing can be made clear. This difference is made most clear by the darker color and distinct starting location of the active corrosion (after testing). It is assumed in this testing that all previous surface corrosion was purely superficial and would have come off completely during either casting or chipping, and all actual surficial or pitting corrosion due to testing conditions would have occurred with or without the initial presence of this light surface corrosion.

As illustrated in Figure 6.6 and Figure 6.7, the excavation of the Ductal® and J3 specimens with 4% and 8% NaCl in the base concrete revealed minor pitting corrosion on a majority of their reinforcing bars, all congregated at the joint, with some traces of this pitting also forming on the base concrete side. Similarly, but to a higher degree, excavation of the ODOT AA specimens (Figure 6.5) revealed significant pitting corrosion on all of its reinforcing bars, starting exactly along the line of the joint and moving along the original ODOT AA (base) concrete side, almost to the point of complete coverage. This kind of corrosion happening only in the base material is exactly what could be expected of these specimens from the “Halo Effect” given the time period of testing.

Excavation of the Phoscrete specimens revealed significant amounts of pitting corrosion along the repair material side, with the 8% NaCl specimen also exhibiting a visible layer of surficial corrosion completely covering the reinforcing steel along the base concrete side.

Figure 6.5. Corrosion state of rebar reinforcing at joint of ODOT Class AA small-scale corrosion specimens with 4% NaCl (left) and 8% NaCl (right)

Figure 6.6. Corrosion state of rebar reinforcing at joint of J3 small-scale corrosion specimens with 4% NaCl (left) and 8% NaCl (right)

Figure 6.7. Corrosion state of rebar reinforcing at joint of Ductal® small-scale corrosion specimens with 4% NaCl (left) and 8% NaCl (right)

Figure 6.8. Corrosion state of rebar reinforcing at joint of Phoscrete® small-scale corrosion specimens with 4% NaCl (left) and 8% NaCl (right)

Figure 6.9. Steel rebar before testing - typical

6.2.3 Results

Ultimately, conclusions about the “Halo Effect” taken from the small-scale corrosion testing can only be made through visual examination, and therefore the adequacy of each of the concrete types can only be evaluated on a relative basis with each other. Both the J3 and Ductal® UHPC materials produced similar results, both outperforming the standard ODOT AA mixture that would be used in a simple bridge deck repair. While there were no voltages, and therefore no macrocell currents, formed across any of the reinforcing bars at the conclusion of this initial testing, there were small amounts of voltages measured between adjacent bars within each of the small-scale corrosion specimens. These are not the readings that would indicate a macrocell forming due to the Halo Effect happening across the two different repair materials, but these readings do show a macrocell forming from just having bars adjacent to each other in each of these specimens.

6.3 Large-Scale Corrosion Testing

6.3.1 Procedure

The retrofitting process for the large-scale joint specimens included cutting the ODOT bridge slabs to an appropriate size (18 in. wide x 60 in. deep x 9 in. thick), chipping away 4 in. of the damaged concrete from the 18 in. width to expose the steel rebar, and casting a 5 in. x 60 in. x 9 in. repair replacement joint, producing a minimum 1 in. cover to the rebar exposed from the chipping process. The exposed No. 5 rebar layer revealed in each slab was connected together using a No. 5 longitudinal bar tied to the far ends of the exposed rebar sections. The longitudinal bar was placed on the topmost layer of reinforcing when laid down flat, putting it closest to what ultimately became the finished surface, to allow for the needed wires to extend out of the top of the specimens. These electrical wires were soldered onto both ends of each connective longitudinal bar to allow for the DC power supplies to be connected after curing of the specimens. The slabs before and after chipping are shown in Figure 6.10 and Figure 6.11, with Figure 6.12 showing the final rebar construction.

Figure 6.10. Large-scale corrosion joint specimens before chipping

Figure 6.11. Large-scale corrosion joint specimens after chipping

Figure 6.12. Large-scale corrosion joint specimen with longitudinal connection bar in place

One joint specimen was cast for all four of the concrete mixes in this testing: ODOT AA, Ductal®, J3, and Phoscrete®. After the joints were cast, they were moist cured for 7 days and air cured for another 21 days. The added longitudinal bars were then connected to a DC power supply capable of supplying up to 3 A of current and the specimens were submerged in a 5% NaCl solution to accelerate the reinforcing bar

corrosion using electrochemical methods similar to Wang et al. (2014, 2017) and Abosrra et al. (2011). This was accomplished using large wooden containers lined with plastic with a 5% NaCl solution at a level 2 in. below the top of the specimens to prevent any damage to the electrical wiring extending out of the specimens, like the setup of the small-scale corrosion specimens. All the wooden containers were given foam “feet” so that when the specimens were placed inside, they were elevated off the ground 1 in., allowing the testing solution to penetrate the bottom of the specimens.

From there, a proven corrosion testing set-up called the “electrochemical method” was utilized. The electrochemical method works by creating a complete circuit that runs through steel reinforcing (or similar conductive metals), which causes the steel reinforcing to release electrons, in turn oxidizing the steel reinforcing and corroding it. For this testing the required complete circuit was achieved by using a stainless-steel rod sitting in the NaCl solution as a cathode (as shown in Figure 6.13) and the longitudinal steel reinforcing bar in the repair material side of each specimen as the anode. From there, each specimen was connected using electrical wiring so that a 0.2 A current could flow continuously from the positive terminal of the power supply to the steel reinforcing, through the concrete and surrounding NaCl solution to the steel rod, and ultimately back to the negative side of the power supply. This test setup is shown in Figure 6.14.

Figure 6.13. Stainless steel rod and electrical wiring for large-scale corrosion testing

Figure 6.14. Large-scale corrosion testing setup showing power supplies (left) and all specimens in place (right)

After one week of supplying a current of 0.2 A through each specimen, the slabs were partially chipped back, starting from the side farthest from the input of the current, so that the first layer of vertical reinforcing could be visibly inspected for corrosion. From there, the slabs were chipped along each reinforcing bar layer by layer until a sufficient amount of corrosion could be observed. Once sufficient corrosion was achieved, chipping was done at the joint interface of each specimen along the same reinforcing bars as those chipped away previously. This was done to confirm if any corrosion had occurred between the base concrete and the repair material, and if so, which side(s) the corrosion occurred on. Once corrosion at the joint was confirmed, roughly ten weeks into the accelerated corrosion process, a final round of chipping was done along the joint, as close to the inflow of current as possible. This was done to observe the highest level of potential corrosion occurring within each specimen. Timing, location, and progression of corrosion were all closely documented for each of the slabs and are detailed in Section 6.3.2.

6.3.2 Testing and Results

During the first week of testing, the water pools of each specimen began to fill with a coating of corrosion that had already begun to leech off, except for Phoscrete®, which secreted a white film of unknown composition. This film is visible in Figure 6.15. After a week, the white film was covered with a corrosion film like the rest of the large-scale corrosion specimens. After two weeks of testing, the corrosion that was now in the water of all four specimens became sufficient to be present in all of the testing water,

but mostly occupied the bottom of the testing containers. This level of corrosion was maintained through to the end of testing and is shown in Figure 6.16.

Figure 6.15. White film in water of Phoscrete large-scale corrosion specimen

Figure 6.16. Corrosion in water of typical large-scale corrosion specimens

During the first week of testing, a corrosion spot along the joint of the Ductal® specimen began to form. By week two, this corrosion spot was in the state shown in Figure 6.17. This could have been due to several reasons relating to a poor joint-face connection between the Ductal® and the old conventional concrete it was cast onto but could also have been due to the Halo Effect occurring rapidly along this joint. The justification for not assuming a simple poor joint-face connection is that previous testing showed that Ductal® possesses exceptional bond strength to substrate (base) concrete, and therefore a poor bond was unlikely in this scenario.

From week three up until testing was concluded after 10 weeks, the surface corrosion along the Ductal® joint progressed at a steady rate, as shown in Figure 6.18. None of the other specimens showed any significant signs of surface corrosion during testing, except along the anticipated reinforcing bar paths.

Figure 6.17. Joint corrosion in Ductal® large-scale corrosion testing specimen during week 2 of testing (Ductal® on left side of image)

Figure 6.18. Joint corrosion in Ductal® large-scale corrosion specimen during week 5 of testing

Though none of the other specimens experienced joint corrosion, a strange interaction did begin to occur at the joint of the Phoscrete® specimen starting roughly 45 days (week 7) after corrosion testing began. A thick, dark green liquid began to appear

around the joint, similar to what leaked out and caused the white film in the surrounding solution in the first week of testing. The makeup and reasoning for this liquid forming are unknown, and no information on this phenomenon was found in the literature. However, it is hypothesized that something in the chemical make-up of Phoscrete® (which contains magnesium, aluminum, phosphate, and multiple other chemicals to try to help prevent corrosion and freeze-thaw damage) reacted with the NaCl in the surrounding solution, and at this point in the testing the solution had made its way far enough into the joint to begin to interact and produce the green substance shown in Figure 6.19.

Figure 6.19. Green liquid in joint of Phoscrete large-scale corrosion specimen during week 7 of testing

Roughly 8 weeks into testing, the Ductal® specimen also began to produce a small amount of green liquid from its joint, however this liquid was much lighter in color than that seen on the Phoscrete® specimen and was accompanied by streams of white liquid that seemed to trail down the joint, as seen in Figure 6.20. It is hypothesized that this liquid was also a by-product of a chemical reaction occurring between the NaCl solution and the Ductal® mix. The final states of these two unexpected chemical reactions happening at the surface of the Phoscrete® and Ductal® specimens are shown in Figure 6.21 and Figure 6.22, respectively.

Figure 6.20. Green liquid in joint of Ductal® large-scale corrosion specimen during week 8 of testing

Figure 6.21. Green liquid in joint of Phoscrete® large-scale corrosion specimen during week 10 of testing

Figure 6.22. Green liquid in joint of Ductal® large-scale corrosion specimen during week 10 of testing

After only a week of testing, the first sign of rebar corrosion was also visible. As shown in Figure 6.23, a thick black liquid began to be produced out of the exposed ends of each specimen. Though no more than a few inches of liquid was ever formed on any one bar, and the amount of each rebar end that was completely corroded off due to the formation of this liquid was never significantly high, only reaching a max of 0.75 in., this level of corrosion could still be cause for concern in the field. This is because the chemistry of steel rebar reacts with NaCl and other corrosive solutions found in the field to produce a volume of reaction products 5 to 10 times that of the original material. This becomes a problem in the field because if internal reinforcing were to experience the kind of corrosion seen on the exposed rebar ends, it could generate large expansive forces that can crack and spall the concrete surrounding the reinforcing steel. By the end of testing, the corrosion of the exposed rebar ends had reached the extent shown in Figure 6.24.

Figure 6.23. Visible confirmation of reinforcing bar corrosion during week 1

Figure 6.24. Typical reinforcing bar corrosion at the conclusion of testing - week 10

Figure 6.25 can be used as a guide to show the order in which sections of each specimen were chipped away to expose the reinforcing bars. Figures 6.26 – 6.29 provide updates of the specimens over the 10-week testing period, while Figures 6.30 – 6.33 show each layer of reinforcing steel immediately after chipping. The last section of steel reinforcing that was excavated and examined, after being completely removed from the testing setup, chipped, and allowed to sit out in open air for 24 hours, is also presented as Figure 6.34.This is significant because with no forced current or surrounding NaCl solution, all reactions of this exposed reinforcing steel came only as a result from what had already occurred within the specimens, and all pitting corrosion that revealed itself was previously present in the steel reinforcing.

Figure 6.25. Chipping sequence of large-scale corrosion specimens

Figure 6.26. Week 1 update for large-scale corrosion specimens using (a) ODOT AA, (b) J3, (c) Ductal®, and (d) Phoscrete®

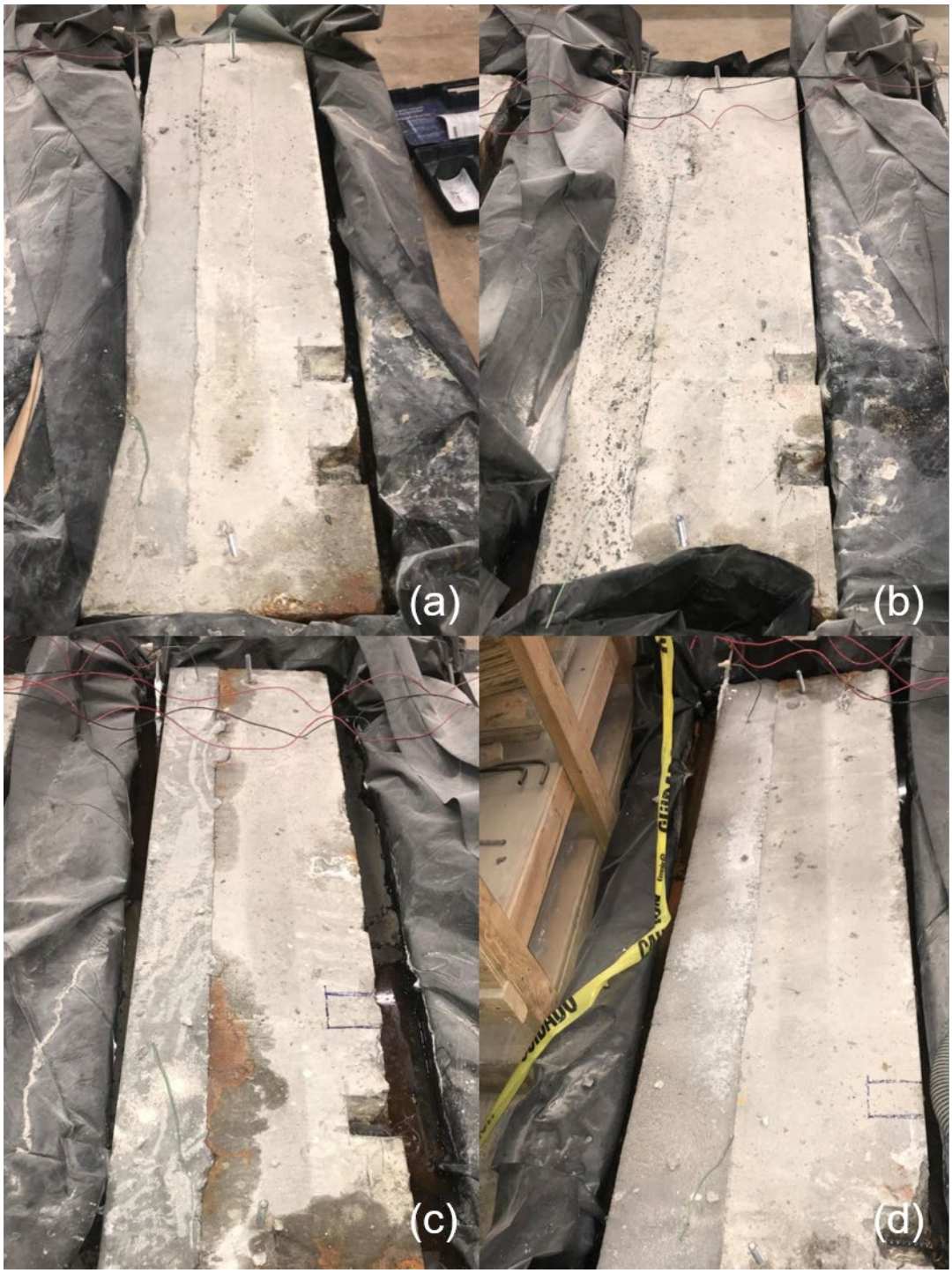

Figure 6.27. Week 3 update for large-scale corrosion specimens using (a) ODOT AA, (b) J3 (c) Ductal®, and (d) Phoscrete®

Figure 6.28. Week 6 update for large-scale corrosion specimens using (a) ODOT AA, (b) J3, (c) Ductal®, and (d) Phoscrete®

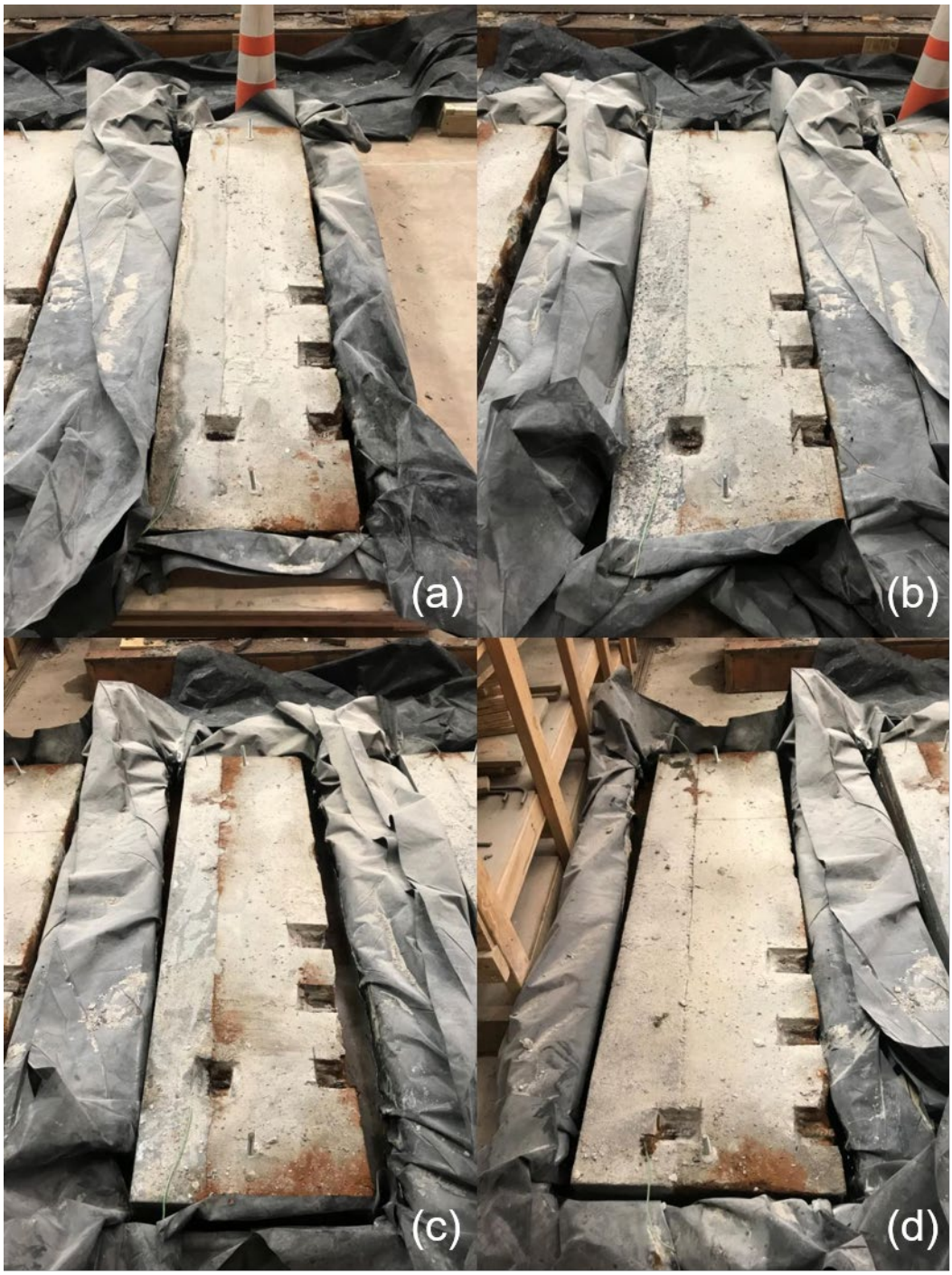

Figure 6.29. Week 10 update for large-scale corrosion specimens using (a) ODOT AA, (b) J3, (c) Ductal®, and (d) Phoscrete®

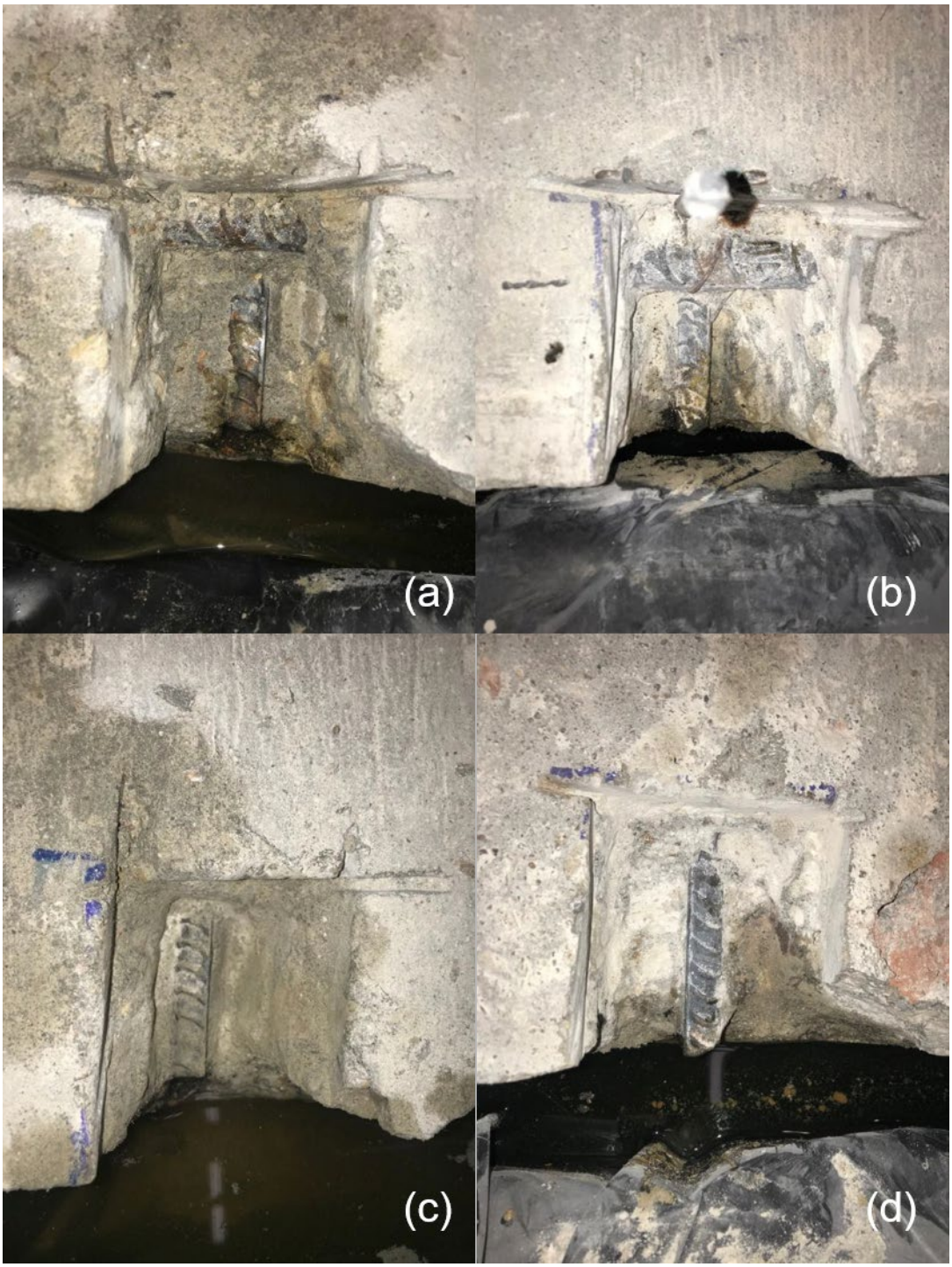

Figure 6.30. First rebar excavation for large-scale corrosion specimens using (a) ODOT AA, (b) J3, (c) Ductal®, and (d) Phoscrete®

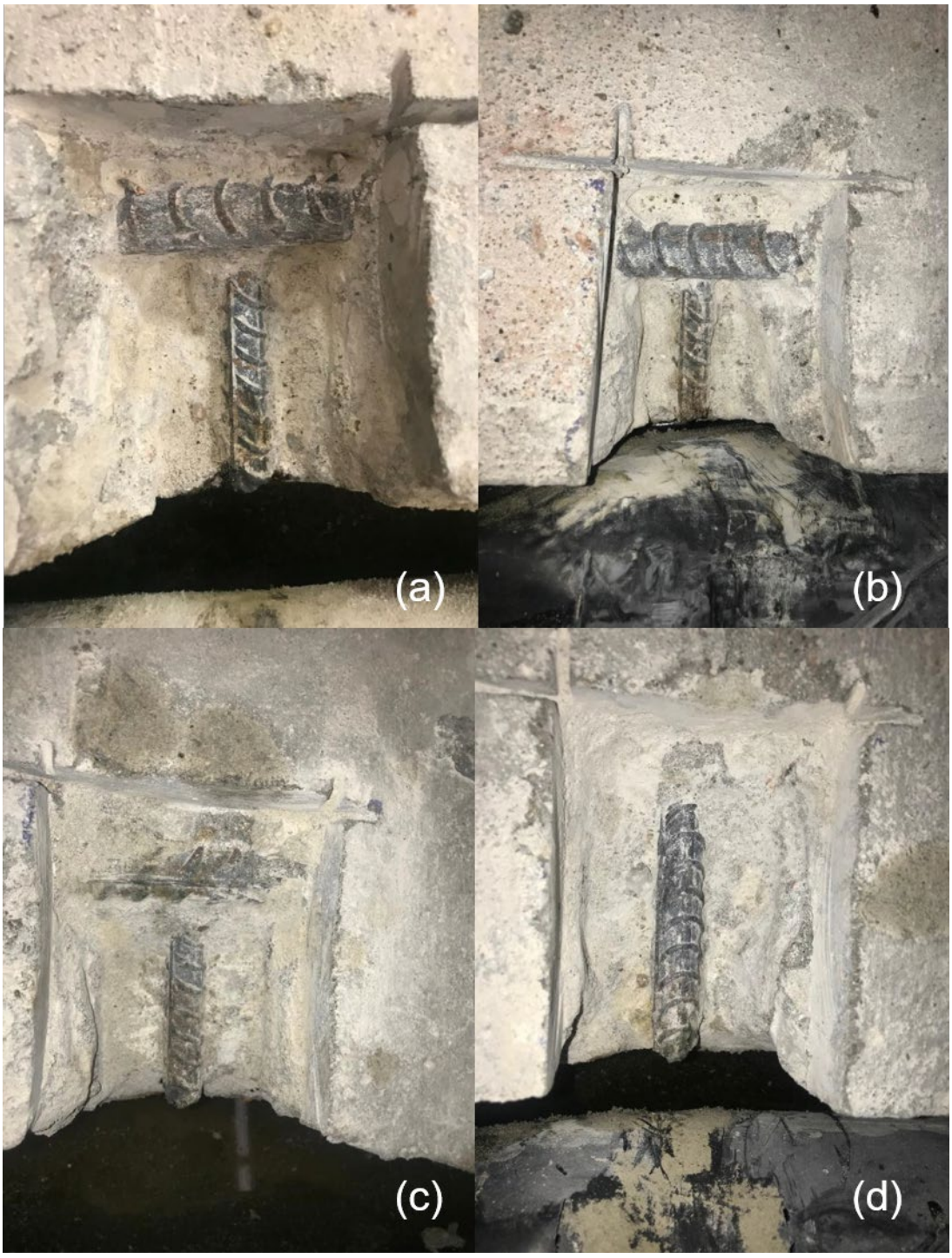

Figure 6.31. Second rebar excavation for large-scale corrosion specimens using (a) ODOT AA, (b) J3, (c) Ductal®, and (d) Phoscrete®

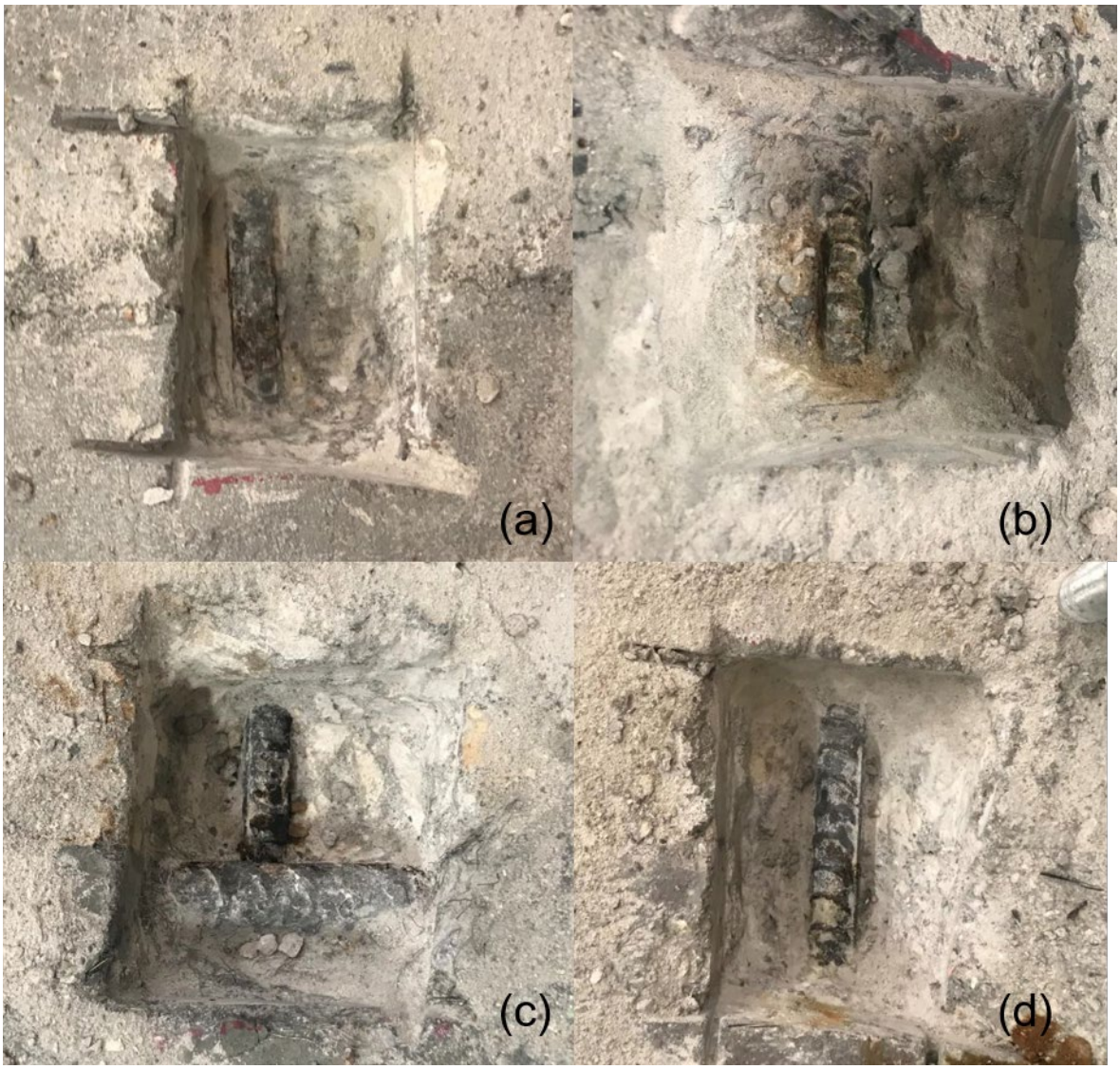

Figure 6.32. Fourth rebar excavation for large-scale corrosion specimens using (a) ODOT AA, (b) J3, (c) Ductal®, and (d) Phoscrete®

Figure 6.33. Fifth rebar excavation for large-scale corrosion specimens using (a) ODOT AA, (b) J3, (c) Ductal®, and (d) Phoscrete®

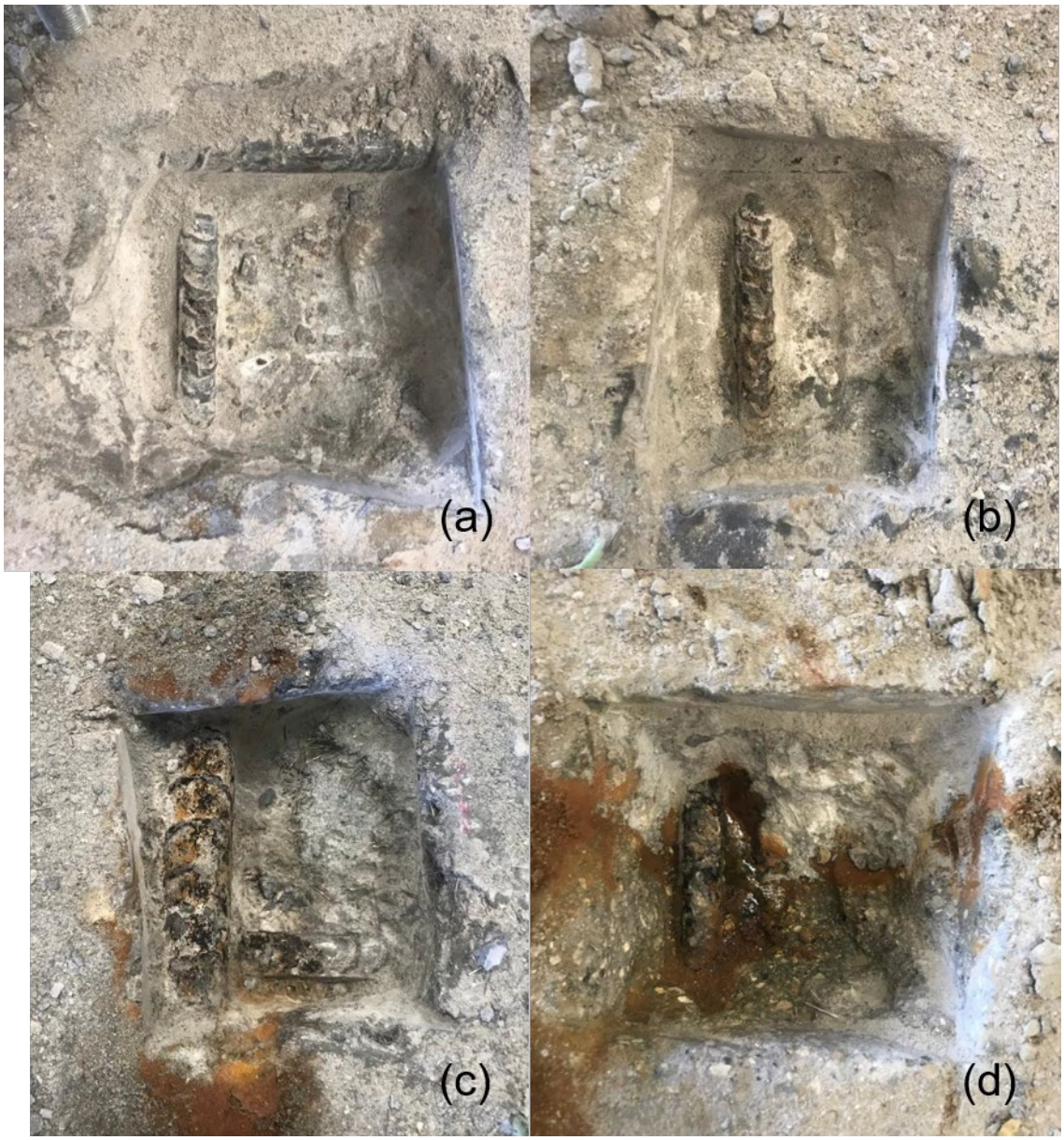

Figure 6.34. Fifth rebar excavation for large-scale corrosion specimens using (a) ODOT AA, (b) J3, (c) Ductal®, and (d) Phoscrete® after 24 hours

The excavation of the reinforcing steel located in the large-scale corrosion specimens for visual examination can be broken up into two parts: excavation of rebar ends (numbers one through three) and excavation of rebar along the joint (numbers four and five). Excavation 1 occurred after 11 days of testing and revealed slight corrosion on the reinforcing steel near the exposed end of the ODOT AA and J3 specimens (up to 0.5 in. maximum), with no corrosion visible on the reinforcing steel of the Ductal® or Phoscrete® specimens. Excavation 2 occurred after 25 days of testing and revealed

slightly more reinforcing steel corrosion than was previously seen on the ODOT AA, J3, and Phoscrete® specimens, with significantly more corrosion now visible on the steel reinforcing of the Ductal® specimen (up to 1.5 in.). Though no photographs were taken of excavation 3, which occurred after 40 days of testing, similar results as those seen in excavation 2 were observed, with at least 1 in. of corrosion visible on the reinforcing steel of all four specimens. This amount of corrosion was sufficient to indicate that reactions could be occurring along the joint of each specimen. For that reason, excavation 4 was done along the same reinforcing bar revealed during excavation one, only now at the joint of each specimen, after 52 days of testing. This excavation revealed roughly 0.5 in. of surficial corrosion on the ODOT AA specimen, starting at the joint and moving into the repair material side, trace amounts of pitting corrosion around the joint of the J3 and Phoscrete® specimens, and heavy amounts of pitting corrosion and staining occurring at the joint of the Ductal® specimen.

Excavation 5 was done after 70 days of testing on the closest layer of rebar to the inflow of current, again along the joint of each specimen to directly monitor the “Halo Effect” occurring in these specimens. This location did overlap the area in which the various liquids were coming out of the joints of the Ductal® and Phoscrete® specimens with the intention of identifying the effect of these liquids on the reinforcing steel.

Ultimately, there was a surprisingly small amount of corrosion revealed on the ODOT AA specimen, likely because its pH was closest to that of the old concrete, so it did not have as strong of a reaction as the other repair materials did to this type of large-scale testing. The two UHPC repair materials did not hold up quite as well, with J3 showing minor surficial corrosion along the joint and Ductal® showing pitting and surficial corrosion starting at the joint and on both of the visible pieces of reinforcing steel on the base concrete side. Figure 6.35 provides evidence for the varying levels of complete surface corrosion by presenting pieces of the concrete that were chipped away during excavation 5 that pulled away surficial corrosion, i.e., Figure 6.35(a) shows a piece of base concrete with minor surficial corrosion on the side that made up the joint of the J3 specimen, while Figure 6.35(b) shows multiple pieces of base concrete that were covered with heavy surficial corrosion on multiple sides, all from the Ductal® specimen.

Within 60 seconds of revealing the reinforcing of the Phoscrete® specimen, a puddle of the green liquid that had been present on the surface of the specimen since week 7 began to leak from the joint, until it reached the point shown in Figure 6.33(d) and seemed to steady out. After 24 hours however, the liquid had spread and corroded to the point shown in Figure 6.34(d). Slight pitting corrosion was also immediately visible along the reinforcing steel at the joint of the Phoscrete® specimen, which was only exacerbated by the presence of the liquid leaking through. This observation proved that the green liquid seen on the surface of the Phoscrete® specimen had to have been coming through the joint to the surface, and was something made and stored within the concrete, since the specimen was taken completely out of the testing set-up and exposed to air for the 24-hour waiting period, so it could not just be the surrounding NaCl solution leaking through.

Figure 6.35(c) shows pieces of the base concrete that was chipped away during excavation five of the Phoscrete® specimen and not only shows the presence of surficial corrosion along the joint of the Phoscrete® specimen (like that shown in Figure 6.35(a) and Figure 6.35(b) for J3 and Ductal®, respectively) but also the presence of the kind of staining caused by the green liquid that has leaked through the joint, indicating that the liquid was present even before excavation.

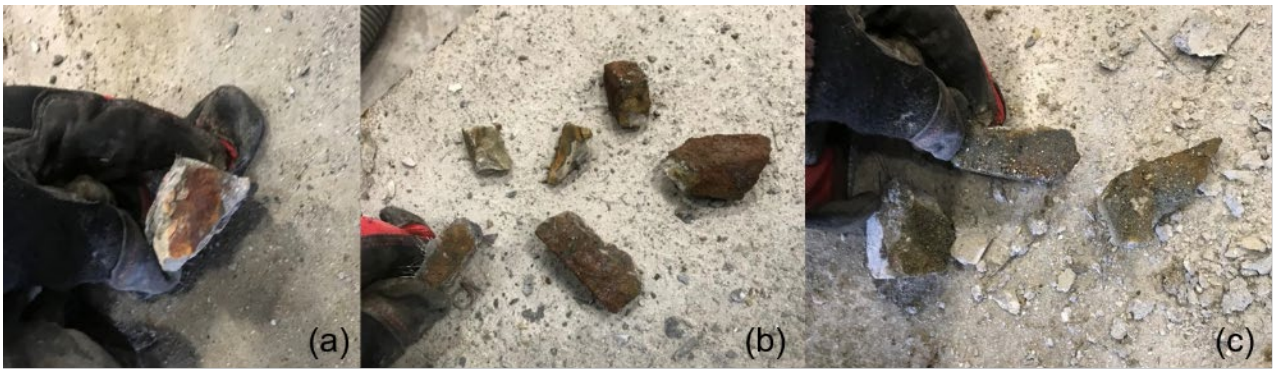

Figure 6.35. Evidence of surficial corrosion on large-scale corrosion specimens using (a) J3, (b) Ductal®, and (c) Phoscrete®

In addition to the visual examination data, measurements of the change in voltage measured by each of the power supplies throughout the study were taken and are presented in Figure 6.36. In other words, the amount of voltage required to supply

each specimen with the 0.2 A of current used throughout testing was recorded on various dates during testing for comparison. This data is important because a larger voltage represents more energy being needed by the power supply to get the 0.2 A of current all the way through the specimen and back to the power supply. This in turn shows the resistance of the specimen to the flow of corrosion-inducing cycles, like the electrochemical (forced current) method used in this testing, with the specimen with the highest voltage readings being the most resistant. Based on these readings J3 showed to be the overall most resistant, with Phoscrete® being the overall least resistant. These findings are very much in line with the visual examinations of both the small- and large-scale specimens.

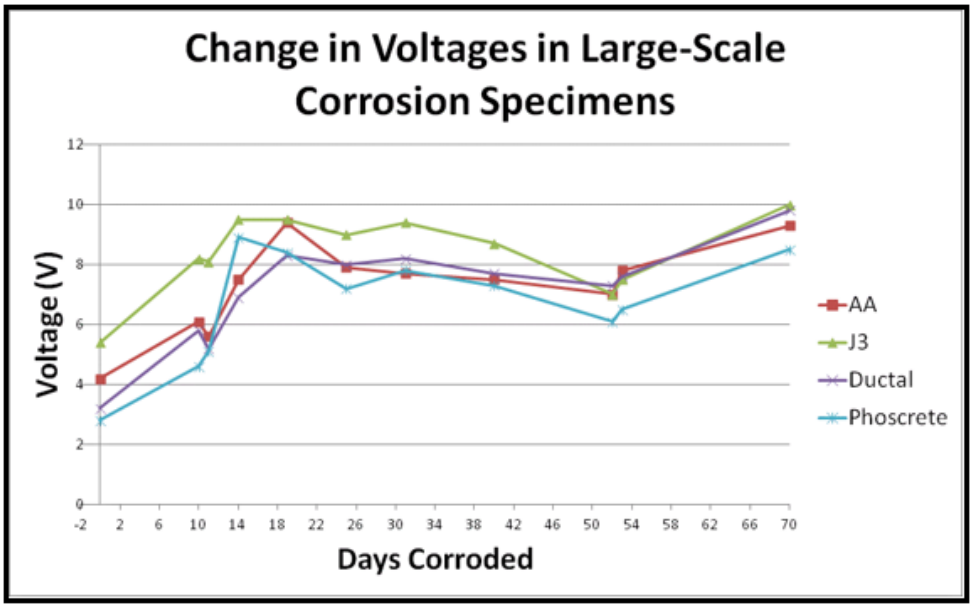

Figure 6.36. Change in voltage over time for all large-scale corrosion specimens

Based on the observed results, additional testing is advised to assess the durability of Phoscrete® and its and corrosion properties to fully understand its behavior in the field. The final state of the south side of the large-scale Phoscrete® corrosion specimen, the side that experienced the secretion of the unknown green liquid, is shown in Figure 6.37, which reveals the entire end to be a dark green color.

Figure 6.37. Final state of Phoscrete® large-scale corrosion specimen after week 10

Cores were taken from the large-scale corrosion specimens to evaluate bond between the repair material and substrate. Split cylinder tests were performed to evaluate the relative level of bond at the substrate/repair material interface. The results of the split cylinder testing from cores taken through the repair material/substrate joint indicated bond strengths of 294 psi, 469 psi, and 597 psi for the Class AA, J3, and Ductal® repair materials, respectively. These results indicate excellent bond of the two UHPC mixes and that any corrosion at the joint between the repair materials and the substrate was not the result of water infiltration due to substandard bond. Photographs of the J3 and Ductal® split cylinder specimens are shown in Figure 6.38.

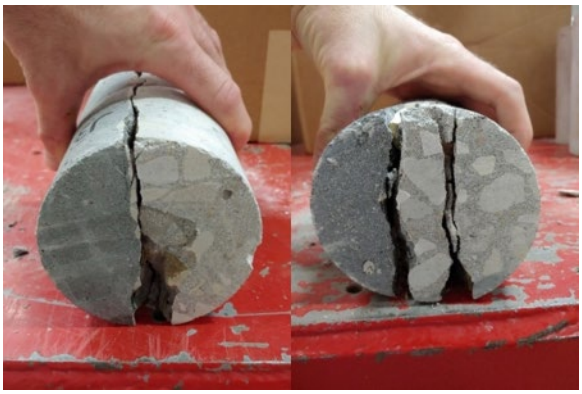

Figure 6.38. J3 (left) and Ductal® (right) split cylinder test specimens

Similar to the small-scale corrosion testing, visual examination is the primary tool available for analyzing the final results of this large-scale corrosion testing. However, based on all of the results, the large-scale joint corrosion testing revealed J3 to have the highest corrosion resistance followed by the Class AA, Ductal®, and Phoscrete® materials.

7.0 Field Implementation

7.1 Overview

The research team coordinated with ODOT to identify two bridges, both in Field Division 6, for field trials of the repair materials and techniques examined in this project. Bridge deck soffit repairs were conducted with MALP concrete instead of end region repairs due to availability of the bridges and continuity connections were repaired using UHPC. Once the bridges were identified the locations were surveyed to develop recommendations for the repairs that were reviewed by the ODOT Division. The research team then coordinated with ODOT on specifications and drawings detailing the extent of concrete removal, any necessary repairs to internal reinforcement, details of the mix designs, mix preparation methods, placement techniques, and locations of any internal data acquisition equipment. Both projects were done by a third-party contractor with the research team providing guidance and monitoring.

7.2 S.H. 3 over Fulton Creek in Beaver County

7.2.1 Overview

The slab cantilevers on the S.H. 3 bridge over Fulton Creek (NBI No.: 21700) were already slated for repair using MALP concrete at the beginning of the project, so this bridge became an obvious choice for inclusion in the project. Plans for the proposed repairs were provided to the research team for comment. The bridge consists of three 70 ft spans and is constructed with precast, prestressed concrete girders and a concrete deck and photos are shown in Figure 7.1. The research team kept in contact with the MALP manufacturer, Phoscrete®, by phone and email through the repair process to discuss plans for and results of the repairs. A meeting was held with Phoscrete® representatives, ODOT Bridge and Division 6 personnel, and the OU research team prior to the repairs to discuss applications and procedures for using the MALP material. A plan was created for documenting the initial condition of the bridge and a plan for instrumenting the proposed repairs to monitor temperature gain and shrinkage was prepared by the OU research team and presented to Division 6 personnel at a meeting in Buffalo, OK on March 19, 2019. ODOT bridge and research

personnel were also present. An initial visit was made to the S.H. 3 bridge over Fulton Creek to take measurements for sensor cables and to better prepare for sensor placement. The slab cantilevers on both the north and south sides of the bridge were repaired using a pneumatic mortar version of the Phoscrete® MALP material and the installation was monitored for approximately 1.5 years after repair for any cracking or evidence of corrosion. This operation was the first overhead placement done with this material in Oklahoma.

Figure 7.1. S.H. 3 bridge over Fulton Creek (NBI No.: 21700)

7.2.2 Initial condition

The initial visit to the bridge indicated substantial spalling damage on the slab cantilever sections on both the north and south sides with more extensive damage on the south side. Exposed reinforcing bars were visible in many locations with most exposed bars showing corrosion damage. Typical spalling and exposed reinforcing bars are shown in Figure 7.2.

Figure 7.2. Typical spalling on slab cantilever of Fulton Creek bridge

7.2.3 Repairs

Two locations were chosen for sensor placement where large portions of the deck concrete had spalled, which would result in a relatively thick repair. One location was near the eastern end of the eastern-most span (span 3) and near the western end of span 3. Both locations were on the south side of the bridge where the damage was most significant and two gauges were to be placed at each location, one parallel to the roadway and one transverse to the roadway. The approximate sensor locations are shown in Figure 7.3.

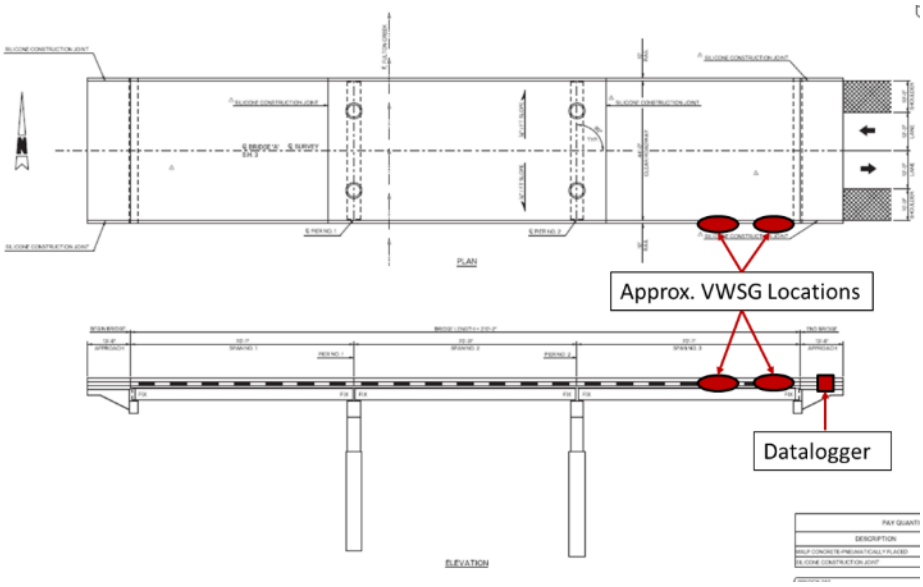

Figure 7.3. Approximate location of vibrating wire strain gauges for monitoring temperature and shrinkage of MALP concrete repair on SH-3 over Fulton Creek bridge

Loose concrete was first removed from the sections of the slab with spalling damage and the edges squared off to create a minimum repair thickness of 1 in. The prepared section is shown in Figure 7.4 and 7.5. Due the chemical nature of the MALP repair, the surface to be repaired was left dry for application of the material.

Figure 7.4. Slab cantilever section after removal of loose material (left) and forms in place for the repair (right)

Phoscrete® MALP pneumatic mortar was used to repair the deck slab overhang on the bridge. Required instrumentation was installed on the southwest side of the bridge on April 11, 2019, after demolition was completed and before the repair material was placed. Two of the strain gauges are shown in Figure 7.5. MALP mortar was dry packed around the strain gages before being placed pneumatically in order to protect the strain gauges without notification of the research team, which reduced the amount of data collected on temperature rise of the repair material. Initial placement of the repair material was conducted on April 15, 2019, but a problem was encountered with the pump used to place the material due to the stiff basalt fibers in the MALP material clogging the nozzle. A new machine was identified by the contractor and work was resumed on April 18, 2019.

Figure 7.5. Strain gauge placement within the area to be repaired on the south side of span 3 of the S.H. 3 bridge over Fulton Creek in Beaver County

Placement of the MALP mortar is shown in Figure 7.6. The mix was adjusted to obtain the proper consistency under the direction of the Phoscrete® representative and the material had to be placed in two thin layers, otherwise it would not properly stick to the underside of the slab. A significant quantity of the initial placement was lost to material rebound, but this improved over time. The Phoscrete® representative indicated some adjustments to the process were not unexpected. A portion of the repair after placement of the first layer of material is shown in Figure 7.7. The Phoscrete® MALP material should chemically bond to itself such that cold joints will not be a problem, but the placement in layers and fast set of the material resulted in a very rough surface as shown in Figure 7.8. As the placement progressed and the mixture was adjusted the surface finish of the material improved significantly and the final placements had a much better appearance, which can be seen in the comparison in Figure 7.9. However, less damage was present on the north side of the bridge, which required less material to be placed. OU research team representatives were present for placement of the first layer on the south side of the bridge (April 18, 2019 and April 19, 2019), and the remainder of the repair was completed during the week of April 22, 2019 to April 26, 2019.

Figure 7.6. Placement of MALP mortar on the S.H. 3 bridge over Fulton Creek in Beaver County

Figure 7.7. Repaired section at the location of the westernmost strain gages (Figure 7.4) after the first layer of MALP was placed

Figure 7.8. Close-up of MALP repair after placement of the first layer

Figure 7.9. Close-up initial MALP placement on the southeast side (left) and later MALP placement on the northeast side (right) showing difference in surface finish of repair

7.2.4 Monitoring

Visits were made to the S.H. 3 bridge over Fulton creek in Beaver County in May, July, September, and December 2019 to download the strain gage datalogger and examine and document the post-repair state of the bridge. Additional visits were conducted to document the post-repair state in June and October 2020 as allowed by the COVID-19 related travel restrictions imposed on OU personnel. Detailed photos were taken of all the repaired areas at each visit by starting 20 ft from the eastern end of the bridge and taking a photo of the underside of the slab cantilever every 10 ft on both north and south sides. Some locations were noted where the repair was very thin, as indicated by reinforcing steel exposed when the drip edge was cut, and some locations were noted where sections had set before completely bonding to the concrete. Over time no additional deterioration was noted around the spots of exposed rebar where the drip edge was cut (Figure 7.10), but a few cracks (4-6 on each side) were noted in the repair material on both the north and south sides of the bridge. Most of these cracks did not appear to grow significantly over time and were primarily attributed to the thin repair. One location of spalling was observed on the north side of span 3 approximately 10 ft east of mid-span that did appear to worsen over time (shown in Figure 7.11). Figure 7.12 shows the repair section around the westernmost strain gauges (also shown in

Figure 7.4 and Figure 7.7) over time. This section is representative of the overall behavior of the repairs.

Figure 7.10. Rust spot in thin section of MALP repair where drip edge was cut on the south side of the bridge

Figure 7.11. Repair spalling on the northeast side of the bridge 18 months after repair

Figure 7.12. Section of completed MALP mortar repair on south side of span 3 of the S.H. 3 bridge over Fulton Creek in Beaver County near the west end of the span 3 months (left), 8 months (middle), and 18 months (right) after placement

Additional information was obtained from an inspection of the S.H. 3 over Fulton Creek bridge made by ODOT personnel on July 9, 2019 that included evaluation of bond strength using a hammer test. Hammer testing indicated adequate bond of the repair material. As previously documented, both inspections showed some exposed rebar where a thin section of repair overlapped with cutting the drip edge on the slab soffit. ODOT personnel also examined the Packsaddle Bridge on US-273 over the Canadian River at the Ellis/Roger Mills county line (NBI No.: 21132), which has a section of slab soffit repaired with a similar MALP material to that used on the Fulton Creek Bridge. The repair on the Packsaddle Bridge was made on March 1, 2017. The MALP material used there was hand placed and did not contain any fibers. A single rust spot was visible within the repaired area at a location where it is believed that either the rebar mat or chair was near the soffit surface. Additional rust spots were observed outside of the repair area. Both areas are shown in Figure 7.13.

Figure 7.13. Rust spot within the MALP repaired area on the Packsaddle Bridge (NBI 21132) (left) and rust spots outside but near the repaired area (right). Photo courtesy of Walt Peters.

While the exposed rebar locations at Fulton Creek and on the Packsaddle Bridge were small and did not exhibit significant deterioration over time, it is recommended that any such defects are coated with clear epoxy to protect from moisture ingress, but to allow for future observation.

The strain gauges placed in the Fulton Creek bridge repairs provided limited information due to the placement of dry packed material in advance of the pneumatic mortar and before the dataloggers were engaged. Figure 7.14 shows the temperature measurements from the gauges over the first month in service. After a spike on casting day, the repair material generally followed the ambient temperature with allowance for the fact that the datalogger was in the shade while the repairs were on the south side and exposed to the sun. Figure 7.15 shows measured strain over time. In general the material shows dimensional stability with no more than 100 microstrain of shrinkage or expansion measured for any gauge except the longitudinal gage on the west end of span 3. This gauge showed a substantial jump in measured strain after approximately two weeks in service. This could be attributed to a delamination of the section at that location; however, the large change is not corroborated by the transverse gauge at the same location.

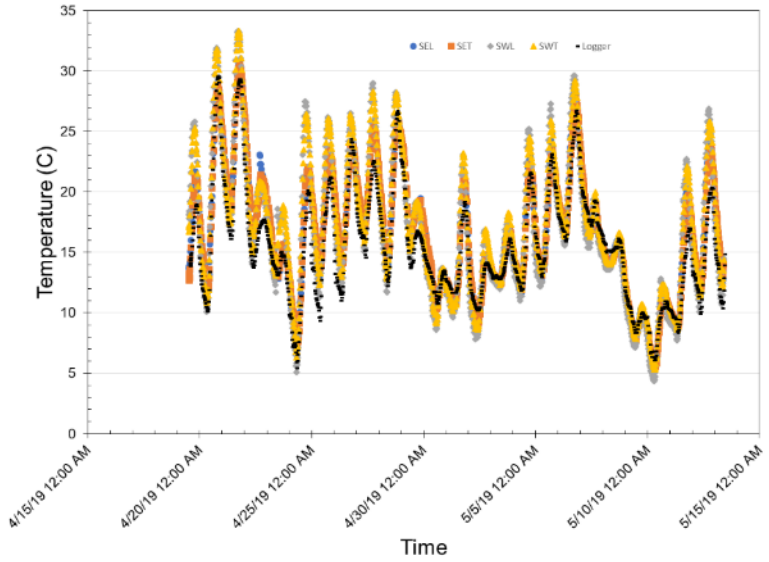

Figure 7.14. Temperature history of MALP repair material on Fulton Creek bridge over the first month in service.

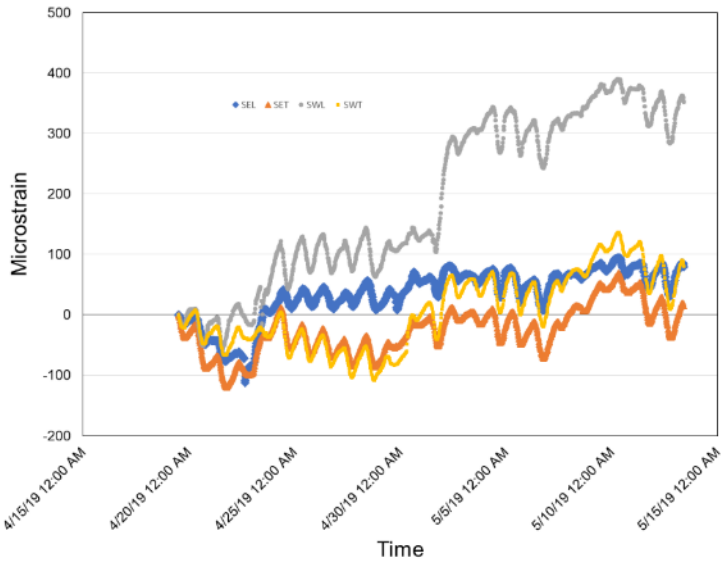

Figure 7.15. Measured strain over time for MALP repair material on Fulton Creek bridge over first month of service

7.3 U.S. 183/412 over Wolf Creek in Woodward County

7.3.1 Overview

The U.S. 183/412 bridge over Wolf Creek in Fort Supply in Woodward County (NBI No.: 21124) was selected for continuity connection repairs using UHPC at the meeting with Division 6 in Buffalo, OK, on March 19, 2019. This bridge is considered to

be representative of a number of in-service bridges in Oklahoma that were designed using simply supported precast, prestressed concrete girders made continuous for live load with approximately 10 in. thick individual continuity joints connecting the two girder ends from each span. These joints were typically connected to the base of the girders using up-turned prestressing strands and mild steel bars and were cast simultaneously with the deck such that the deck reinforcement served as the negative moment reinforcement. Creep and shrinkage strain in the precast concrete girders over time combined with restraint of the system caused positive moments at the continuity joint locations. For many bridges, these moments, were large enough to cause cracking at the base of the linkage blocks such as that shown for the Wolf Creek bridge in Figure 7.16. All continuity connections were demolished from the bridge and replaced with a proprietary UHPC material. Load tests were conducted before and after retrofit of the bridge to evaluate the effectiveness of the repair at restoring continuity.

Figure 7.16. Example of positive moment cracking in a continuity joint of the U.S. 183/412 bridge over Wolf Creek

7.3.2 Bridge Description

The bridge evaluated in this study was constructed in 1985 and its National Bridge Inventory number is 211240000000000. The bridge carries U.S. 183/412 and crosses over Wolf Creek in Fort Supply, OK. A plan view and a cross-section of the bridge are shown in Figure 7.17 and Figure 7.18. Each of the five spans consist of five AASHTO Type IV girders spanning approximately 85 ft that are spaced 9.75 ft across the width of

the deck. There is a 3.5 ft deck overhang beyond each exterior girder. The deck is 9.25 in. thick. Spans one and five are simply supported, while spans two through four are connected at piers 2 and 3 with continuity joints. There are a total of ten continuity joints which only connect the individual girders and do not connect the adjacent five girders across the width of the bridge as a diaphragm. The design intent of the continuity joints was to create continuous spans for live load. The joints located on pier three are shown in Figure 7.19. The damage evident on the joints appears to be cause by positive moment bending that could have been cause by creep, shrinkage, and potentially thermal loading. This damage was seen in all ten joints in the bridge. The bridge has been deemed safe for public use by ODOT when assumed behaving as five simply supported spans, but the bridge load rating was reduced to reflect the loss of continuity.

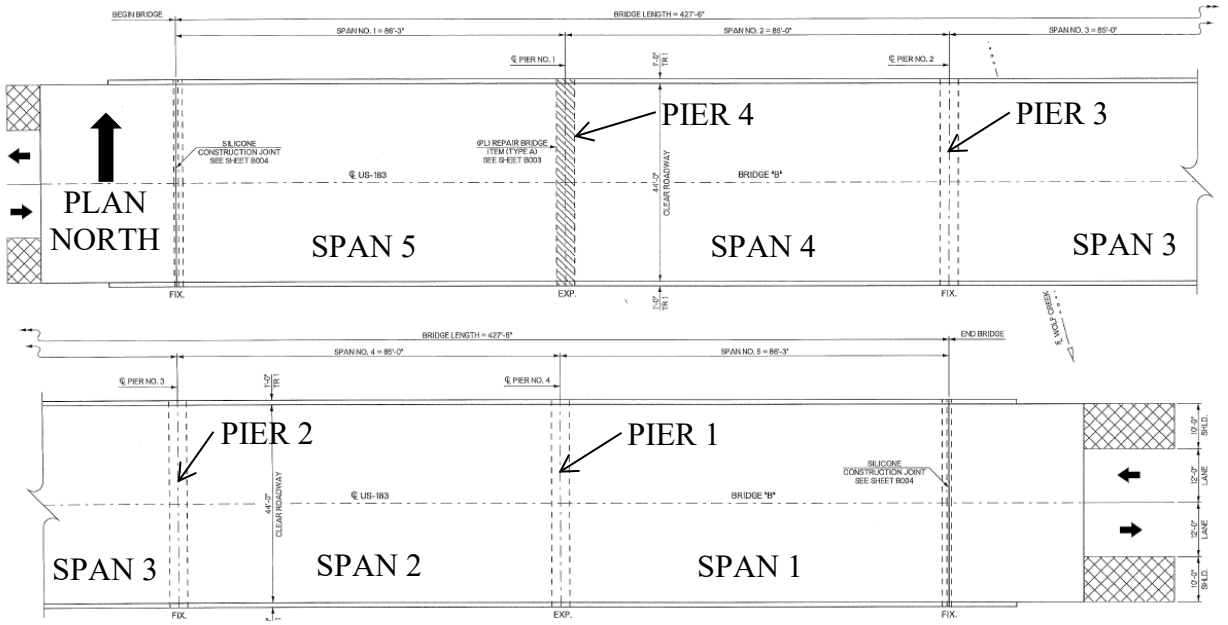

Figure 7.17. Plan view of U.S. 183/412 over Wolf Creek bridge

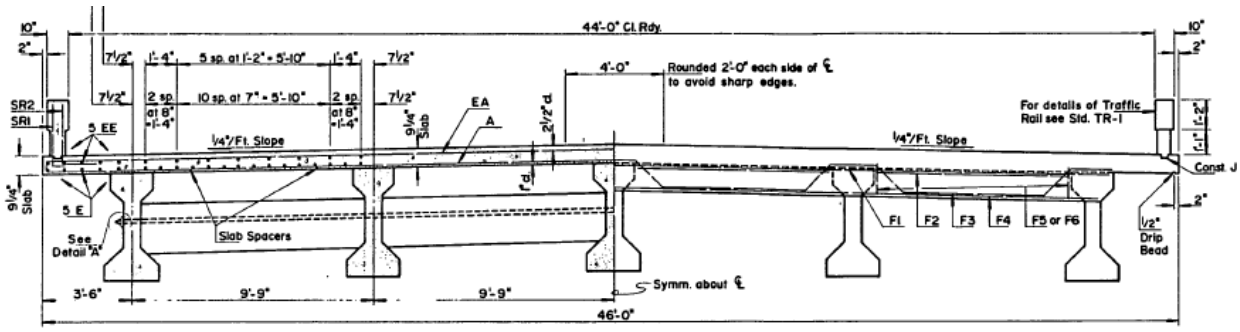

Figure 7.18. Cross-section view of U.S. 183/412 over Wolf Creek bridge

Figure 7.19. Joints at pier 3 prior to repair (left) and typical damage (right)

The original details used for the joint construction are shown in Figure 7.20. To construct the joint, the girders were placed on the pier cap with their ends 10 in. apart. Each continuity joint was reinforced with both prestressing strand and mild steel reinforcing bars. Six prestressing strands at the bottom of the girder extended a length of 3 ft past the girder ends and were bent at a 90° angle approximately 6 in. from the girder face. At the top of the joint, six No. 4 Grade 60 reinforcing bars that were bent to a 90° angle were placed at the top of the joint with the 18 in. leg tired to the bottom deck bars and the 32 in. leg extending down into the joint. Six straight 18 in. long bars were placed perpendicular to the girder span with two at the top and bottom and two in the middle. The joint was formed to be the same width as the top bell of the girder with that width extending down until it intersected the bottom bell, then the joint was formed to match the contour of the bottom bell.

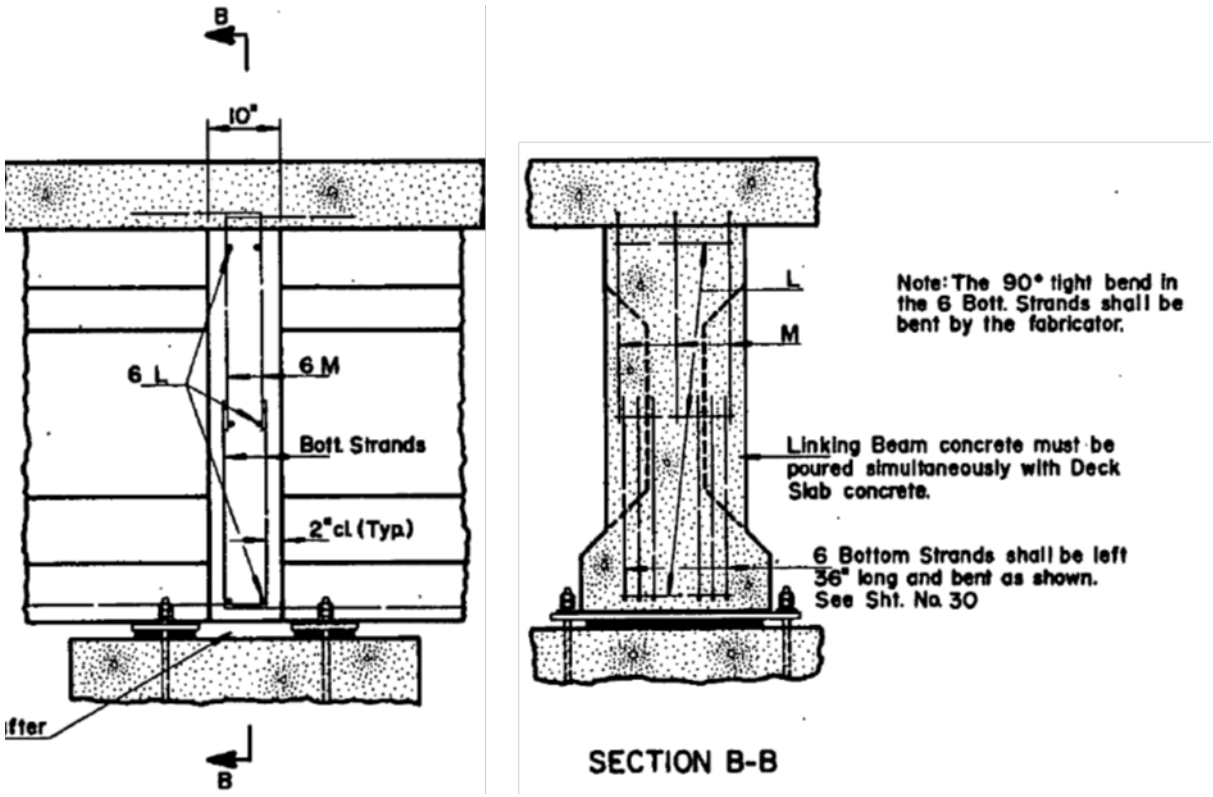

Figure 7.20. U.S. 183/412 over Wolf Creek continuity joint details from original drawings

7.3.3 Load Test Procedure

Displacement measurements were taken at the center of span 4 on all five girders during controlled load tests conducted before and after repair to assess the continuity of the spans at each girder location. The primary measurement method involved using a Craftsman® Laser Distance Measurer, which can measure to the nearest 1 mm. Individual stands made of steel tube welded to a 12 in. long C12 base were centered under the midspan of each girder and stabilized by burying the channel in the surrounding sand and then placing a 60 lb tube of sand over the base. Care was taken to ensure each stand was completely plumb prior to burying the base by placing a 2 ft level to each side of the tube. After the stands were leveled, the laser distance measurers were attached to the vertical tubes using small C-clamps and were also plumbed prior to tightening the clamp. Once attached, a test measurement was taken to ensure the laser was aimed at the bottom bell of the girder.

Secondary measurements were taken using plumb bobs hung from each girder and wooden rulers. A woodworking clamp was attached to the bottom bell of each girder and a length of string with a plumb bob attached to its end was attached to the clamp arm. After placing the string, a stake was driven into the ground directly beside the hanging plumb bob to a sufficient depth to ensure it did not move during the duration of the test. Once the stake was driven in, a wooden ruler was centered on the end of the plumb bob, leveled, and taped to the side of the stake. This setup allowed for the researchers to line the end of the plumb bob up with the ruler using a speed square and take a reading at each loading condition to manually monitor the deflection to the nearest mm. The main purpose of this measurement method was as a check on the laser distance measurer. The completed measurement setup is shown in Figure 7.21.

Figure 7.21. Laser measurer and plumb bob setup (left), clamp on the girder bottom (middle), and method used for measurement with the plumb bob (right)

A third method of measurement was also used on the southern exterior girder to verify the other two measurement methods on a single girder. A scale with 3 mm precision was printed onto a sheet of standard letter paper and taped to the outside face of the exterior girder on span 4 at midspan. A standard surveyor level was placed approximately 100 ft away on the embankment and lined up with the scale. This allowed for readings to be taken from the side of the girder during the load test. The main purpose of this form of measurement was to provide a secondary check on both the laser distance measurer and the plumb bob at the exterior girder.

The girders were numbered with girder 1 being on the south side of the deck and girder 5 being on the north side of the deck. The bridge was loaded using two dump trucks filled with approximately 9 m^3 of 3/8 in. chipped crushed stone. The trucks were measured to ensure that the center of the truck's wheelbase was placed at the center of the span under consideration for each load stage. The total truck weight was ultimately limited due to a limit on the overall length. Due to the relatively short bridge span length, a smaller wheelbase truck was necessary to ensure the wheels did not spread the load too close to the girder ends. Table 7.1 shows the dimensions and weights of the trucks. Note that Truck 2 was the same truck for both tests.

Table 7.1 Truck information

Truck	Truck 1 Pre-Repair	Truck 2 Pre-Repair	Truck 1 Post-Repair	Truck 2 Post-Repair
ID	86-5048	86-4891	86-5114	86-4891
Weight (lb)	50780	51060	55260	55880

Once all the measurement methods were put in place and prior to truck placement on the bridge, initial measurements were taken as a starting point for the bridge. Flaggers were used to reduce traffic to one lane through the duration of the load test. Traffic was restricted to the north lane and the loaded trucks placed in the south lane throughout testing. Care was taken to ensure deflection readings were taken when no additional truck traffic was on the bridge along with the loaded dump trucks. During the load stages when both trucks were on the same span simultaneously, traffic was halted completely, and a truck was placed in each of the traffic lanes for the measurement. The trucks were staged at various locations on the bridge simultaneously to assess the level of continuity provided by the joint before and after repair. The truck locations at each load stage are shown in Figure 7.22. At each load stage, the trucks were stopped on the designated span such that the center axle was located at the midspan of the girders and a measurement was taken using each method. The initial measurement was then subtracted from each loaded measurement to obtain deflection. The trucks at Load Stage 6 are shown in Figure 7.23.

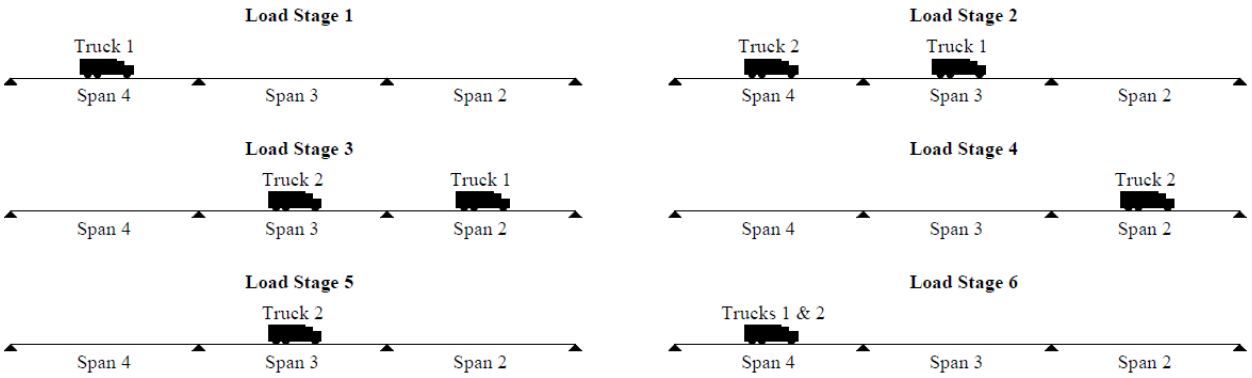

Figure 7.22. Truck locations for each load stage

Figure 7.23. Trucks located for Load Stage 6

7.3.4 Continuity Joint Instrumentation and Repair

After the initial load test was conducted, the process of replacing the conventional concrete continuity joints with UHPC was started. The existing continuity joints were completely demolished. After the concrete was removed and before the UHPC was placed, researchers embedded a foil strain gauge and a vibrating wire strain gauge in the center and south exterior joints located at pier 3. Prior to field installation, foil gauges with 6 mm gauge lengths were attached to 8 in. lengths of sacrificial No. 3 reinforcing bar. The bars with the foil gauges attached were tied to the bottom layer of prestressing strand extending from each girder end using steel tie wire. Then the vibrating wire strain gauges were attached to the top layer of exposed bottom strands using plastic cable ties. The vibrating wire strain gauges used for this project were 6 in. gauge length Geokon® model 4200 gauges with built-in thermistors. Foam blocks were

placed between the strands and the vibrating wire strain gauge to protect it and give the ends room to be fully encased in UHPC. Each gauge was placed parallel to the span of the girders to monitor bending strains. The final gauge placement is shown in Figure 7.24. The wiring for each gauge was tired to the bar or strand for strain relief directly beside each gauge and then was routed along a girder end before being fed through the formwork to allow for connection to lead wires for the final load test.

Figure 7.24. Strain gauge placement in the joint

Once the gauges were placed in the two continuity joints, the formwork was closed for UHPC placement. The proprietary UHPC product, Ductal®, was chosen for use in the continuity joints. This is a prepacked UHPC material consisting of bags of the dry constituents, superplasticizer, and 2% steel fibers by volume. Placement of the UHPC for the linkage blocks was done in three pours on November 6, 8, and 20, 2019. At least one representative from the OU research team was on site to observe each pour and a representative from LafargeHolcim was present on site during all pours to direct mixing of the Ductal® UHPC, run fresh property tests, and cast compressive strength cylinder specimens. An ODOT inspector was also on-site monitoring progress of the job, and several Division 6 personnel were present for the first two days of placement to observe. Bagged Ductal® premix was delivered to the site along with the associated steel fibers and high range water reducer and all materials were kept in a large storage container. The contractor provided the mixing water. All UHPC materials were heated to the temperatures specified on the plans using portable heaters placed at

the opening of the storage container where the materials were stored on the bridge site. Mixing water was warmed with a portable water tank heater. Water and steel fibers were weighed for each batch using a portable scale. The material was mixed in 750 lb batches (approximately 4.7 ft^3) using a high shear pan mixer rented from LafargeHolcim (Figure 7.25) that was placed on span 3 between the two linkage block locations (piers 2 and 3). A backup mixer was also on site in case any problems were encountered with the first mixer. The time at beginning of mixing, time water was added to the mixer, time the mix was discharged, temperature, and flow were recorded for all batches by the LafargeHolcim representative, ODOT inspector, and OU research team.

Figure 7.25. High shear pan mixer in place on the bridge deck (left) and placement of UHPC materials in the mixer (right)

A one-half size trial batch was mixed on November 6, 2019 before any placements were made to ensure that all equipment was working properly, that the material would achieve the required flowability, and to allow the contractor to become familiar with the mixing process. The trial batch was successfully completed with a 69° F temperature and 8 in. flow, and six compressive strength cylinders were cast. The inside of the forms and the beam ends were then prewetted using a garden sprayer placed through the pour holes. UHPC was poured into the continuity joints through 2.5 in. holes cored through the top of the bridge deck centered on the joints. Since Ductal® requires a sacrificial 3/8 in. pour height above the top of the deck, a 1.5 in. tall piece of lumber with the same size hole was attached to the bridge deck to provide the additional height to the pour. The pour holes are shown in Figure 7.26. Initially the

material was placed into the fill holes in the deck using a steel funnel as shown in Figure 7.27 but was eventually poured directly into the pour holes from the plastic five-gallon buckets used to transport the material from the mixer.

Figure 7.26. Pour holes for UHPC joints on the Wolf Creek bridge

Figure 7.27. Placement of UHPC into fill hole in the bridge deck

The joints were replaced in two stages to allow for traffic in one lane while the contractor worked on the other half of the bridge. Mobile traffic lights placed at each end of the bridge were used to automatically control traffic. The first stage of replacement was on four joints on the north side of the deck (two on pier 2 and two on pier 3) on November 6, 2019. Since this project was the first time the contractor used UHPC, a test batch was scheduled with the Ductal® representative to familiarize the contractor with the unusual mixing procedure, quality control testing, and workability. Directly after the test batch, a full batch was mixed to start pouring into the continuity joint forms. However, after filling approximately half of the first joint, the forms began to leak around

the edges. The leak appeared to be caused by hydrostatic pressure that UHPC creates due to its tremendous flowability. Each joint was more than 5 ft tall which resulted in significant pressure on the bottom of the formwork. The contractor was unable to stop the leak, so the forms were removed, the joint was cleaned out, and the formwork replaced for a second attempt. Even though the material had been in the forms for over an hour, the material flowed out of the linkage block formwork, off of the pier cap, and onto the ground to form a puddle on the ground (Figure 7.28). Compressed air and a pressure washer were used immediately to clean the remaining material out of the joint. Braces were wedged between the forms to force the forms against the girders and brace against lateral movement to reduce the chance of leaking. For the exterior girder the braces were supported by lumber directly attached to the deck soffit and to the girder bottom flange. The braced forms are shown in Figure 7.29.

Figure 7.28. UHPC from failed formwork

During the second attempt at pouring the four north joints, the foam board used to support the bottom of the form compressed under the weight of the UHPC as it was poured into two separate joints, which caused the joints to leak through the bottom seam. The contractor was able to wedge the bottom form into place quickly so very little material was lost. The remaining joints on the north pour were then filled without any additional issues. Wood bases were used in lieu of foam board for the second stage of six joints on the south half of the deck to ensure this issue did not occur again. Once the UHPC reached at least 14,000 psi, the traffic lane was switched to allow the contractor to work on the remaining six continuity joints.

Figure 7.29. Final joint forms after adding bracing

The continuity connections on the southwest side of the bridge were cast on November 20, 2019 from a total of 9 full batches (750 lb each) and one-half batch. It began to rain during the next to last batch of UHPC, but the mixer was covered, the pour holes covered between placement, and no detrimental effects were observed. The center joint and the south exterior joint on pier 3 where the gauges were installed were filled during the second pour. One form wall failed during the pour due to failure of a concrete anchor, but the contractor was able to reinstall the formwork for the affected joint while filling the other joints. Also, small leaks were observed on several joints at the form seams where it appeared the sealant used did not completely seal the seam. These leaks did not create a large loss of material and stopped soon after starting, likely due to blockages caused by the fibers. The six joints in the second stage were filled the same day. No leaks occurred in the instrumented joints.

Another issue that occurred during placement was constant settlement of the UHPC in the joints after the initial top-off of the forms. The material was poured into a 2.5 in. hole and the top bell of the girder was 20 in. wide, which left a 90° jog along the bottom of the bridge deck. As the UHPC reached the bottom of the bridge deck, air was trapped in the corners of the forms. Due to its viscosity and slow setting time, the entrapped air took up to several hours to be released through the hole. This delay in air release caused the top of the pour to slowly settle after form top-off, leaving the top surface as much 8 in. below the top of deck in several joints. However, no joint settled

below the bottom of the bridge deck, so each joint was filled completely. A completed UHPC continuity joint is shown in Figure 7.30. Once the wood was removed from around the pour holes on the bridge deck, the contractor manually dug out the voided surface at the top of the UHPC pour then used Rapid Set® Concrete Mix to fill the holes to the top of the deck.

Figure 7.30. Completed UHPC continuity joint after form removal

7.3.5 Post-Repair Load Test

The post-repair load test was conducted approximately one year after the joints were cast. The same measurement methods were employed on the second load test for direct comparison of test results. In addition, the two embedded strain gauges were used to collect strain data throughout testing. The foil gauge was monitored continuously during the test using a National Instruments® data acquisition and the program LabVIEW®. Lead wires were attached to the foil gauge wires extending out of the joint and the lead wires were attached to a National Instruments® 9236 Input Module. The additional resistance caused by the long lead wires was accounted for in the data collection program. The vibrating wire strain gauge data was collected throughout testing and manually during each load stage using a Geokon® data logger. The same load stages used for the initial load test were repeated.

7.3.6 Discussion of Results

7.3.6.1 UHPC Joint Construction Data

Eighteen compression test cylinders were cast for the first UHPC pour and shipped to the ODOT Materials Division for testing after being allowed to cure for three days. Testing was planned for 4, 7, 14, and 28 days along with six cylinders to be provided to the OU research team for companion testing. At the time of the four-day tests it was discovered that the ODOT materials division cylinder grinder was not capable of grinding 3 in. by 6 in. cylinders. The four-day cylinders were tested with only sawcutting used for end preparation resulting in a compressive strength of 10,010 psi, less than the required 14,000 psi. The cylinders were then transported to Fears Lab for grinding on day 5. The OU research team ground the remaining cylinders and returned them to ODOT Materials Division for testing. The OU research team tested a comparison cylinder at 5 days of age that achieved a compressive strength of 16,140 psi. Results of all compressive strength tests are shown in Table 7.2. The average 28-day compressive strength of the UHPC used for all of the joint pours was over 24,000 psi. No individual test was below 21,700 psi. All joint material was able to reach the strength required for resumption of traffic and form removal after five days. On the pour day for the south six joints, the Geokon® data collection system used to monitor the vibrating wire strain gauges, was programmed to take readings every 15 minutes to monitor the heat gain during curing. The heat gain and ambient temperatures are shown plotted in Figure 7.31. The UHPC placement including the instrumented joints began at approximately 8:00 a.m. There is a slight increase in temperature upon initial curing, but the curing temperatures remained relatively low. This could be due to the colder ambient temperatures, as well as the tendency for UHPC to cure at a slower rate due to the high dosage of high range water reducing admixture (Floyd et al. 2019 and Russel and Graybeal 2013).

Table 7.2. Compressive strength test results for the UHPC used on Wolf Creek bridge

Concrete Age (days)	Casting 2, November 8, 2019 Tested at ODOT Lab (psi)	Casting 2, November 8, 2019 Tested OU (psi)	Casting 3, November 20, 2019 Tested at OU (psi)
3	NA	NA	11,100
4	10,010	NA	NA
5	NA	16,140	15,750
7	16,500	18,070	18,800
14	20,640	NA	19,780
28	24,110	NA	25,340

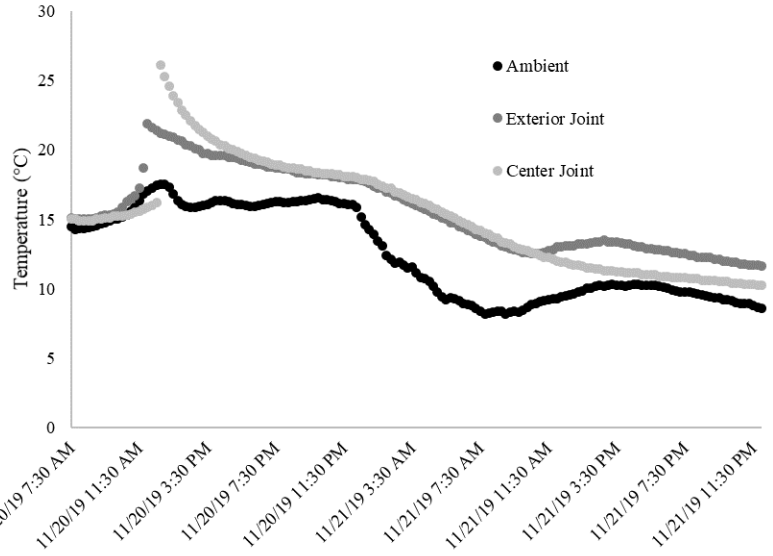

Figure 7.31. UHPC heat evolution for center and exterior joint on pier 3

7.3.6.2 Load Test Results

The midspan deflections obtained for span 4 using the laser distance measurer are shown in Figure 7.32. This figure shows a comparison of results from each load stage before and after continuity joint replacement.

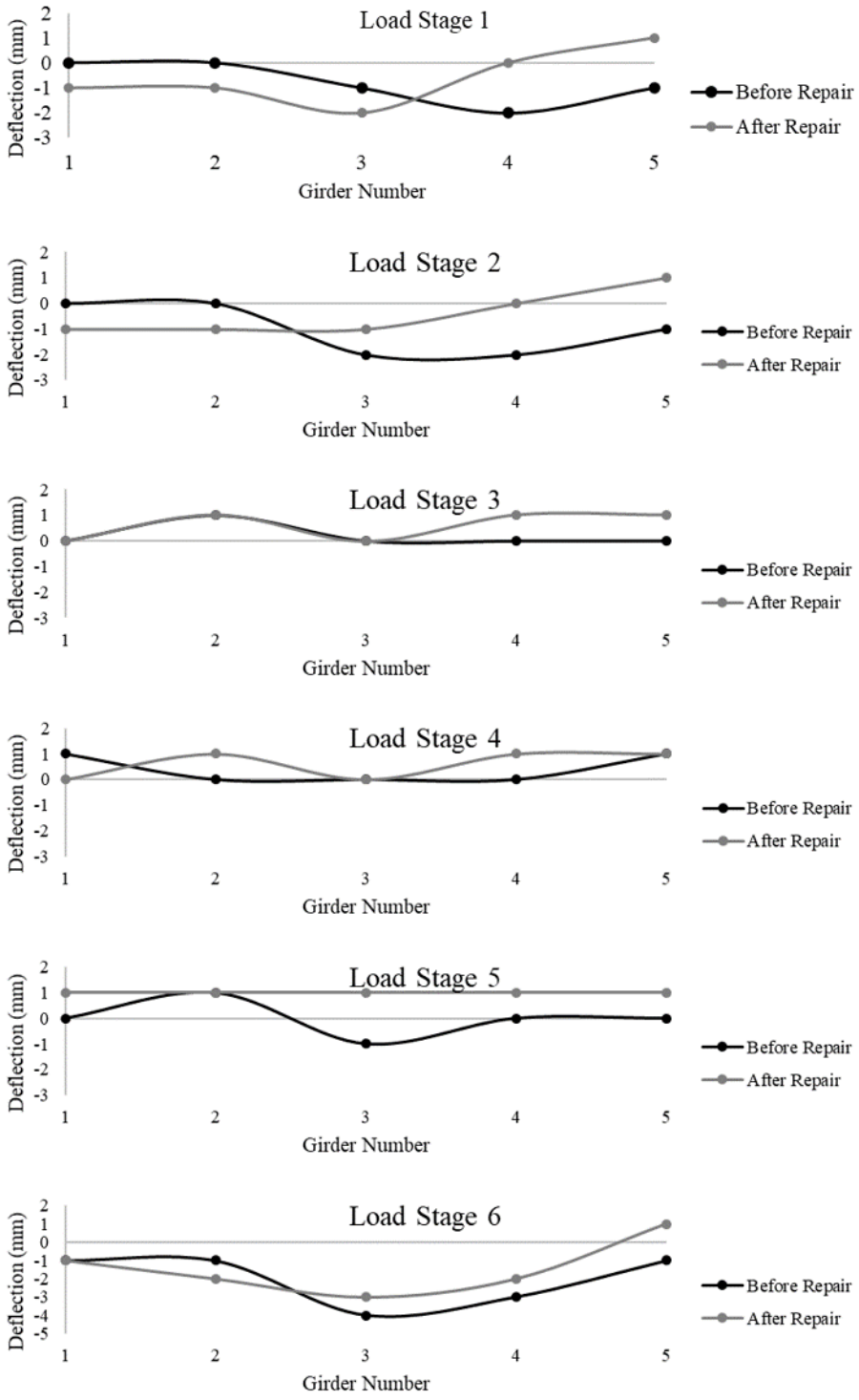

Figure 7.32. Span 4 midspan deflections during each of the six load stages

Due to the stiffness of the bridge, all measured deflections were very small. The largest deflection was observed on load stage 6 of the pre-repair load test, when both

trucks were centered on span 4. Results from load stages 1 through 4 do not appear to show a clear change in behavior due to joint repair. However, there does appear to be a change in behavior for load stages 5 and 6. There is a clear upward deflection measured for load stage 5 post-repair, which is the expected behavior of a continuous beam when loaded on the adjacent span. Also, there was generally less deflection measured in load stage 6 after the repair, which could indicate load sharing across the repaired joint, creating continuous behavior.

Since the measured deflections were so small, hand calculations were completed to verify the test results. A simple calculation was conducted using the parallel axis theorem to determine the overall moment of inertia of the entire bridge deck and girder system using the dimensions from the original construction drawings. The deck was assumed flat and consistently thick throughout the width to simplify the calculations. Once an overall moment of inertia was estimated, deflection calculations assuming both simple supports and assuming continuous supports at the continuity joint locations were conducted. The truck loads were assumed to be point loads centered at the geometric center of the truck wheels. This was done since the actual center of mass of each truck was not determined individually, but care was taken to place the center axle of each truck at midspan of span 4 for each load stage. The expected deflection for the case assuming simple supports was calculated using a standard pre-derived equation for a simple beam subjected to a single point load placed at midspan. The expected deflection for the case assuming a continuous support was calculated using the program Multiframe®. The concrete compressive strength was assumed to be 28 MPa based on ODOT specification requirements for concrete used in bridge superstructures. An analysis was then run using the bridge spans, support conditions, and calculated deck properties.

The results of the hand deflection calculations are shown in Table 7.3. The calculated deflections match closely with those determined during the load tests. When comparing the calculated values to the measured deflections, it appears that the original continuity joint was damaged enough to significantly reduce the level of continuity it provided. Furthermore, the measurements and calculations appear to show that the

UHPC joints are providing continuity for the girder system to behave as continuous system.

Table 7.3. Measured vs. calculated deflections (mm) for center girder of span 4

Load Stage	Measured Before Repair	Calculated for Simple Span	Measured After Repair	Calculated for Continuous Spans
1	-1	-2	-2	-1.5
2	-2	NA	-1	-1.0
3	0	NA	0	0.3
4	0	NA	0	-0.2
5	-1	NA	1	0.5
6	-4	-4	-3	-3.1

Note: NA indicates not applicable for those load stages

7.3.6.3 Strain Gauge Results

The collected foil strain gauge data are shown in Figure 7.33. Since one lane was left open to traffic during load stages 1 through 5, there was additional measured strain even after final truck placement, which is apparent in the spikes during the load stages. The spikes did not occur during load stage 6, since traffic was completely halted while a truck was placed in each lane. The strain values between spikes were averaged for each load stage to remove the effect of the local traffic and isolate the strain caused only by the trucks. In addition to the foil gauges, measurements from the vibrating wire strain gauges were manually collected at discrete points during each load stage. The average foil gauge and vibrating wire gauge readings are shown in Figure 7.34.

The same general trend was observed for each type of gauge and both sets of gauge readings tend to show continuous behavior. The two highest strains were recorded at load stages 2 and 6, which are the truck locations expected to produce the highest moment transfer across the measured joint at pier 3. Also, at load stage 4, a positive moment is recorded by both gauges. This is also expected behavior at pier 3 when a truck is placed at the last span of a continuous three-span system. In all exterior joint readings, the foil gauge measurement was higher than the vibrating wire gauge. This was expected since the foil gauge was placed closer to the extreme edge of the cross-section (see Figure 7.24). However, in all but one reading for the center joint the foil gauge reading was lower than the vibrating wire strain reading. Nevertheless, the

data collected from each set of gauges display the same continuous behavior throughout the test.

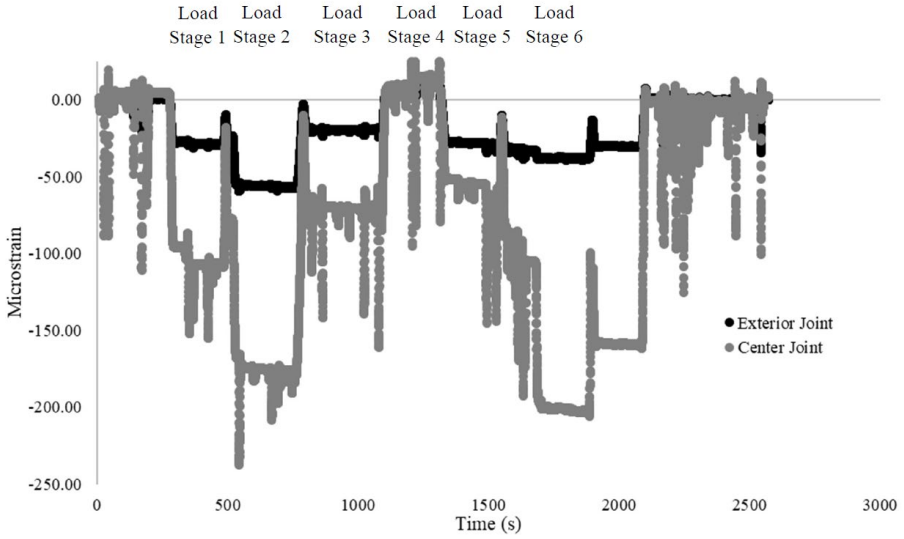

Figure 7.33. Foil strain gauge data for post-repair load test

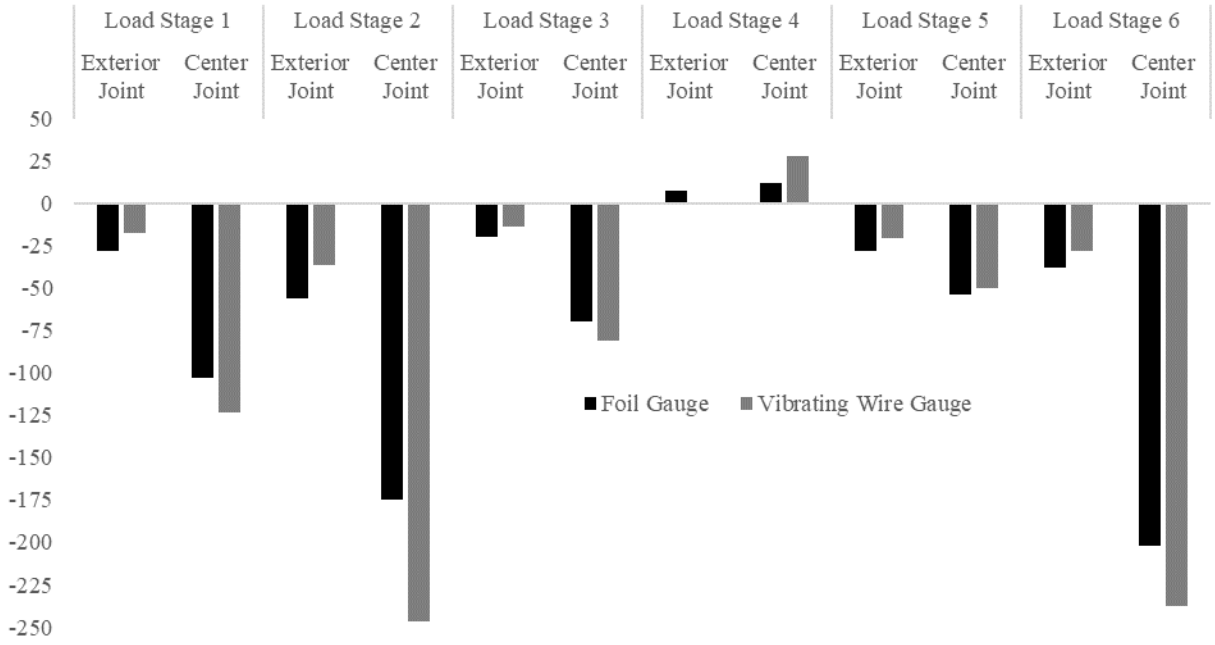

Figure 7.34. Collected average strain gauge readings

7.3.7 MALP Deck Slab Cantilever Repairs

Repairs to the deck slab cantilever soffit were also made with MALP concrete on the Wolf Creek bridge. There repairs began on November 12, 2019 after the first UHPC placement was completed. Additional placements were made in between UHPC pours. Instead of using the shotcrete application, the dry pack Phoscrete® VO material intended for overhead placement was utilized due to smaller areas requiring repair than initially anticipated. A member of the OU research team was present for the first day of placement and photos of patch placement and a finished patch are shown in Figure 7.35. Two vibrating wire strain gages were placed in one of the larger patches on the south side of the bridge, just east of the creek to monitor temperature rise after placement (Figure 7.36). The contractor experienced difficulties getting the material to stick to the bridge deck and the material was still cold twenty minutes after placement. A magnesium oxide accelerator was added to address the problem. The material for the first patch was still moldable after two hours and the material surface temperature was only 15° F higher than the surrounding concrete. A smaller than expected temperature rise was measured at the strain gage location, likely due to the cold temperatures and large thermal mass of the bridge deck. The maximum measured temperature was only 82° F. Monitoring of the gages continued over time, but little additional useful information was gleaned from the data. Hammer soundings were conducted on the patch that exhibited suspect behavior approximately one week after placement. No indication of delamination was observed.

Figure 7.35. Placement of a representative MALP concrete patch (left) and completed patch (right)

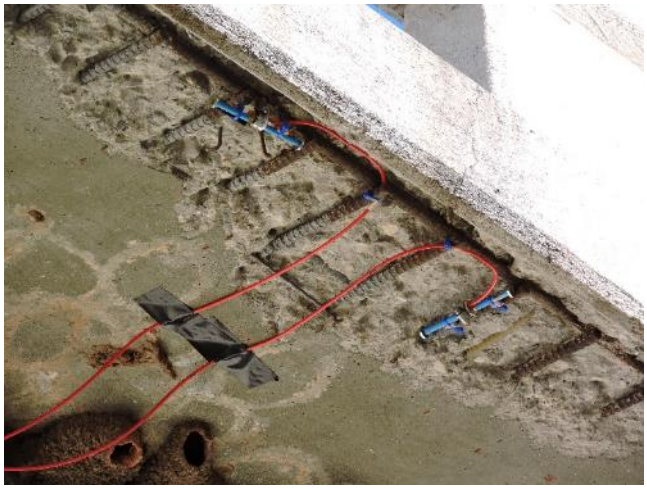

Figure 7.36. Vibrating wire strain gages placed for shrinkage and temperature monitoring

7.3.8 Monitoring

Visits were made to the Wolf Creek bridge on the same increments as for the Fulton creek bridge after November 2019. No deterioration was observed over time in the UHPC continuity connections or surrounding beam locations. No visible deterioration was observed in the MALP deck concrete patches over time either.

8.0 Specification Development

8.1 Overview

Specifications from other DOTs, FHWA, MALP manufacturer Phoscrete, and the UHPC supplier Lafarge were investigated along with reports from the literature specifically focused on prestressed concrete girder repair (e.g., Shanafelt and Horn 1980, Shanafelt and Horn 1985, PCI 2006, Harries et al. 2009) were examined to produce recommendations for draft specifications. Initial procedures, plan notes, and specifications were used in casting the Fulton Creek bridge repair and Wolf Creek joint replacement described in Section 7. A number of areas were identified during the implementation projects where additional information and detail would be useful, primarily related to material preparation before mixing and procedures required for cold-weather conditions. The following sections outline recommendations for the materials tested as part of this project and for the repair applications considered.

8.2 UHPC

UHPC is a relatively new material with limited application in common transportation structures. It is therefore not included in the typical ODOT Standard Specifications (2009). Its composition, mixing requirements, fresh properties, material properties, and required quality control testing methods are significantly different from those of conventional concrete materials.

8.2.1 Material Selection and Preparation

- The Lafarge product Ductal® is an acceptable proprietary material when UHPC is specified.
- Certification of proprietary UHPC performance shall be provided by the manufacturer in the form of test data for the material tests listed in Table 8.1. Specific proprietary materials may be specified by the engineer.
- Certification of non-proprietary UHPC performance shall be provided in the form of independent test data for the material tests listed in Table 8.1.

- When a non-proprietary mix design is specified mixture constituents from the exact same supplier (i.e., cement, supplementary cementitious materials, aggregates, admixtures, fillers) used when certifying the mix design as UHPC shall be used in the field unless the new mixture is subjected to the same tests used to certify the original mix design and is approved by the engineer.
- Water used for mixing UHPC shall meet the requirements for conventional concrete.
- Chemical admixtures shall meet the existing requirements for admixtures and as specified by the UHPC manufacturer.
- Steel fibers shall have a tensile strength greater than 300 ksi or as specified by the UHPC manufacturer to meet the properties listed in Table 8.1. Steel fiber percentage shall be sufficient to meet the properties listed in Table 8.1.
- All materials including but not limited to cement, aggregate, steel fibers, and admixtures, shall be stored according to the UHPC manufacturer's recommendations or in such a way to protect the materials against deterioration of physical and mechanical properties.

Table 8.1. UHPC material property requirements

Property	Test Method	Requirement
Flow, (in.)	ASTM C1856	7 - 10
Minimum 28-Day Compressive Strength[1,2], (ksi)	ASTM C1856 ASTM C39	17.00
Minimum 4-Day Compressive Strength, (ksi)	ASTM C1856 ASTM C39	12.00
Minimum Prism Flexural Cracking Strength[1,2], (ksi)	ASTM C1856 ASTM C1609	1.3
Maximum 28-Day Shrinkage, (microstrain)	ASTM C157	1000
Maximum Rapid Chloride Ion Permeability[2], (coulombs)	ASTM C1202	250
Scaling Resistance	ASTM C672	y < 3
Alkali Silica Reactivity, % Maximum Expansion at 14 days	ASTM C1260	0.1

[1]Use 3 in. x 6 in. cylinders. [2]Ends of cylinders must be ground, saw cutting, capping or use of neoprene pads are not permitted. [3]Material should be tested without steel fibers. [4]Testing shall be after 7-day standard cure and 21 days of water curing at 100 °F.

8.2.2 Mixing Procedure

- Wear PPE as recommended by the UHPC manufacturer.
- Equipment sufficient to mix the UHPC material shall be identified based on the recommendations of the UHPC manufacturer. High shear mixers shall be utilized. For non-proprietary UHPC data shall be provided showing flow meeting the requirement in Table 8.1 using that material.
- The starting temperature of the UHPC constituent materials shall be above 60 °F.
- Perform trial batches, at least one day prior to the expected UHPC placement using the UHPC materials and equipment proposed for construction to demonstration the UHPC can be mixed and placed properly. Conduct a flow test to ensure the material meets the requirement in Table 8.1.
- UHPC shall be mixed according to the UHPC manufacturer's recommendations.
- The following procedures may be used for mixing UHPC:
    - Weigh all materials and add ½ of the required HRWR to mixing water.
    - Mix premix or dry components dry for 2 minutes for proprietary UHPC, 10 minutes for non-proprietary UHPC.
    - Add water (with ½ HRWR) slowly over the course of 2 minutes.
    - Continue mixing for 1 minute.
    - Add the remaining HRWR over the course of 1 minute.
    - Mix will turn from powder to paste to flowable material (time for this varies but can take up to 30 minutes).
    - Once mix turns to flowable material, add steel fibers over the course of 2 minutes.
    - Mix for an additional 1 minute after fibers are dispersed.
    - Typical average total mixing time is approximately 20 minutes.
    - Discharge an amount sufficient for temperature and flow measurements.

- Add additional HRWR if flow is insufficient.
- Retest temperature and flow if adjustments were made.

8.2.3 Quality Control

- Perform all testing based on recommendations of ASTM C1856 “Standard Practice for Fabricating and Testing Specimens of Ultra-High Performance Concrete” when applicable. At a minimum, the tests listed in Table 8.2 should be conducted.
- Conduct flow and temperature measurements at completion of mixing. Measure ambient temperature in addition to fresh concrete temperature.

Table 8.2. UHPC quality control testing requirements

Property	Test Method	Frequency
Flow	ASTM C1856	Every Batch
Temperature	ASTM C1064	Every Batch
Compressive Strength (3 in. x 6 in. cylinders)	ASTM C1856 ASTM C39	At least 3 sets per production day[1,2]

[1]Each set consists of 3 cylinders, [2]make sets of cylinders at intervals throughout the UHPC pour

- At a minimum, test a set of 3 cylinders at end of any heat curing, 4 days after casting, 14 days after casting, and 28 days after casting. Cylinders shall be cured using the same method of curing as in the field.
- Record and report the following for each batch of UHPC:
  - Batch time
  - Testing time
  - Ambient temperature
  - Mix temperature
  - Flow
  - Premix lot (if applicable)
  - Location of placement

- Notes on weather conditions, deviation from these instructions, and any other issues encountered

8.2.4 Formwork and Surface Preparation

- Consult the UHPC material manufacturer (if applicable) for recommendations for formwork design and fabrication.
- Provide impermeable watertight formwork constructed at least ¼ in. higher than required to allow for grinding to the final surface elevation. This extra ¼ in. may be omitted if testing for that particular mix design shows it is unnecessary and results are approved by the engineer.
- A formwork mock-up and placement at least two weeks prior to the UHPC placement is recommended.
- Provide formwork with an impermeable rigid top to prevent moisture loss. Provide a minimum of two holes in the formwork top, one for placement and one to vent at the opposite end. As an alternative, material may be placed directly into the forms and the formwork top placed when the forms have been filled.
- Use a funnel or equivalent apparatus to place the UHPC in order to provide elevation head pressure on the material within the formwork.
- Prepare concrete adjacent to the section to be cast by roughening with an air chisel or sandblasting. Concrete surfaces UHPC will be cast against should be saturated surface dry at the time of concrete casting.
- The temperature of formwork and concrete substrate shall be above 60 °F at the time of casting. Portable heaters may be used to raise the temperature of the formwork and concrete substrate.
- Do not remove formwork until the UHPC has reached a compressive strength of 12 ksi.

8.2.5 Placement

- Prior to the initial placement of UHPC, arrange for an onsite pre-pour meeting with the UHPC manufacturer’s representative (if applicable), and the engineer.

The objective of the meeting is to clearly outline the procedures for mixing, transporting, placing, and curing the UHPC material.

- Only place UHPC if the outside ambient temperature is above 40 °F and below 100 °F.
- Place UHPC following the manufacturer's instructions, if applicable, and as discussed in the pre-pour meeting.
- Transport material from the mixer to joint using plastic buckets, wheelbarrows, or other watertight transport container.
- Pour material into funnel end (or directly into open formwork) and allow to flow with no external consolidation.
- New material shall be placed into already placed material to produce a single flow direction within the formwork. No cold joints shall be permitted between layers of UHPC.
- Do not finish UHPC.
- Fill joint formwork until material comes out of the vent hole and comes to equilibrium with fill hole if using the top formed and vent method. If placing directly into the forms, fill until concrete reaches the top of the forms, then place a section of formwork top on the downhill side of the pour leaving space open to continue placement into already placed material. A hole should be cut into the final section of formwork for placement under pressure head.
- Leave joint under head for curing if possible.
- The UHPC shall be cured according to the manufacturer's recommendations at a minimum of 60 °F to attain the desired strength.
- Heat curing is acceptable if the method is shown to produce the desired curing temperature, does not result in moisture loss in the UHPC, and is approved by the engineer. Curing temperature shall not exceed 190 °F.

8.3 FR-SCC

FR-SCC is a relatively new material with limited application in common transportation structures. It is therefore not included in the typical ODOT Standard Specifications (2009). Its composition, mixing requirements, fresh properties, material properties, and required quality control testing methods are similar to conventional concrete materials, but some special considerations are required.

8.3.1 Material Selection and Preparation

- Cementitious materials, aggregates, and water used for FR-SCC should be adequate for use in conventional concrete.
- Chemical admixtures shall meet the existing requirements for admixtures.
- Certification of FR-SCC performance shall be provided in the form of independent test data for the material tests listed in Table 8.3.
- Specified mixture constituents from the exact same supplier (i.e., cement, supplementary cementitious materials, aggregates, admixtures, fillers) used when certifying the mix design as FR-SCC shall be used in the field unless the new mixture is subjected to the same tests used to certify the original mix design and is approved by the engineer.
- Synthetic fibers shall meet existing requirements for fibers in portland cement concrete and their quantity shall be selected such as to meet the properties listed in Table 8.3.
- All materials including but not limited to cement, aggregate, steel fibers, and admixtures, shall be stored in such a way to protect the materials against deterioration of physical and mechanical properties.

Table 8.3. FR-SCC material property requirements

Property	Test Method	Requirement
Flow, (in.)	ASTM C1611	26 - 30
Minimum 28-Day Compressive Strength, (ksi)	ASTM C39	4
Air Content, (%)	ASTM C231 ASTM C173	6 ± 1.5
Maximum 28-Day Shrinkage, (microstrain)	ASTM C157	600

8.2.2 Mixing Procedure

- Wear PPE sufficient for conventional concrete.
- Mixing equipment sufficient for conventional concrete is sufficient for mixing FR-SCC.
- The concrete producer or contractor shall perform trial batches, at least one month prior to concrete placement to show that the mix can be successfully produced and the requirements for slump flow in Table 8.1.
- The following procedures may be used for mixing FR-SCC:
    - Weigh all materials.
    - Add all the aggregates with half the water and mix for one minute.
    - Add cementitious materials.
    - Add HRWR and then the remaining water to get the desired flow.
    - Add one full dose of citric acid along with the polypropylene fibers.
    - Mix all the materials for 3 minutes, then allow materials to rest for 3 minutes, followed by 2 minutes of mixing.
    - Keep the mixer turning until the repair casting is finished and add an additional full citric acid dose after every 15 minutes to retard the setting of cement. The dose can be reduced proportionally to the remaining concrete.

8.2.3 Quality Control

- Perform all testing based on the applicable ASTM standards. At a minimum, the tests listed in Table 8.4 should be conducted.
- Conduct flow and temperature measurements at completion of mixing. Measure ambient temperature in addition to fresh concrete temperature.

Table 8.4. FR-SCC quality control testing requirements

Property	Test Method	Frequency
Slump Flow	ASTM C611	Every Batch
Temperature	ASTM C1064	Every Batch
Compressive Strength	ASTM C39	At least 3 sets per production day[1]

[1]make sets of cylinders at intervals throughout the FR-SCC pour

- At a minimum, test a set of cylinders at end of curing and 28 days after casting. Cylinders shall be cured using the same method of curing as in the field.
- Record and report the following for each batch of FR-SCC:
    - Batch time
    - Testing time
    - Ambient temperature
    - Mix temperature
    - Slump Flow
    - Location of placement
    - Notes on weather conditions, deviation from these instructions, and any other issues encountered

8.2.4 Formwork and Surface Preparation

- Provide impermeable watertight formwork designed for full hydrostatic pressure of the concrete.
- If using closed formwork or placement through the bridge deck provide a minimum of two holes in the formwork top, one for placement and one to vent at the opposite end.
- A formwork mock-up and placement at least two weeks prior to the FR-SCC placement is recommended.
- Prepare concrete adjacent to the section to be cast by roughening with an air chisel or sandblasting. Concrete surfaces FR-SCC will be cast against should be saturated surface dry at the time of concrete casting.

- The temperature of formwork and concrete substrate shall be above 60 °F at the time of casting. Portable heaters may be used to raise the temperature of the formwork and concrete substrate.
- Do not remove formwork for a minimum of 7 days.

8.2.5 Placement

- Only place FR-SCC if the outside ambient temperature is above 40 °F and below 100 °F.
- Place material directly from a mixer truck or transport material from the mixer/mixer truck to repair location using a watertight transport container.
- Pour material into funnel end (or directly into open formwork) and allow to flow with no external consolidation.
- New material shall be placed into already placed material to produce a single flow direction within the formwork. No cold joints shall be permitted between layers of FR-SCC.
- Fill joint formwork until material comes out of the vent hole and comes to equilibrium with fill hole if using the top formed and vent method. If placing directly into the forms, fill until concrete reaches the top of the forms.
- Wet curing of FR-SCC is recommended if possible given the constraints of a specific placement.

8.4 MALP Concrete

8.4.1 Material Selection and Preparation

- A proprietary magnesium-alumino-liquid-phosphate (MALP) concrete product shall be specified by the engineer. The variant of material used shall be selected based on the requirements of the specific application. Any substitution shall be approved by the engineer.
- Certification of MALP performance shall be provided by the manufacturer for the specific application.

- Only the materials provided by the manufacturer shall be utilized. Nothing shall be added to the mixture unless provided by the manufacturer.
- Fibers and set modifying admixtures may be used per the manufacturer's recommendations.

8.4.2 Mixing Procedure

- Wear PPE as recommended by the MALP manufacturer and the safety data sheets for the material.
- Equipment sufficient to mix the MALP material shall be identified based on the recommendations of the MALP manufacturer.
- The starting temperature of the MALP materials shall not exceed 80 °F.
- Perform trial batches, at least one day prior to the expected MALP placement using the MALP materials and equipment proposed for construction to demonstrate the MALP can be mixed and placed properly.
- MALP shall be mixed according to the UHPC manufacturer's recommendations.

8.4.3 Quality Control

- Conduct tests as specified in Table 8.5.
- Conduct temperature measurements at completion of mixing. Measure ambient temperature in addition to fresh concrete temperature.
- Temperature of placed material shall be monitored using an infrared thermometer to ensure that excessive temperatures, as defined by the engineer, are not exceeded.

Table 8.5. UHPC quality control testing requirements

Property	Test Method	Frequency
Temperature	ASTM C1064	At least once per hour
Compressive Strength	ASTM C39	At least 1 set per production day[1,2]

[1]Each set consists of 3 cylinders, [2]make sets of cylinders at intervals throughout the UHPC pour

- At a minimum, test a set of 3 cylinders at end of any heat curing, 1 day after casting. Cylinders shall be cured using the same method of curing as in the field.
- Record and report the following at least once for each MALP placement:
    - Batch time
    - Testing time
    - Ambient temperature
    - Mix temperature
    - Flow
    - Material lot
    - Location of placement
    - Notes on weather conditions, deviation from these instructions, and any other issues encountered

8.4.4 Formwork and Surface Preparation

- Consult the MALP material manufacturer (if applicable) for recommendations for formwork design and fabrication.
- Prepare concrete adjacent to the section to be cast by roughening with an air chisel or sandblasting. Concrete surfaces MALP will be cast against should be completely dry at the time of casting.

8.4.5 Placement

- A manufacturer's representative shall be on site at the beginning of the first MALP placement and shall be on site for a minimum of one production day.
- Prior to the initial placement of MALP, arrange for an onsite pre-pour meeting with the MALP manufacturer's representative, and the engineer. The objective of the meeting is to clearly outline the procedures for mixing, transporting, and placing the MALP material.

- Place MALP following the manufacturer’s instructions, if applicable, and as discussed in the pre-pour meeting.
- Transport material from the mixer to repair location using plastic buckets.
- New material may be placed onto already hardened MALP material with no additional surface preparation.

9.0 Summary and Conclusions

9.1 Summary

Ultra-high performance concrete (UHPC), fiber-reinforced self-consolidating concrete, and magnesium-alumino-liquid-phosphate (MALP) concrete all have significant potential for use in bridge repair in Oklahoma. However limited data are available for performance of these materials in repair applications. The project described in this report examined the use of these materials in repairs of prestressed concrete girder continuity connections and beam end regions including both experimental testing and field implementation.

Mixing and placement methods, bond between the repair materials and conventional concrete, and corrosion behavior were examined for each repair material. Material property tests were conducted to evaluate the properties of FR-SCC as a repair material to use when strengthening failing existing structures. Twelve composite beam and continuity joint specimens were loaded to induce damage and repaired using FR-SCC, MALP concrete, and UHPC. The repaired specimens were then loaded for either positive or negative moment to represent behavior in the field. All repair materials restored capacity of the joints. Six approximately half-scale AASHTO Type II girder specimens were loaded to failure and repaired using FR-SCC, MALP concrete, and UHPC. Repaired specimens exhibited similar performance for all three repair materials and measured capacities exceeded those for the original beams in all cases.

The soffit of the bridge deck cantilevers on the S.H. 3 bridge over Fulton Creek in Beaver County, Oklahoma was repaired using pneumatically placed MALP mortar and the repairs were monitored over time. Some difficulties were encountered in placing the material, but it exhibited good performance over time. The U.S. 183/412 bridge over Wolf Creek in Fort Supply, Oklahoma exhibited signs of continuity joint failure and was slated for repair using UHPC. A load test was conducted before and after the joint repair to assess the change in behavior after replacing the joints with UHPC. The load test consisted of positioning dump trucks loaded with crushed stone at midspan of each continuous span in various stages and measuring deflections and strains to evaluate behavior of the bridge system.

9.2 Conclusions

9.2.1 Mixing and Placement Methods

- An FR-SCC mix design with adequate flowability, compressive strength, and other material properties was identified.
- The sand-blasted surface finish provided the highest concrete to concrete bond strengths for FR-SCC.
- Higher flowability in general resulted in higher bond strengths for FR-SCC, but it should be noted that none of these mixes exhibited segregation that could adversely affect bond strength.
- Failure of concrete bond specimens using proprietary UHPC typically occurred in the base concrete indicating excellent performance.
- The J3 UHPC material typically exhibited lower bond strength than the proprietary UHPC material, but could achieve similar concrete to concrete bond with proper surface preparation. Sufficient workability is also required to achieve high bond strengths between UHPC and conventional concrete.
- In general, either an exposed aggregate surface or a sandblasted surface prepared with a pressure washer produced the best concrete bond results for UHPC.

9.2.2 Continuity Connection Repairs

- All three repair materials restored the full positive and negative flexural capacities of the damaged continuity joints.
- All three repair materials restored the typical load-deflection response of a reinforced concrete flexural element over the full range of loading.
- The positive moment reinforcement in the continuity joints for all specimens reached yield during the pre-cracking phase, representing the most severe level of damage the joint could receive.
- The FR-SCC was the easiest of the three repair materials to place, followed by the J3 UHPC material, and finally the Phoscrete.

9.2.3 Beam End Region Repairs

- All repair materials effectively restored shear capacity of the beam specimens and increased capacity of the beams beyond both the calculated capacity and measured experimental capacity.
- The UHPC end region repair led to the largest increase in capacity, even with a smaller repair thickness.
- The repaired specimens exhibited significantly less cracking than the original specimens at the same loading increments indicating that these repairs have potential for both shear strengthening and protecting the end region from corrosion.

9.3.4 Corrosion Testing

- The J3 UHPC material exhibited similar performance to the proprietary material Ductal® in all durability testing and even surpassed Ductal® in some aspects of corrosion resistance.
- Results indicated that ODOT Class AA concrete is sufficient for use in the field in moderate-corrosive environments, and causes very little corrosion in steel reinforcing due to the Halo Effect during repairs.
- The J3 UHPC exhibited durability performance sufficient for use in projects where UHPC's additional durability is desirable, such as highly corrosive environments or areas prone to freezing and thawing.
- Phoscrete exhibited some results relative to corrosion resistance that suggest further testing is needed.

9.2.5 Field Implementation

Once the initial problems encountered in application of the MALP pneumatic mortar on the S.H. 3 bridge over Fulton Creek were overcome, the repair method was successfully implemented and appeared to perform well over time. The majority of the repaired areas exhibited no deterioration after 1.5 years in service.

The following conclusions relative to the field implementation at the U.S. 183/412 bridge over Wolf Creek were determined from this study.

- Additional form bracing compared to conventional concrete was required to counter the hydrostatic pressure developed during the tall UHPC pours. Also, several small leaks were found at formwork joint seams that stopped shortly after starting. These issues highlight the importance of building watertight formwork designed for the expected pressure when casting UHPC to ensure no leaks occur.
- Due to its high flowability, it is possible to efficiently pour UHPC through a hole in the deck as small as 2.5 in. in diameter to elements below. However, using such a small hole delays entrapped air from reaching the top surface until hours after topping off the pour, causing settlement of the pour. A larger pour hole or the use of vent holes could further facilitate release of entrapped air, reducing the risk of this settling.
- No excessive heat gain was measured with the vibrating wire strain gauges during curing. This could be due to the cool ambient temperature, as well as the tendency of UHPC to cure slowly.
- The midspan deflection measurements made during the load tests were small and did not conclusively show improved continuity after joint replacement. Due to the short spans, truck length was limited to ensure the load was not spread too far across the span. This truck length limitation created an upper limit on total weight. The truck load stages 1 through 4 appeared very similar, but results from load stages 5 and 6 imply a switch from simple to continuous behavior with the upward deflection noted on load stage 5 and the reduced deflection during load stage 6 after the repair.
- Comparisons were made between measured deflection data with calculations assuming a flat bridge deck and using construction drawing dimensions. While the measured deflections were small, they track very closely with the calculated

deflections assuming simple and continuous behavior. This provides evidence that the UHPC joint replacement UHPC created continuous behavior.

- Foil gauge and vibrating wire strain gauge data displayed the exact same trends throughout testing. Positive moment strains were recorded at pier 3 when a single truck was placed at the far span, which is the expected behavior of a continuous system. Also, the largest strain was measured when a truck was on each span adjacent to pier 3, which is also the expected behavior of a continuous system.
- Overall, the deflection measurements before and after repair, along with the strain gauge data collected after repair, appear to show improved continuity after replacement of damaged conventional concrete continuity joints with UHPC joints.

References

2009 Standard Specifications Book, Construction Engineering Standards, Specifications, Materials and Testing, http://www.okladot.state.ok.us/c_manuals/specbook/oe_ss_2009.pdf, Oklahoma Department of Transportation, 2009.

AASHTO (2014) *AASHTO LRFD Bridge Design Specifications*, 5th edition, American Association of State Highway and Transportation Officials, Washington, D.C.

AASHTO (2017) AASHTO LRFD Bridge Design Specifications 8th Edition, Washington, D.C.

Abosrra, I., Ashour, A. F., and Youseffi, M. (2011) "Corrosion of Steel Reinforcement in Concrete of Different Compressive Strengths," *Construction and Building Materials,* 25(10): 3915-3925.

Aaleti, S., Honarvar, E., Sritharan, S., Rouse, M. and Wipf, T. (2014) “Structural Characterization of UHPC Waffle Bridge Deck and Connections,” IHRB Project TR-614, Iowa Highway Research Board, Ames, IA.

ACI Committee 318 (2014). “Building Code Requirements for Structural Concrete and Commentary.” ACI 318-14, American Concrete Institute Farmington Hills, MI.

ACI Committee 546. (2006) “Guide for the selection of materials for the repair of concrete.” ACI 546.3R-06, American Concrete Institute Farmington Hills, MI.

American Concrete Institute (2013). “Code Requirements for Evaluation, Repair, and Rehabilitation of Concrete Buildings.” ACI 562M-13.

ASTM Standard C39 (2016) “Standard Test Method for Compressive Strength of Cylindrical Concrete Specimens,” ASTM International, West Conshohocken, PA.

ASTM Standard C78. (2016). “Standard Test Method For Flexural Strength of Concrete (Using Simple Beam with Third-Point Loading),” ASTM International, West Conshohocken, PA.

ASTM Standard C496 (2017) ”Standard Test Method for Splitting Tensile Strength of Cylindrical Concrete Specimens,” ASTM International, West Conshohocken, PA.

ASTM Standard C882 (2013a) ”Standard Test Method for Bond Strength of Epoxy-Resin Systems Used with Concrete by Slant Shear,” ASTM International, West Conshohocken, PA.

ASTM Standard C1583 (2013) ”Standard Test Method for Tensile Strength of Concrete Surfaces and the Bond Strength or Tensile Strength of Concrete Repair and Overlay Materials by Direct Tension (Pull-Off Method),” ASTM International, West Conshohocken, PA.

ASTM Standard C1611 (2014) ”Standard Test Method for Slump Flow of Self-Consolidating Concrete,” ASTM International, West Conshohocken, PA.

ASTM Standard C1856 (2017) “Standard Practice for Fabricating and Testing Specimens of Ultra-High Performance Concrete,” ASTM International, West Conshohocken, PA.

Berry, M., Snidarich, R., and Wood, C. (2017) “Development of Non-Proprietary Ultra-High Performance Concrete”, FHWA/MT-17-010/8237-001, Montana DOT, Helena, MT.

Bruce, S. M., McCarten, P. S., Freitag, S. A., and Hasson, L. M. (2008) "Deterioration of Prestressed Concrete Bridge Beams," Land Transport New Zealand Research Report 337.

Campos, R. (2020) “Effect of fiber content on tensile strength of non-proprietary ultra-high performance concrete,” MS Thesis, University of Oklahoma, Norman, OK.

Casey, C. (2019) “Ultra-High Performance Concrete for Connections of Precast, Prestressed Girders Made Continuous for Live Load,” M.S. Thesis, The University of Oklahoma, Norman, OK.

Chea, K. S. V. (2020) “Comparative study of proprietary and non-proprietary ultra-high performance concrete as partial depth joint replacement,” MS Thesis, University of Oklahoma, Norman, OK.

Climaco, J. C. T. S., and Regan, P. E. (2001). "Evaluation of bond strength between old and new concrete in structural repairs." Magazine of Concrete Research, 53(6), pp. 377-390.

Coggins, F. B. and French, C. W. (1990) "Chloride Ion Distribution in Twenty-Year-Old Prestressed Bridge Girders," *ACI Materials Journal,* 87(5): 479-488.

Choate, J. (2018). “Implementing Fiber-Reinforced, Self-Consolidating Concrete as a Repair Material for AASHTO Prestressed Concrete Girders.” MS thesis, University of Oklahoma, Norman, OK.

Coleman, R. (2018) “Comparative Study of Surface Preparation and Bond Angle Combinations for Bridge Repair Using Ultra-High Performance Concrete Alternative,” M.S. Thesis, The University of Oklahoma, Norman, OK.

“Concrete Repair Products - See Our Data Guides.” (2020) Phoscrete Corporation. https://www.phoscrete.com/data-guides/.

Connecticut Department of Transportation (2016) “Repair of Steel Beam/Girder Ends with Ultra High-Strength Concrete – Phase II,” SPR 2295, Newington, CT.

Denarie, E., and Bruhwiler, E., “Structural Rehabilitations with Ultra-High Performance Fibre Reinforced Concretes (UHPFRC),” *Restoration of Buildings and Monuments*, Vol. 12, No. 5/6, 2006, pp. 453-468

Diab, A. M., Eldin, M. R. T., and Elmoaty, (2016) A. E. M. A., “Slant Shear Bond Strength Between Self Compacting Concrete and Old Concrete,” *Construction and Building Materials* 130, pp.73-82.

Ding, Z. and Li, Z. (2005) “High-Early-Strength Magnesium Phosphate Cement with Fly Ash,” *ACI Materials Journal*, 102(6): 375-381.

Ding, Z., Dai, J.G., Sarfraz, M. (2014) “Study on an Improved Phosphate Cement Binder for the Development of Fiber-Reinforced Inorganic Polymer Composites,” *Polymers*, 6: 2819-2831.

Dyachkova, Y. (2020) “Effect of Steel Fiber Content on Mechanical Properties of Non-proprietary Ultra-High Performance Concrete,” MS Thesis, University of Oklahoma, Norman, OK.

El-Batanouny, M. K., Mangual, J., Ziehl, P. H., and Matta, F. (2014) "Early Corrosion Detection in Prestressed Concrete Girders Using Acoustic Emission," *Journal of Materials in Civil Engineering,* 26(3): 504-511.

El-Tawil, S., Alkaysi, M., Naaman, A. E., Hansen, W., and Liu, Z. (2016) “Development, Characterization and Applications of a Non Proprietary Ultra High Performance Concrete for Highway Bridges, RC-1637, Michigan Department of Transportation, Lansing, MI.

El-Tawil, S., Tai, Y.S., Meng, B., Hansen, W., and Liu, Z. (2018) “Commercial Production of Non-Proprietary Ultra-High Performance Concrete, RC-1670, Michigan Department of Transportation, Lansing, MI.

El-Tawil, S., Tai, Yuh-Shiou, and Belcher II, J. A. (2018) “Field Application of Nonproprietary Ultra-High-Performance Concrete, *Concrete International*, January 2018.

Fantilli, A.P., Vallini, P., Chiaia, B. (2011) “Ductility of Fiber-Reinforced Self-Consolidating Concrete Under Multi-Axial Compression,” *Cement and Concrete Composites*, 33(4): 520-527.

Floyd, R. W., Pei, J. S., Murray, C. D., Cranor, B., Tang, P. F. (2016) “Understanding the Behavior of Prestressed Girders after Years of Service,” Report No. FHWA-OK-16-03, Oklahoma Department of Transportation, Oklahoma City, OK, December, 184 pp.

Floyd, R. W., Volz, J. S., Funderburg, C. K., McDaniel, A. S., Looney, T., Choate, J., Roswurm, S., Casey, C., Coleman, R., Leggs, M, and Chea, K. S. V., (2021) “Evaluation of Ultra-High Performance Concrete for Uses in Bridge Connections and Repair,” (under review), Oklahoma Department of Transportation, Oklahoma City, OK.

Fournier, P. (2014) “Bridge Maintenance Experts Evaluate MALP Concrete Repair Technology Applied to Route 26 Span, *Constructioneer*, August 2014, ACP Indianapolis, IN.

Freyermuth, C. L. (1969) “Design of Continuous Highway Bridges with Precast, Prestressed Concrete Girders,” *PCI Journal*, 14(2): 14-39.

Funderburg, C. (2018). “Evaluation of Surface Preparation and Bond Angle Combinations for Joint Replacement Using Ultra-High Performance Concrete.” MS Thesis, University of Oklahoma, Norman, OK.

Gangi, M., Jones, M., Liesen, J., Zhou, J., Pino, V., Cousins, T.E., Roberts-Wollmann, C.L., Koutromanos, I., and Nanni, A. (2018) “Evaluation of Repair Techniques for Impact-Damaged Prestressed Beams,” Report No. FHWA/VTRC 18-R8, Virginia Department of Transportation, Richmond, VA, 78 pp.

Graybeal, B. (2006) *Material Property Characterization of Ultra-High Performance Concrete*, FHWA-HRT-06-103, Federal Highway Administration, McLean, VA.

Graybeal, B. and Tanesi, J. (2007) “Durability of Ultra-High Performance Concrete.,” *Journal of Materials in Civil Engineering*, 19(10): 7 pp. https://doi.org/10.1061/(ASCE)0899-1561(2007)19:10(848)

Graybeal, B., (2011) “Tech Note | Ultra-High Performance Concrete,” FHWA-HRT-11-038, Federal Highway Administration, McLean, VA.

Graybeal, B. (2013) “Development of Non-Proprietary Ultra-High Performance Concrete for Use in the Highway Bridge Sector”, FHWA-HRT-13-100, Federal Highway Administration, McLean, VA.

Graybeal, B., (2014) “Design and Construction of Field-Cast UHPC Connections,” FHWA-HRT-14-084, Federal Highway Administration, McLean, VA.

Graybeal, B.A. (2014). Splice Length of Prestressing Strand in Field-Cast Ultra-High Performance *Concrete Connections*, FHWA-HRT-14-041, Federal Highway Administration, Department of Transportation, McLean, VA.

Graybeal, B. (2016) “Bond of Field-Cast Grouts to Precast Concrete Elements.” FHWA-HRT-16-081, Federal Highway Administration, McLean, VA.

Habel, K., Denarie, E., and Bruhwiler, E., (2004) “Structural response of composite ‘UHPFRC-concrete’ members under bending,” Proceedings of the International Symposium on Ultra High Performance Concrete, Kassel, Germany.

Haber, Z.B., Munoz, J.F., Graybeal, B.A. (2017). “Field Testing of an Ultra-High Performance Concrete Overlay.” FHWA-HRT-17-096, Federal Highway Administration, McLean, VA.

Hansson, C.M., Poursaee, A., and Laurent, A. (2006) “Macrocell and Microcell Corrosion of Steel in Ordinary Portland Cement and High Performance Concretes.” *Cement and Concrete Research*, 36(11): 2098-2102.

Harries, K.A., Kasan, J., Aktas, C. (2009) “Repair Methods for Prestressed Concrete Girders”, Report No. FHWA-PA-2009-008-PIT 006, The Pennsylvania Department of Transportation, Harrisburg, PA. 169 pp.

Harries, K.A. and Miller, R. (2012) “Updated Research for Collision Damage and Repair of Prestressed Concrete Beams,” NCHRP Project 20-07, Task 307, University of Pittsburgh, Pittsburg, PA, 228 pp.

Higgins, C., Williams, G., Mitchell, M., Dawson, M, and Howell, D. (2012) “Shear Strength of Reinforced Concrete Girders with Carbon Fiber-Reinforced Polymer: Experimental Results,” *ACI Structural Journal*, 109(6): 805-814.

Jones, D. A. (1966) *Principles and Prevention of Corrosion*. Prentice-Hall.

Kassimi, F. (2013) “Development and Performance of Fiber-Reinforced Self-Consolidating Concrete for Repair Applications.” PhD dissertation, University of Sherbrooke, Sherbrooke, Quebec.

Kassimi, F., El-Sayed, A., and Khayat, K. (2014) “Performance of Fiber-Reinforced Self-Consolidating Concrete for Repair of Reinforced Concrete Beams.” *ACI Structural Journal*, 111(6): 1277-1286.

Khayat, K. and Aitcin, P. (1998). “Use of Self-Consolidating Concrete in Canada - Present Situation and Perspectives.” Proceedings, Workshop on Self-Compacting Concrete, JSCE Concrete Engineering Series 30, Kochi, Japan, Ed. Ozawa, K. and Ouchi, M., August, pp. 11-22.

Khayat, K., Petrov, N., Assaad, J., Morin, R., and Thibault, M. (2005) “Performance of SCC Used in Repair of Retaining Wall Elements.” Proceedings, 2nd North American

Conf. on the Design and Use of Self-Consolidating Concrete, Ed. Shah, S., Chicago, IL, November, 9 p.

Khayat, K.H. and Abdelrazik, A. (2017) “Performance of Fiber-Reinforced Self-Consolidating Concrete for Repair of Bridge Sub-Structures and Fiber-Reinforced Super Workable Concrete for Infrastructure Construction,” TR2015-05, Sept. 2017, Missouri Department of Transportation, Jefferson City, MO.

Khayat, K.H. and Valipour, M. (2018). “Design and Performance of Cost-Effective Ultra High Performance Concrete for Bridge Deck Overlays.” CMR 18-006, Missouri Department of Transportation, Jefferson City, MO.

Leggs, M. (2019) “Evaluation of Durability and Corrosion Behavior of Ultra-High Performance Concrete for use in Bridge Connections and Repair,” MS Thesis, University of Oklahoma, Norman, OK.

Li, W., Huang, Z., Zu, T., Shi, C., Duan, W. H., and Shah, S. P. (2016) “Influence of Nanolimestone on the Hydration, Mechanical Strength, and Autogenous Shrinkage of Ultrahigh-Performance Concrete,” *ASCE Journal of Materials in Civil Engineering*, 28(1): 04015068.

Looney, T., McDaniel, A., Volz, J., and Floyd, R. (2019) “Development and Characterization of Ultra-High Performance Concrete with Slag Cement for Use as Bridge Joint Material”, *British Journal of Civil and Architecture Engineering*, 1(2): 1-14.

Looney, T., Coleman, R., Funderburg, C., Volz, J., and Floyd, R. (2021) “Concrete Bond and Behavior of Non-Proprietary Ultra-High Performance Concrete Bridge Slab Joints,” *ASCE Journal of Bridge Engineering*, 26(2): 11 pp., DOI: 10.1061/(ASCE)BE.1943-5592.0001669.

Mayhorn, D. (2016). “Investigation of the Effects of End Region Deterioration in Precast, Prestressed Concrete Bridge Girders,” MS thesis, University of Oklahoma, Norman, OK.

Mayhorn, D. T., Murray, C. D., Floyd, R. W., and Prinz, G. S. (2018) “Effect of Corrosion on End Region Behavior of Pretensioned, Prestressed Bridge Girders,” 2018 PCI Convention and National Bridge Conference, Denver, CO, February 20-24, 2018.

McDaniel, A. (2017) “Development Of Non-Proprietary Ultra-High-Performance Concrete Mix Design”, M.S. Thesis, University of Oklahoma, Norman, OK.

Miller, R. A., Castrodale, R., Mirmiran, A., and Hastak, M. (2004) “Connection of Simple-Span Precast Concrete Girders for Continuity,” NCHRP Report 519, Transportation Research Board, Washington, D.C.

Mintz, B. (February 1, 2018) “Expansion Joint Headers”, Retrieved from https://phoscrete.com/expansion-joint-headers/ on July 1, 2018.

Mintz, B. (February 2, 2018) “Concrete Spall Patches”, Retrieved from https://phoscrete.com/concrete-spall-patches/, on July 1, 2018.

Mobasher, B., Arora, A., Aguayo, M., Kianmofrad, F., Yao, Y., and Neithalath, N. (2019) “Developing Ultra-High-Performance Concrete Mix Designs for Arizona Bridge Element Connections, FHWA-AZ-19-745, Arizona Department of Transportation, Phoenix, AZ.

Momayez, A., Ehsani, M. R., Ramezanianpour, A. A., and Rajaie, H., (2005) “Comparison of Methods for Evaluating Bond Strength Between Concrete Substrate and Repair Materials”, *Cement and Concrete Research*, Vol. 35, No. 4, pp. 748-757.

Munoz, M.A.C., Harris, D.K., Ahlborn, T.M., Froster, D.C. (2014). “Bond Performance Between Ultrahigh-Performance Concrete and Normal-Strength Concrete.” ASCE 04014031, *J. Mater. Civ. Engin.*, 26(8):1-8.

Murray, C. D. (2017) “Understanding Ultimate Shear Behavior of Prestressed Concrete Girder Bridges as a System Through Experimental Testing and Analytical Methods, Ph.D. Dissertation, The University of Oklahoma, Norman, OK.

Oesterle, R.G., Glikin, J.D., and Larson, S.C. (1989) “Design of Precast Prestressed Bridge Girders Made Continuous,” NCHRP Report 322, Transportation Research Board, Washington, D.C.

Ozyildirim, C. (2013). “Use of SCC for the Repair of Bridge Substructures.” Presentation, ACI 2013 Spring Convention.

Pape, T. M. and Melchers, R. E. (2013) "Performance of 45-year-old corroded prestressed concrete beams," *Structures and Buildings,* 166(SB10): 547-559.

Pei, J.S., Martin, R.D., Sandburg, C.J., and Kang, T.H.-K. (2008) “Rating Precast Prestressed Concrete Bridges for Shear,” Report No. FHWA-OK-08-08, Oklahoma Department of Transportation, Oklahoma City, OK, 118 pp.

Phares, B. (2014) “Laboratory and Field Evaluation of an Alternative UHPC Mix and an Associated UHPC Bridge,” Project in Progress, Iowa Department of Transportation, Ames, IA.

Phoscrete (July 11, 2014) “MALP Concrete Performance Specifications”, Retrieved from https://phoscrete.com/wp-content/uploads/2018/02/MALP-Concrete-Performance-Specification.pdf, on July 1, 2018.

Pough, K., Mayhorn, D., Prinz, G. S., and Floyd, R. W., “Evaluation and Repair of Existing Bridges in Extreme Environments, Report No. SPTC14.1-58-F, Southern Plains Transportation Center, Norman, OK, January 2017, 199 pp.

Precast/Prestressed Concrete Institute (PCI) (2006) *Manual for the Evaluation and Repair of Prestressed Concrete Bridge Products,* PCI MNL-137-06, Precast/Prestressed Concrete Institute, Chicago, IL.

Ramanathan, K. and Harries, K.A. (2008) “Influence of FRP Width-To-Concrete Substrate Width (b_f/b) on Bond Performance of Externally Bonded FRP Systems, *Proceedings of the 12th International Conference on Structural Faults and Repair*, Edinburgh, Scotland

Reed, C.E. and Peterman, R.J. (2004) “Evaluation of Prestressed Concrete Girders Strengthened with Carbon Fiber Reinforced Polymer Sheets, *ASCE Journal of Bridge Engineering*, 9(2): 60-68.

Reed, C.E., Peterman, R.J., Rasheed, H., and Meggers, D. (2007) “Adhesive Applications Used During Repair and Strengthening of 30-Year-Old Prestressed Concrete Girders, *Transportation Research Record*, 1827: 36-43.

Rogers, R. A., Wotherspoon, L., Scott, A., and Ingham, J. M. (2012) "Residual strength assessment and destructive testing of decommissioned concrete bridge beams with corroded pretensioned reinforcement," *PCI Journal,* 57(3): 100-118.

Saadeghvaziri, M., Spillers, W., and Yin, L. (2004) “Improvement of Continuity Connection over Fixed Piers,” FHWA-NJ-2004-017, Federal Highway Administration, Department of Transportation, Newark, NJ.

Sarkar, J., (2010) “Characterization of the Bond Strength between Ultra High Performance Concrete Bridge Deck Overlays and Concrete Substrates,” Michigan Technological University.

Shafei, B., Phares, B., and Shi, W. (2020). “Beam End Repair for Prestressed Concrete Beams,” IHRB Project TR-715, Iowa Department of Transportation, Ames, IA.

Shanafelt, G.O. and Horn, W.B. (1985) “Guidelines for Evaluation and Repair of Prestressed Concrete Bridge Members, NCHRP Report 280, Transportation Research Board, Washington, D.C., 93 pp.

Shanafelt, G.O. and Horn, W.B (1980) “Damage Evaluation and Repair Methods for Prestressed Concrete Bridge Members,” NCHRP 226, Transportation Research Board, Washington, D.C., 77 pp.

Shield, C. and Bergson, P. (2018) “BR27568 – Experimental Shear Capacity Comparison Between Repaired and Unrepaired Girder Ends,” Report No. MN/RC 2018-07, Minnesota Department of Transportation, St. Paul, MN, 144 pp.

Szilard, R. (1969) "Corrosion and Corrosion Protection of Tendons in Prestressed Concrete Bridges," *ACI Journal,* 66(1): 42-59.

Tabatabai H., Ghorbanpoor, A., and Turnquist-Naas, A. (2004) “Rehabilitation Techniques for Concrete Bridges,” Report No. WHRP 05-01, Wisconsin Department of Transportation, Madison, WI, 315 pp.

Tackett, A., Floyd, R., Ruiz, E., and Hale, W. (2009) “Effect of Mixer Type on the Performance of Ultra-High Performance Concrete”. Proceedings of the 11th Annual International fib Symposium, London, United Kingdom, June 22-24, 2009.

Tayeh, B. A., Abu Bakar, B. H., Mehat Johari, M. A., and Voo, Y. L., (2013) "Evaluation of bond strength between normal concrete substrate and ultra-high performance fiber concrete as a repair material," Procedia Engineering 54 pp. 554-563.

Wang, L., Yi, J., Zhang, J., Jiang, Y., Zhang, X. (2017) “Effect of corrosion-induced crack on the bond between strand and concrete,” *Construction and Building Materials*, 153: 598-606.

Wibowo H. and Sritharan, S. (2018). “Use of Ultra-High-Performance Concrete for Bridge Deck Overlays.” IHRB Project TR-683, Ames, IA.

Wille, K. (2013) *Development of Non-Proprietary Ultra-High Performance Concrete for Use in the Highway Bridge Sector*, Report No. PB2013-110587, NTIS, Springfield, VA.

Wille, K., Naaman, A., and Parra-Montesinos, G. (2011) “Ultra-High Performance Concrete with Compressive Strength Exceeding 150 MPa (22 ksi): A Simpler Way,” *ACI Materials Journal*, 108(1): 46-54.

Williams, E. M., Graham, S. S., Reed, P. A., and Rushing, T. S. (2009) *Laboratory Characterization of Cor-Tuf Concrete With and Without Steel Fibers*, ERDC/GSL TR-09-22, U.S. Army Engineer Research and Development Center, Vicksburg, MS.

Wirkman, C. (2016). “Performance of Fiber-Reinforced Self-Consolidating Concrete for Repair of Bridge Sub-Structures.” MS thesis, University of Oklahoma, Norman, OK.

Yue, L. and Bing, C. (2013) “Factors that affect the properties of magnesium phosphate cement”, *Construction and Building Materials* 47: 977-983.

Zmetra, K.M. (2015). “Repair of Corrosion Damaged Steel Bridge Girder Ends by Encasement in Ultra-High Strength Concrete.” PhD Dissertation, University of Connecticut, Hartford, CT.